

Endterm Submission

LAT Aerospace High Prep PS

Team 21

We have implemented high lift concepts including Co-Flow Jets, Upper surface, flaps and morphed wings. CFD simulations were performed to determine aerodynamic characteristics. We have made tools (from scratch) to do calculations for and design a preliminary thrust producing device. We have used RL to design our own high lift airfoil.

Abstract

This report presents a comprehensive aerodynamic, propulsion, and systems-level design for an advanced powered-lift wing intended to achieve extraordinarily high lift coefficients while maintaining efficient cruise performance. The design is motivated by the mission need for a compact 1.4 m wingspan lifting surface capable of attaining effective wing lift coefficients in the range of $CL \approx 6\text{--}8$ during take-off and approach, enabled through strong interaction between multi-element high-lift devices, distributed electric propulsion, upper-surface blowing (USB), jet-flap effects, and Co-Flow Jet (CFJ) mechanisms. The resulting configuration provides a high-performance solution for STOL-type operation while preserving structural practicality and trim feasibility.

Baseline Airfoil Selection and Modification

A detailed screening of candidate airfoils—including the NACA 23- and 44-series, S1223, and E423—was performed using XFOIL/XFLR5 at $Re = 5 \times 10^5$ and $M = 0.244$. High-performance STOL sections such as S1223 and E423 offered the strongest promise, with the S1223 delivering $CL_{\max} \approx 2.3$ but exhibiting a sharp stall and large nose-down moment. After parametric geometric refinement, a **modified S1223** was selected as the final single-element baseline. The modified version features:

- Increased thickness ($t/c \approx 18.2\%$) for structural volume and CFJ ducting,
- Retained high camber suited for powered-lift integration,
- Improved stall angle ($\alpha_{\text{stall}} \approx 13.3^\circ$),
- High cruise efficiency ($C_L/C_D \approx 70.9$ at $\alpha \approx 0^\circ$).

This airfoil provides an excellent foundation for both multi-element lift enhancement and momentum-based flow control.

Multi-Element High-Lift System

To achieve unblown sectional lift levels of $CL_{\max,2D} \gtrsim 3$, a high-performance **single slotted flap** was adopted, balancing aerodynamic gain with mechanical complexity.

Literature-backed ranges for flap gap, chord ratio, and deflection were established, followed by CFD-driven refinement. Key characteristics include:

- Optimal flap chord ratio $c_f/c \approx 0.30$,
- Gap varied over 1–4% of chord for design-space exploration,
- Deflection angles in the range of 30° – 50° ,
- Slot design enabling delayed separation and strong lift augmentation under blowing.

This system ensures linear lift build-up over a wide AoA range, maintains attached flow under strong turning, and supports high powered-lift effectiveness.

Powered-Lift Concepts: USB, CFJ, and Blown Flaps

Three momentum-based lift augmentation mechanisms were analysed and integrated:

1. **Upper Surface Blowing (USB)** — Jet attachment over the main element and flap enhances circulation and induces a powerful jet-flap turning effect.
2. **Blown Slotted Flaps** — Slot momentum injection delays separation and enables large flap deflections without stall penalties.
3. **Co-Flow Jet (CFJ)** — A combination of suction near the leading edge and blowing over the aft surface re-energises boundary layers and increases effective camber, improving both lift and stall margin.

CFD and mathematical models demonstrate that the synergy between these mechanisms offers significantly higher lift augmentation than any single system alone.

Distributed Electric Propulsion (DEP) and EDF Design

A detailed analysis of propeller slipstream effects, momentum addition, and wing-prop aerodynamic coupling led to the deployment of distributed electric propulsion modules. These modules are optimised through:

- Streamwise and spanwise placement studies,
- Slipstream-airfoil interaction modelling,
- Off-design thrust and torque modelling,
- A full rotor-stator EDF design using BEMT, free-vortex methods, and CFD.

The EDF subsystem was designed from first principles, including blade aerodynamics, stator swirl recovery, centrebody/nacelle shaping, and structural verification via FEA. Thrust bench testing and degradation modelling further validated the design.

Upper-Surface Blowing CFD, Jet-Flap Theory, and Integration

Jet-flap theory and thick-jet USB models were implemented to determine jet attachment, circulation enhancement, and turning efficiency. CFD studies confirmed:

- High-efficiency jet turning over large flap deflections,
- Strong increases in CL proportional to momentum coefficients,
- Delayed separation on both main element and flap.

Combined with DEP, USB and CFJ yield the required powered-lift performance.

Final Results

The final 2-D simulations gave a C_L value at take-off of 9.49 and a L/D value at cruise as 19.

Contents

1 Airfoil Selection	13
1.1 Single-Element Reference Section	13
1.1.1 Desired Characteristics	13
1.1.2 Candidate Airfoil Families	14
1.1.3 Compatibility with USB, CFJ, and Blown Flaps	14
1.2 Baseline Airfoil Screening and Final Selection	15
NACA 23012	15
NACA 4412	16
NACA 4415	16
S1223	16
E423	16
Interim Conclusion	16
1.3 Multi-Element High-Lift Section	19
1.3.1 Desired Characteristics	19
1.3.2 Typical Multi-Element Configuration	19
1.3.3 Compatibility with USB, CFJ, and Blown Flaps (Multi-Element) .	20
1.4 Flap Design	21
1.4.1 Philosophy and Methodology	21
1.4.2 Obtaining initial bounding ranges	22
1.4.3 Making the flap geometry	29
2 High Powered Lift Concepts Considered	31
2.1 Co-Flow Jet (CFJ) Airfoils	32

2.1.1	Solving the case of a circle	34
2.1.2	Transforming between shapes	34
2.1.3	Introducing Co-Flow Jet	35
2.1.4	CFD Results using Co-Flow Jets	36
2.1.5	Experimental results for NACA 6415 from literature	37
3	Thrust Producing Devices	40
3.1	Placement of the Distributed Electric Propulsion Modules	40
3.1.1	Introduction	40
3.1.2	Literature Review	40
	Effect of propeller slipstream on wing lift distribution	40
	Effect of propeller slipstream on wing :	40
	Effects of Wing on the Propeller :	40
	Effect of Propeller Spacing	41
	Effect of Propeller Location (Streamwise)	41
	The Effect of Jet Location on the Performance of a Blown Wing	42
3.1.3	Effect of Motor Mount Angle	44
3.1.4	Optimum Propeller Diameter and Number	45
	Design Architecture and Constraints	45
	Justification for 5-inch Diameter Selection	45
	Aerodynamic Performance Validation (Rotor and Stator Design)	45
	Powertrain Selection and Safety Margin Verification	46
	Margin Analysis	47
3.1.5	Methodology	48
	Model Setup	48
	Assumptions :	49
	Iterations	50
	Explanation:	52
	53
3.1.6	Conclusion	53
3.2	Rotor and Stator Design for EDF	53
3.2.1	Introduction	53
3.2.2	Non Dimensional Constants	54
	Flow Coefficient Assumption	54
	Definition and Selection	54
	Calculation of Velocities	55
	Step 1: Specific Work Calculation (Δh_0)	55
	Step 2: Determining Blade Speed (U_m) and Angular Velocity (ω)	55
	Step 3: Calculating Axial Velocity (V_x)	56
	Summary of Design Logic	56
3.2.3	Topology Optimization: Blade Count Selection	56
	Rotor Blade Count Optimization	57

Prandtl Tip Loss Factor and Induced Power	57
Profile Power and Reynolds Number Scaling	57
Stator Vane Count and Acoustics	58
Acoustic Interaction and the Coprime Rule	58
3.2.4 Aerodynamic Design Methodology	60
Free-Vortex Flow Model	60
Tangential Velocity Distribution	60
Radial Equilibrium and Axial Velocity	61
Blade Element Momentum Theory (BEMT)	61
Thrust and Torque Formulation	61
Iterative Chord Scaling	61
3.2.5 Geometric Parameters and Airfoil Selection	62
Airfoil Selection: NACA 4412	62
Lift Coefficient and Angle of Attack	62
Justification of Assumption	62
Resulting Angle of Attack	62
Chord Distribution and Diffusion Factor	62
Bezier Chord Distribution	63
Lieblein Diffusion Factor (DF)	63
Twist and Pitch	63
Hub-to-Tip Ratio	63
3.2.6 Stator Design: Swirl Recovery	64
Swirl Removal Logic	64
Stator Airfoil and Loading	64
3.2.7 Conclusion	66
3.3 EDF Centrebody and Nacelle Design	68
3.3.1 Centerbody Aerodynamics: The Spinner Cone	68
Geometry Selection: High L/D Elliptical Profile	69
Skin Friction and Boundary Layer Analysis	69
3.3.2 Exhaust Cone Design: Diffusion and Structural Integration	71
Pressure Recovery and Profile	71
Weight Optimization: Hollow Shell Architecture	72
Structural Mounting: M2 Bolt Analysis	72
Load Case Definition	72
Bolt Stress Calculation	72
Thread Pull-Out Analysis	73
3.3.3 Nacelle Aerodynamics and Variable Thickness	74
Inlet Lip Optimization	74
Variable Thickness Outer Mold Line (OML)	74
Tip Vortex Reduction: The Duct Effect	75
3.3.4 Conclusion	76
3.4 Complete Assembly of Electric Ducted Fan and Off Design Performance	78

3.4.1	Fundamental Constraint: Constant Power	78
3.4.2	Environmental Parameters	79
3.4.3	Aerodynamic Drag Decomposition	79
	External Flow Regime (Nacelle OML)	79
	Internal Flow Regime (Spinner & Tailcone)	79
3.4.4	Numerical Integration Scheme	80
3.5	Mathematical Model- Fluid Interaction	81
3.5.1	Introduction	82
	Filament Vortices	82
	Setting the Stage	83
	Weight Function	84
3.5.2	Making the Grid	85
3.5.3	Trailer Vortices	86
3.5.4	Distinction in Components of Velocities	86
	2-D case of Velocity Separation	86
	3-D Case of Velocity Separation	87
3.5.5	Thrust and Torque Calculation	87
3.5.6	Notes	88
	Post-stall polar extension using the Viterna–Corrigan method	88
	Axial Velocity input	89
	Γ considerations	89
	Biot Savart Applications considerations	90
3.5.7	Calculating Values	90
3.6	Mathematical Model- Stress Analysis	91
3.6.1	Notation and units	91
3.6.2	Blade geometry and chord law	91
3.6.3	Airfoil cross-section and section properties	92
3.6.4	Aerodynamic loading using polars	93
3.6.5	Centrifugal axial tension	93
3.6.6	Shear force and bending moment (resultants)	94
3.6.7	Thin-walled shear-flow slice method	94
3.6.8	Torsional shear	95
3.6.9	Beam model (Euler-Bernoulli) for flapwise bending	95
3.6.10	Stress computation (outer fiber)	96
3.7	Numerical Analysis- Stresses and Fluid Interaction	96
3.7.1	Static Structural Analysis of the Rotor	96
	Geometry and Engineering Data	96
	Material Properties	96
	Mesh Quality Metrics	97
	Grid Independence Study	97
	Loads and Boundary Conditions	97
	Boundary Conditions Setup :	98

Analysis Setup	98
Results	98
3.7.2 Structural Analysis of the Stator	99
Geometry and Engineering Data	99
Material Properties	99
Mesh Quality Metrics	99
Grid Independence Study	100
Loads and Boundary Conditions	100
Analysis Setup	100
Results	101
3.7.3 CFD of the Rotor	101
Computational Domain and Boundary Conditions	101
Mesh Quality metrics	102
Grid Independence Study	102
Numerical Setup	102
Viscous model :	102
Material properties :	103
Cell Zone Conditions :	103
Boundary Conditions :	103
Solution Methods :	103
Results	104
Flow Field Visualization :	104
Key observations :	104
3.8 Controls Framework and Test Setup for EDF	105
3.8.1 Throttle Control for Testing	105
3.8.2 Throttle Adjustments due to Degradation	106
3.8.3 Further Optimisation for Distributed Propulsion	107
3.8.4 Test Bench for Electric Ducted Fan (EDF)	107
Design Philosophy	108
Structural Architecture	108
Base Plate	108
MGN15H Linear Guideway	108
Top Plate and Slider Assembly	108
Load Cell and Mount	108
Dynamic Considerations	109
Instrumentation	109
Material Selection	110
Safety Measures	110
Conclusion	110
3.9 Degradation Modelling for EDF	110
3.9.1 Introduction	110
3.9.2 Design Justification & Trade-off Analysis	110

3.9.3	System Physics & Mathematical Modeling	111
	Parameter Identification	111
	State-Space Formulation	111
	Electrical Dynamics	112
	Mechanical Dynamics	112
	Thermal Dynamics	112
3.9.4	System Architecture & Sensing	112
	Physical Configuration	112
	Sensor Suite	112
3.9.5	Multi-Rate Control Framework	113
	Fast Loop (1 kHz / 1000 μ s)	113
	Medium Loop (50 Hz / 20 ms)	113
	Slow Loop (1 Hz / 1000 ms)	114
3.9.6	Estimation Algorithms	114
	Extended Kalman Filter (EKF)	114
	Recursive Least Squares (RLS)	115
	Electrical Health RLS	115
	Mechanical Health RLS	115
	Tuning the Forgetting Factor	115
3.9.7	Simulation & Validation Scenario	116
	Mission Profile	116
	Fault Injection	116
	Validation Results	116
	Interpretation of Graphs:	116
3.9.8	Interpretation of Results	117
	Row 1: State Estimation Performance	117
	Row 2: Electrical Health Monitoring	117
	Row 3: Mechanical Health Monitoring	118
	Rapid Diagnosis Guide	119
	Analysis of Physical Test Data	119
	Operational Utility for the End User	120
3.10	Prototype Fabrication and Experimental Setup	120
3.10.1	Manufacturing and Material Selection	120
3.10.2	Assembly and Integration	121
3.10.3	Experimental Test Bench Setup	121
	Results	121
3.10.4	Proposed Material Selection for Flight Hardware	122
3.11	Scaling Analysis and Comparation : Medium Bypass Turbofans, Electric Ducted Fans, and Arrays of Small Turbofans	123
3.11.1	Introduction	123
3.11.2	Core scaling relations	123
3.11.3	Medium BPR turbofan: scaling implications and expected performance	124

3.11.4	Electric Ducted Fans: scaling and energy considerations	124
3.11.5	Scaling Analysis and Comparative Evaluation of Medium Bypass Turbofans, Electric Ducted Fans, and Arrays of Small Turbofans	125
	Introduction	125
	Fundamental scaling relations	125
	Medium bypass turbofan scaling	126
	EDF architectures and power scaling	127
	Arrays of small turbofans	127
	Clarifying the scaling trade through an illustrative example	128
	Aerodynamic integration and DEP potential	128
	Conclusion from scaling analysis	129
	Mission scaling and twin medium BPR turbofan design point	129
3.12	Comprehensive Scaling Analysis, Propulsion Architecture Evaluation, Distributed Turbofan Assessment, and Final C17-Inspired Turbofan Design Point	131
3.12.1	Introduction	131
3.12.2	Scaling Laws for Ducted Propulsion	131
3.12.3	Medium Bypass Ratio Turbofans	132
3.12.4	Electric Ducted Fan Propulsion	132
3.12.5	Distributed Arrays of Small Turbofans	133
	Thermodynamic penalties	133
	Structural and mechanical duplication	133
	Installation drag and inlet penalties	133
	Acoustic penalties	133
	Conclusion on distributed turbofans	133
3.12.6	Mission Scaling and Twin Turbofan Reference Design	133
3.12.7	Distributed Small Turbofan Array: Literature-Based Design Point .	134
3.12.8	Final C17-Inspired Medium Bypass Turbofan Design Point	135
3.12.9	Final recommendation	135
3.13	One-Dimensional Thermodynamic Analysis, State Points, and Material Selection for a Literature-Anchored Micro-Turbofan Engine	136
3.13.1	Introduction	136
3.13.2	Literature Anchors and Baseline Parameters	136
3.13.3	Thermodynamic Assumptions	137
3.13.4	One-Dimensional Stationwise Analysis	137
	Station 0 to 2: Inlet	137
	Station 2 to 2f: Fan Compression	137
	Station 2c to 3: Core Compressor	138
	Station 3 to 4: Combustion	138
	Station 4 to 5: Turbine Work Balance	138
	Station 5 to 6/7: Nozzle Expansion	139
	Specific Fuel Consumption	139

3.13.5	Material Selection Based on Thermodynamic Loading	139
Compressor	139
Combustor Liner	140
Turbine Blades	140
Fan and Bypass Duct	140
Shafts and Discs	140
3.13.6	Conclusion	140
4	Upper Surface Blowing and Jet Flaps	140
4.1	Thin Jet Flap Theory	141
4.1.1	Introduction	141
4.1.2	Assumptions Made	142
4.1.3	Mathematical Model	143
4.1.4	Results	145
4.2	Upper Surface Blowing (Thick Jet)	146
4.2.1	Introduction	146
4.2.2	Assumptions	146
4.2.3	Mathematical Formulation	147
Influence-Coefficient System	147
Aerodynamic Coefficients	149
4.2.4	Implementation	149
Boundary Conditions:	150
4.2.5	Lift and Circulation	152
4.2.6	Results	153
4.3	CFD Simulations - Upper Surface Blowing with Flaps	155
4.3.1	Mesh Independence	155
4.3.2	Final Mesh Settings	155
4.3.3	Set-Up	156
4.3.4	Determination of the height of the thrust producing device	157
4.3.5	Shape optimisation of the main element trailing edge	158
4.3.6	Determination of the optimal flap deflection angle	159
5	RL Optimization of Airfoils for Co-Flow Jets	160
6	Background: RL-Based Airfoil Optimization à la Dussauge et al.	162
6.1	Airfoil parameterization	162
6.2	MDP formulation	162
6.3	Results	163
6.4	Limitations	163
7	NeuralFoil-Based RL for Airfoil Shape Optimization	164
7.1	Environment definition	164
State representation	164

Action space	164
Aerodynamic evaluation via NeuralFoil:	165
Reward function.	165
7.2 Advantages of NeuralFoil over XFOIL in RL	165
7.3 Results	166
8 Extending RL to Trailing-Edge Flaps	166
8.1 Action and state augmentation	166
8.2 Flap kinematics and geometry construction	166
8.3 Effect on RL dynamics	167
8.4 Results	167
9 FastFOIL and the Grand RL Environment	168
9.1 FastFOIL	168
Geometric and Actuation Parameters.	168
Modification to the Potential Field.	168
Boundary-Layer Momentum Adjustment.	168
Adaptive CFJ-driven XFOIL Execution.	169
9.2 Combined RL state and action spaces	169
Geometry control points.	169
CFJ parameters.	169
Flap parameters.	169
Action vector.	170
Geometry constraints.	170
Observation vector	170
9.3 Reward and evaluation	170
9.4 Results	171
10 Gradient-Based Parameter Search with AeroSandbox	172
10.1 Problem formulation	172
10.2 Advantages of RL over raw parameter search	172
1. Handling non-smooth, non-convex objectives.	172
2. Flexible action space and discrete decisions.	173
3. Sequential design and multi-step policies.	173
4. Robustness to solver failures.	173
5. Reuse of learned policies.	173
11 Effect of Training Time and Further Improvements	174
12 Morphing Wing	174
12.1 Aerodynamic Design Philosophy	174
12.1.1 The Multi-Point Design Problem	174
12.1.2 Airfoil Selection & Hybridization	174

12.1.3 The Telescoping Chord Rationale	175
12.2 Structural Mechanism & Actuation	175
12.2.1 Distributed Actuation Topology	175
Optimization of Actuator Placement	175
12.2.2 The Scissor-Rib (Pantograph) Mechanism	176
12.3 Morphing Skin Technology: Material Selection	176
12.3.1 Option A: Elastomeric Skins (Polyurethane)	176
12.3.2 Option B: Sliding Composite Shells (CFRP) — SELECTED	176
12.3.3 Selection Justification	177
12.4 Mathematical Formulation & Simulation Logic	177
12.4.1 Assumptions and Constants	177
12.4.2 Geometric Parameterization (Bézier Curves)	177
12.4.3 Structural Optimization Logic	178
12.4.4 Flight Control Logic (Kinematic Smoothing)	178
12.4.5 Aerodynamic Force Buildup	178
A. Required Lift ($C_{L,req}$)	178
B. Profile Drag ($C_{D,profile}$)	179
C. Induced Drag ($C_{D,induced}$)	179
D. USB Scrubbing Drag ($C_{D,scrub}$)	179
12.5 Performance Simulation Results	179
13 Final High Powered Lift Design	180
13.1 Take-Off Conditions	180
13.2 Cruising Conditions	181
13.2.1 Results	181
13.3 Aerodynamic Centre	182
14 Final Results	183

1 Airfoil Selection

Methodology to select an airfoil (and associated high-lift system) suitable for a high-powered, distributed propulsion wing.

The focus is on achieving very high lift coefficients under strong blowing (propeller slipstream, upper-surface blowing, Co-Flow Jet, blown flaps), while still maintaining acceptable cruise performance at the design cruise speed and having desirable stall and flow separation characteristics.

1.1 Single-Element Reference Section

1.1.1 Desired Characteristics

- **High baseline lift capability:** Unblown 2D $C_{l,\max}$ in the range of approximately 1.4–1.8, to allow powered-lift effects and high-lift devices to realistically push the effective wing C_L into the 6–8 envelope at low approach and take-off speeds.
- **Moderate-to-high camber, moderate thickness:** Thickness-to-chord ratio $t/c \approx 0.12\text{--}0.16$ and camber on the order of 3–4%:
 - Sufficient camber to generate strong circulation and a favourable upper-surface pressure distribution.
 - Enough thickness to house spars, ducts, and possible Co-Flow Jet (CFJ) plenums without excessive structural penalties.
- **Good stall behaviour and manageable pitching moment**
- **Upper-surface shape compatible with blowing:**
 - A relatively smooth suction peak near the leading edge, followed by a long region of mild adverse pressure gradient where blown momentum can re-energise the boundary layer.
 - Avoid excessively sharp suction peaks or strong adverse gradients that might separate prematurely when the flow is strongly turned by jets or propeller slipstreams.
- **Good interaction with propeller slipstream:**
 - The airfoil should retain predictable lift response under local dynamic pressures significantly higher than the freestream (e.g., $q_{\text{local}} \approx 2\text{--}4 q_\infty$ in the slipstream).
 - Lift coefficient C_l should scale approximately linearly with local angle of attack and dynamic pressure over the operational blowing range, to ensure controllable behaviour in distributed propulsion.

1.1.2 Candidate Airfoil Families

- **NACA 23-series and 44-series (e.g. NACA 23012, 23015, 4412, 4415):**
 - Widely used, with extensive data and experience in STOL and propeller-driven configurations.
 - Offer good stall characteristics, decent unblown lift, and acceptable cruise L/D .
- **STOL-optimised sections (e.g. Selig / Eppler families):**
 - Provide very high 2D $C_{l,\max}$ at low-to-moderate Reynolds numbers.
 - Can exhibit sharper stall and stronger nose-down moments; may be more sensitive to Reynolds number, roughness, and blowing, and thus require additional tailoring.
- **Custom-thickened / cambered variants:**
 - Start from a well-known baseline
 - Locally increase thickness inboard to accommodate structure and ducts.

1.1.3 Compatibility with USB, CFJ, and Blown Flaps

The single-element geometry must be compatible with the different powered-lift concepts considered:

- **Upper Surface Blowing (USB):**
 - Requires a smoothly curved upper surface from mid-chord to the trailing edge, so that a jet issuing from an over-wing engine or nozzle can attach and be turned downward (Coandă effect).
 - A moderate trailing-edge thickness and radius can help maintain jet attachment as the flow is turned.
- **Blown / Jet Flaps:**
 - The aft region of the airfoil must allow a relatively large flap chord (approximately 25–35% of the main chord) with structural depth and hinge space.
 - Thin, razor-edged aft sections are undesirable because they provide limited structural volume and poor integration for blowing slots.
- **Co-Flow Jet (CFJ):**
 - Requires internal volume for a plenum and ducting: a thickness of $t/c \approx 0.14\text{--}0.18$ near the root is beneficial.
 - The leading-edge region must accommodate a suction slot, while the upper surface must provide a practical location for the blowing slot (e.g. in the

mild adverse pressure gradient region or close to the flap shoulder), without introducing excessive curvature or shock formation.

Overall, the baseline single element is deliberately non-extreme: moderately thick and cambered, with gentle stall and a surface geometry that accepts various blowing concepts.

1.2 Baseline Airfoil Screening and Final Selection

Operating Point and Target Coefficients

The design point for the wing section is fixed by the aircraft cruise condition:

- Cruise speed: $V_\infty = 80$ m/s at 10,000 ft.
- Wing span: $b = 1.4$ m, aspect ratio $AR = 8$, planform area $S = 0.245$ m², chord $c = 0.175$ m.
- Atmospheric properties at 10,000 ft: $\rho = 0.90504$ kg/m³, $T = 268.35$ K, $a = 328.364$ m/s, $M = 0.244$.
- Relevant Reynolds number: $Re \approx 5 \times 10^5$ (based on chord).

Balancing weight and lift at cruise,

$$2mg = \frac{1}{2}\rho V_\infty^2 C_L S$$

for $m = 15$ kg per lifting surface gives the required cruise lift coefficient

$$C_{L,\text{cruise}} \approx 0.415.$$

Baseline Airfoil Screening

The following candidate sections were evaluated in XFOIL/XFLR5 at $Re = 5 \times 10^5$ and $M = 0.244$.

NACA 23012

- Thickness: $t/c = 12\%$ at $x/c \approx 0.30$.
- Maximum camber: 1.83% at $x/c \approx 0.13$.
- $C_{L,\text{max}} \approx 1.4$, stall at $\alpha \approx 14^\circ$ with acceptable but not outstanding stall behaviour.
- $C_L/C_D \approx 45$ at $C_{L,\text{cruise}}$.
- Pitching moment: $C_m(\alpha)$ slope slightly *positive* near $\alpha = 0^\circ$ (nose-up unstable).

Decision: rejected due to positive $dC_m/d\alpha$ at cruise.

NACA 4412

- $t/c = 12\%$ at $x/c \approx 0.30$; camber 4% at $x/c \approx 0.40$.
- $C_{L,\max} \approx 1.35$, stall at $\alpha \approx 10^\circ$; stall behaviour better than NACA 23012.
- $C_L/C_D \approx 56$ at $\alpha \approx 0^\circ$.
- $dC_m/d\alpha < 0$ at $\alpha = 0^\circ$, with $C_m \approx -0.10$ (slightly high nose-down but acceptable).

NACA 4415

- $t/c = 15\%$ at $x/c \approx 0.30$; camber 4% at $x/c \approx 0.40$.
- $C_{L,\max} \approx 1.44$, stall at $\alpha \approx 13-14^\circ$; stall behaviour similar to NACA 4412.
- $C_L/C_D \approx 52$ at $\alpha \approx 0^\circ$.
- $C_m \approx -0.09$ at $\alpha = 0^\circ$, slightly better (less nose-down) than NACA 4412.

S1223

- $t/c = 12\%$ at $x/c \approx 0.20$; maximum camber 8.7% at $x/c \approx 0.50$.
- $C_{L,\max} \approx 2.32$; stall at $\alpha \approx 12^\circ$ with relatively sharp stall.
- $C_L/C_D \approx 80$ at $\alpha \approx 0^\circ$.
- $C_m \approx -0.27$ at $\alpha = 0^\circ$ (strong nose-down), requiring a robust tail volume.

E423

- $t/c = 12.5\%$ at $x/c \approx 0.24$; maximum camber 10% at $x/c \approx 0.45$.
- $C_{L,\max} \approx 2.03$; stall at $\alpha \approx 11.3^\circ$ with better stall behaviour than S1223.
- $C_L/C_D \approx 90$ at $\alpha \approx 0^\circ$.
- $C_m \approx -0.24$ at $\alpha = 0^\circ$; large nose-down moment but manageable with tail sizing.
 $C_m(\alpha)$ slope strongly negative, which is favourable for static stability.

Interim Conclusion High $C_{L,\max}$ and excellent C_L/C_D of S1223 and E423 make them attractive candidates for a powered-lift STOL configuration. However:

- S1223 exhibits relatively sharp stall and a very large negative C_m .
- E423 displays smoother stall and more better characteristics despite its high camber.
- S1223 isn't very thick, thickness is preferred to host CFJ mechanism within the wing.

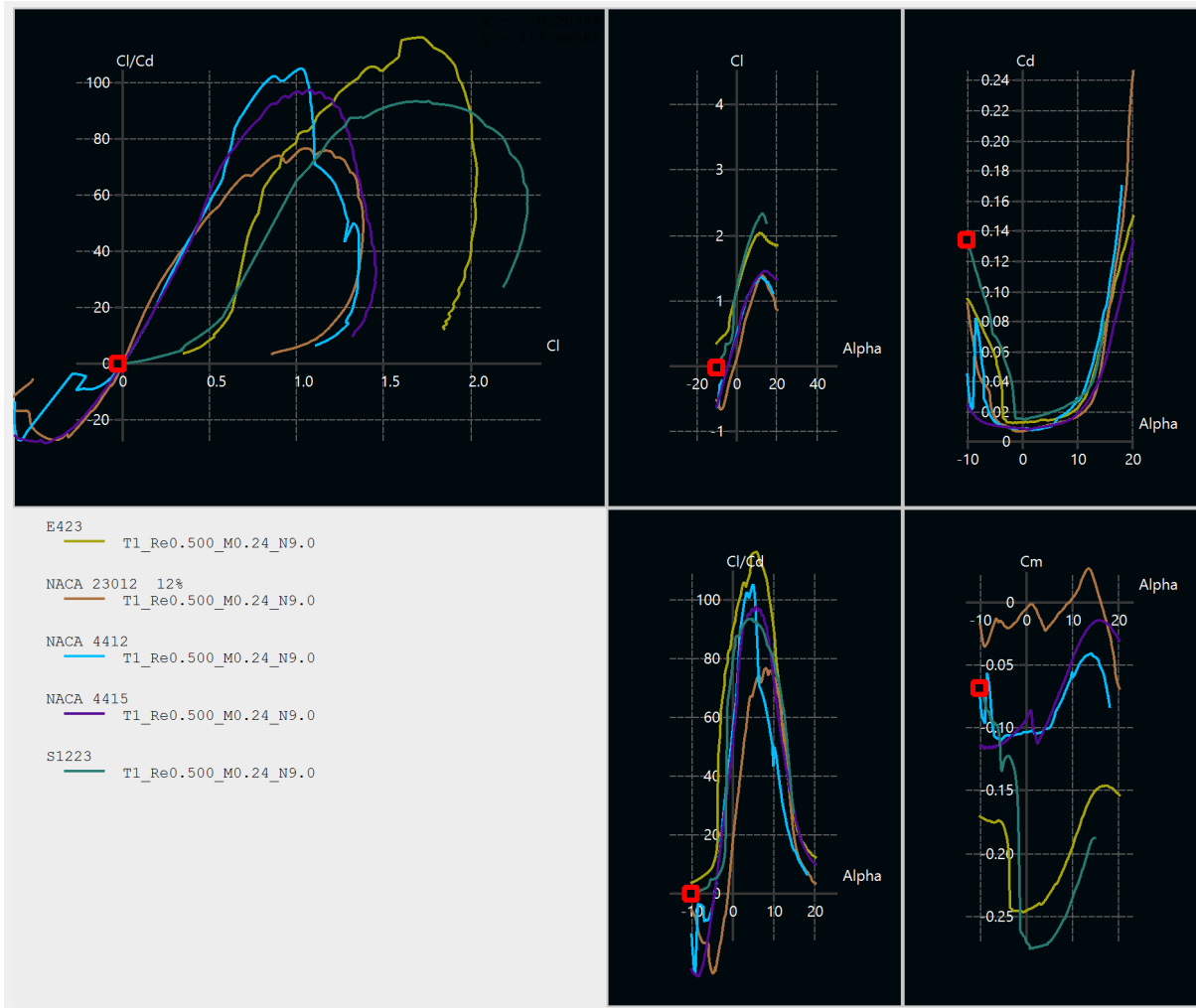


Figure 1: Baseline Airfoil Screening

Airfoil Modification and Final Choice

Both E423 and S1223 were parametrically modified in XFOIL/XFLR5 using custom scripts to adjust thickness. Key observations:

- Increasing thickness of E423 led to a higher *reduction* in $C_{L,\max}$, which is undesirable for the targeted powered-lift $C_{L,\max}$.
- S1223, when carefully thickened and slightly reshaped, offered a better compromise between $C_{L,\max}$ and stall behaviour.

The final baseline section is a **modified S1223** with the following characteristics:

- Thickness: $t/c \approx 18.2\%$ at $x/c \approx 0.20$ (larger thickness preferred due to the high camber and structural/high-lift integration needs).
- Maximum camber: unchanged at 8.7% at $x/c \approx 0.50$.
- $C_{L,\max} \approx 2.27$ (slightly reduced from the original S1223, but still very high).

- Stall angle: $\alpha_{\text{stall}} \approx 13.3^\circ$, improved compared to the sharp stall of the unmodified S1223.
- $C_L/C_D \approx 70.9$ at $\alpha \approx 0^\circ$.
- Pitching moment: $C_m \approx -0.25$ at $\alpha = 0^\circ$, slightly less negative than the baseline S1223 but still requiring a well-designed tail for trimming.

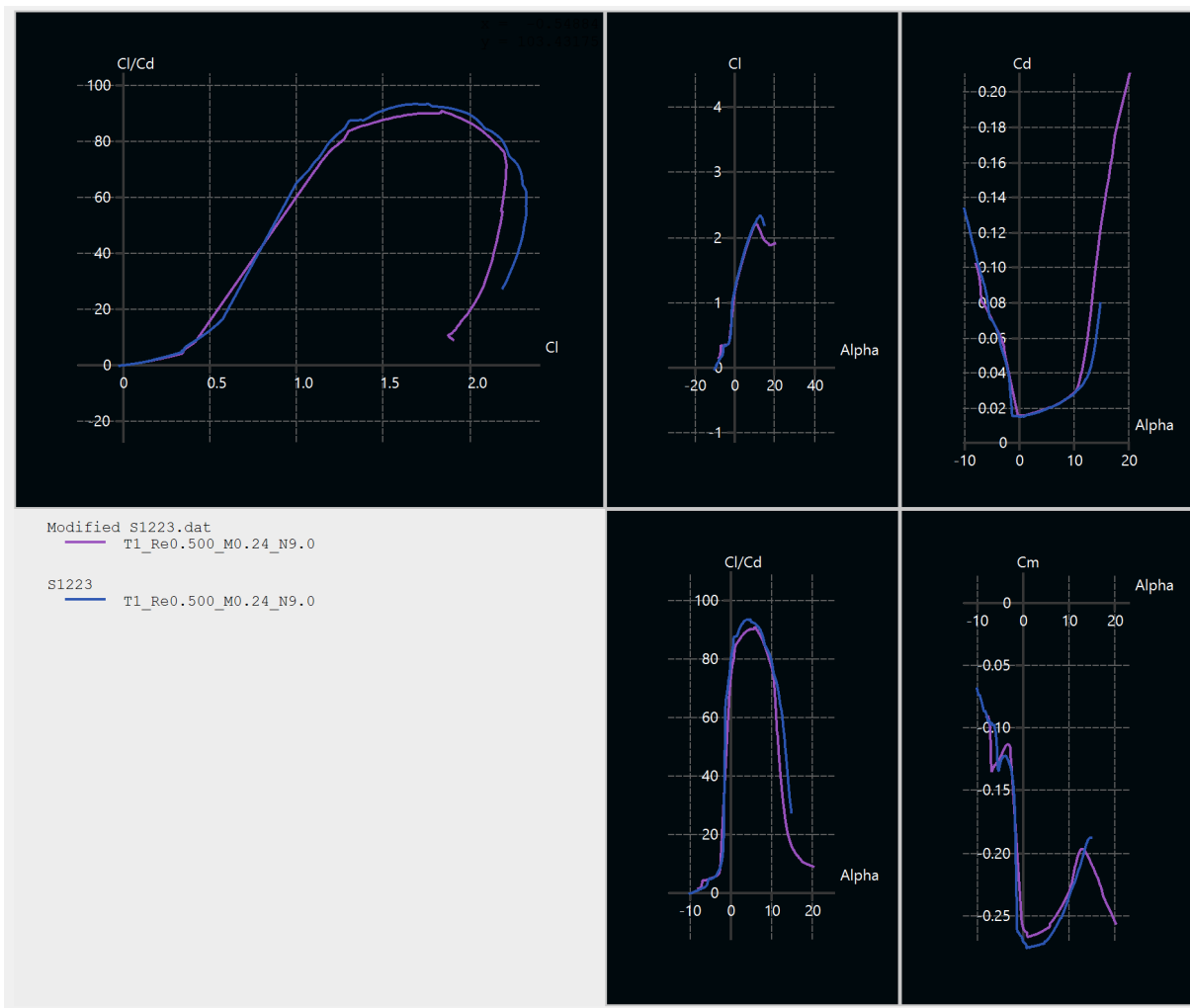


Figure 2: Comparison between S1223 and the modified airfoil

Final selection: the modified S1223 is adopted as the baseline airfoil for subsequent high-lift system design (slotted/flown flaps, powered-lift devices) and planform optimisation. Its combination of very high $C_{L,\text{max}}$, improved stall characteristics, and acceptable C_m behaviour makes it well-suited for achieving the target wing $C_{L,\text{max}} > 8$ under powered-lift operation.



Figure 3: Selected Airfoil

1.3 Multi-Element High-Lift Section

1.3.1 Desired Characteristics

The multi-element configuration (main element plus trailing-edge and possibly leading-edge devices) must achieve the very high lift levels demanded by the powered-lift mission:

- **High unblown 2D maximum lift:**
 - Target unblown $C_{l,\max,2D} \gtrsim 3$ for the multi-element section.
 - This provides a robust starting point for additional lift from blowing and 3D effects, making overall wing C_L in the 6–8 range plausible at low approach speeds.
- **Large linear lift range and delayed stall:**
 - The lift curve should remain approximately linear to high angles of attack, with separation postponed by slotted flaps and boundary-layer control.
 - The system should provide sufficient angle-of-attack margin between take-off angle and stall angle.
- **Effective flaps with strong lift increment:**
 - Slotted flaps with chord fraction around 25–35% and deflections in the range of 30°–40° (take-off) and 40°–50° or more (landing / maximum-lift).
 - High ΔC_l per degree of flap deflection, while maintaining attached flow via slot design and/or blowing.
- **Trim and pitching moment constraints:**
 - The multi-element system should not produce an excessively nose-down C_m , which would demand very large tail forces or tail deflections.
 - Balance between high lift and manageable overall pitching moment is required.

1.3.2 Typical Multi-Element Configuration

A representative powered-lift section will be based on:

- **Main element:** Modified airfoil with high enough thickness inboard, chosen for stall and structural volume.
- **Trailing-edge system:**
 - Single slotted flap of chord fraction $\approx 0.25\text{--}0.35$.
 - A single slotted flap is selected as the baseline high-lift device because it offers a significantly higher lift increment and later stall onset than a plain or split flap, while remaining mechanically much simpler than double- or triple-slotted systems. The slot allows high-energy flow from the lower surface of the main element to re-energise the flap boundary layer, enabling large flap deflections without premature separation. This is particularly advantageous in the present powered-lift configuration, where upper-surface blowing and Co-Flow Jet (CFJ) concepts rely on an attached, controllable flow over a strongly deflected flap to convert jet momentum into additional lift efficiently.
- **Leading-edge device (optional):**
 - Drooped leading edge or Krueger flap to increase effective nose radius and delay leading-edge stall at high lift.
 - Can be left unblown initially to reduce complexity, with all blowing concentrated on the upper surface or flap.
 - Leading-edge refinement (via a drooped nose, Krueger flap, or slat) is a powerful way to increase the stall angle of attack and to convert a sharp leading-edge stall into a more better, trailing-edge-type stall. In the present powered-lift configuration, however, the required high lift coefficients are primarily obtained through large trailing-edge flap deflections and strong blowing (propeller slip-stream, upper-surface blowing, or CFJ), rather than by operating the wing at very high geometric angles of attack. For the expected landing and take-off operating points, the target C_L can be achieved at moderate angles of attack (on the order of $10^\circ\text{--}12^\circ$), where a suitably cambered main element with a slotted flap still has adequate stall margin even without a dedicated leading-edge device. Consequently, the leading-edge device is treated as an optional second-order design knob in the initial design loop: it is introduced only if detailed analysis shows that the baseline main-element and flap system cannot provide sufficient angle-of-attack margin or stall behaviour within the overall mass, complexity, and drag constraints.

1.3.3 Compatibility with USB, CFJ, and Blown Flaps (Multi-Element)

- **USB with multi-element:**
 - Over-wing engines or propellers direct the jet over the main element and flap.
 - Large flap deflections strongly turn the blown jet downward, amplifying lift.

- The geometry must provide sufficient vertical separation between nozzle and surface so that the jet footprint lands where desired (typically around mid-flap).

- **Blown slotted flap:**

- The slot exit at the flap shoulder (between main element and flap) or on the flap upper surface allows high-energy flow to keep the flap boundary layer attached.
- The flap geometry is tailored so that the jet remains attached before exiting at a high downward angle.

- **Co-Flow Jet (CFJ):**

- Suction slot near the leading edge and blowing slot on the upper surface (or at the flap shoulder) can be integrated with the multi-element arrangement.
- The internal volume of the main element and flap can house the CFJ plenum and ducts without unacceptable structural or weight penalties.

1.4 Flap Design

1.4.1 Philosophy and Methodology

The methodology we followed for designing the flaps involves first parameterizing the geometry into as few parameters as possible. We will then generate bounds for the obtained parameters based on literature review and our math model. The output of this review is a range of possible values that we can use for each of those parameters. Now we have a vector space where each point is one combination of values, each of which lies in the prescribed ranges. These are lattice points of our analysis. We eventually perform CFD on each of these lattice points to find the optimum parameters. We can speed up this process as well by choosing parameters have the highest impact and varying those first. This works on the principle that the cluster in the vector space corresponding to each value of a high impact parameter is far away from another cluster with a different value of that high impact parameter. So much so that the variation of the lower impact parameters can not cross the gap. Therefore, finding a significant gap in between these clusters (or simply identifying these clusters) is enough to rule out any combination of low impact parameters with that specific value of that high impact parameter. This cuts down the number of simulations we need to run and makes the workflow much more efficient. Once we have determined the bounding lattice points, we can now have much smaller ranges which are considered optimal. We can repeat this process with the new bounding ranges as the optimal bounding lattice points until the required tolerance/range of parameters is obtained. The parameters obtained in this respect are:

- x coordinate of leading edge of flap
- y coordinate of leading edge of flap
- angle at which the flap is deflected

- chord length of flap (with respect to chord length of clean main element)

1.4.2 Obtaining initial bounding ranges

The bounding ranges obtained in this stage are very rough, they are just for reference to being CFD. Therefore, we do not need analyses of the exact same conditions. Based on [LLK15]:

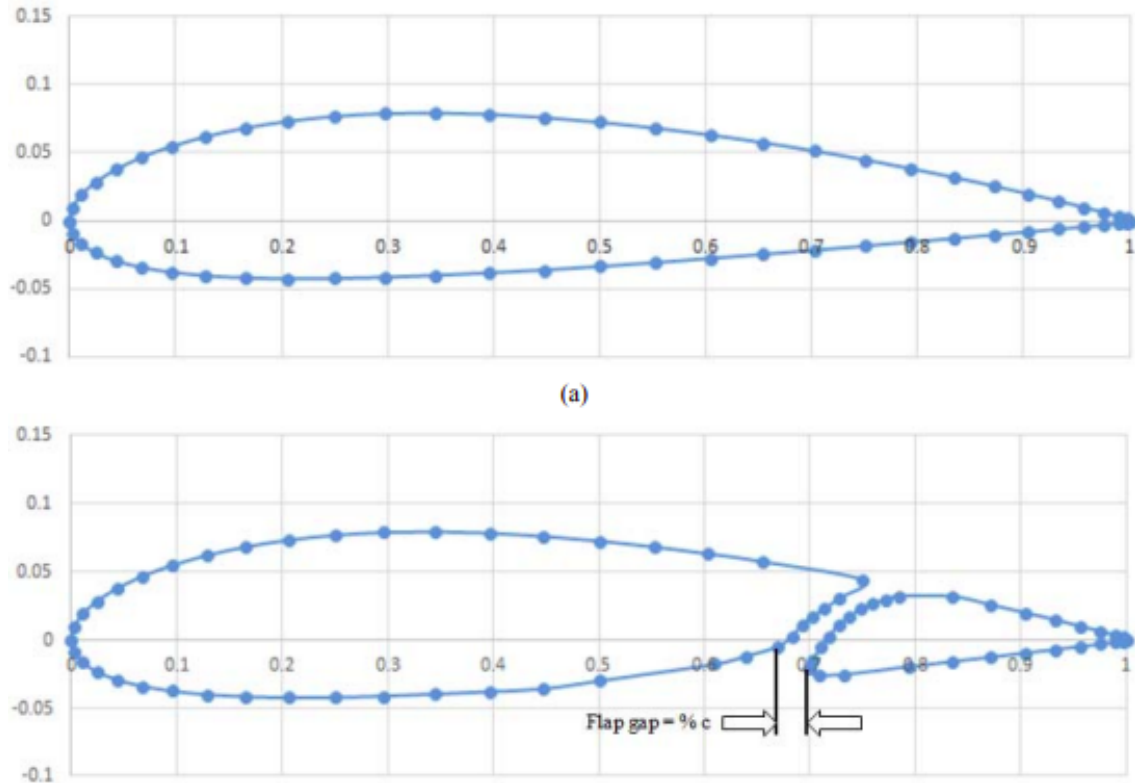


Figure 4: Reference of gap in [LLK15]

This parameter should vary from 1.7 to 3.2%. This is a slightly larger bound than given on the paper. That is because the paper is at a different Reynold's Number. This value will of course be optimized with CFD. This is the gap when the flap is not deployed.

Another parameter is this gap given in [McL70]

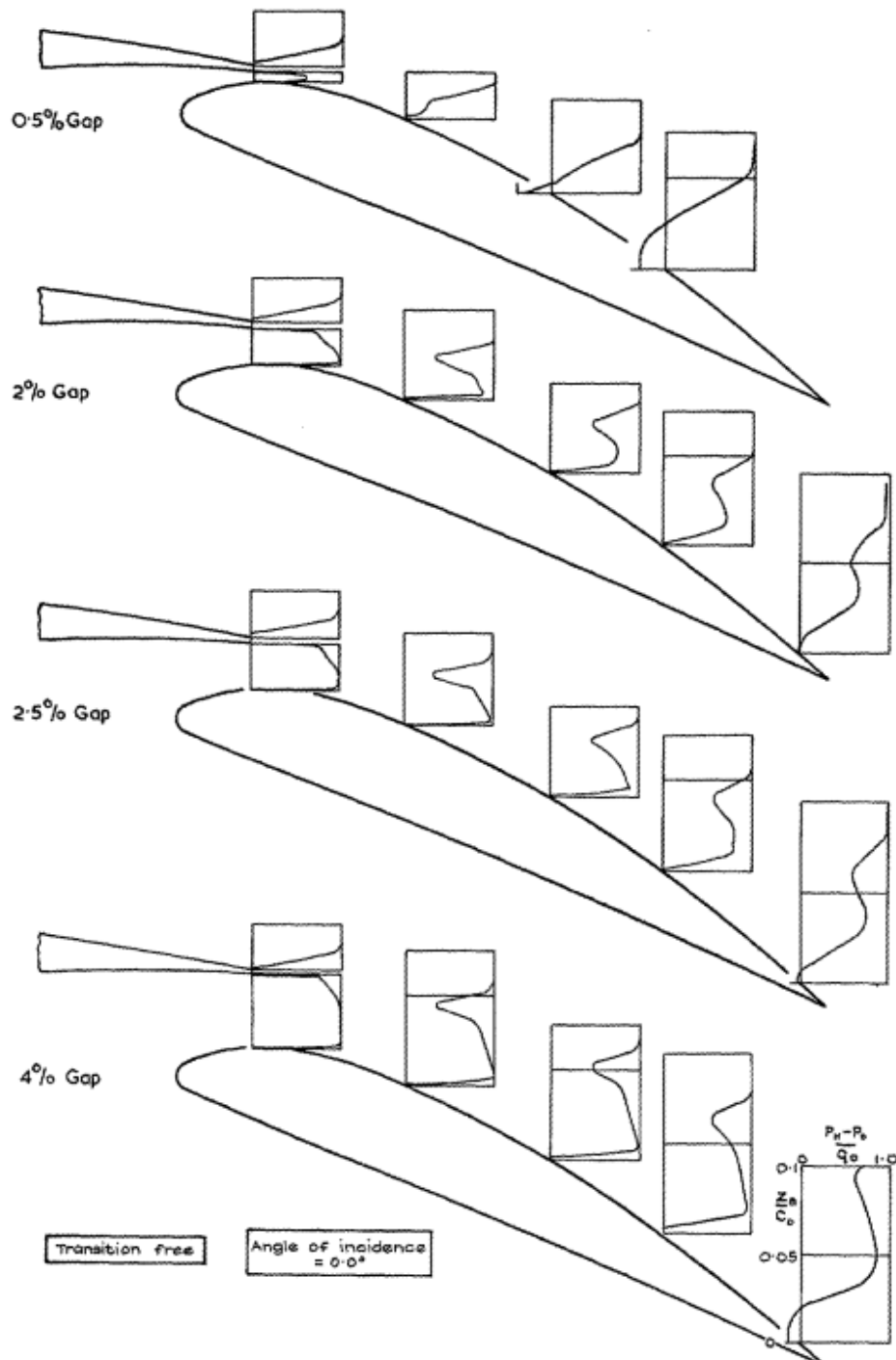
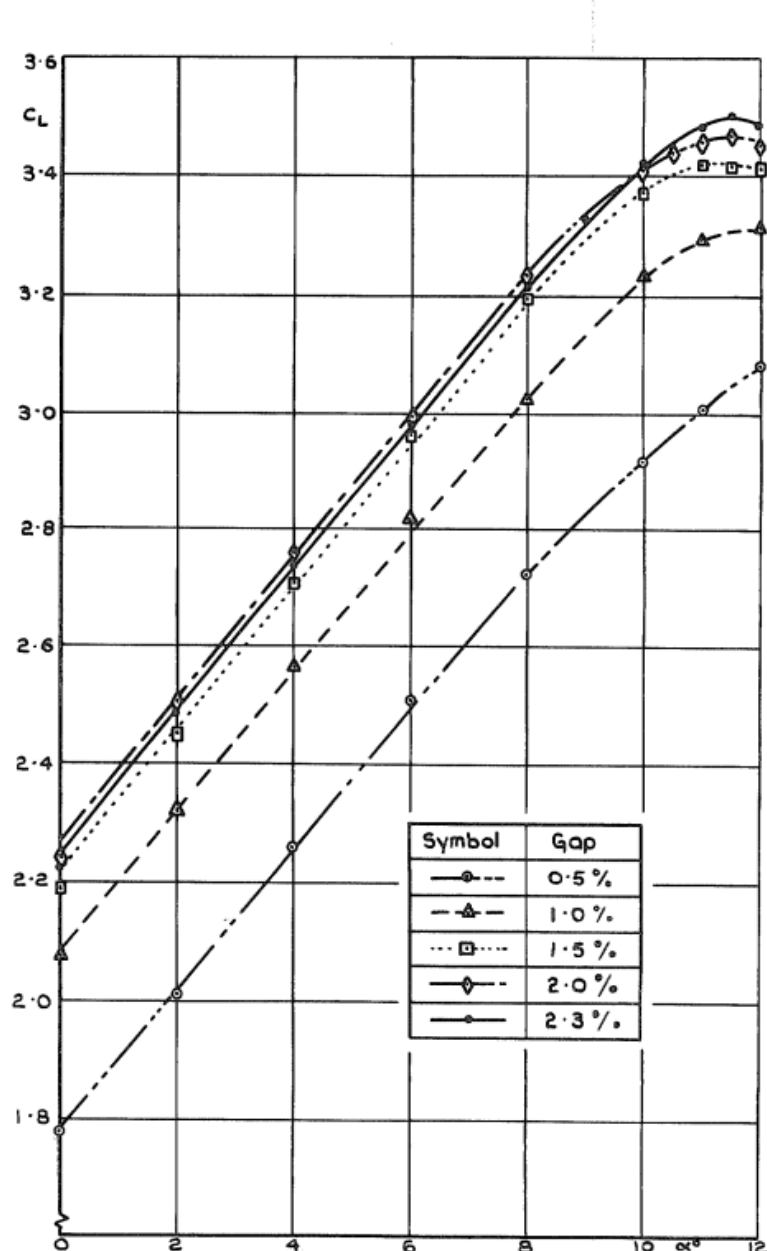


Figure 5: Variation of gap with gap

The diagram below starts with quite a small gap and as it increments the gap (as a percentage of the chord), the wing creates more lift for the same angle of attack. This effect saturates however, as the ΔC_L change between graphs isn't that much.

Figure 6: C_L vs α for different gap

The following graph shows that the effect reverses as we go above a gap of 2.3%. We can conclude there is a specific gap percentage that works best, with a significant delta from even a few percent chord lengths difference.

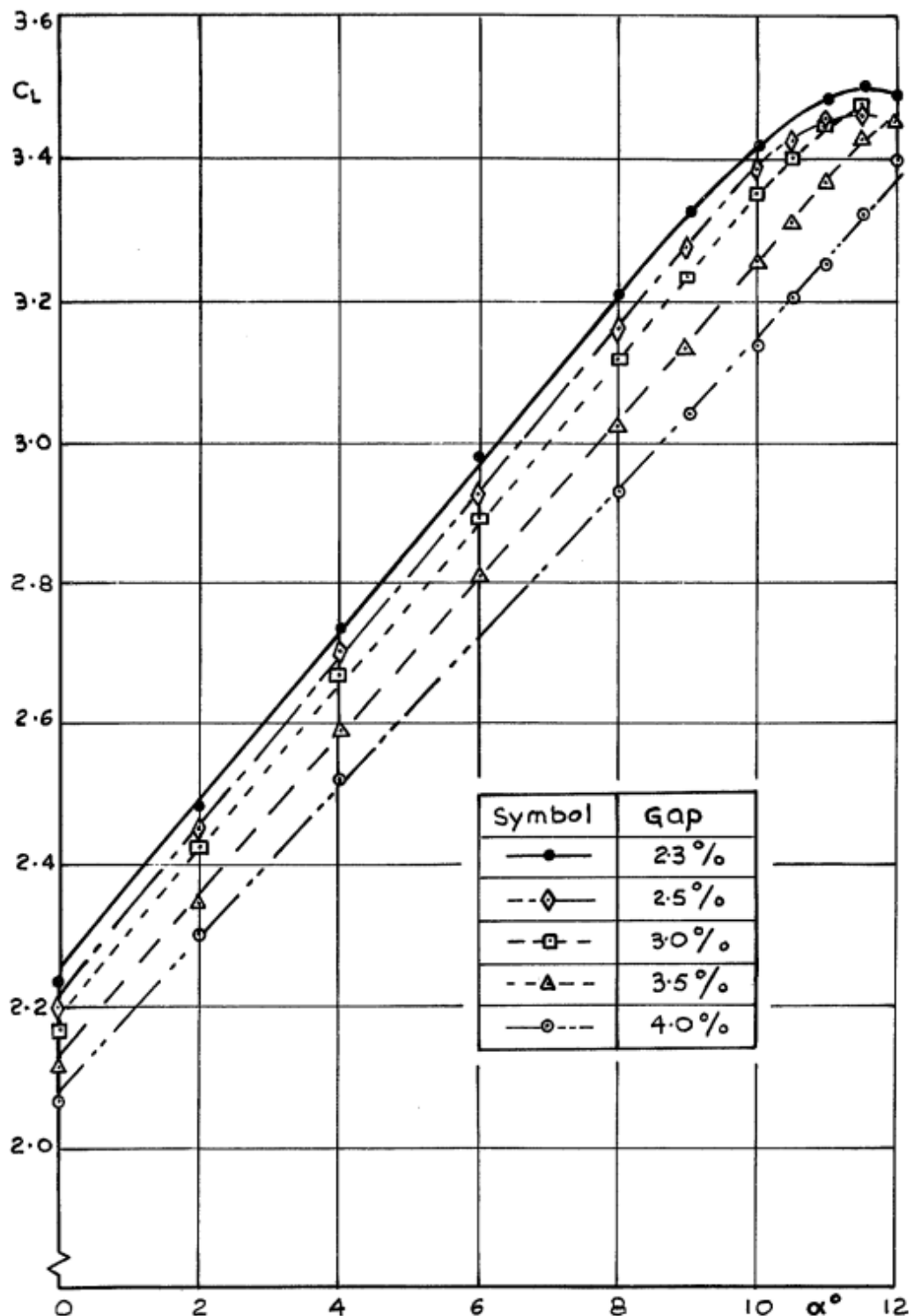
FIG. 10b. Effect of gap on lift. Gap $\geq 2.3\%$, Flap deflection 30° .

Figure 7: Different values of gap from previous graph

The optimum angle for this configuration is 2.3° but this is different than our Reynolds Number and airofil shape. Therefore for the range of values that we will investigate with

CFD, we experiment with a larger range of values, from about 1% to 5% of the overall chord length. This should give us a wide enough range of values.

The other two parameters (length of chord and the angle of the flap) are quite inter-dependent. As seen in [T⁺⁹³]

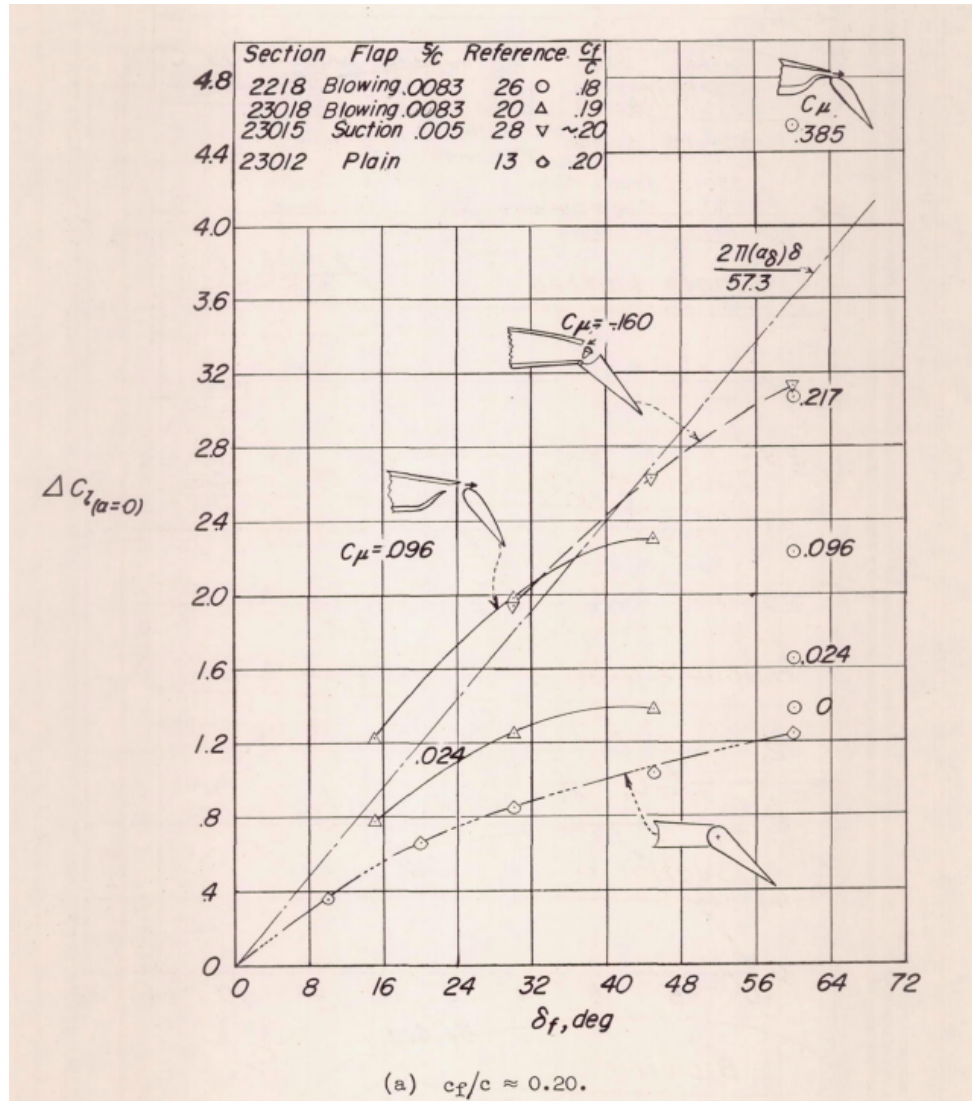
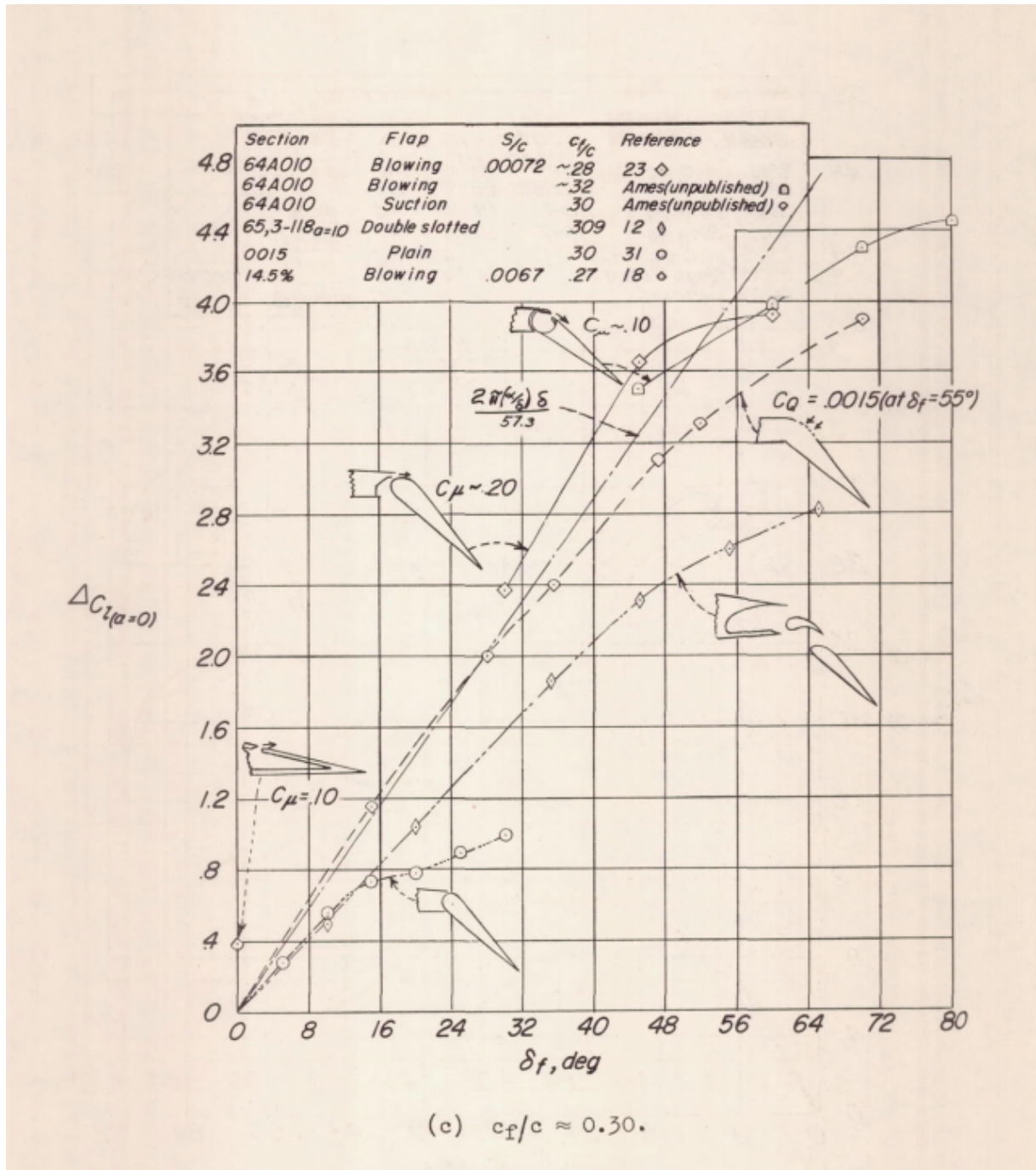
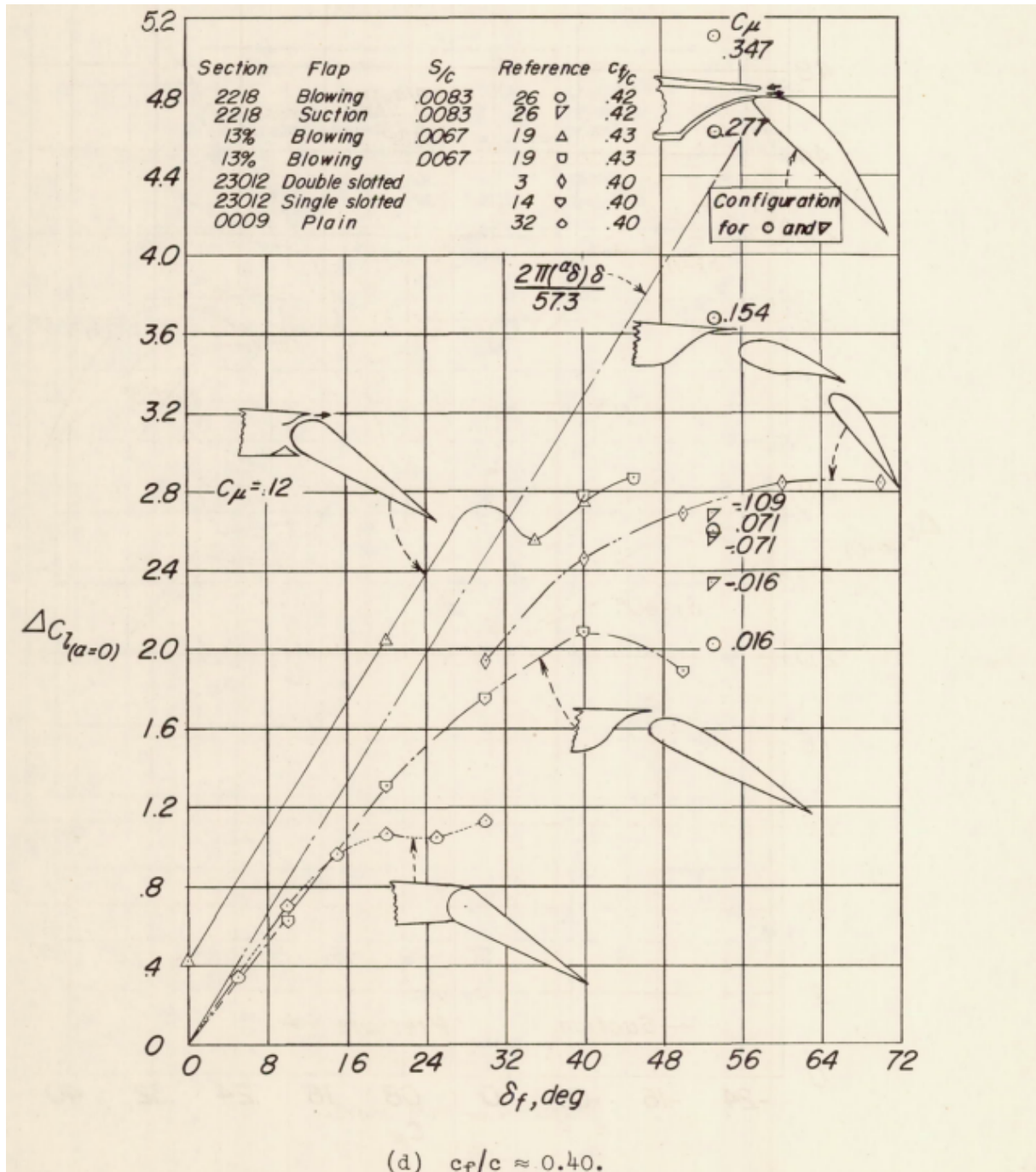


Figure 8: $c_f/c = 0.2$ [T⁺⁹³]

Figure 9: $c_f/c = 0.3$ [T+93]

Figure 10: $c_f/c = 0.4$

The optimal c_f/c is 0.3 as is visible from this data. It is arguable that this data is not for our specific conditions, but this seems to be a general trend. There is data to support this choice even for our case of the S1223 family. This paper [HLGP06] that suggests 35% chord length for the chord of the flap. Also [Kat95] suggests that 25% to 40% is an optimal range for this chord length. These suggest the optimum ranges are still in the 30% range. Lastly we have found a paper [K⁺24] that uses 30% chord length of the total wing to be the chord of the flap. Therefore, we can fix the this parameter instead of varying this with CFD. This greatly decreases the number of simulations needed to run. The corresponding

angle of deflection of flap in [T+93] is roughly in the range of 30 to 50 degrees. Therefore we will explore this region.

Decided ranges for CFD investigation:

- gap - 1% to 4%
- angle at which the flap is deflected - 15 to 45 degrees
- chord length of flap - 30% of main chord

1.4.3 Making the flap geometry

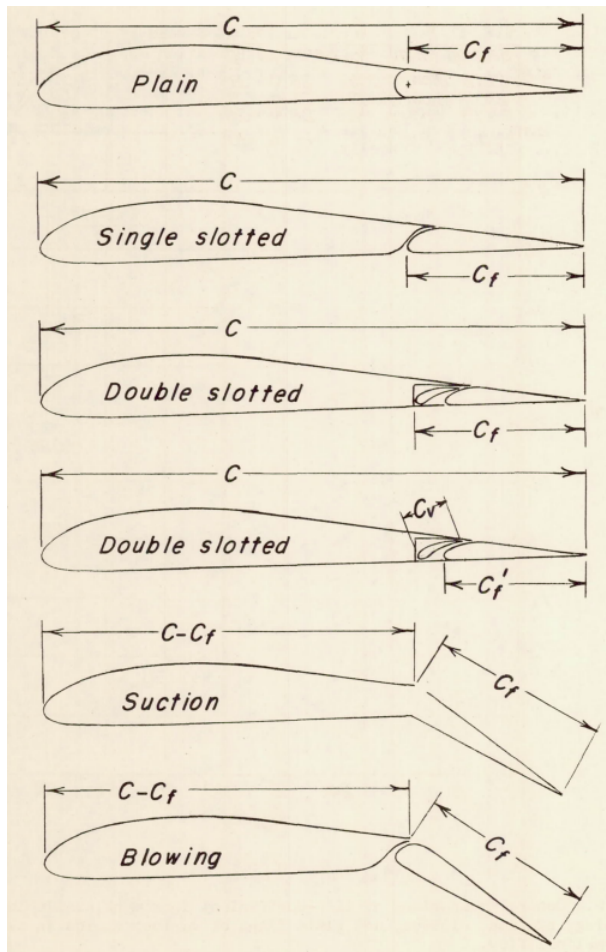


Figure 11: Types of flaps

To balance complexity of the mechanism with the effectiveness (ΔC_L) we are choosing single slotted flaps. As shown in the graphs above, single slotted flaps are much more effective than just plain flaps. However, double and triple slotted flaps have a lot of extra complexity. To manage the drag at cruise when the flaps are retracted, we need to construct the geometry such that they all fit together. Doing this while optimizing the airflow between the gaps (energizing the boundary layer with air from below the wing) is quite tricky. They do have significant gains but those are can be sacrificed for simplicity (especially because with these flaps, adding upper surface blowing and then layering co-flow

jet should bring us above the required amount.

The method of action of the slots is by 5 main mechanisms [LK⁺96]. The peak pressure on the flap is reduced by the induced velocity by the circulation on the main element. This delays the flow separation by relieving pressure recovery. The circulation induces more circulation on the main element because its trailing edge is in a region that has high velocity made by the leading edge of the flap. The trailing edge is in a region of higher velocity it sheds its boundary layer at a large velocity. This effect will also delay flow separation because by Bernoulli's Principle, this higher velocity means a lower pressure rise across the main element airfoil. That means pressure is recovered "off-the-surface" rather than the less efficient recovery when in contact with a wall. Both the flap and main element benefit from a fresh boundary layer from the leading edge of each of them. The thin boundary layers can now withstand stronger adverse pressure gradients than if it was thicker.

The nature of just the inviscid effects imply that smaller gaps are more beneficial, however just the viscous effects demand large slots. This is where the issue of balancing the slot size comes in. This is the issue we will solve with our CFD optimization. Ill-designed gaps will cause the merging of wakes, which gives rise to very thick boundary layers (that are quite prone to separating).

The main decision to make regarding the flaps is the shape of the leading edge. This is something that is quite important. An ill-designed shape can cause premature flow separation, this means we can not push the lift characteristics of this flap as much as possible. Also, there should be no sharp points as they cause vortices and thereby reduce efficiency. This limits the effectiveness of interpolating curves for the shape of this edge as there is a large possibility of having a sharp edge when using interpolation/spline to extend the edges and create a leading edge.

This problem was solved by using a Bezier curve and B-splines through Knob curves. These curves are used to interpolate airfoil shapes [J⁺10]. Control points were taken such that there is no discontinuity or non-differentiability. The finalized leading edge of the flap is shown below:

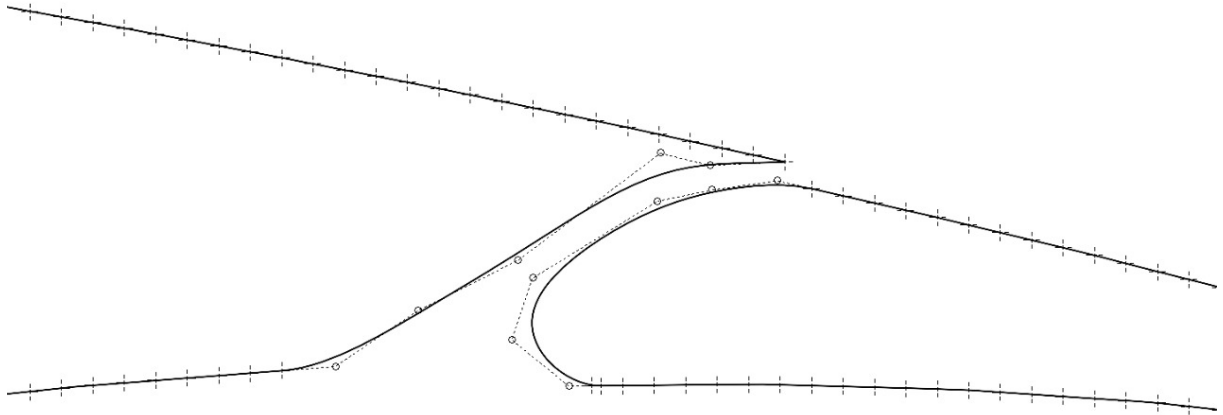


Figure 12: Flap Leading Edge Control Points

There are 6 control points, meaning the curve is of 5th order. This is a common order because having less points leads to a less flexible system. That system can not contain all of our conditions. Not only do we have the geometric constraints of continuity and differentiability, but also we need to make further refinements such as making the bulge/bulb of the leading edge of the leading edge go on the lower section. The reason for this is that the aforementioned configuration leads to helps reduce flow separation, meaning the flap can be deflected to a larger angle than without said flap. This can be reasoned from the flow visualisations shown in this paper [Q⁺12]. After adjusting all of those constraints we get the given shape.

The flap parameters are determined by performing CFD simulations with other powered lift components.

2 High Powered Lift Concepts Considered

Achieving high-powered lift is essential in short take-off and landing (STOL) aircraft where large lift coefficients must be generated at low forward velocities without excessive drag penalties. Several aerodynamic–propulsive interaction techniques have been proposed and validated in prior research. The following sections summarize the primary methodologies under consideration, their underlying mechanisms, and analytical relations supporting their lift augmentation capabilities.

2.1 Co-Flow Jet (CFJ) Airfoils

The co-flow jet (CFJ) concept, developed by Shen and collaborators [She12, SS15], employs a closed-loop flow system in which air is suctioned near the trailing edge and reinjected near the leading edge tangentially to the surface. The injected jet adds momentum to the boundary layer, preventing separation and generating additional circulation even at high angles of attack. [ZJR⁺18a]

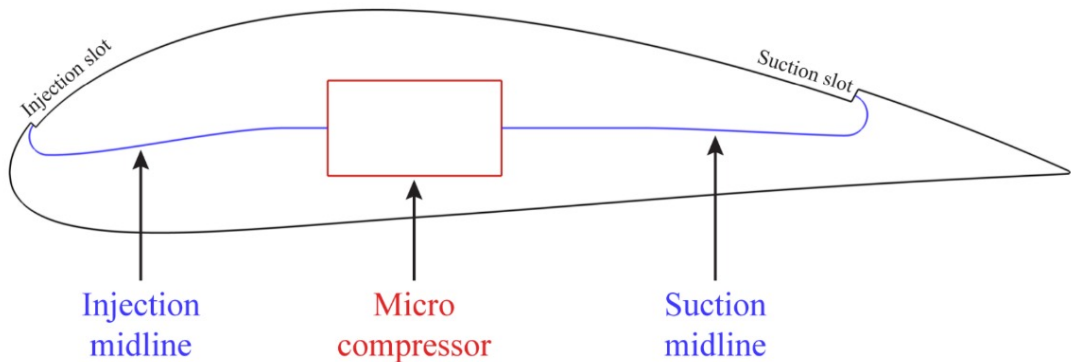


Figure 13: CFJ Diagram [She12, SS15]

A 3D model of the co-flow jet configuration was also developed.



Figure 14: Side-view of wing with co-flow jet

The injection slot (near the leading edge) and the suction slot (near the trailing edge) run throughout the span of the wing (1.4 m). There is a small compressor in the centre that helps extract air through the suction slot, energise a small amount of air, and tangentially re-inject it through the injection slot. The existing battery can be used to power the compressor.



Figure 15: Isometric view of wing with co-flow jet

Analytically, the CFJ airfoil can be modeled by superimposing line-source and line-sink distributions on an inviscid base potential flow:

$$\phi(x, z) = \phi_0(x, z) + \frac{\sigma_j}{2\pi} \int \frac{1}{r_j} dx' - \frac{\sigma_s}{2\pi} \int \frac{1}{r_s} dx', \quad (1)$$

where σ_j and σ_s represent the injection and suction mass flux strengths, and r_j , r_s are local distances to the slot positions. The net momentum added to the outer flow results in an effective circulation increment

$$\Delta\Gamma_{CFJ} = \frac{\dot{m}_j(V_j + V_s)}{\rho U_\infty}. \quad (2)$$

Experiments show that CFJ systems can increase lift coefficients by 50 to 150% and delay stall to angles beyond 25° while maintaining laminar-like pressure recovery [She12]. The system's efficiency is tied to the power input required to drive the jet, but because suction and injection occur in a closed loop, the net mass flow exchange with the atmosphere is minimal. This makes CFJ attractive for compact, electrically powered STOL vehicles where low jet mass flow but high momentum addition is desired.

The following mathematical models are used to model the additional lift due the co-flow jet configuration

We will model fluid flow around airfoils using inviscid, incompressible flow theory. We will neglect viscosity because we are modeling only the flow outside of the boundary and have density as constant under subsonic conditions , where compressibility is minimal. The Kutta condition is applied, ensuring smooth flow at the trailing edge for valid lift generation on the airfoil at low angles of attack. The assumption also uses the fact that ($\omega = \nabla \times V = 0$). We will then be using conformal mapping in this method to transform between a complex shape into a simpler problem (such as a circle) while having the local angles as constant. [KTT08]

2.1.1 Solving the case of a circle

- Uniform flow: $\phi = V_\infty r \cos(\theta)$ and $\Psi = V_\infty r \sin(\theta)$
- Doublet flow: There is a coupled source and sink, with $\phi = \frac{\kappa}{2\pi} \frac{\cos(\theta)}{r}$ and stream function $\Psi = -\frac{\kappa}{2\pi} \frac{\sin(\theta)}{r}$
- Vortex flow: $\phi = -\frac{\Gamma\theta}{2\pi}$, where Γ is the circulation

Upon combining these,

$$\phi = V_\infty r \cos(\theta) - \frac{\Gamma}{2\pi} \theta + \frac{\kappa}{2\pi} \frac{\cos(\theta)}{r}$$

Here L' is the Lift per unit span on the object, which is given as (by the Kutta-Joukowski theorem),

$$L' = \rho V_\theta \Gamma$$

In this specific case, the circulation of the circle

$$\Gamma = 4\pi V_\infty R \sin(\beta + \alpha)$$

R is the radius, β is the cylinder orientation and α is the angle of attack.

Note that the circulation Γ is:

$$\Gamma = \oint \vec{V} \cdot d\vec{s} = \iint_S (\nabla \times \vec{V}) \cdot d\vec{S} = \iint_S \vec{\omega} \cdot d\vec{S}$$

2.1.2 Transforming between shapes

We have solved the case of the circle and can now transform from this into the specific airfoil that we want. Applying this transformation onto the complex potential of the flow, we obtain what it will be in the case of the flow in the complex airfoil. The Joukowsky transformation maps circles (simple geometry) into airfoil-like shapes (complex geometry) in the complex plane. It is given by:

$$w(z) = z + \frac{\lambda^2}{z}$$

λ is the transformation parameter, equal to $\lambda = b - |s|$ (The circle is shifted and s is the center point, b is the radius of the circle). This transformation has to be modified, which then results in the desired airfoil shape. The above transformation leads to an airfoil that approximates NACA airfoils. Applying that transformation onto the complex potential will give the descriptions of the flow in the cylindrical case. Using this method, we have obtained a shape of NACA 9412 airfoil.

2.1.3 Introducing Co-Flow Jet

To account for the co-flow jet we will modify the lift equation:

$$L' = \rho V_\theta \Gamma$$

Divide Γ into two pieces. This assumes potential flow, which holds outside the boundary layer. The co-flow jet near the boundary layer will still be considered potential. This will give us inaccurate drag values but it will give a decent approximation for the lift.

$$\Gamma = \Gamma_{\text{cfj}} + \Gamma_{\text{airfoil}}$$

The Γ_{airfoil} is calculated as normal. To account for Γ_{cfj} , we will use a series of approximations. Some of the first assumptions are:

- The velocity of the co-flow jet is roughly constant along the jet
- The end effects of the entrance and exit of the jet are neglected

Upon taking the points on the airfoil's upper surface, we interpolate a polynomial on the top surface.

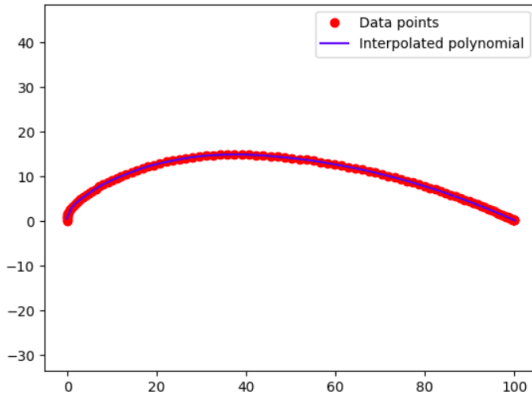


Figure 16: A plot of the airfoil vs the interpolated polynomial

We use this polynomial and find the circulation through it.

$$\Gamma = \oint \vec{V} \cdot d\vec{s}$$

We know the velocity at all points except between the source and sink of the jet (due to the co-flow jet itself) is zero, so we can just integrate

$$\Gamma = \int_a^b \vec{V} \cdot d\vec{s}$$

Here, b and a are the end and start points of the co-flow jet. The velocity is assumed

constant along the jet, so we can pull the velocity out of the integral and simplify

$$\Gamma = \int_a^b \vec{V} \cdot d\vec{s} = V \int_a^b d\vec{s} = V \int_{x_1}^{x_2} \sqrt{1 + f'^2(x)} dx$$

Where $f(x)$ is the interpolated polynomial.

Upon calculating both the circulations, we can find the coefficient of lift:

$$C_l = \frac{L'}{\frac{1}{2}\rho V^2 c}$$

V is the free-stream velocity, c is the chord length, C_l is the lift coefficient.

$$C_l = \frac{\rho V_\theta \Gamma}{\frac{1}{2}\rho V^2 c} = \frac{(V_{\text{jet}} \int_{x_1}^{x_2} \sqrt{1 + f'^2(x)} dx + \Gamma_{\text{transform}})}{\frac{1}{2} V c}$$

$$C_l = (C_l)_{\text{standard}} + \frac{2(V_{\text{jet}} \int_{x_1}^{x_2} \sqrt{1 + f'^2(x)} dx)}{V c}$$

So, finding the integral numerically between the required positions of the co-flow jet inlet and outlet as the limits of the integral to obtain the constant value that is multiplied into the ratio of velocities.

2.1.4 CFD Results using Co-Flow Jets

We ran multiple simulations to optimize the selection of our airfoil using Co-flow jets. From the literature review, we chose 3 airfoils and tested them using Ansys Fluent. Our choices of airfoils initially were :

- NACA 6415
- NACA 6421
- S1223

The following design parameters for the co-flow jet for all airfoils are listed below:

- Injection slot
 - Position - 20% c
 - Size - 0.65% c
- Suction slot
 - Position - 80% c
 - Size - 1.42% c where c represents the chord length of the airfoil.

A rectangular bounding box with dimensions of length of 25c and width of 10c was constructed. The airfoil is at a distance of 10c from the left edge. The mesh is quadrilateral, with the following parameters:

Parameter	Dimension	Inflation
Edge sizing – airfoil	1 mm	1st layer thickness – 0.01 mm
Edge sizing – CFJ inlet	0.01 mm	Nil
Edge sizing – CFJ outlet	0.01 mm	Nil
Face meshing – near the jet stream	1 mm	Nil
Edge sizing – above jet stream	0.1 mm	Nil

Table 1: Meshing parameters for co-flow jet configuration - CFD setup

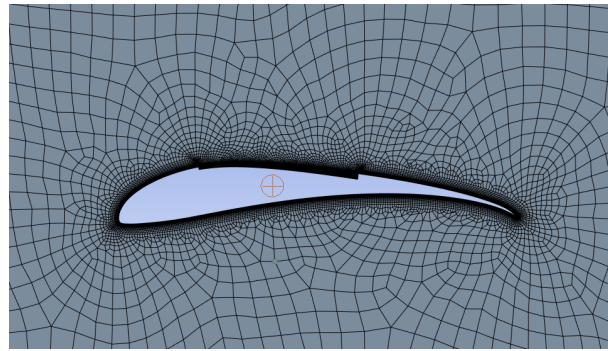


Figure 17: Mesh for CFJ

The boundary conditions for the simulation are tabulated below:

Type of boundary	Magnitude	Location
Dirichlet – freestream velocity	20 m/s	Bounding box inlet (left edge)
Dirichlet – pressure outlet	0 Pa (gauge pressure)	Bounding box outlet (right edge)
Dirichlet – velocity at jet inlet	55.47 m/s	Jet inlet
Dirichlet – pressure at jet outlet	5 Pa (gauge pressure)	Jet outlet
Walls – no slip	0	Bounding box (top and bottom), airfoil

Table 2: Boundary conditions for the co-flow jet simulation

The results are as follows:

2.1.5 Experimental results for NACA 6415 from literature

From [DKZ10]

α	Injection Gauge	Suction Slot (kg/s)	% Error Slot (kg/s)	CL	CD	Lift (N)	Drag (N)
0	0.077	0.07765	0.46058	0.89327	0.0324	38.299	1.39
5	0.077	0.07527	2.61857	1.476	0.0387	63.29	1.658
10	0.077	0.07655	0.96259	2.0343	0.04925	87.221	2.112
15	0.077	0.07338	5.06387	2.5278	0.0645	108.38	2.767
20	0.077	0.07571	2.04932	2.9028	0.088997	124.457	3.8158

Table 3: Results for NACA 6415

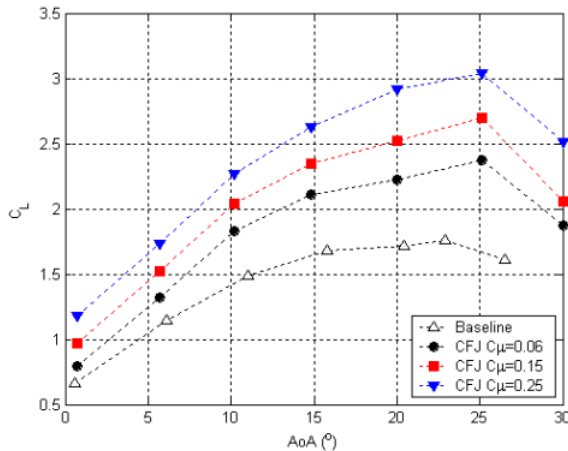


Figure 18: Cl vs AoA

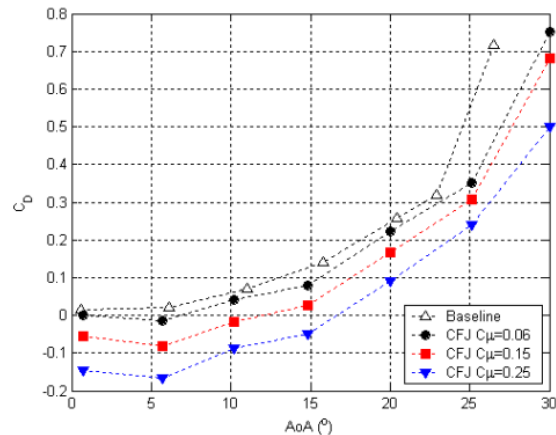


Figure 19: Cd vs AoA

The results obtained from simulations performed using the NACA 6415 airfoil matched with experimental results, which ensures mesh credibility.

The results obtained using the NACA 6421 and the S1223 airfoil using the same mesh settings are tabulated below.

Case – NACA 6421

- Injection Slot (kg/s) – 0.0772
- Suction Slot (kg/s) – 0.0768
- % Error – 0.197
- CL – 1.02
- CD – 0.0349
- Lift (N) – 43.7325
- Drag (N) – 1.4
- L/D – 29.226

Case – S1223

- Injection Slot (kg/s) – 0.0772
- Suction Slot (kg/s) – 0.0769
- % Error – 0.1968
- CL – 1.23
- CD – 0.035
- Lift (N) – 53.04
- Drag (N) – 1.506
- L/D – 35.219

As can be seen from the tables above, the S1223 airfoil produced the highest C_L . However, to accommodate the compressor, the thickness of the original S1223 airfoil was modified from 12% c to 18% c . Simulations were run on the modified S1223 airfoil as well.

Results of S1223 - Thickened :

- Case – S1223 Modified
- Injection Slot (kg/s) – 0.0772
- Suction Slot (kg/s) – 0.077141
- % Error – 0.1979
- CL – 1.307
- CD – 0.0342

- Lift (N) – 56.08
- Drag (N) – 1.47
- L/D – 38.14

Comparing the two tables of S1223 airfoil, the modified airfoil provided better C_L values. So for the rest of our design, we have used the Modified S1223 airfoil.

3 Thrust Producing Devices

3.1 Placement of the Distributed Electric Propulsion Modules

3.1.1 Introduction

DEP offers the ability to enhance wing performance by accelerating airflow over the surface through multiple propulsors. The placement of propulsors is one of the most defining design variables in a DEP aircraft. Changes in the vertical, streamwise, or spanwise placement can affect slipstream immersion, lift distribution, and overall efficiency. The following subsections focus on identifying suitable placement regions for the DEP modules by analysing wing-slipstream interaction through literature findings and use of a low-fidelity analysis tool(OpenVSP) for wake visualisation.

3.1.2 Literature Review

Effect of propeller slipstream on wing lift distribution

Effect of propeller slipstream on wing : The axial and the swirl velocity created by the propeller have a distinct influence on the flow over the wing [WGLY23]. The axial velocity increases the dynamic pressure over the wing whereas the swirl velocity changes the angle of attack in different parts of the wing. The upward blade raises the local wing angle of attack, while the downward blade reduces it [WGLY23]. When the wing is at a positive angle of attack, it produces positive lift, resulting in higher lift on the upward blade side and decreased lift on the downward blade side.

Effects of Wing on the Propeller : Wings create an upstream effect by changing the inflow at the propeller disc owing to in-plane and out-of-plane generated velocities [WGLY23]. The out-of-plane-induced velocity is a combination of the wing blockage and the velocity produced by the wing bound vortex [WGLY23].

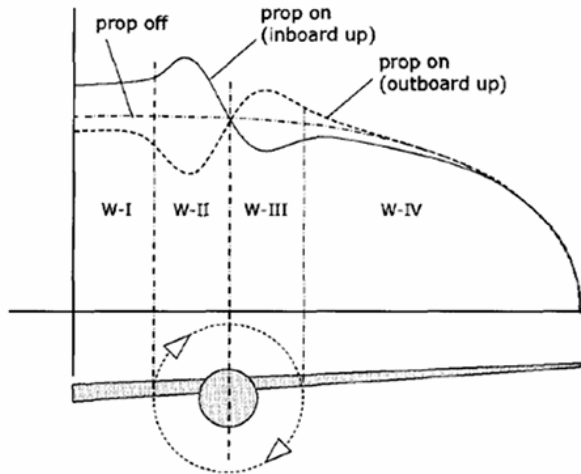


Figure 20: Lift distribution in wing sections influenced by propeller-slipstream-produced velocity [WGLY23].

Effect of Propeller Spacing The effect of the propeller swirl extends well outside the disk area of the propeller, typically 3 propeller radii if multiple propellers are used [Haw24]. The swirl cancels at the boundary between propellers, and if their direction of rotation is opposite, the swirl superimposes. Placing propellers close restricts jet expansion [Haw24]. Optimum performance is achieved by overlapping propellers so that their fully contracted slipstreams are adjacent [Haw24]. Optimum spacing, s/D_p , is therefore a function of propeller thrust and streamwise location (where s is the span and D_p is the propeller diameter) [Haw24].

Effect of Propeller Location (Streamwise) Moving the propeller upstream increases wing lift due to additional contraction of the propeller slipstream [Haw24]. 85% of this contraction occurs within one propeller diameter of the disk, and hence the propellers should be placed at a distance of one propeller diameter upstream of the wing leading edge as a compromise between aerodynamic and structural considerations [Haw24].

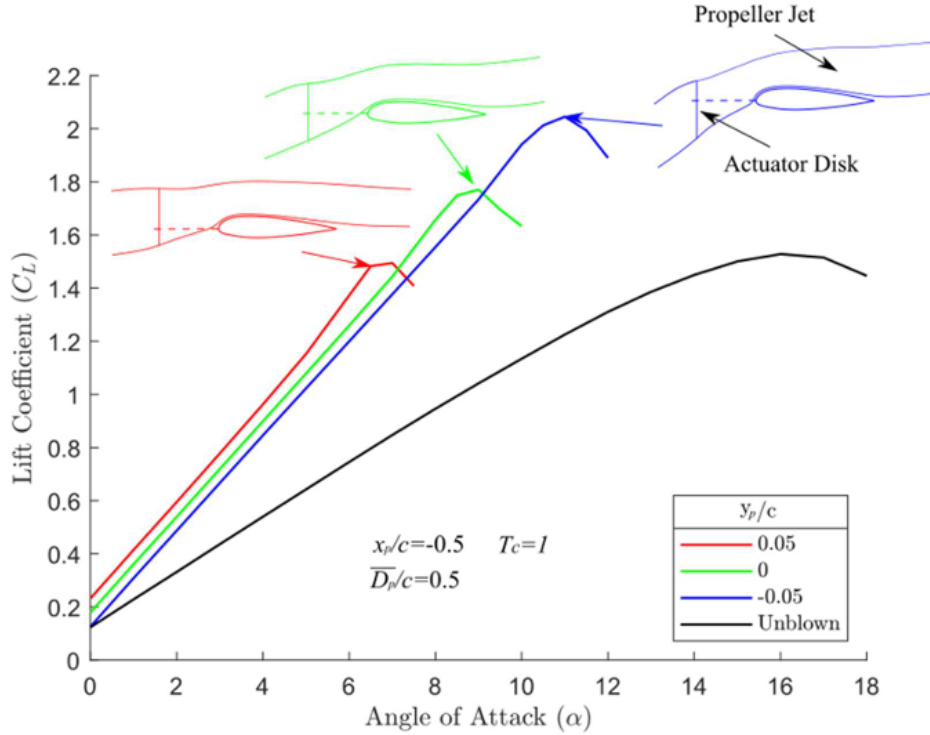


Figure 21: The effect of propeller vertical position on stall incidence ($T_c = 1$, $\bar{D}_p/c = 0.5$). The unblown wing is shown in black along with three blown wings shown in blue ($y_p/c=0.05$), green ($y_p/c=0$), and red ($y_p/c=0.05$). [Haw24].

The Effect of Jet Location on the Performance of a Blown Wing Detailed study using viscous RANS simulations on NACA 43018 aerofoil performed across a range of incidence angles up to stall in [Haw24]. The simulations evaluated three vertical offsets of the actuator disk above, on, and below the wing chord line. The jet location determines whether the wing is fully or partially immersed within the propeller slipstream [Haw24]. At low incidence, moving the jet down reduces the lift coefficient because of a reduction in the amount of jet passing over the wing suction surface. However, bringing the jet down below the wing centreline increases the stall angle of the wing, leading to a higher maximum lift coefficient [Haw24].

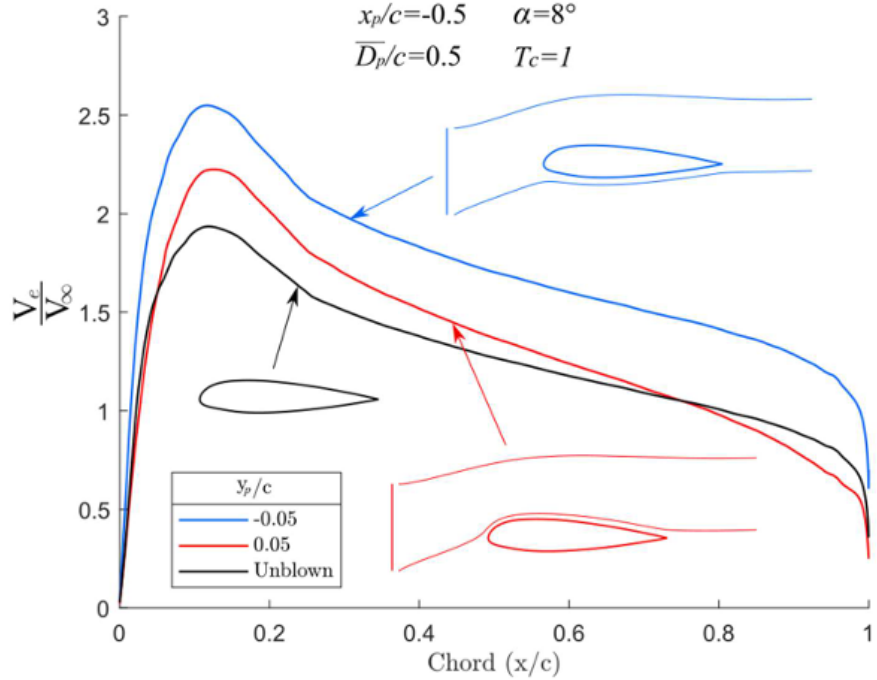


Figure 22: The effect of jet location on the aerofoil suction surface velocity distribution (inviscid cases shown). Moving the jet from fully immersing the wing (blue) to only passing above the wing suction surface (red) increases the suction surface boundary layer diffusion compared to the unblown wing (black). [Haw24]

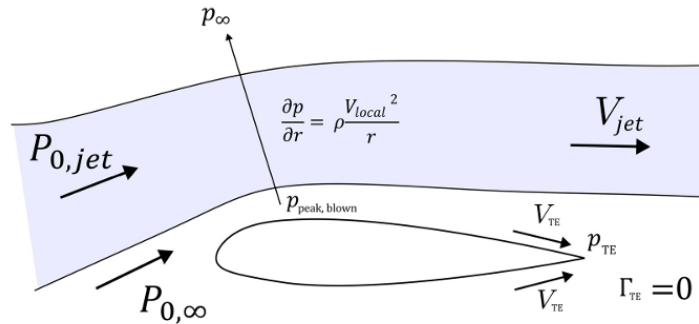


Figure 23: Schematic of a wing with the jet passing above the suction surface. The pressure gradient caused by turning the additional momentum of the jet leads to an increased boundary layer diffusion relative to an unblown wing. [Haw24]

If the jet is to follow the freestream flow, the wing has to turn the momentum of the jet around the suction surface, as shown. This leads to an increased pressure gradient from the far-field to the wing surface for the blown case compared to the unblown case given by:

$$\frac{\partial p}{\partial r} = \rho \frac{V_{local}^2}{r} \quad (3)$$

where V_{local} is the local velocity of the jet above the wing [Haw24].

When the jet moves upward (the turning radius of the jet increases), it lowers the pressure gradient, decreasing the lift on the suction side [Haw24]. Based on these results, a geometric condition was proposed in [Haw24] to ensure full immersion of the wing in the jet flow for all angles of attack. To avoid premature stall, the wing should therefore be fully submerged in the propeller jet at all operating points. This implies that the range of incidences over which the wing remains un-stalled is a strong function of the size and position of the propulsors. To ensure that the jet fully immerses the wing at any given incidence, we can therefore say that:

$$\frac{\bar{D}_p}{2} - y_p \geq f(x_p) \quad (4)$$

- D_p : Propeller diameter
- y_p : Vertical coordinate of the center of the propeller
- $f(x_p)$: Equation of vertical coordinate of the stagnation streamline

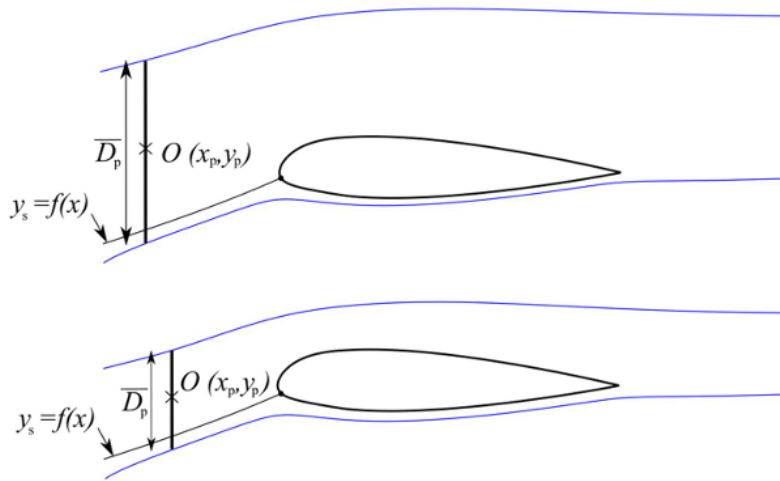


Figure 24: The streamline pattern for two jets of different size and position around a blown wing. To avoid premature stall, the propeller jet should intersect the wing stagnation streamline [Haw24].

3.1.3 Effect of Motor Mount Angle

[Lon21] investigated the effect of motor tilt angles of 0° , 10° , and 20° downward from the chordline. The 20° mount showed negligible changes in lift coefficient, while the 0° mount produced a notable increase in both the lift coefficient and maximum lift coefficient. Therefore, a 0° mount is found to have better propeller performance according to [Lon21]. According to [Haw24], tilting the propeller axis by 20° to blow air upwards onto the wing increases the wing angle of attack, improving lift and the lift-to-drag ratio (L/D) by 20% relative to an installation angle of 0° . However, this increased loading leads to earlier stall.

3.1.4 Optimum Propeller Diameter and Number

Design Architecture and Constraints The propulsion system architecture was optimized to meet a total design(takeoff) thrust requirement of 100 N while satisfying strict constraints on vehicle integration, acoustic signature, and safety. A Distributed Electric Propulsion (DEP) configuration was selected over a centralized large-propeller approach.

The optimization process evaluated the trade-off between propulsive efficiency (typically higher with larger diameters) and airframe integration penalties (drag, structural weight, and ground safety). The selected configuration consists of **four (4) modular propulsors**, each sized for a target thrust of 25 N.

Table 4: System Architecture Targets

Parameter	Value
Total Target Thrust (T_{total})	100 N
Number of Modules (N)	4
Thrust per Module (T_{module})	25 N
Selected Propeller Diameter (D)	5 inch (127 mm)
Propeller Type	High-Solidity 11-Blade Fan

Justification for 5-inch Diameter Selection The selection of a 5 inch diameter is driven by the need for high-density integration. Unlike standard 9-10 inch propellers, the 5 inch high-solidity fan enables:

- 1. Embedded Integration:** The compact diameter allows the propulsors to be fully shrouded or embedded into the wing structure, significantly reducing parasite drag during forward flight compared to open rotors.
- 2. Acoustic Shift:** The combination of high blade count ($B = 11$) and high RPM shifts the acoustic signature to higher frequencies, which are more readily attenuated by the atmosphere, resulting in a lower perceived noise level at distance. The exact optimisation process for the number of blades in the rotor and stator is given in the *Rotor and Stator Design* section.
- 3. Ground Safety:** The smaller swept area and shrouded design minimize risk to personnel compared to large exposed propeller blades.

Aerodynamic Performance Validation (Rotor and Stator Design) The aerodynamic feasibility of generating 25 N of thrust from a 5 inch disk was validated using Blade Element Momentum Theory (BEMT). The BEMT analysis provided the critical *Rotor and Stator Design* operating points required to achieve the high disk loading.

Data obtained from the BEMT simulation is presented below:

$$\text{Required Thrust per Module: } T_{req} = 25.0 \text{ N} \quad (5)$$

Based on the **Rotor and Stator Design** output, the required rotational speed and torque are:

$$\text{Design RPM } (n): 13,898 \text{ RPM} \quad (6)$$

$$\text{Design Torque } (Q): 0.8969 \text{ Nm} \quad (7)$$

To validate the feasibility of this operating point, we calculate the required mechanical shaft power (P_{mech}):

$$P_{mech} = Q \times \omega \quad (8)$$

Where ω is the angular velocity in rad/s:

$$\omega = 13,898 \times \frac{2\pi}{60} \approx 1,455.4 \text{ rad/s} \quad (9)$$

Substituting the values:

$$P_{mech} = 0.8969 \text{ Nm} \times 1,455.4 \text{ rad/s} \approx \mathbf{1,305 \text{ W}} \quad (10)$$

Analysis: The requirement of 1,305 W mechanical power for a 5 inch propulsor confirms that the system operates in a high-performance "Cinelifter" or "EDF" regime. Standard drone motors (typically 300-400 W) are insufficient. This necessitates a specific high-torque powertrain solution.

Powertrain Selection and Safety Margin Verification To satisfy the demanding torque and power requirements derived from the Rotor and Stator Design, the **T-Motor Velox V3115 (900KV)** was identified as the optimal candidate. This motor features a large stator volume (31mm \times 15mm) specifically designed for high-load applications.

We verify the electrical feasibility assuming a system efficiency (η_{sys}) of 85% and a 6S LiPo power source ($V_{load} \approx 21.0 \text{ V}$ under sag):

$$P_{elec} = \frac{P_{mech}}{\eta_{sys}} = \frac{1305}{0.85} \approx 1,535 \text{ W} \quad (11)$$

The resulting current draw (I_{req}) is:

$$I_{req} = \frac{P_{elec}}{V_{load}} = \frac{1535}{21.0} \approx 73.1 \text{ A} \quad (12)$$

Test Item	KV900	Configuration	12N14P
Internal Resistance	38.08mΩ	Motor Dimensions	φ37.2*51.1mm
Shaft Diameter	INS OUT5	Lead	18AWG 250mm
Weight (Incl. Cable)	113.1g	Idle Current(10V)	1.57A
Max. Power (10s)	1894W	Peak Current (10s)	83A

Figure 25: Motor Datasheet

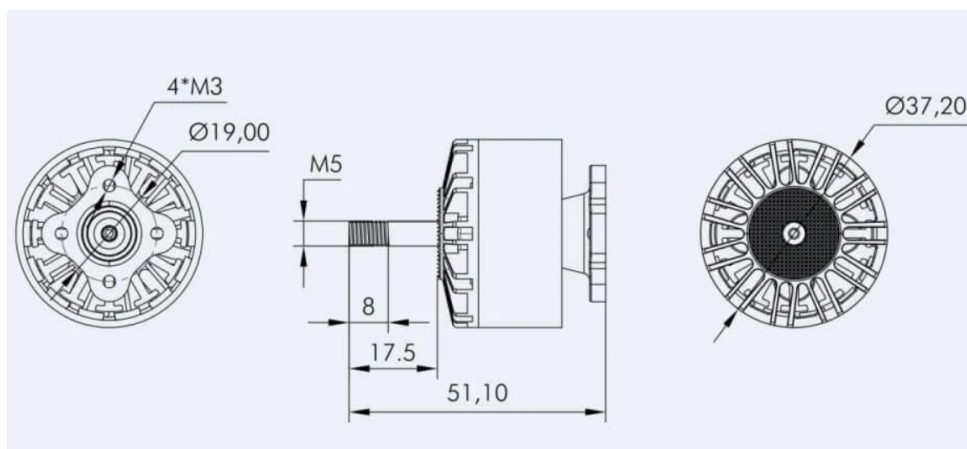


Figure 26: Motor Drawing

[T-M24]

Margin Analysis Comparing the calculated requirements against the manufacturer's rated limits for the T-Motor V3115:

Table 5: Hardware Capability Verification (10s Burst Ratings)

Parameter	Requirement (Calculated)	Motor Limit (Rated)	Safety Margin
Peak Power	1,535 W	1,894 W	+18.9%
Peak Current	73.1 A	83.0 A	+11.9%

Conclusion: The selected powertrain provides an 18.9% power safety margin and an 11.9% current safety margin over the BEMT-derived requirements. This confirms that the 5 inch high-solidity fan configuration is not only aerodynamically capable of meeting the 100 N total thrust target but is also supported by available commercial hardware.

3.1.5 Methodology

The objective analysis in the following section was to understand how slipstreams from multiple electric propellers interact with the wing, and how propeller placement influences this interaction. Since high-fidelity CFD cannot easily accommodate rapid geometric iteration and requires significant computational time, iterative sweeps of multiple rotor positions are not practically feasible with it hence a low-fidelity approach using OpenVSP and VSPAero was adopted to visually analyze wake characteristics and establish favourable placement regions for DEP modules.

Although VSPAero has demonstrated good accuracy for lift and drag estimation in conventional configurations, its fidelity reduces considerably when modelling multi-rotor blown-wing scenarios with strong jet gradients and swirl. Therefore, in this work, VSPAero was used solely for qualitative flowfield visualization, slipstream contraction analysis, and wake-interaction mapping—not for aerodynamic coefficient prediction. **No estimation of C_l , C_d , or stall margin has been extracted from the tool. Instead, the methodology was aimed at identifying slipstream immersion, jet expansion behavior, swirl interaction between adjacent propellers, and sensitivity to geometric positioning.**

Only the flow visualization outputs from OpenVSP/VSPAero were used to guide placement decisions, with the support of findings from literature. These results serve as the starting point for the CFD . The final propulsor positions are expected to lie close to the ones identified here.

Model Setup

SIMULATION TECHNICAL DATA SHEET

Global Geometry & Setup

Parameter	Value	Parameter	Value
Wing Geometry			
Span (b)	1.40000 m	Chord (Root)	0.17500 m
Projected Span	1.40000 m	Chord (Tip)	0.17500 m
Planform Area (S)	0.24500 m^2	MAC	0.17500 m
Aspect Ratio (AR)	8.00000	Airfoil	NACA 6412
Curved Area	0.12250 m^2	Thickness/Chord	0.12000
Propeller Geometry			
Outer Diameter (D)	0.12700 m	Blade Count	11
Propeller Mode	Blades	Blade Mode	Unsteady Rotating
RPM	13 989	Hub/Tip Ratio	N/A

Flow & Boundary Conditions			
Parameter	Value	Parameter	Value
Freestream Vel. (V_∞)	20 m/s	Reynolds No. (Re)	1.0×10^5
Air Density (ρ)	1.225 kg/m ³	Mach Number (M)	0.06
Angle of Attack (α)	0°	Stall Mode	ON

VSPAERO Solver Settings			
Parameter	Value	Parameter	Value
Wake Iterations	5	Time Step (Δt)	0.00017 s
Number of Nodes	8	Num of Time Steps	180
Thin Set	Shown	Hover Ramp	0.1

Assumptions :

- NACA6412 Airfoil is used .
- Rectangular Wing is assumed. Hence root chord and tip chord are equal.
- Sweep, Twist and Dihedral and AOA for the wing are assumed to be zero .
- The default propeller blade geometry in OpenVSP was used.
- All the default tessellation and mesh settings were used without going into much detail.
- Direction of rotation of propeller is inboard up [WGLY23].
- VSPAERO visualization capabilities allow for the identification of propeller wake structures. As the slipstream is defined by the wake boundary, it can be inferred that if the visualized wake envelope encompasses the wing surface, the wing is fully submerged within the propeller slipstream.
- For conventional aircraft configurations, the lift coefficient (C_L) during the cruise phase typically falls within the range of 0.4 to 0.6. For this design, the lower limit of the cruise regime is selected alongside a target Aspect Ratio (AR) of 8.
 - Target Lift Coefficient: $C_{L_{\text{cruise}}} = 0.4$
 - Aspect Ratio: $AR = 8$

The required planform area (S) is derived from the fundamental lift equation:

$$C_L = \frac{L}{\frac{1}{2}\rho V_\infty^2 S} \quad (13)$$

Rearranging the equation to solve for the planform area:

$$S = \frac{L}{\frac{1}{2}\rho V_\infty^2 C_L}$$

$$\Rightarrow S \approx 0.255 \text{ m}^2 \quad (\text{Preliminary Calculation})$$

With the area established, the tip-to-tip wingspan (b) is determined using the definition of Aspect Ratio:

$$AR = \frac{b^2}{S}$$

$$b = \sqrt{AR \cdot S}$$

$$b = \sqrt{8 \cdot 0.255}$$

$$b \approx 1.42 \text{ m}$$

To optimize the geometry for the OpenVSP simulation setup and manufacturing constraints, the values are adjusted as follows:

$$b_{\text{final}} = 1.40 \text{ m}$$

$$S_{\text{final}} = 0.245 \text{ m}^2$$

Finally, assuming a rectangular planform, the mean geometric chord (c) is calculated:

$$c = \frac{S_{\text{final}}}{b_{\text{final}}} = \frac{0.245}{1.40} = 0.175 \text{ m}$$

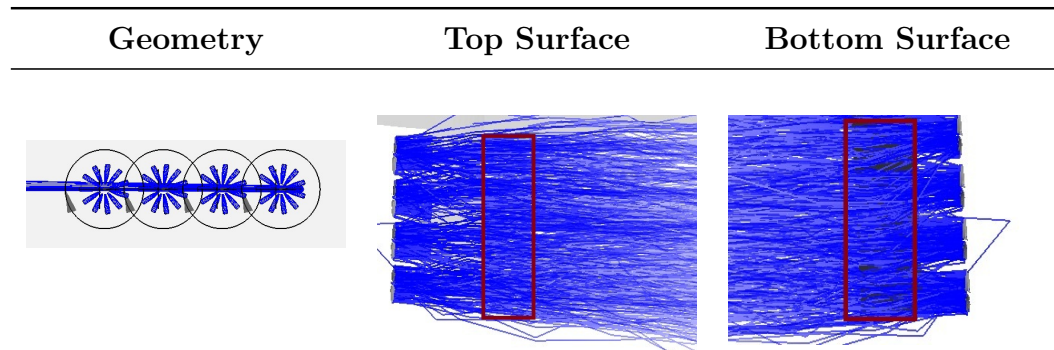
Iterations : x : Streamwise Distance Of Propeller from Leading edge (equal to 1 diameter of propellers [Haw24]) in m.

z : Vertical Height of Propeller from Chord Line in m.

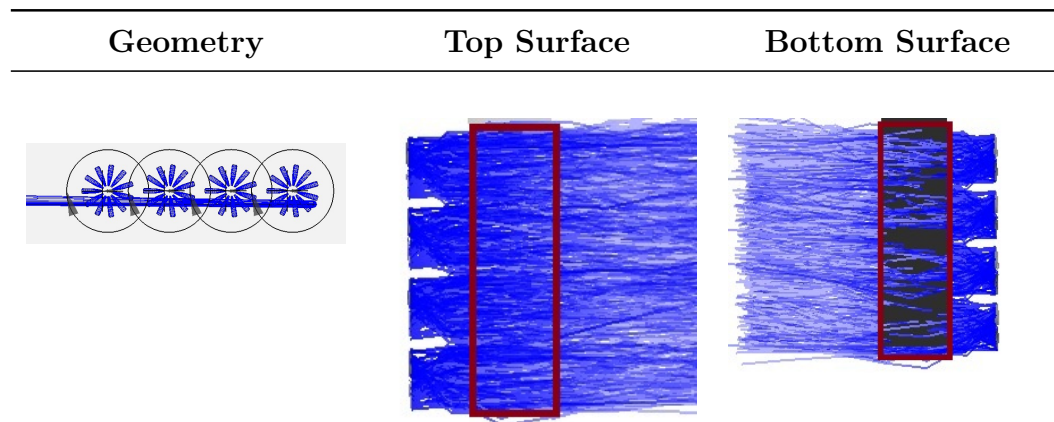
d_r : Distance of the first Propeller from Root Chord in m.

I. Placement Without considering Duct Thickness

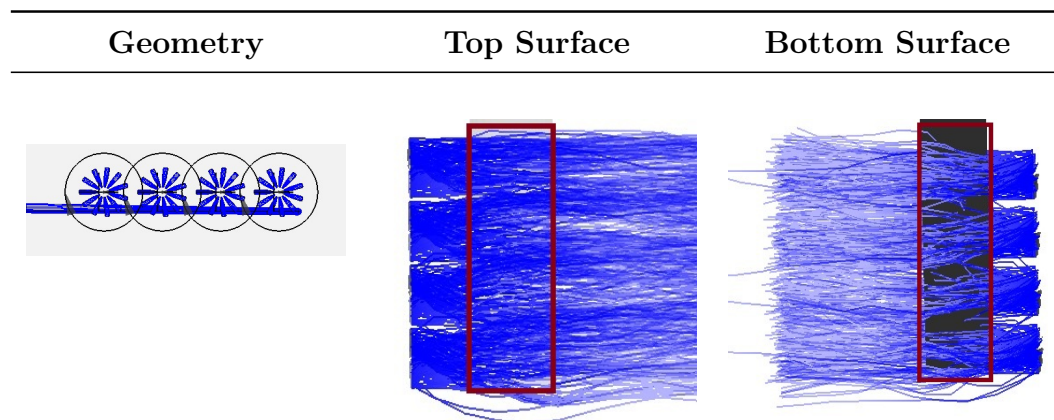
i. $x = 0.127m$ $z = 0m$ $d_r = 0.2m$



ii. $x = 0.127m$ $z = 0.25D_p \approx 0.032m$ $d_r = 0.2m$



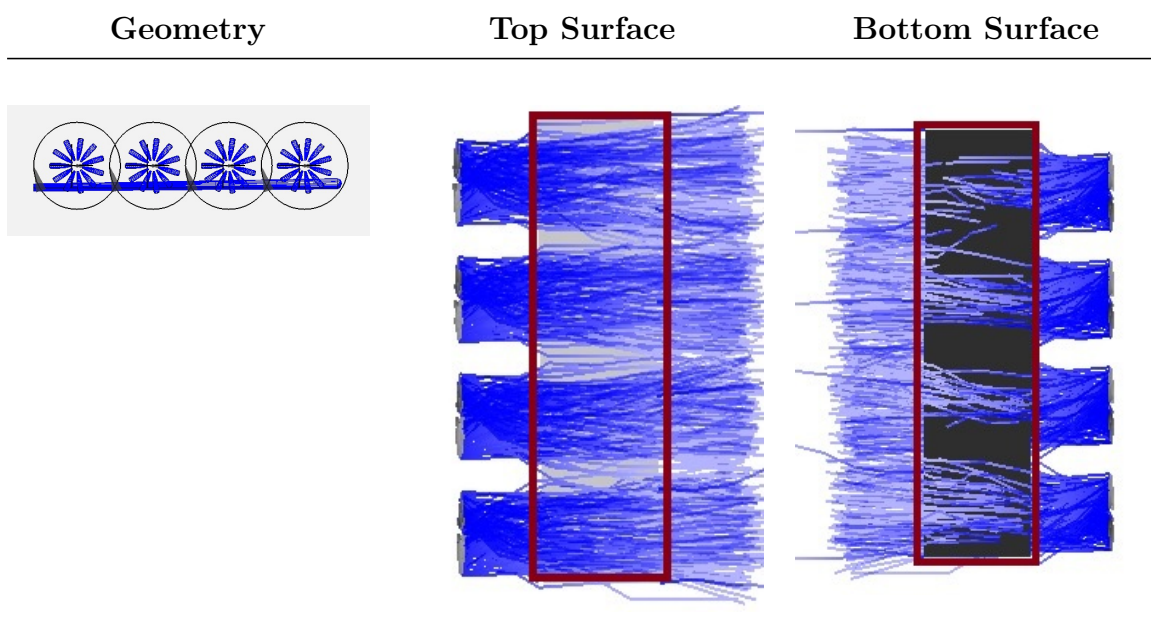
iii. $x = 0.127m$ $z = 0.4D_p \approx 0.05m$ $d_r = 0.2m$



II.

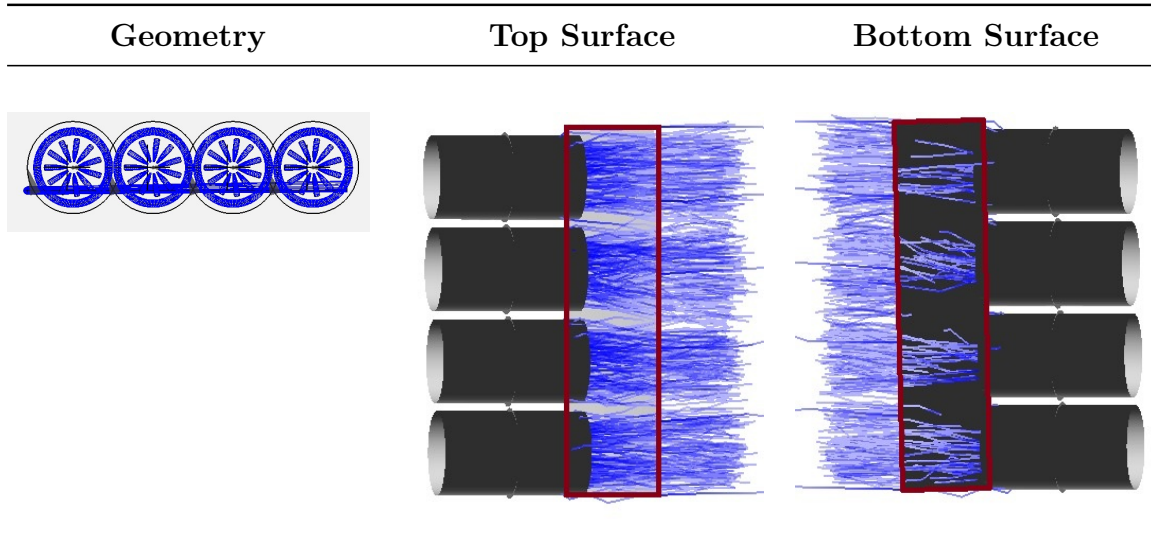
Placement Considering Duct Thickness but without Duct

i. $x = 0.127m$ $z = 0.05m$ $d_r = 0.100m$



Placement Considering Ducts

i. $x = 0.127m$ $z = 0.05m$ $d_r = 0.100m$



Explanation: *The red outline represents the wing planform.

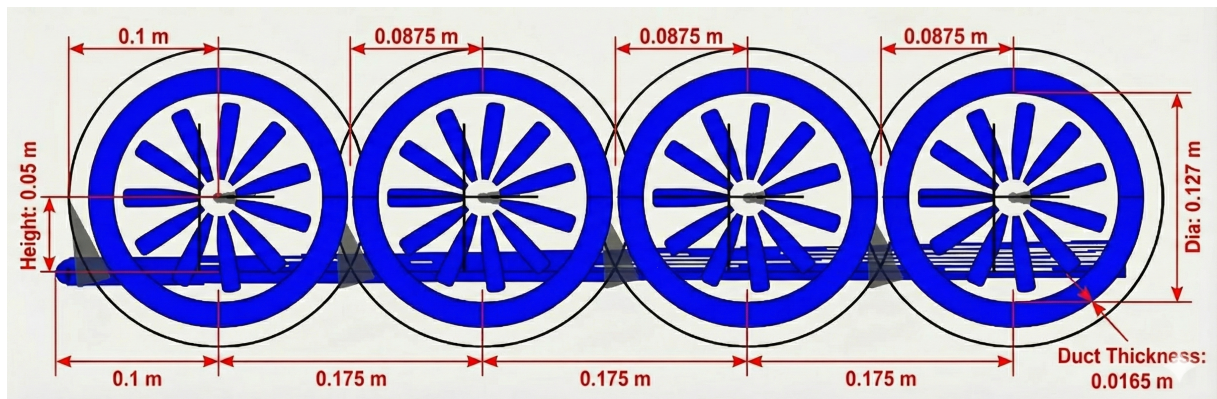
The first configuration neglects duct thickness, setting the inter-propeller spacing to 0.15 m. Three vertical positions relative to the chord line are evaluated: $z = 0$ m, $z = 0.25D_p \approx 0.032$ m [Haw24], and $z = 0.4D_p \approx 0.05$ m. Consistent with literature, the propeller slipstreams are expected to overlap; this behavior is confirmed across all

three cases on the top surface. It is observed that even at the increased vertical height of $z = 0.05$ m, the slipstreams continue to fully submerge the wing. Consequently, subsequent iterations are performed exclusively at $z = 0.05$ m.

The second configuration accounts for duct thickness (1.65 cm in the propeller plane) within the spacing but excludes the physical duct geometry. Here, the distance between propeller centers is increased to 0.175 m, and slipstream overlap is again observed. In the third configuration, which includes the physical ducts, the slipstreams are observed to contract, as expected. Despite this contraction, the wing remains submerged within the slipstreams, as visible on the bottom surface.

3.1.6 Conclusion

The final placement of the EDF's as obtained from the above analysis is as shown below .



This placement should be the starting point for the final CFD analysis with wing.

3.2 Rotor and Stator Design for EDF

3.2.1 Introduction

The design of the rotor and stator for an Electric Ducted Fan (EDF) system is critical to achieving high thrust-to-weight ratios with minimal drag. Unlike open propellers, EDFs operate in a constrained flow environment where tip losses are mitigated by the shroud, but duct friction and wake interactions become significant.

The aim of this design is to optimize the propulsion stage for a static/take-off condition (Design Point: $V_\infty = 20$ m/s, Thrust = 25 N), ensuring adequate acceleration. The methodology combines low-order physics models (BEMT) with higher-order constraints (Lieblein Diffusion Factors) to generate a manufacture-ready geometry.

3.2.2 Non Dimensional Constants

The sizing of any axial flow turbomachine begins with the selection of appropriate non-dimensional parameters that define the velocity triangles at the design point. For this EDF design, two critical parameters were assumed based on literature recommendations for high-efficiency fans:

1. **Flow Coefficient (ϕ):** Relates the axial velocity to the blade tip speed.
2. **Stage Loading Coefficient (ψ):** Relates the specific work (enthalpy rise) to the blade tip speed squared.

This document dissects the code implementation of these parameters found in `airfoil_optimisation.py` and `Propeller_Generator.py` to explain how the physical operating conditions (V_x and ω) are derived.

Flow Coefficient Assumption

Definition and Selection The flow coefficient ϕ is a dimensionless measure of the axial throughput of the fan relative to its rotational speed. It is defined at the mean radius r_m as:

$$\phi = \frac{V_x}{U_m} \quad (14)$$

Where:

- V_x is the axial flow velocity (assumed constant across the annulus).
- $U_m = \omega r_m$ is the blade tangential speed at the mean radius.

Code Assumption: The design script explicitly sets this parameter to a fixed value.

$$\phi_{\text{mean}} = \frac{V_x}{U_m}$$

$$V_x = \phi_{\text{mean}} U_m$$

Justification: A value of $\phi_{\text{mean}} = 0.75$ is selected. According to Smith's charts for axial compressors and fans [Smi66], high efficiencies for subsonic stages are typically found in the region of $0.6 < \phi < 0.8$.

- **Low ϕ (< 0.5):** Implies high swirl relative to axial flow, leading to high twist and potential hub separation.
- **High ϕ (> 1.0):** Implies very high axial velocity, increasing through-flow losses (friction) and likely requiring a larger duct for the same mass flow.

The choice of 0.75 balances mass flow capacity with blade loading limits.

Calculation of Velocities The calculation of physical velocities (V_x and ω) is not arbitrary; it is derived from the required thrust (T_{des}) and the energy definitions.

Step 1: Specific Work Calculation (Δh_0) The code first calculates the required change in stagnation enthalpy (specific work) to generate the target thrust. Using simple momentum theory for a static/low-speed case where the exit pressure matches ambient:

$$T = \dot{m}V_{jet} = (\rho A V_{jet})V_{jet} = \rho A V_{jet}^2 \quad (\text{Approximate for static}) \quad (15)$$

However, the code uses a more rigorous energy formulation derived from the Bernoulli equation and actuator disc theory.

$$\Delta h_0 = \frac{1}{2}V_{jet}^2 \quad (16)$$

Since thrust $T \approx \dot{m}\Delta V \approx \rho A V_{jet}^2$ (for static, $V_{in} = 0$), we can relate work directly to thrust per unit area (Disk Loading).

$$T = \frac{1}{2} \rho A V_4^2$$

$$V_4 = \sqrt{\frac{2T_{des}}{\rho A_{annulus}}}$$

$$\Delta h_0 = \frac{1}{2}V_4^2$$

Step 2: Determining Blade Speed (U_m) and Angular Velocity (ω) To find the physical rotational speed, the code utilizes the Stage Loading Coefficient (ψ).

$$\psi = \frac{\Delta h_0}{U_m^2} \quad (17)$$

This parameter dictates how much work the blade performs for a given tip speed. The code assumes $\psi_{des} = 0.4$.

- A value of $\psi \approx 0.4$ is typical for light-loading fans (like turbofan by-pass stages), ensuring the blades are not stalled by trying to turn the flow too sharply [Cum89].

Rearranging for the mean blade speed U_m :

$$U_m = \sqrt{\frac{\Delta h_0}{\psi_{des}}} \quad (18)$$

And finally, the angular velocity ω (radians/sec) is found using the mean radius r_m :

$$\omega = \frac{U_m}{r_m} \quad (19)$$

$$\psi = \frac{\Delta h_0}{U_m^2} \implies U_m = \sqrt{\frac{\Delta h_0}{\psi_{\text{des}}}}$$

$$\omega = \frac{U_m}{r_m}$$

$$\text{RPM} = \frac{\omega 60}{2\pi}$$

Step 3: Calculating Axial Velocity (V_x) With the blade speed U_m determined from the energy requirement, the axial velocity is simply resolved using the flow coefficient assumption from Section 2:

$$V_x = \phi_{\text{mean}} \cdot U_m \quad (20)$$

This V_x is then applied as a constant across the entire span (`Vx = np.full_like(r, Vx_const)`), which satisfies the Free-Vortex radial equilibrium condition:

$$\frac{dH}{dr} = 0 \text{ and } V_\theta r = \text{const} \implies V_x = \text{const} \quad (21)$$

Summary of Design Logic The logic flow in the code is circular but closed:

1. Requirement: We need Thrust T .
2. Physics: Thrust requires Energy Δh_0 .
3. Turbomachinery Choice: We choose a specific loading style ($\psi = 0.4$) and flow style ($\phi = 0.75$) appropriate for EDFs.
4. Result: These choices dictate the exact RPM (ω) and Flow Velocity (V_x) required to meet the thrust target efficiently.

This methodology avoids "guessing" an RPM. Instead, the RPM is a *result* of the aerodynamic requirements.

3.2.3 Topology Optimization: Blade Count Selection

Before detailed geometric sizing, the topology of the turbomachinery—specifically the number of rotor blades (B_{rotor}) and stator vanes (B_{stator})—must be optimized. This decision is not arbitrary; it is the result of a trade-off between aerodynamic efficiency and acoustic signature.

Rotor Blade Count Optimization The selection of B_{rotor} is driven by two competing power loss mechanisms: Induced Power (Vortex Loss) and Profile Power (Friction Loss).

Prandtl Tip Loss Factor and Induced Power With a finite number of blades, the pressure difference between the pressure and suction sides leaks over the blade tip, creating tip vortices. This reduces the effective lift near the tip. The design code utilizes the Prandtl Tip Loss Factor (F) to quantify this efficiency drop. The factor F represents the ratio of the actual circulation to the circulation of a rotor with infinite blades:

$$F = \frac{2}{\pi} \arccos \left(\exp \left(-\frac{B}{2} \frac{R_{tip} - r}{R_{tip} \sin \phi} \right) \right) \quad (22)$$

Where ϕ is the relative flow angle.

- **Low Blade Count ($B < 5$):** The factor F decreases significantly, implying high vortex losses. The gaps between blades are large, allowing significant radial flow and tip leakage.
- **High Blade Count ($B > 15$):** F approaches 1.0, meaning the rotor behaves like an ideal actuator disc. However, this introduces the second penalty: friction.

Implementation Logic: The following math demonstrates how the tip loss factor acts as a penalty multiplier on the ideal induced power. Note how a low F increases the power loss.

$$\begin{aligned} f_{\text{exp}} &= -\frac{B_{\text{rotor}}}{2} \frac{R_{\text{tip}} - r}{R_{\text{tip}} \sin \phi} \\ F &= \frac{2}{\pi} \cos^{-1}(\exp(\max(f_{\text{exp}}, -20))) \end{aligned}$$

$$P_{\text{ideal, induced}} = T_{\text{des}} v_i$$

$$P_{\text{induced, loss}} = P_{\text{ideal, induced}} \left(\frac{1}{\max(F, 0.01)} - 1 \right)$$

Profile Power and Reynolds Number Scaling As the blade count increases, the total wetted surface area of the rotor increases (assuming solidity is maintained or chord constraints are met). This increases the skin friction drag. The optimization code specifically accounts for Low-Reynolds number effects, which are critical for small-scale EDFs.

The drag coefficient (C_d) is modeled with a Reynolds number penalty:

$$C_d = C_{d,base} \times \left(\frac{Re_{ref}}{Re} \right)^{0.4} \quad (23)$$

Where $Re_{ref} = 500,000$. For small chords associated with high blade counts, Re drops, drastically increasing C_d due to laminar separation bubbles and viscous dominance.

Decision: The optimizer sweeps blade counts from 3 to 22. The intersection of the decreasing induced loss curve and the increasing friction loss curve yielded an optimal count of **11 blades**. This provides a balance where tip losses are contained without incurring excessive viscous penalties.

Stator Vane Count and Acoustics The stator count (B_{stator}) is selected based on flow straightening requirements and acoustic signature mitigation.

Acoustic Interaction and the Coprime Rule A major source of noise in turbomachinery is the interaction between the viscous wakes shed by the rotor blades and the leading edges of the stator vanes. If B_{rotor} and B_{stator} share a common factor, multiple blades pass multiple vanes simultaneously, causing constructive interference of pressure pulses (noise).

To mitigate this, the design enforces a **Coprime Condition**:

$$\gcd(B_{rotor}, B_{stator}) = 1 \quad (24)$$

With $B_{rotor} = 11$, the optimizer evaluated stator counts. $B_{stator} = 13$ was selected because 11 and 13 are coprime numbers [And20]. This ensures that only one blade passes a vane at any single instant, distributing the acoustic energy across a broader spectrum rather than distinct tonal peaks.

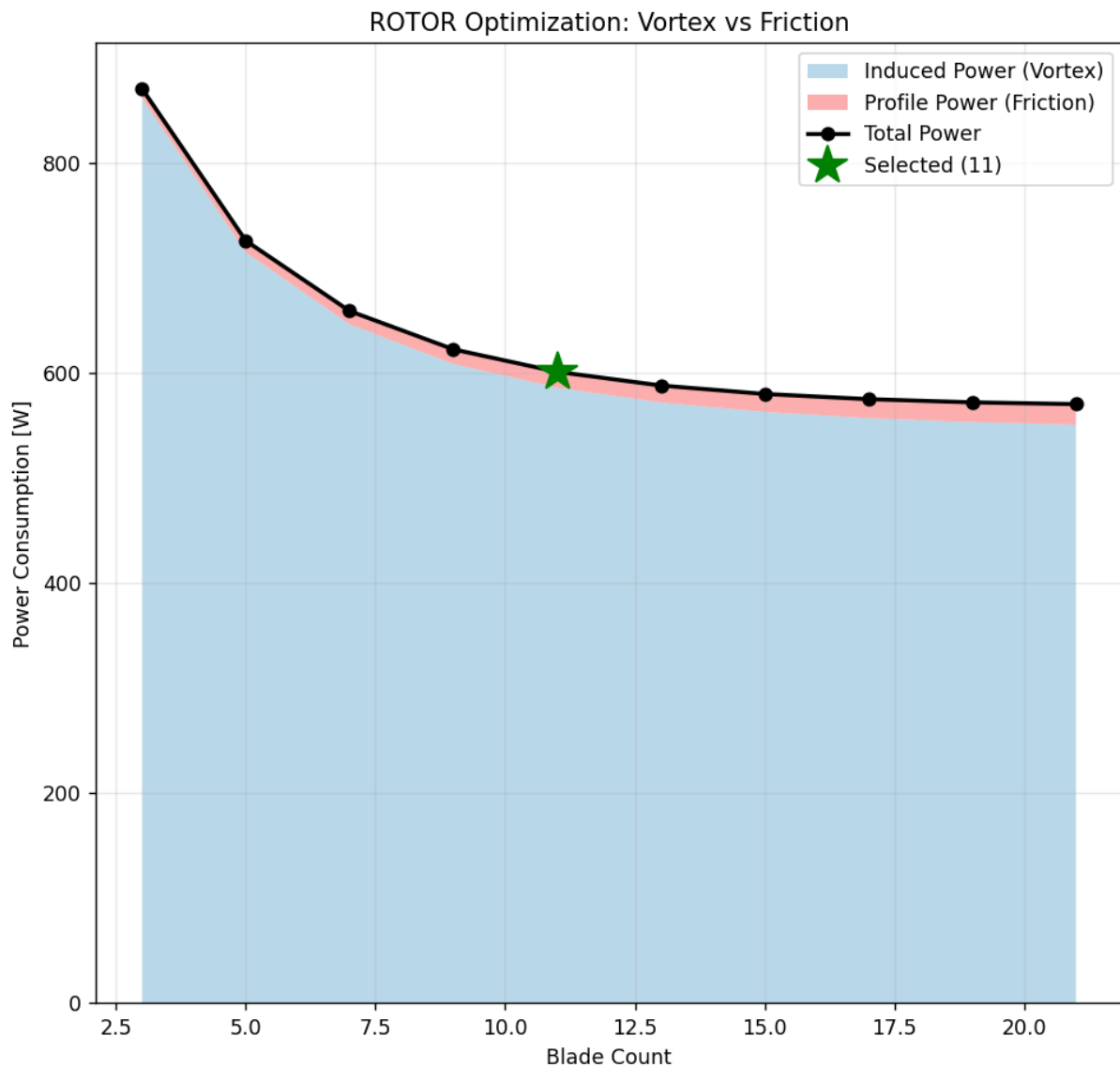


Figure 27: Rotor Blade Count Optimisation

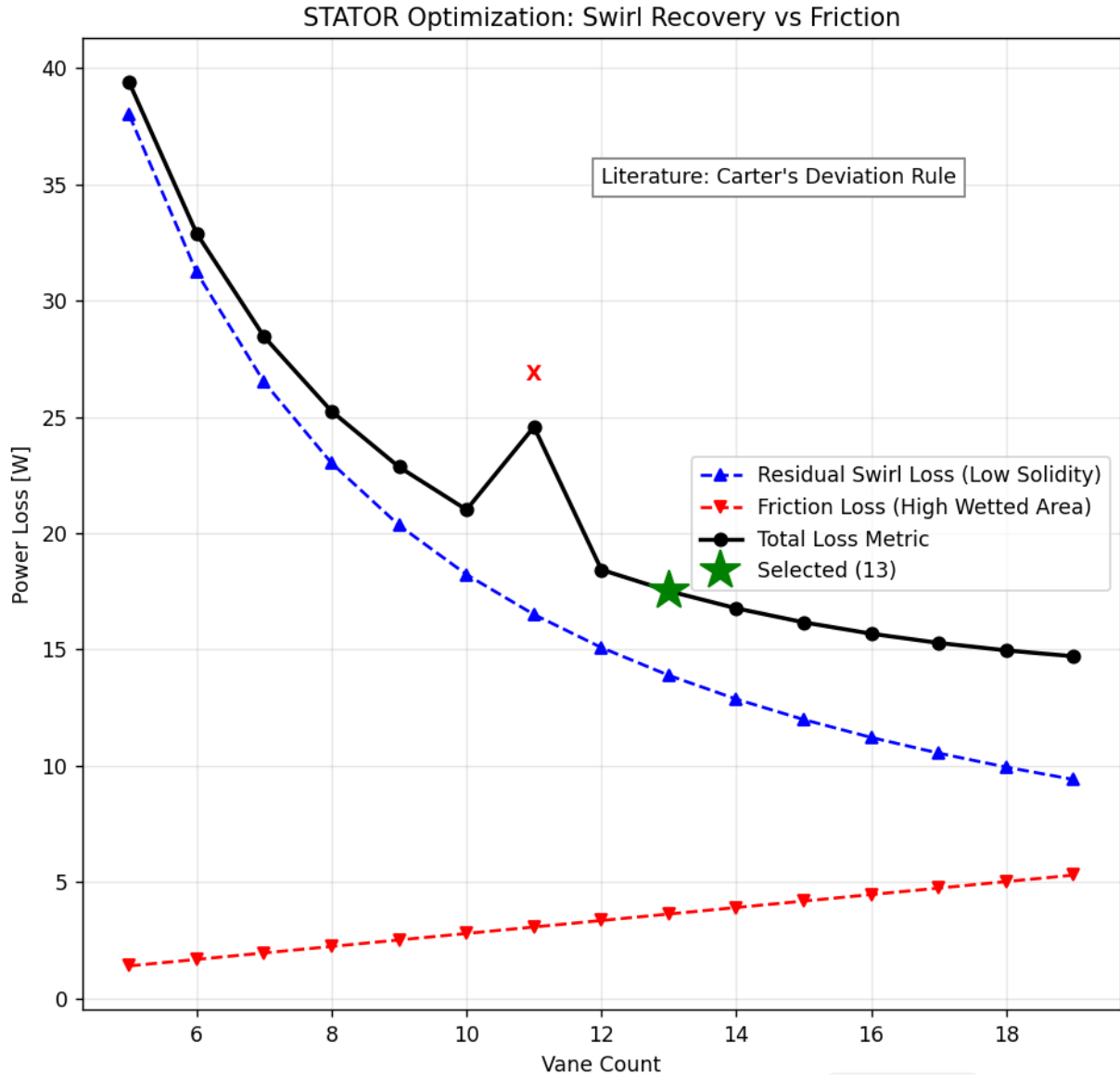


Figure 28: Stator Blade Count Optimisation

3.2.4 Aerodynamic Design Methodology

Free-Vortex Flow Model The radial distribution of flow properties is a critical design choice. The Free-Vortex Flow model is widely adopted for axial-flow fans due to its ability to satisfy the radial equilibrium equation with constant enthalpy and axial velocity.

Tangential Velocity Distribution The model assumes that the tangential velocity component, $V_\theta(r)$, varies inversely with the radial distance r . This distribution ensures that the curl of the velocity field is zero (irrotational flow) outside the boundary layer. The distribution is defined as:

$$V_\theta(r) = \frac{\Delta h_0}{U} = \frac{\Delta h_0}{\Omega r} \quad (25)$$

Where Δh_0 is the change in stagnation enthalpy (work done). This implies that the work done per unit mass is constant along the entire span of the blade.

Radial Equilibrium and Axial Velocity A consequence of the free-vortex assumption ($\frac{d}{dr}(rV_\theta) = 0$) is that it simplifies the Simple Radial Equilibrium Equation (SRE). Assuming isentropic flow and constant total enthalpy, this condition implies that the axial velocity profile remains uniform across the span:

$$\frac{\partial V_a}{\partial r} = 0 \implies V_a(r) = \text{constant} \quad (26)$$

In the design code, this is implemented by setting a constant flow coefficient $\phi_{mean} = 0.75$, such that $V_a = \phi_{mean} \cdot U_{mean}$. This simplifies the twist calculation significantly, as the vector triangles at every station rely on a fixed V_a .

Blade Element Momentum Theory (BEMT) The rigorous sizing is performed using BEMT, which discretizes the blade into N radial annuli. The code uses a discrete summation approach to approximate the integrals of thrust and torque.

Thrust and Torque Formulation The differential thrust dT and torque dQ on a blade element of width dr are given by:

$$dL = \frac{1}{2}\rho W^2 c C_L \quad (27)$$

$$dD = \frac{1}{2}\rho W^2 c C_D \quad (28)$$

Resolving these forces into the axial (Thrust) and tangential (Torque) directions:

$$dT = B(dL \cos \phi - dD \sin \phi) \quad (29)$$

$$dQ = Br(dL \sin \phi + dD \cos \phi) \quad (30)$$

Where ϕ is the relative inflow angle, $\phi = \arctan(V_a/(\Omega r - V_\theta/2))$.

Iterative Chord Scaling A unique feature of the generator code is the **Thrust Matching Loop**.

1. A baseline chord distribution is generated.
2. The total thrust T_{BEMT} is calculated by summing dT across all annuli.
3. This is compared to the Design Requirement ($T_{des} = 25$ N).
4. A scaling factor $S_c = T_{des}/T_{BEMT}$ is computed.
5. The entire chord distribution is scaled by S_c (linearly) to match the target thrust exactly, ensuring the physical hardware matches the theoretical requirement.

3.2.5 Geometric Parameters and Airfoil Selection

Airfoil Selection: NACA 4412 The rotor employs the **NACA 4412** airfoil.

- **Camber (4%):** The high camber provides a high maximum lift coefficient ($C_{L,max}$), which is essential for generating the required 25N of thrust within the small 125mm diameter disc.
- **Thickness (12%):** This thickness provides sufficient structural volume for the blade root while maintaining a reasonably low form drag [NAS47].
- **Aerodynamic Justification:** At the low Reynolds numbers ($\sim 10^5$) typical of this EDF, laminar separation is a risk. The NACA 4-digit series is robust and has predictable stall characteristics compared to more sensitive laminar flow airfoils.

Lift Coefficient and Angle of Attack A critical assumption in the design code is the target design lift coefficient:

$$C_{L,design} = 0.9 \quad (31)$$

Justification of Assumption Standard cruise propellers are often designed for maximum L/D , which typically occurs around $C_L = 0.6 - 0.7$. However, EDF rotors are "thrust-dense" machines [Smi19a]. To minimize the chord length (and thus solidity) for a given thrust, the blades must be loaded higher.

- A C_L of 0.9 is near the "knee" of the lift curve for NACA 4412 but safely below the stall point ($C_{L,max} \approx 1.2 - 1.4$).
- This assumption allows for smaller, lighter blades with less wetted area.

Resulting Angle of Attack The code calculates the required Angle of Attack (α) using a linear lift slope model:

$$\alpha = \frac{C_{L,target}}{a_0} + \alpha_{L=0} \quad (32)$$

With a lift slope $a_0 \approx 0.11$ per degree and zero-lift angle $\alpha_{L=0} \approx -4^\circ$ for NACA 4412:

$$\alpha \approx \frac{0.9}{0.11} - 2.0^\circ \approx 6.18^\circ \quad (33)$$

This confirms the user's observation of $\approx 6.2^\circ$. This provides a safety margin of approximately 6° before stall (typically at $12^\circ - 14^\circ$).

$$C_L = a(\alpha - \alpha_0)$$

$$\alpha = \frac{C_{L,target}}{a} + \alpha_0$$

Chord Distribution and Diffusion Factor

Bezier Chord Distribution The chord length $c(r)$ is defined using a cubic Bezier curve. This allows for a non-linear distribution that is structurally robust at the hub (c_{root}) and slender at the tip (c_{tip}).

- **Hub** ($c_{root} \approx 0.18R$): Thick to withstand centripetal and bending moments.
- **Tip** ($c_{tip} \approx 0.06R$): Thin to minimize induced drag and noise.

Lieblein Diffusion Factor (DF) A critical aerodynamic constraint applied in the code is the Diffusion Factor (DF). This metric predicts boundary layer separation on the suction surface of the blade due to flow deceleration.

$$DF = 1 - \frac{V_2}{V_1} + \frac{\Delta V_\theta}{2\sigma V_1} \quad (34)$$

Where σ is the solidity ($Bc/2\pi r$).

Constraint Logic: The design enforces a limit of $DF < 0.4$. If the initial Bezier chord results in a $DF > 0.4$ (implying the blade is too narrow to turn the flow without separating), the code *automatically increases the local chord length*. This "Aerodynamic Clamping" ensures that the beautiful Bezier curve does not violate physics, preventing compressor stall at the root where turning angles are highest.

$$\left(\frac{s}{c}\right)_{req} = \left(DF_{\text{limit}} - 1 + \frac{V_2}{V_1}\right) \left(\frac{2V_1}{\Delta V_\theta}\right)$$

$$c_{DF} = \frac{s_{\text{pitch}}}{(s/c)_{req}} \quad (\text{only if } (s/c)_{req} > 0)$$

$$c = \max(c_{\text{pref}}, c_{DF})$$

Twist and Pitch The geometric twist of the blade is derived from the velocity triangles.

- **Flow Angle (β_1):** The angle of the incoming relative wind.
- **Pitch Angle (θ):** The physical angle of the blade relative to the plane of rotation.

$$\theta(r) = \beta_1(r) - \alpha_{\text{design}} \quad (35)$$

Note: The code subtracts α because the convention used defines flow angle relative to the axial direction, requiring careful orientation in the CAD generation phase.

Hub-to-Tip Ratio The design fixes the hub-to-tip ratio ($\nu = R_{hub}/R_{tip}$) at **0.30**.

- A lower ν increases annular area, allowing for higher mass flow.
- However, as $r \rightarrow 0$, the required twist for a Free-Vortex blade approaches infinity. $\nu = 0.30$ is a standard compromise that avoids extreme twist at the root while

maintaining sufficient motor housing volume.



Figure 29: Rotor Geometry

3.2.6 Stator Design: Swirl Recovery

The stator is positioned downstream of the rotor to recover the rotational energy imparted to the flow.

Swirl Removal Logic The rotor imparts a swirl velocity V_θ . Without a stator, this kinetic energy ($0.5\rho V_\theta^2$) would be dissipated in the wake as heat, reducing propulsive efficiency. The stator is designed to turn the flow such that the exit tangential velocity is zero:

$$V_{\theta,\text{exit}} = 0 \quad (36)$$

This conversion of dynamic swirl pressure into static axial pressure provides a "free" thrust boost.

Stator Airfoil and Loading

- **Airfoil:** NACA 0012 (Symmetric). Since the stator does not need to generate lift in a specific direction (it acts as a flow guide), a symmetric foil minimizes profile drag at zero incidence.

- **Loading ($C_L = 0.4$):** The stator is loaded lightly compared to the rotor. High loading on stators can cause aggressive separation due to the adverse pressure gradient in the diffusion passage [Jam18].
- **Solidity:** The stator chord is linked to the rotor chord (typically 80%) but optimized to ensure the Diffusion Factor remains below 0.45, ensuring the flow stays attached during the aggressive turning process.

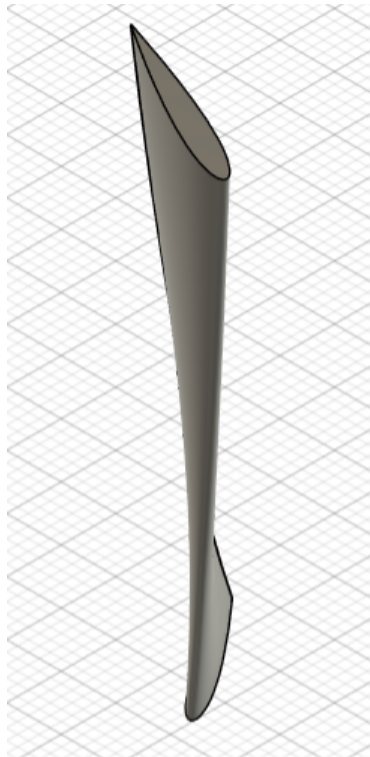


Figure 30: Stator Geometry

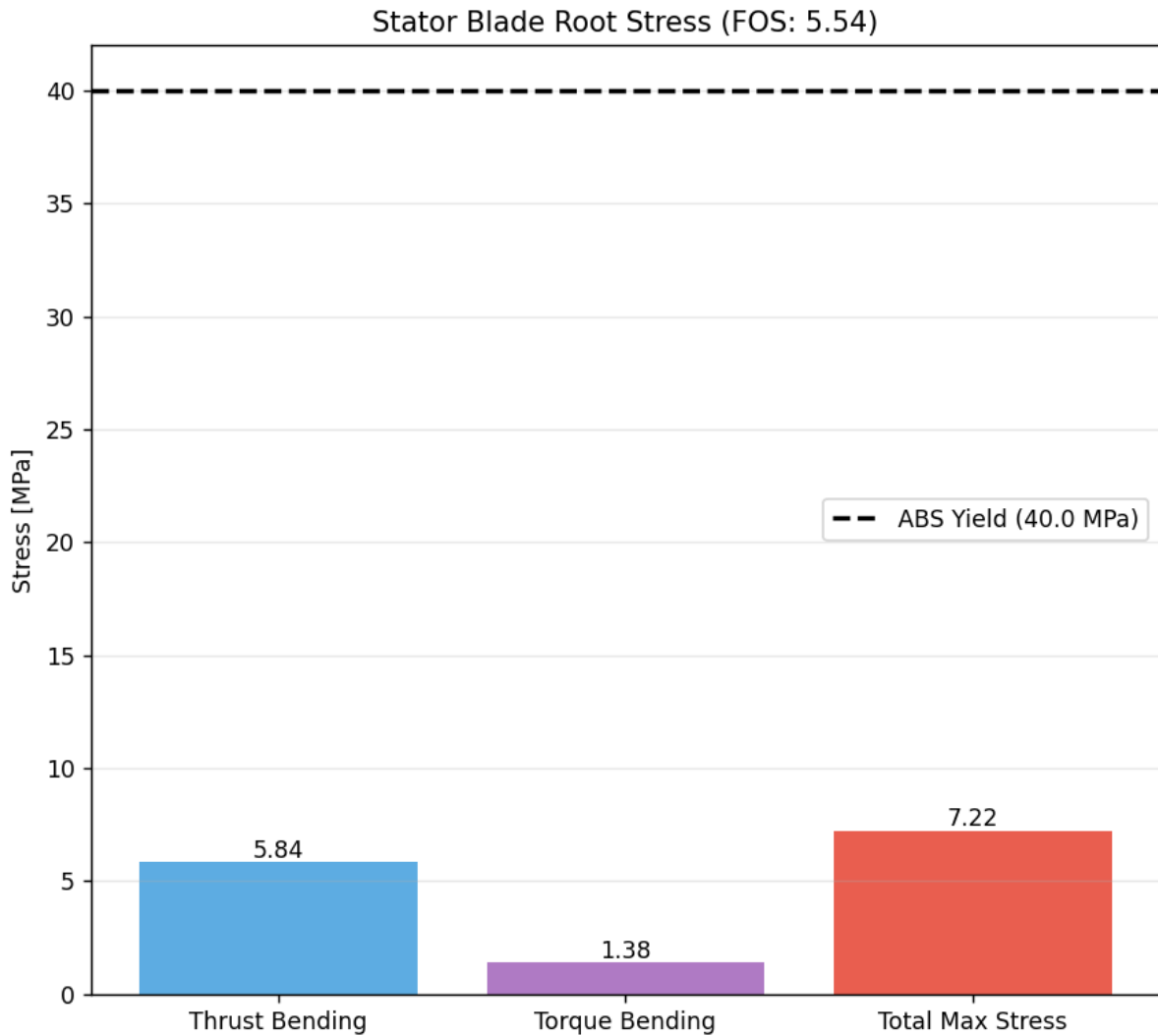


Figure 31: Stator Root Stress

3.2.7 Conclusion

The presented design methodology robustly integrates fundamental aerodynamic theory with practical constraints. By optimizing the blade count to 11 (Rotor) and 13 (Stator), the system minimizes acoustic interference and vortex losses. The adoption of a Free-Vortex design with a $C_L = 0.9$ loading strategy ensures a compact, high-thrust rotor suitable for the target operating point. Finally, the integration of Lieblein's Diffusion Factor as a hard constraint ensures that the resulting geometry is not only theoretically efficient but physically viable, free from gross flow separation.

PROPELLOR TECHNICAL DATA SHEET

Global Geometry & Setup

Parameter	Value	Parameter	Value
Outer Diameter (D)	125.0 mm	Design Thrust (T_{des})	25.00 N
Hub/Tip Ratio	0.300	Blade Count (R/S)	11 / 13
Ref. Density (ρ_{SL})	1.2250 kg/m ³	Design RPM	13 989 rpm

Component Aerodynamics

<i>Rotor (BEMT-Optimised)</i>		<i>Stator (Swirl Recovery)</i>	
Momentum Δh_0	1827.5 J/kg	Stator Drag	≈ 0.232 N
BEMT Thrust	25.000 N	Mean C_L	0.400
BEMT Torque	0.8969 N m	Mean C_D	0.012
Mean C_L / C_D	0.900 / 0.015	Annulus Area	0.011 167 m ²

Performance Envelope

Parameter	Static	Takeoff (Design)	Cruise
Condition	0 m/s (SL)	20 m/s (SL)	80 m/s (10k ft)
Thrust (N)	31.050	25.000	12.042
Shaft Power (W)	1046.0	1046.0	1046.0
Mass Flow (kg/s)	0.461	0.572	0.878
Jet Speed V_4 (m/s)	67.375	63.679	93.720
Disc Speed V_2 (m/s)	33.688	41.839	86.860

Rotor Geometry Distribution

Station	Span (r/R)	Chord (c)	Metal Angle (β_m)
Root	0.31	17.1 mm	54.7°
Mid	0.67	19.1 mm	33.5°
Tip	0.99	22.5 mm	23.0°

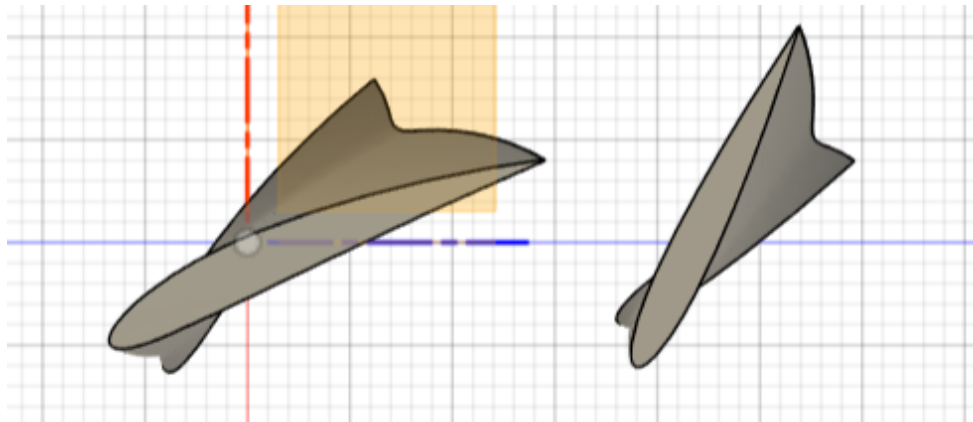


Figure 32: Rotor and Stator Relative

3.3 EDF Centrebody and Nacelle Design

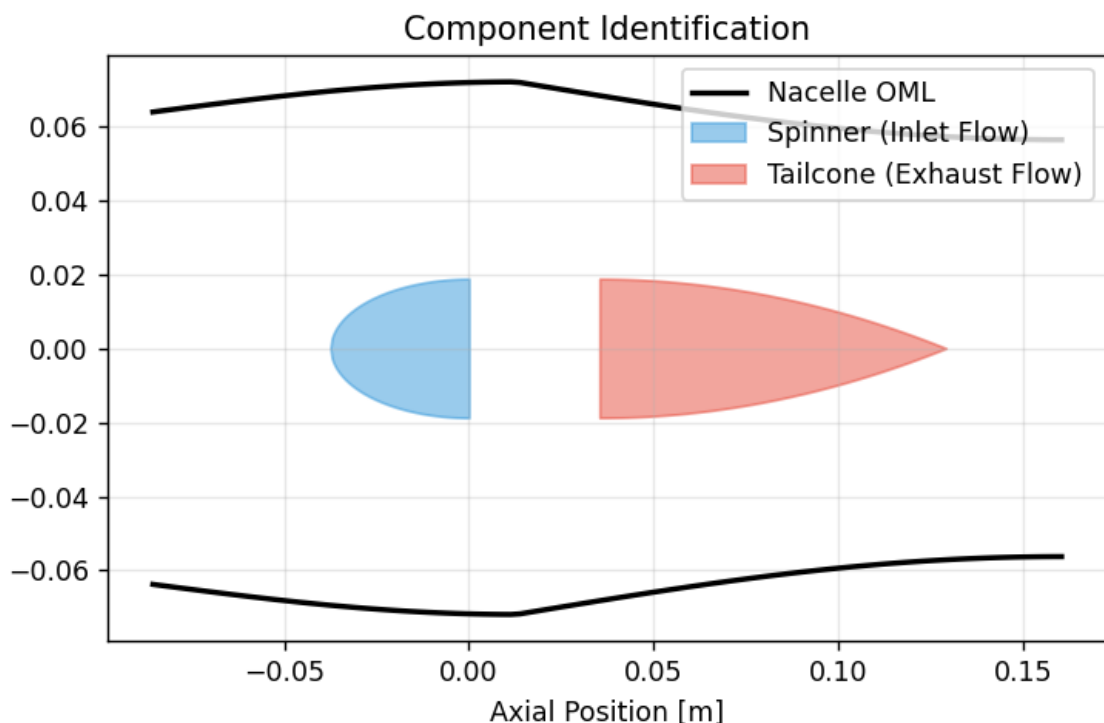


Figure 33: Component Overview

3.3.1 Centerbody Aerodynamics: The Spinner Cone

The spinner cone serves as the aerodynamic vanguard of the propulsion system. Its primary function is to condition the freestream air (\mathbf{V}_∞) before it enters the rotor disc, specifically ensuring that the boundary layer at the hub root remains attached. Flow separation at the spinner would result in the ingestion of a turbulent wake by the blade roots, significantly degrading the efficiency of the inner span of the rotor blades.

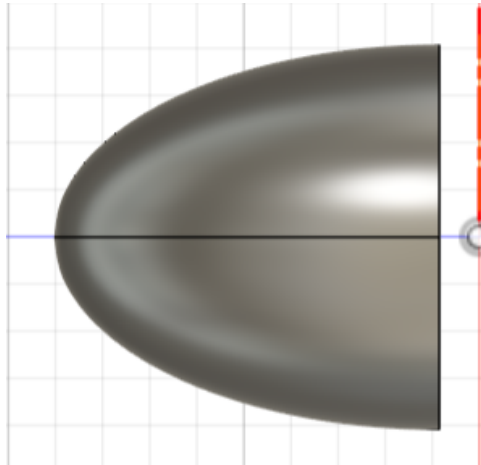


Figure 34: Spinner Cone

Geometry Selection: High L/D Elliptical Profile While many low-speed fans utilize hemispherical spinners, our design adopts a prolate spheroid (elliptical) profile with a Length-to-Diameter (L/D) ratio of 1.0. This geometry is generated mathematically in the `Cone_Generator.py` script:

$$r_{spin}(x) = R_{hub} \sqrt{1 - \left(\frac{x}{L_{spin}}\right)^2} \quad \text{for } x \in [-L_{spin}, 0] \quad (37)$$

Justification for High L/D: A higher fineness ratio minimizes the magnitude of the adverse pressure gradient ($\frac{dP}{dx} > 0$) as the flow decelerates towards the stagnation point and subsequently accelerates over the shoulder of the cone. By extending the axial length L_{spin} to equal the hub diameter D_{hub} , we ensure a gradual acceleration of the flow. This delay in the pressure recovery peak promotes laminar flow stability, delaying the transition to turbulence and reducing the skin friction coefficient.

Skin Friction and Boundary Layer Analysis The drag contribution of the spinner is dominated by skin friction rather than pressure drag (form drag), assuming attached flow. To rigorously quantify this, we employ the integral boundary layer method utilized in `DragDistribution(Centrepiece).py`.

The local Reynolds number Re_s is calculated along the curvilinear surface coordinate s :

$$Re_s = \frac{\rho V_{local} s}{\mu} \quad (38)$$

Where:

- $\rho = 1.225 \text{ kg/m}^3$ (Sea Level Density)
- $V_{local} \approx V_\infty = 20 \text{ m/s}$ (Design Take-off Speed)
- $\mu = 1.81 \times 10^{-5} \text{ Pa} \cdot \text{s}$ (Dynamic Viscosity)

For the spinner length of approximately 0.04 m (derived from $D_{hub} \approx 37$ mm), the maximum Reynolds number at the spinner trailing edge is:

$$\text{Re}_L = \frac{1.225 \times 20 \times 0.04}{1.81 \times 10^{-5}} \approx 5.41 \times 10^4 \quad (39)$$

Since $\text{Re}_L < 5 \times 10^5$ (the critical Reynolds number for flat plate transition), the flow over the spinner is predicted to be entirely laminar. Consequently, the Blasius solution for the skin friction coefficient C_f is applicable:

$$C_f(s) = \frac{0.664}{\sqrt{\text{Re}_s}} \quad (40)$$

Code Implementation: The design implements a switching logic to handle transition if speeds increase, but defaults to the laminar solution for our design point.

$$\text{Re}_s = \frac{\rho V_{\text{flow}} s}{\mu}, \quad \text{Re}_s \geq 1.$$

$$C_f = \begin{cases} \frac{0.664}{\sqrt{\text{Re}_s}}, & \text{Re}_s < 5 \times 10^5 \\ \frac{0.455}{(\log_{10} \text{Re}_s)^{2.58}}, & \text{Re}_s \geq 5 \times 10^5 \end{cases}$$

Integrating this shear stress $\tau_w = \frac{1}{2}\rho V^2 C_f$ over the wetted area yields a spinner drag force of less than 0.05 N, confirming that the aerodynamic penalty of the nose cone is negligible compared to the pressure recovery benefits it provides.

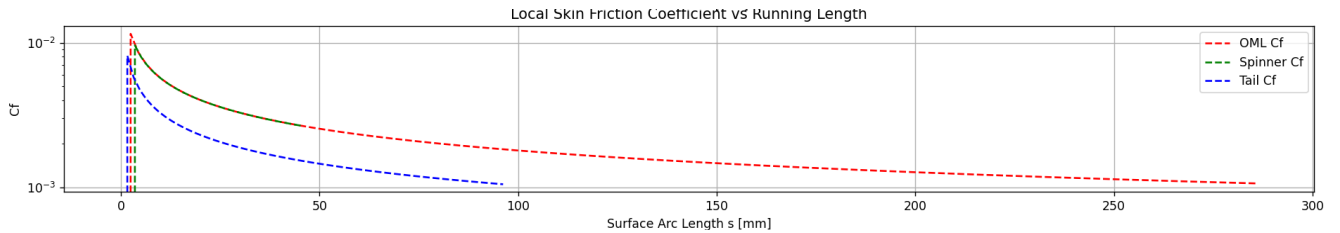


Figure 35: Skin Friction Coefficient

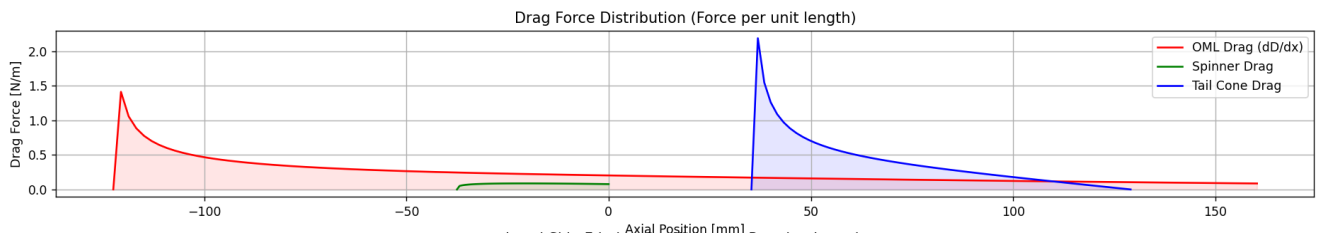


Figure 36: Drag Profile

3.3.2 Exhaust Cone Design: Diffusion and Structural Integration

The exhaust cone (or tailcone) is critical for managing the flow downstream of the stator. Without a tailcone, the hub would terminate abruptly, creating a large base area $A_{base} = \pi R_{hub}^2$. This would result in a massive region of separated recirculating flow, causing significant base drag.

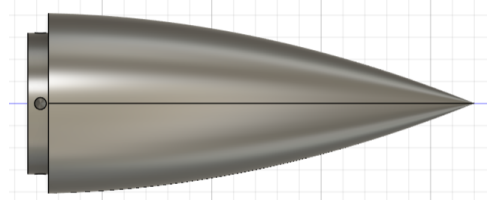


Figure 37: Exhaust Cone(to avoid immediate expansion after stator)

Pressure Recovery and Profile The tailcone profile is designed to facilitate pressure recovery, converting the kinetic energy of the flow near the hub back into static pressure. We utilize a parabolic closing profile with a high fineness ratio ($L/D = 2.5$) defined in `Cone Generator.py`:

$$r_{tail}(x) = R_{hub} \left[1 - \left(\frac{x}{L_{tail}} \right)^2 \right] \quad (41)$$

This extended length ($L_{tail} \approx 90$ mm) ensures that the flow streamlines close gradually. According to Hoerner's *Fluid-Dynamic Drag*, a boat-tail angle of less than 15° is required to prevent afterbody separation [Hoe65]. Our parabolic profile maintains a tangent angle well below this threshold for 80% of its length.

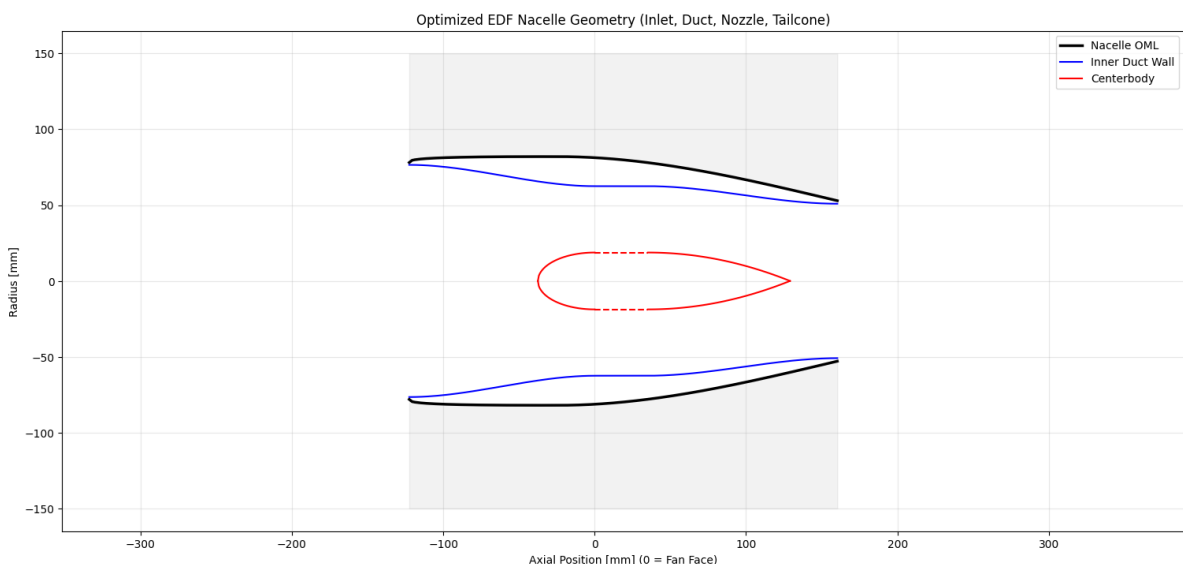


Figure 38: Optimised EDF Geometry

Weight Optimization: Hollow Shell Architecture A solid 3D-printed tailcone of this volume would add unnecessary mass to the aircraft, negatively impacting the Thrust-to-Weight (T/W) ratio. To optimize for weight, the component is designed as a thin-walled hollow shell.

This allows the tailcone to weigh less than 15 grams while maintaining sufficient buckling stiffness to withstand the dynamic pressure of the jet ($q_{jet} = 0.5\rho V_{jet}^2$). The internal volume is effectively dead air, which does not contribute to structural loads.

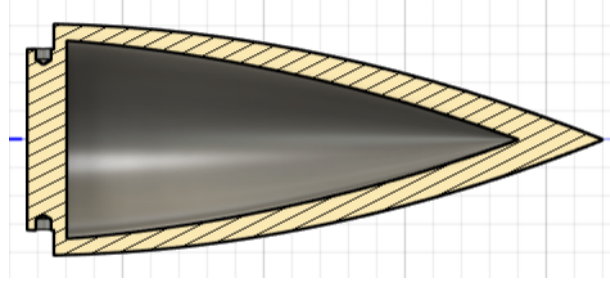


Figure 39: Sectional View of Exhaust

Structural Mounting: M2 Bolt Analysis The mechanical integration of the tailcone to the stator hub is a critical structural interface. The design utilizes four M2 Steel Bolts (Class 8.8) engaging into heat-set brass inserts within the ABS stator hub.

Load Case Definition The primary load acting on the tailcone is the aerodynamic drag force D_{cone} . From the CFD approximation in `Drag@DifferentVel.py`, the maximum drag on the tailcone at cruise ($V_{jet} \approx 40$ m/s) is approximately $D_{cone} = 2.0$ N.

Bolt Stress Calculation We verify the structural integrity using the method provided in `Stress.py`. The stress area A_s for a standard metric M2 coarse thread is:

$$A_s = \frac{\pi}{4}(d_{maj} - 0.938p)^2 \quad (42)$$

For M2 ($d_{maj} = 2.0$ mm, pitch $p = 0.4$ mm):

$$A_s = \frac{\pi}{4}(2.0 - 0.938(0.4))^2 \approx 2.07 \text{ mm}^2 = 2.07 \times 10^{-6} \text{ m}^2 \quad (43)$$

The tensile stress σ_t distributed across $N = 4$ bolts is:

$$\sigma_t = \frac{D_{cone}}{N \cdot A_s} = \frac{2.0}{4 \cdot 2.07 \times 10^{-6}} = 2.41 \times 10^5 \text{ Pa} = 0.24 \text{ MPa} \quad (44)$$

Comparing this to the yield strength of Class 8.8 Steel ($\sigma_y = 640$ MPa), the Factor of Safety (FOS) is:

$$\text{FOS}_{bolt} = \frac{\sigma_y}{\sigma_t} = \frac{640}{0.24} \approx 2666 \quad (45)$$

Conclusion: The bolts are structurally over-designed for tensile failure.

Thread Pull-Out Analysis A more critical failure mode is the stripping of the plastic threads or pull-out of the brass insert. The shear area for pull-out is the cylindrical surface area of the insert:

$$A_{shear} = \pi \cdot D_{insert} \cdot L_{engage} \quad (46)$$

For a 3.5 mm diameter insert with 5 mm engagement length:

$$A_{shear} = \pi \cdot 0.0035 \cdot 0.005 \approx 5.5 \times 10^{-5} \text{ m}^2 \quad (47)$$

The shear stress in the ABS plastic is:

$$\tau_{ABS} = \frac{2.0/4}{5.5 \times 10^{-5}} \approx 9090 \text{ Pa} \approx 0.009 \text{ MPa} \quad (48)$$

With the shear strength of ABS $\approx 25 \text{ MPa}$, the FOS is > 2000 . This confirms the interface is robust.

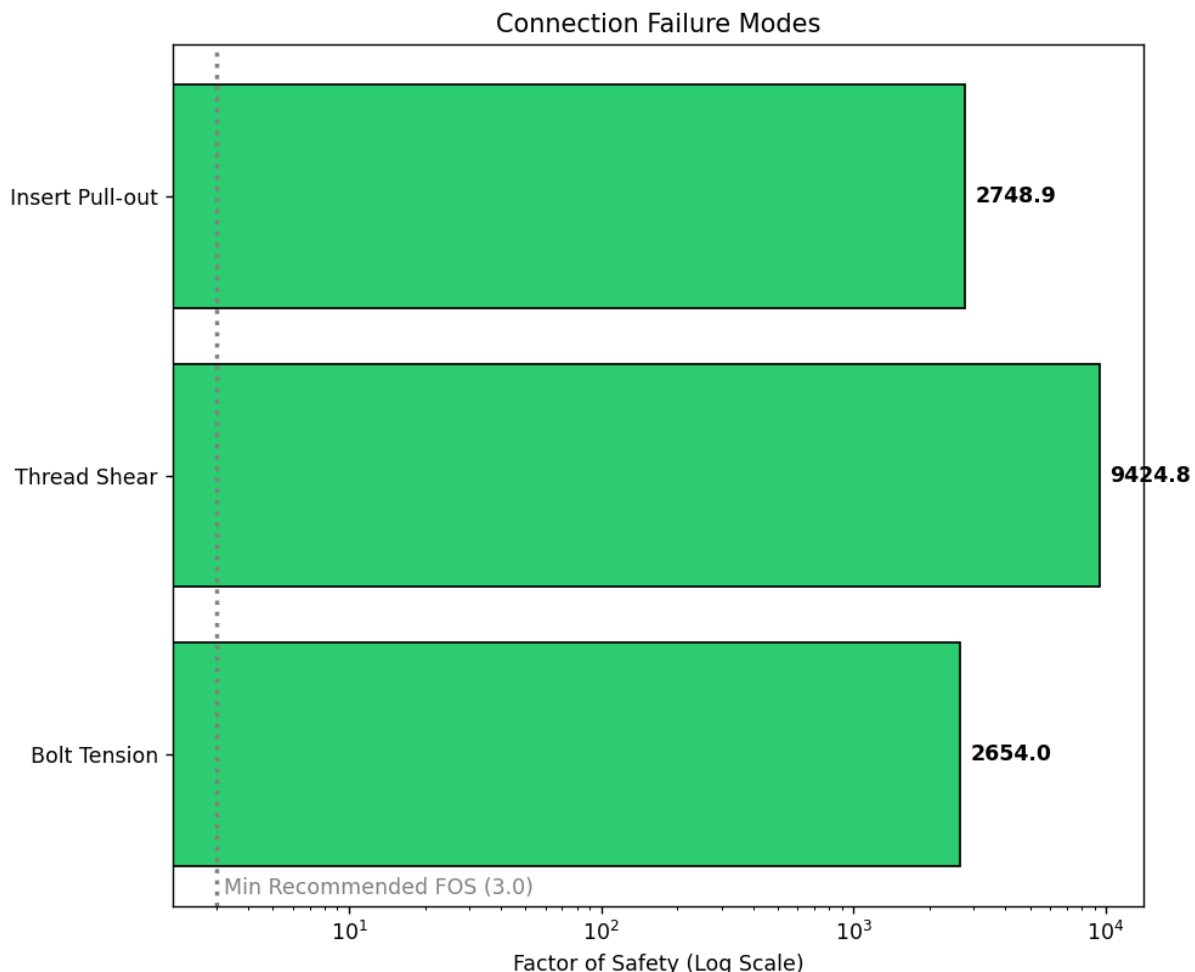


Figure 40: Failure Modes and Factor of Safety

3.3.3 Nacelle Aerodynamics and Variable Thickness

The nacelle is not merely a fairing; it is a lifting surface and a flow conditioner. Its design is governed by the conflicting requirements of minimizing frontal area for drag reduction and maximizing internal volume for motor integration.

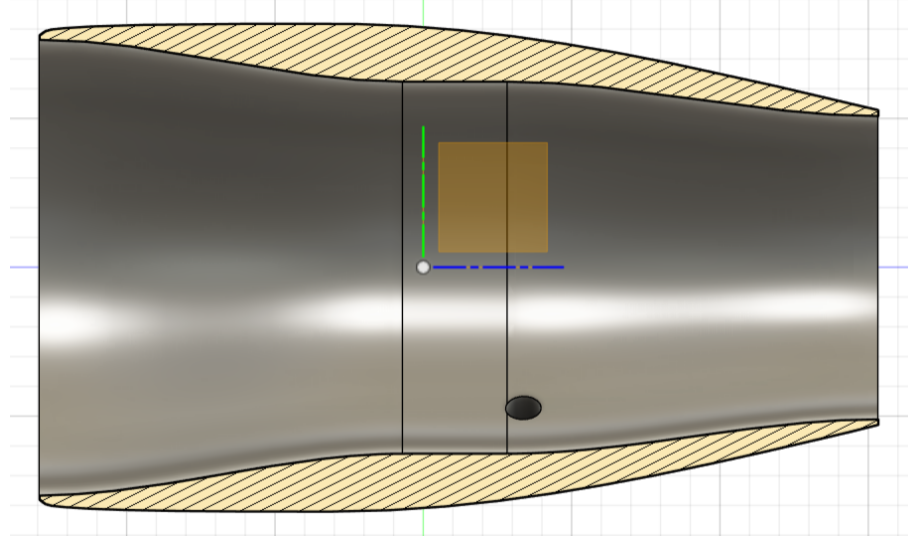


Figure 41: Nacelle

Inlet Lip Optimization The inlet lip shape is critical for performance at the low speeds (20 m/s) and high incidence angles typical of STOL takeoff. A sharp lip would cause flow separation, starving the fan face. We employed the Seddon and Goldsmith criteria within `Inlet.py` to optimize the Contraction Ratio (CR):

$$CR = \left(\frac{D_{highlight}}{D_{throat}} \right)^2 \quad (49)$$

The optimization sweep balanced two penalties:

1. **Lip Loss (Separation):** Decreases with higher CR (rounder lips).
2. **Skin Friction:** Increases with higher CR (larger wetted area).

The code converged on an optimal $CR = 1.3$. This ensures the flow remains attached even during static suction, preventing inlet distortion.

Variable Thickness Outer Mold Line (OML) Unlike a simple tube, the nacelle OML features a sophisticated variable thickness distribution defined by cubic splines.

Design Logic:

- **Forebody (Thick):** The region immediately aft of the inlet lip is thickened. This provides the necessary volume to house the stator mounting ring and the motor

flux ring. Aerodynamically, this creates a "suction peak" near the lip, generating a component of forward thrust (lip thrust) that offsets the drag.

- **Afterbody (Thin):** As the flow moves past the fan plane, the nacelle tapers aggressively. The wall thickness reduces to the structural minimum (1.5 mm) near the nozzle exit. This minimizes the base area at the trailing edge, reducing wake drag.

Tip Vortex Reduction: The Duct Effect The most significant aerodynamic advantage of the nacelle is the suppression of tip vortices. In an open propeller, the pressure differential between the pressure side and suction side of the blade drives a leakage flow over the tip, creating a vortex that induces drag and reduces effective lift.

The duct wall acts as a physical barrier (an infinite end-plate) to this leakage. The design models this phenomenon by modifying the Prandtl Tip Loss Factor F . Instead of the geometric tip radius R_{tip} , the code calculates losses based on an "Effective Radius" R_{eff} :

$$R_{eff} = R_{tip} + \delta_{gap} \quad (50)$$

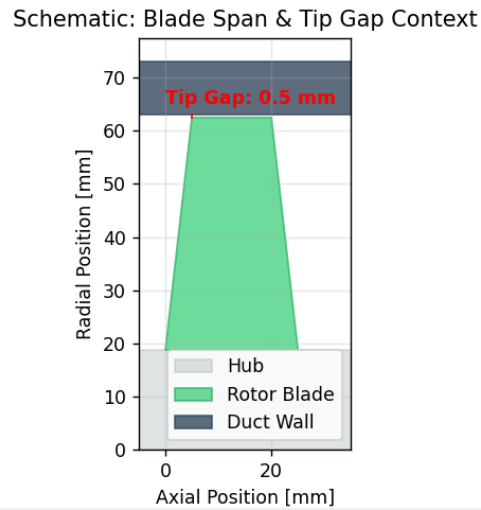


Figure 42: Tip Clearance

Because the gap is extremely small (0.5 mm), the exponential decay of the circulation is arrested.

$$F_{ducted} = \frac{2}{\pi} \arccos \left(\exp \left(-\frac{B}{2} \frac{R_{eff} - r}{R_{tip} \sin \phi} \right) \right) \quad (51)$$

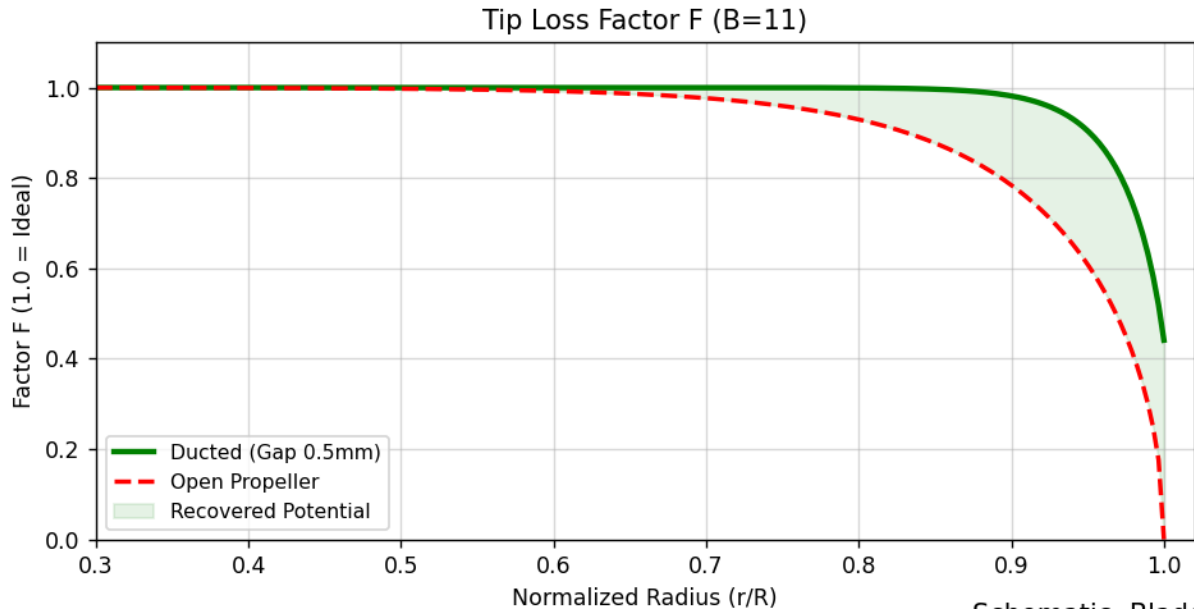


Figure 43: Tip Loss Factor

This modification allows the rotor blades to maintain high lift coefficients ($C_L \approx 0.9$) right up to the 95% span location, whereas an open propeller would see lift drop off significantly past 85% span. This area under the lift curve represents the "Powered Lift" gain inherent to the ducted architecture.

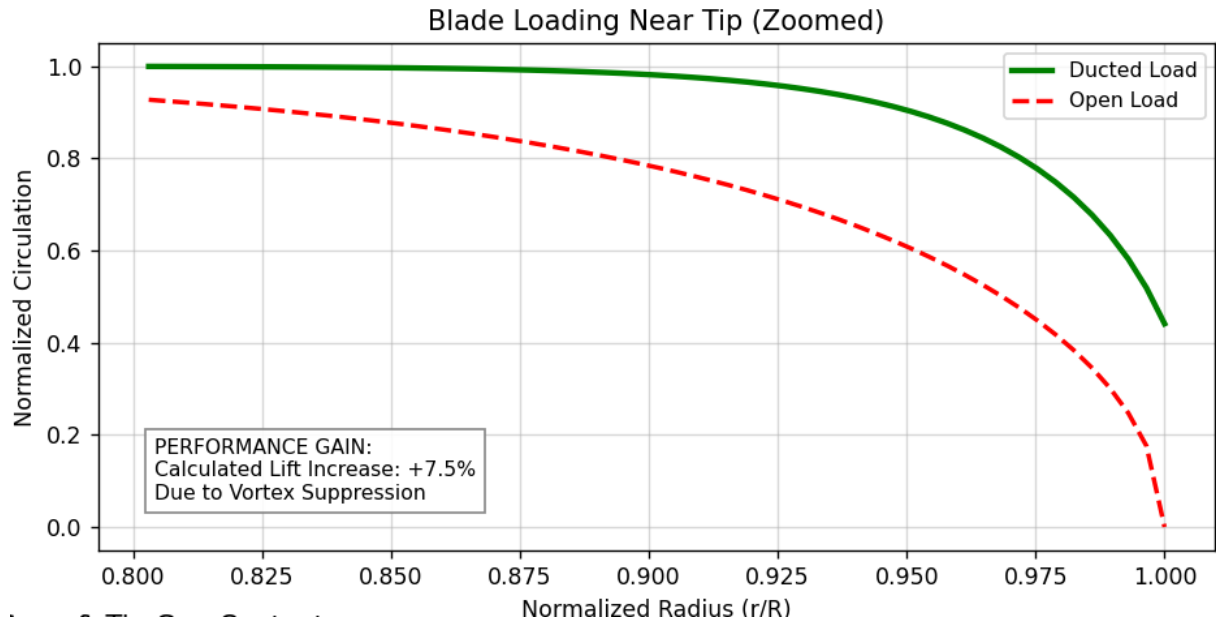


Figure 44: Performance of Ducted vs Open for this case

3.3.4 Conclusion

The centerbody and nacelle assembly presented here is not merely a housing but an active aerodynamic component. The high L/D spinner ensures laminar inflow; the hollow, bolted exhaust cone provides efficient pressure recovery with minimal weight; and the

variable-thickness nacelle optimizes the trade-off between structural volume and drag while actively suppressing tip vortices. This integrated design approach ensures the propulsion system meets the stringent T/W and efficiency targets mandated by the STOL mission profile.

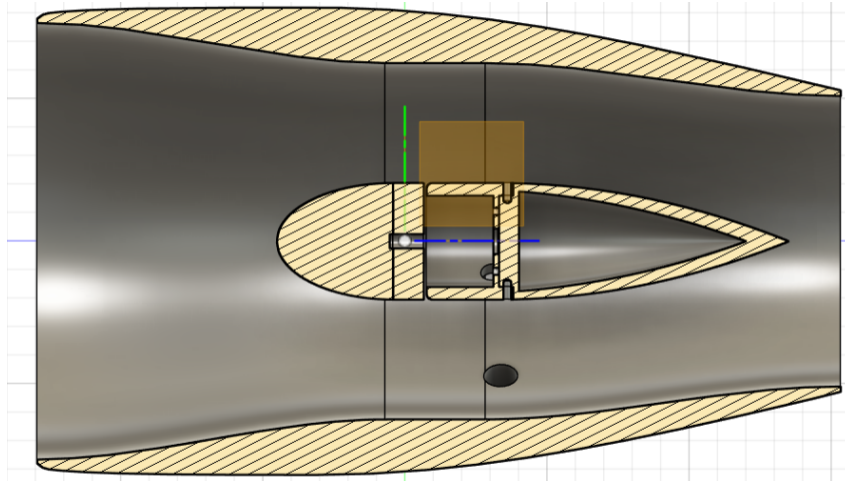


Figure 45: Centrebody and Nacelle

NACELLE AERODYNAMICS & STRUCTURAL INTEGRITY

Nacelle Geometry Parameters			
Inlet Parameter	Value	Nozzle Parameter	Value
Inlet Contraction Ratio	1.500	Nozzle Contraction Ratio	1.506
Inlet Opt. L/D	0.800	Design Jet Velocity	61.0 m/s
Parasitic Drag Analysis (Housing Only)			
Component	Takeoff Drag (N) (SL, 20 m/s)	Cruise Drag (N) (3048 m, 80 m/s)	
OML (Outer Mold Line)	0.0527	0.9282	
Spinner	0.0030	0.0203	
Tailcone	0.0390	0.0608	
Total Parasitic Drag	0.0947	1.0093	
Structural Stress Analysis (Material: ABS)			
<i>Stator Assembly</i> (Yield Strength: 40 MPa)			
Max Bending (Thrust)	5.84 MPa	Total Max Stress	7.22 MPa
Max Bending (Torque)	1.38 MPa	Factor of Safety	5.54
<i>Exhaust Cone Assembly</i> (4x M2 Bolts + Brass Inserts)			
Load per Bolt	0.50 N	Bolt Tensile FOS	> 2000
Brass Shear Stress	0.021 MPa	Thread Shear FOS	> 9000
ABS Pull-Out Stress	0.009 MPa	Pull-Out FOS	> 2000

3.4 Complete Assembly of Electric Ducted Fan and Off Design Performance

The aerodynamic performance of the propulsion system was evaluated at two distinct operating points: the design point (Takeoff) and the primary off-design point (Cruise). The transition between these states is governed by specific power constraints and environmental changes defined by the International Standard Atmosphere (ISA) model.

3.4.1 Fundamental Constraint: Constant Power

The primary constraint imposed on the off-design model is the conservation of shaft power (P_{shaft}). It is assumed that the electric motor operates at its maximum continuous power rating across both flight regimes.

$$P_{shaft,cruise} = P_{shaft,takeoff} = \text{Constant} \quad (52)$$

Given the baseline design parameters:

- **Design Power (P_0):** 1046 W
- **Control Strategy:** The system RPM adjusts naturally to balance the torque required by the rotor at the new air density and inflow velocity, maintaining constant power absorption.

3.4.2 Environmental Parameters

The flight environment changes significantly between takeoff and cruise. The model updates the freestream density (ρ_∞) based on the ISA model for geopotential altitude.

Table 6: modeled Environmental Conditions

Parameter	Takeoff (Design)	Cruise (Off-Design)
Altitude (h)	0 m (Sea Level)	3048 m (10 000 ft)
Freestream Velocity (V_∞)	20.0 m/s	80.0 m/s
Air Density (ρ_∞)	1.2250 kg/m ³	0.9049 kg/m ³

3.4.3 Aerodynamic Drag Decomposition

A critical aspect of the off-design analysis is the decoupling of drag sources based on the local flow field they experience. The nacelle components are categorized into two flow regimes:

External Flow Regime (Nacelle OML) The Outer Mold Line (OML) of the nacelle is exposed to the freestream velocity. As the aircraft accelerates from takeoff to cruise, the dynamic pressure acting on the housing increases with the square of the flight speed.

$$D_{OML} \propto \frac{1}{2} \rho_\infty V_\infty^2 C_{f,OML} S_{wet} \quad (53)$$

Since V_∞ increases from 20 m/s to 80 m/s (a 4× increase), the dynamic pressure increases by a factor of 16, resulting in the dominant drag penalty observed at cruise (0.93 N).

Internal Flow Regime (Spinner & Tailcone) Components inside the duct (Spinner and Tailcone) are shielded from the freestream. Their drag is driven by the internal Jet Velocity (V_{jet}), which is determined by the actuator disk theory balanced against the constant power constraint.

$$D_{internal} \propto \frac{1}{2} \rho_\infty V_{jet}^2 C_{f,int} S_{wet} \quad (54)$$

Because the propulsor is a ducted fan, the jet velocity increases much less drastically than the flight speed (from $\approx 61 \text{ m/s}$ to $\approx 93 \text{ m/s}$). Consequently, the drag increase on internal components is relatively mild compared to the external housing.

Flow Conditions & Results

Parameter	Takeoff	Cruise
Flight Speed	20.0 m/s	80.0 m/s
Altitude	0 m	3048 m
Jet Velocity	61.0 m/s	92.6 m/s
Total Drag	0.095 N	1.009 N
OML Drag %	55.6%	92.0%

Figure 46: Flow Condition at Different Velocities

3.4.4 Numerical Integration Scheme

The parasitic drag for each component is calculated using a streamwise skin friction integration method. The geometry is discretized into axial stations (x_i), and the local skin friction coefficient ($C_{f,i}$) is computed based on the local Reynolds number (Re_x).

The total profile drag is obtained via trapezoidal integration:

$$D_{component} = \int_0^L q_{local} \cdot C_f(x) \cdot \pi d(x) dx \approx \sum_i \bar{q}_i \bar{C}_{f,i} (\pi \bar{d}_i) \Delta x_i \quad (55)$$

Where:

- q_{local} is the local dynamic pressure ($0.5\rho V^2$).
- $d(x)$ is the local diameter of the component at station x .

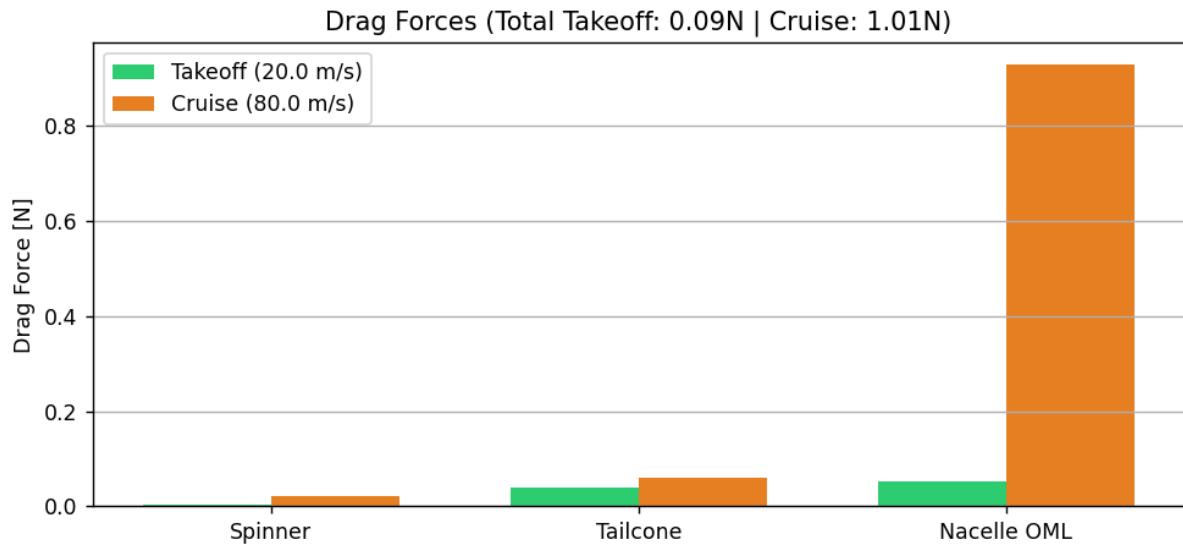


Figure 47: Drag at Different Velocities

The complete EDF design is made by joining the previously designed parts. The hollow part in the stator hub is for the motor housing. The hole visible in the nacelle and the stator hub is for the wiring of the motor to pass.

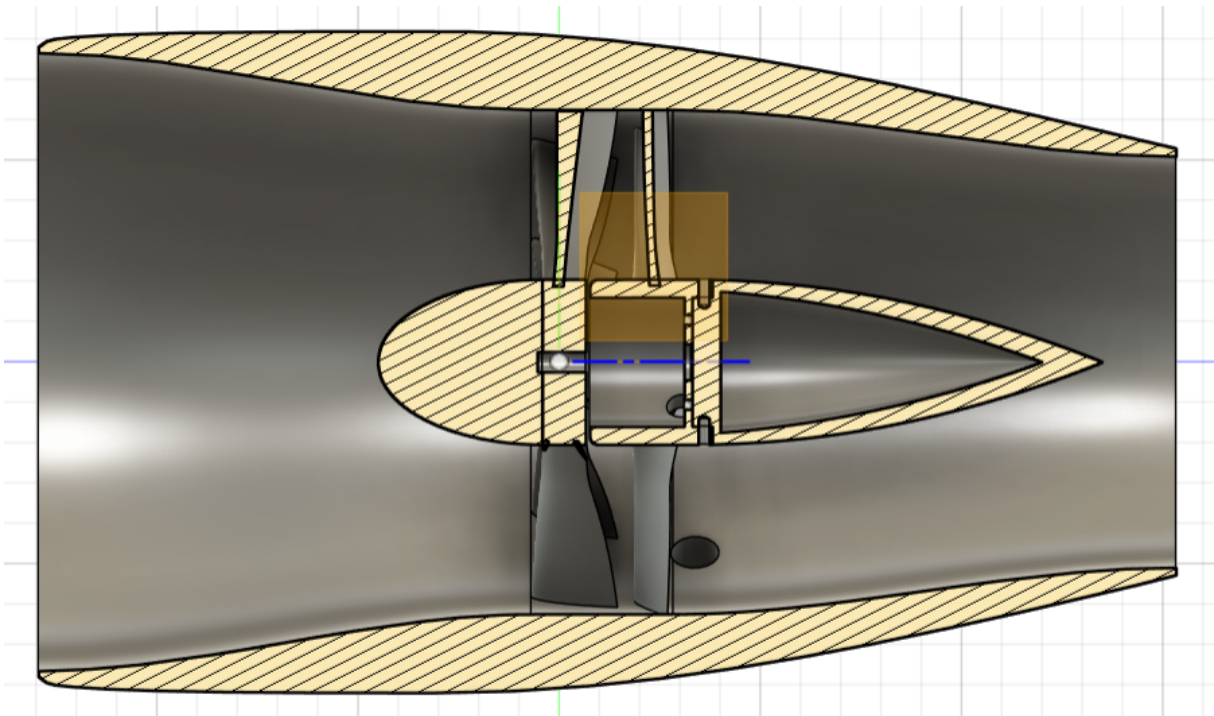


Figure 48: Sectional View of EDF

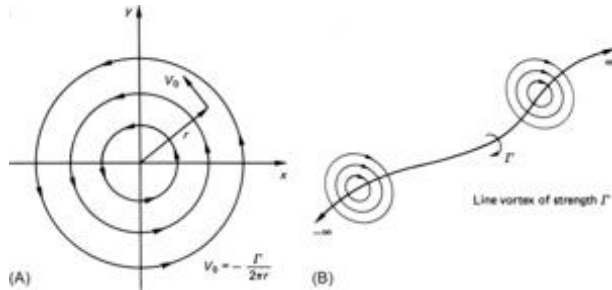
3.5 Mathematical Model- Fluid Interaction

This section deals primarily with the mathematical model of the thrust producing device and will provide a method to characterize the thrust and drag (without CFD simulations).

We are going to use the vortex lattice method to analyze the propeller and derive the required quantities. For this we will introduce some mathematical foundations that will be used for this.

3.5.1 Introduction

Filament Vortices We will extensively use straight-line vortices in this section. These are a model to get the velocity distribution by considering a concentrated vortex core that has a constant circulation as we go along the length of the straight-line. The corresponding velocity distribution necessitates a decay of velocity with radius.



As given in the figure the relation between the velocity and the radius is [HB14]

$$u_\theta = \frac{\Gamma}{2\pi r}$$

We can now use Biot-Savart Law to get the velocity at a point. We can intuit this with an analogy to magnetic field induced around a current-carrying wire.

$$v(r) = \frac{\Gamma}{4\pi} \int \frac{ds \times (r - s)}{|r - s|^3}$$

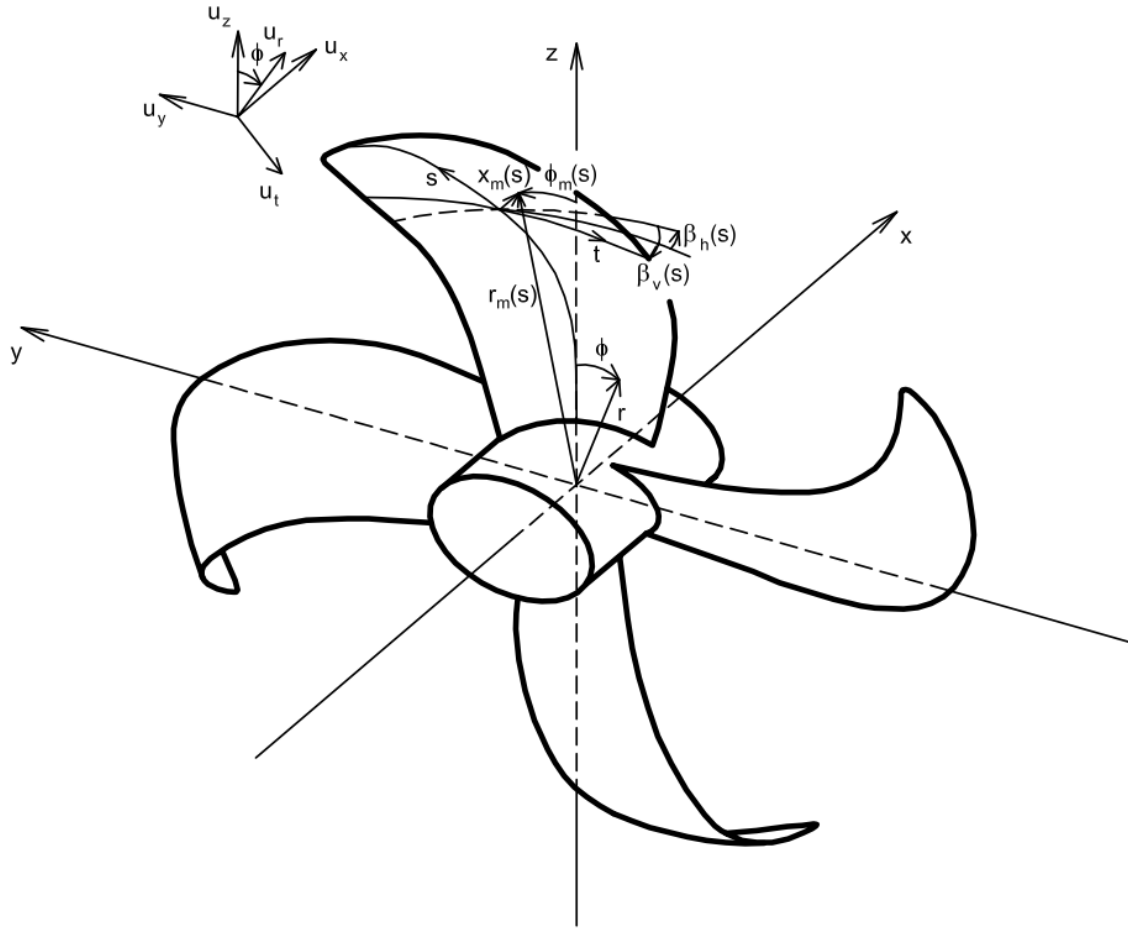


Figure 49: Propeller coordinate system

Setting the Stage We will define two non-dimensional quantities that will be used in the grid generation:

- s : It is the arc length parameter along the midchord line. Its equal to the radius r for conventional propellers.
- t : It is the dimensionless chordwise parameter. It is $-\frac{1}{2}$ at the trailing edge and $\frac{1}{2}$ at the leading edge.

We can parameterize the shape of the propeller like so:

$$\vec{R}(s, t) = \begin{cases} x_m(s) + c(s) \cos(\beta_v(s)) \sin(\beta_h(s))t \\ r_m(s) + c(s) \sin(\beta_v(s))t \\ -r_m(s)\phi_m(s) + c(s) \cos(\beta_v(s)) \cos(\beta_h(s))t \end{cases} \quad (56)$$

In this equation, $r_m(s)$ is the radius, $\phi_m(s)$ is the skew of the midchord (angle from the z axis), $\beta_h(s)$ is the pitch angle of the nose-tail line. Another pitch can be added, labeled β_v , which adds another degree of variability. This will allow the profile show an incline with

respect to a cylindrical system whose axis is along the x direction (at the radius $r_m(s)$). This extra pitch can be kept as zero for designing purposes, it is useful for analyzing a given propeller with that form of pitch.

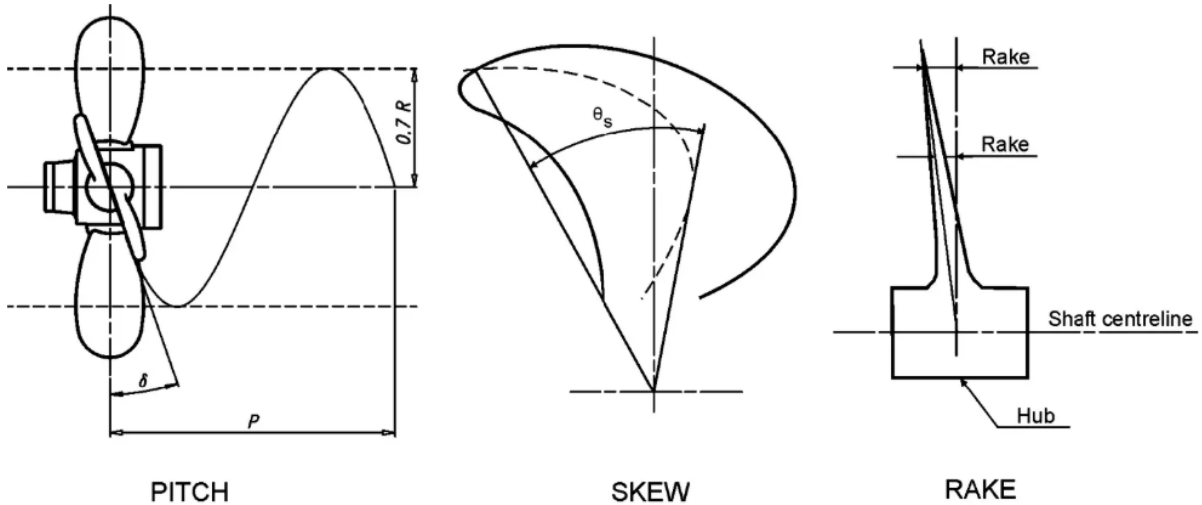


Figure 50: Visual describing different terms [HLGP06]

NOTE: The circulation along a shared edge will just be the difference between the circulation of each panel. This is intuitive from the superposition of two panels that have circulation in the same sense. [Kat95]

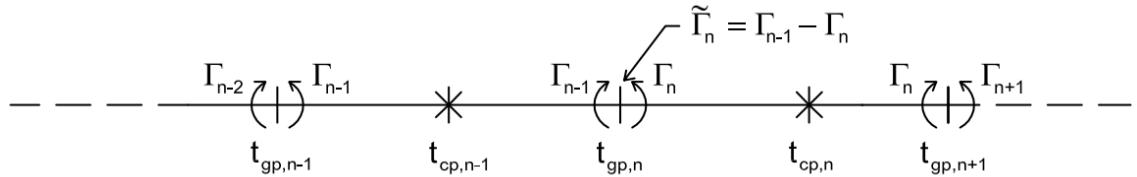


Figure 51: A side view of the panel with the grid points

Weight Function According to von Karman [Q⁺12], the drag of a surface only depends only the total circulation on a chord and not on the distribution along this. Therefore, we can simply make the distribution of circulation chordwise to be the optimal distribution of circulation for a given total circulation of a chord strip (this model will not lose any information). For this we will use the weight function from Feifel [LK⁺96]. Instead of that, we could also use the weighting function to introduce external constraints we wish to impose onto the propeller. The definition of this is:

$$\tilde{\kappa}_n = \frac{\tilde{\Gamma}_n}{\Gamma_{tot}}$$

Here $\tilde{\Gamma}_n$ is grid point n's total circulation. This, as mentioned previously, is the difference

in circulation between two adjacent panels. From Lan [Lan74] the weight function can be simplified by:

$$\tilde{\Gamma}_n = c \int_{t_{cp,n-1}}^{t_{cp,n}} \gamma(\chi) d\chi$$

Here, cp is the control point, which is the point where the boundary condition is imposed. We calculate the induced velocity from the filament vortices at these points. The parameterization will be given in a later section.

$$\begin{aligned} \tilde{\kappa}_1 &= 0 \\ \tilde{\kappa}_n &= \frac{\Gamma_{n-1} - \Gamma_n}{\Gamma_{tot}} = \frac{\Gamma_{N_{ch}}}{\Gamma_{tot}} \\ \Rightarrow \tilde{\kappa}_n &= \frac{\gamma(t_{gp,n}) \sqrt{(\frac{1}{2} - t_{gp,n})(\frac{1}{2} + t_{gp,n})}}{\sum_{i=1}^{N_{ch}+1} \gamma(t_{gp,i}) \sqrt{(\frac{1}{2} - t_{gp,i})(\frac{1}{2} + t_{gp,i})}} \quad \text{for } n = 1, 2, \dots, N_{ch} + 1 \end{aligned}$$

3.5.2 Making the Grid

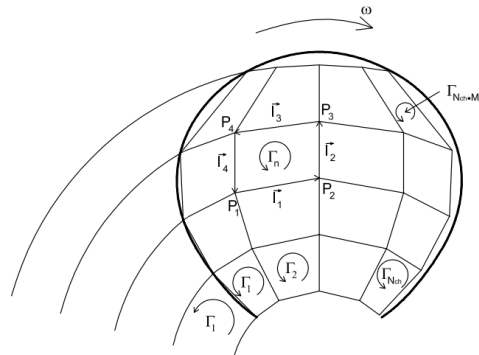


Figure 52: Grid for a propeller with trailers and circulation

To make the grid we will section the foil into panels with circulation positive counterclockwise along the sides of the panels. The corners of each panel is labeled P_1 to P_4 (also going counterclockwise with the circulation). The sides are vectors \vec{l}_1 to \vec{l}_4 (\vec{l}_1 is from P_1 to P_2). We will section the foil into panels according to James [Jam72].

Note:

- if b is the semi-span of the foil, $s = y/b$. Here y is in reference to the coordinate system for analyzing one foil.
- t is the non-dimensional chord parameter referenced, $t = x/c$ (where c is chord length).
- M_{sp} is the number of panels along the span and N_{ch} is the number of panels along the chord.

We want fine spacing at the leading and trailing edge along the chord and along the span we want equidistant spacing as no specific region is of more importance.

$$\begin{aligned} s_{gp,i} &= \frac{4i - 3}{4M_{sp} + 2}(s_{tip} - s_{hub}) + s_{hub} && \text{for } i = 1, 2, \dots, M_{sp} + 1 \\ s_{cp,i} &= \frac{1}{2}(s_{gp,i} + s_{gp,i+1}) && \text{for } i = 1, 2, \dots, M_{sp} \end{aligned}$$

gp refers to grid control points and *cp* refers to control points. The chordwise discretisation is

$$\begin{aligned} t_{gp,1} &= 0 && \text{located at T.E.} \\ t_{gp,i} &= \frac{1}{2} \left(1 - \cos \left(\frac{(i - \frac{3}{2})\pi}{N_{ch}} \right) \right) && \text{for } i = 2, 3, \dots, N_{ch} + 1 \\ t_{cp,i} &= \frac{1}{2} \left(1 - \cos \left(\frac{(i - 1)\pi}{N_{ch}} \right) \right) && \text{for } i = 1, 2, \dots, N_{ch} \end{aligned}$$

3.5.3 Trailer Vortices

There are trailer vortices in the grid shown that result from the shed vortices from the propeller. The sheet of vortices is represented by a collection of horseshoe vortices that have two sides extending downstream following the flow infinitely. We assume they are helices that have constant pitch and radius. To satisfy the Kutta Condition [K+24], we must have the circulation along the edge as zero. This implies the circulation in the edge panel and the trailer are the same.

3.5.4 Distinction in Components of Velocities

For ease of calculation, we break down the velocity at some point into two components, namely the onset flow and induced flow. The onset flow is the velocity from the air flowing onto the propeller (relative to the propeller) and the induced flow is the resultant of the superposition of the velocities due to the summation of all the filament vortices. Let us examine a simple 2-D case then later extend it to 3-D.

2-D case of Velocity Separation Let $\vec{U}(\vec{x})$ be the total velocity, $\vec{U}_0(\vec{x})$ is the onset and $\vec{u}(\vec{x})$ is the induced velocity. As described earlier we use the Biot-Savart law for each filament then sum it for the 4 sides of the panel.

$$\vec{u}_i^*(\vec{x}) = \frac{\Gamma_i}{4\pi} \sum_{k=1}^4 \int_0^{s_k} \frac{d\vec{\chi} \times \vec{R}}{|\vec{R}|^3} = \Gamma_i \vec{q}_i^*(\vec{x}) \quad (57)$$

We are given $\vec{U}_0(\vec{x})$ and so we can find $\vec{U}(\vec{x})$ by summation.

3-D Case of Velocity Separation In the case of the rotating propeller we need to take it relative, so that involves considering the velocity of the propeller due to rotation as well (this means adding a ωr term). According to de Jong [J⁺10], we can divide the wake of the propeller into two regions, the transition wake (which extends 4 radii downstream) and the ultimate wake (which is after the transition wake till infinity). The transition wake is a regular helix, which we will replace with filament vortices. Then we can again use Biot-Savart law for each filament and sum them all together.

$$\vec{U}(\vec{x}) = \sum_{j=1}^{M_{sp}} \vec{\Gamma}_{1+(j-1)N_{ch}} \sum_{i=1}^{N_{ch}} \kappa_i \vec{q}_{i+(j-1)N_{ch}}^*(\vec{x}) + \vec{U}_0(\vec{x}) \quad (58)$$

Note that in the code we compute local convection at the trailing edge panel and align it with the wake. This changes the wake dynamically without having to manually check for cases. This method makes the wake axial when its in the "hover condition" and it will trail back at some angle when its moving at a high speed.

3.5.5 Thrust and Torque Calculation

Using the lattice-vortex method framework, we can calculate the force on this foil using the Kutta-Joukowsky law [ZYR⁺18b]

$$\vec{F} = \rho \vec{U}(\vec{x}) \times \vec{\Gamma}_{side} = \rho \Gamma_{side} (\vec{U}(\vec{x}) \times \vec{l}_{side})$$

And to find the corresponding moment we use:

$$\vec{M} = \vec{r} \times \vec{F}_{side}$$

Those are the definitions that we use to calculate. Alternatively we can expand the cross-product to make it more recognizable (this is slightly cumbersome though).

$$\begin{aligned} T &= F_x \\ &= \rho Z \sum_{m=1}^{M_{sp}} \Gamma_{1+(m-1)N_{ch}} \left\{ \sum_{n=1}^{N_{ch}} \kappa_n \sum_{k=1}^4 \left[l_{z,n+(m-1)N_{ch},k} U_y(\vec{x}_{n+(m-1)N_{ch},k}) \right. \right. \\ &\quad \left. \left. - l_{y,n+(m-1)N_{ch},k} U_z(\vec{x}_{n+(m-1)N_{ch},k}) \right] - l_{z,1+(m-1)N_{ch},4} U_y(\vec{x}_{1+(m-1)N_{ch},4}) \right. \\ &\quad \left. + l_{y,1+(m-1)N_{ch},4} U_z(\vec{x}_{1+(m-1)N_{ch},4}) \right\} \end{aligned} \quad (59)$$

Where the subscript y or z indicates its the component of that vector along that unit vector. Also $\vec{x}_{n+(m-1)N_{ch},k}$ is the midpoint of side k of the $n + (m - 1)N_{ch}$ 'th panel. The

torque is:

$$Q = -M_x = - \sum_{i=1}^{\text{sides}} (yF_z - zF_y)_i$$

We can similarly expand the cross product similar to the above but we will not because it is not very helpful in practicality and is also quite cumbersome.

Note: Pitch is: $2\pi(0.7R_{tip}) \tan(\theta_{pitch})$

We numerically integrate over all the panels (adding up the thrust) to get the final thrust.

3.5.6 Notes

Post-stall polar extension using the Viterna–Corrigan method The 2D airfoil polar obtained from XFOIL or wind-tunnel data is typically available only up to a finite angle of attack range, for example $\alpha \in [\alpha_{\min}, \alpha_{\max}]$, where α_{\max} is at or slightly beyond static stall. In order to use the airfoil in a lifting-line or vortex-lattice method that may encounter larger angles of attack, the polar must be extrapolated into the post-stall regime in a physically plausible way. This is because the induced velocities will also be considered when finding an effective angle of attack relative to the blade. This new effective angle can go very high, extending beyond the polar data provided. The Viterna–Corrigan method provides such an extrapolation by smoothly blending the measured polar to a flat-plate-like behaviour at high angles of attack.

Let α_s denote the chosen stall (or matching) angle of attack, with corresponding lift and drag coefficients

$$C_{L,s} = C_L(\alpha_s), \quad C_{D,s} = C_D(\alpha_s).$$

Furthermore, let $C_{D,90}$ be the target drag coefficient at $\alpha = 90^\circ$, representing the “flat-plate” limit of the airfoil. All angles in the following equations are understood in radians.

For post-stall angles α satisfying $\alpha_s < |\alpha| \leq \frac{\pi}{2}$, the Viterna–Corrigan model approximates the drag and lift coefficients as

$$C_D(\alpha) = B_1 \sin^2 \alpha + B_2 \cos \alpha, \tag{60}$$

$$C_L(\alpha) = A_1 \sin(2\alpha) + A_2 \frac{\cos^2 \alpha}{\sin \alpha}. \tag{61}$$

The constants A_1 , A_2 , B_1 and B_2 are determined by matching the known polar at α_s and the chosen flat-plate limit at $\alpha = \frac{\pi}{2}$. A common choice is

$$B_1 = C_{D,90},$$

so that (60) reduces to $C_D(\frac{\pi}{2}) = C_{D,90}$. Enforcing continuity of C_D at the stall angle α_s

then gives

$$C_{D,s} = B_1 \sin^2 \alpha_s + B_2 \cos \alpha_s,$$

from which

$$B_2 = \frac{C_{D,s} - B_1 \sin^2 \alpha_s}{\cos \alpha_s}.$$

The lift model (61) is obtained by analogy with a flat plate and is constructed so that $C_L(\alpha)$ remains finite and continuous at stall and decays smoothly towards high angles of attack. A simple and widely used parameterization is

$$A_1 = \frac{C_{L,90}}{2}, \quad A_2 = (C_{L,s} - A_1 \sin(2\alpha_s)) \frac{\sin \alpha_s}{\cos^2 \alpha_s},$$

where $C_{L,90}$ is an effective lift coefficient at $\alpha = 90^\circ$. For a symmetric flat plate one often sets $C_{L,90} \approx 0$, which implies $A_1 = 0$, while for cambered airfoils a small non-zero value can be used to better match experimental data.

In our use, the extended polar is constructed as follows:

- For $|\alpha| \leq \alpha_s$, the original 2D polar $C_L(\alpha)$, $C_D(\alpha)$ from XFOIL is used.
- For $\alpha_s < |\alpha| \leq \frac{\pi}{2}$, the lift and drag coefficients are given by the Viterna-Corrigan relations (60)–(61).
- For $|\alpha| > \frac{\pi}{2}$, one may either apply symmetry relations or revert to a simple flat-plate model, depending on the requirements of the rotor/propeller analysis.

This procedure yields a continuous, bounded representation of $C_L(\alpha)$ and $C_D(\alpha)$ over a much wider angle-of-attack range than the original polar, while remaining consistent with both the measured stall characteristics at α_s and the expected high-angle flat-plate behaviour near $\alpha = 90^\circ$.

The Importance of This:

This is a major change from other open source tools, which ask for inputs of the polar and then directly use spline interpolation. When doing spline, the values grow much larger at the extremes (150 degrees for example) due to the nature of how this interpolation works. This will give **completely wrong** values of thrust. Our tool sidesteps this and extends the polars reasonably.

Axial Velocity input The axial inflow to the propeller is not just the free stream velocity, there is an additional component due to the suction. The calculation for this component is given above. Add this to the free stream velocity.

Γ considerations The circulation and induced velocity is coupled in a nonlinear way, a Γ increase makes increases in the induced velocities, which will alter the effective α . If we have a fixed-point iteration (`gamma = gamma_target`), then it will not converge whenever induced effects are non-negligible.

We are providing under-relaxation and damping these oscillations. The mechanism of this is we take the weighted mean of the old Γ and the target Γ . We can change this weighting parameter to achieve convergence in the solution. This is simple and doesn't need us to invoke a stronger nonlinear solver (eg Newton-Raphson).

Biot Savart Applications considerations If we were to apply the Biot-Savart law according to the given formula, we are dividing by zero when we evaluate for a point on the vortex. This will cause a large velocity (Biot-Savart is inversely proportional to the square of the radius).

When add a finite (but small) size to the vortex, the denominator at the point on the vortex is now non-zero radius. This will bound the velocity outputs. We also make have checks for the endpoints.

3.5.7 Calculating Values

The above methods obviously require us to computationally evaluate the values. A more napkin-friendly method is proposed in our mid-term report (if quick calculation is required). For the vortex lattice method we have developed an open-source tool (fully in house) to implement and calculate the values. The tool is written purely in Julia. The input values defining the geometry of the blade and such are attached in the solution files (file name "rotor_data"). All inputs to the Julia REPL should of the form provided in the example input for the VLM solver given in the github (just change values for differing states). Note the example input provided has the exact blade geometry and polar data as the ones used in our problem statement. **To use this code to analyze the propeller proposed in this solution, simply change the axial inlet velocity as everything else is as provided. This axial inlet velocity should include the suction velocity due to the rotor and the freestream as well.**

3.6 Mathematical Model- Stress Analysis

3.6.1 Notation and units

Geometry & Material Properties			
$R_{\text{tip}}, R_{\text{hub}}$	Radii (m)	ρ_s	Material density (kg m^{-3})
r	Radial coordinate from rotation axis. (m)	$A(r)$	Cross Area(Airfoil polygon) (m^2)
$c(r)$	Chord length at r (m)	$I(r)$	2nd moment area(abt flapwise bending)(m^4)
$t_{\text{skin}}(r)$	uniform local thickness (m)	$J(r)$	Torsion constant (m^4)
E	Young's Modulus. (Pa)		
Aerodynamics & Kinematics			
Ω	Rotation rate (rad s^{-1})	ρ_{air}	Air density (kg m^{-3})
V_{∞}	Freestream Axial speed (m s^{-1})	V_{rel}	Relative speed (m s^{-1})
Loads & Stresses			
$q(r)$	Lift/span (N m^{-1})	$T(r)$	Internal axial tension(centrifugal) at r (N)
M_{aero}	Sectional pitch moment. (N m m^{-1})	$V(r)$	Shear Force(flapwise) at r (N)
$m(r)$	Mass/length (kg m^{-1})	$M(r)$	Bending moment(flapwise) at r . (N m)
σ, τ	Normal/Shear stress (Pa)	T_{tor}	Internal torque about blade axis due to distributed M_{aero} (N m)
σ_{VM}	Von Mises Eq.Stress(Pa)		

3.6.2 Blade geometry and chord law

The blade span parameter

$$t = \frac{r - R_{\text{hub}}}{R_{\text{tip}} - R_{\text{hub}}}, \quad 0 \leq t \leq 1,$$

is used in the Bernstein-like cubic chord law :

$$c(t) = (1 - t)^3 a_0 + 3(1 - t)^2 t a_1 + 3(1 - t)t^2 a_2 + t^3 a_3,$$

where the constants a_0, \dots, a_3 are chord coefficients in metres (or scaled accordingly).

For station-based input (root, mid, tip) a cubic spline or the above polynomial may be used to recover $c(r)$.

3.6.3 Airfoil cross-section and section properties

The unit-chord NACA4412 coordinates are generated with cosine spacing yielding a closed polygon (x_i, y_i) , $i = 1 \dots N$. The scaled coordinates for local chord c are

$$X_i = c x_i, \quad Y_i = c y_i.$$

Using Green's theorem (polygon formulas) the cross-sectional area A and centroid (\bar{X}, \bar{Y}) are computed by

$$A = \frac{1}{2} \sum_{i=1}^N (X_i Y_{i+1} - X_{i+1} Y_i),$$

$$\bar{X} = \frac{1}{6A} \sum_{i=1}^N (X_i + X_{i+1})(X_i Y_{i+1} - X_{i+1} Y_i), \quad \bar{Y} = \frac{1}{6A} \sum_{i=1}^N (Y_i + Y_{i+1})(X_i Y_{i+1} - X_{i+1} Y_i),$$

with indices taken cyclically.

The second moments of area about the polygon reference axes are

$$I_{xx}^{(ref)} = \frac{1}{12} \sum_{i=1}^N (Y_i^2 + Y_i Y_{i+1} + Y_{i+1}^2) (X_i Y_{i+1} - X_{i+1} Y_i),$$

$$I_{yy}^{(ref)} = \frac{1}{12} \sum_{i=1}^N (X_i^2 + X_i X_{i+1} + X_{i+1}^2) (X_i Y_{i+1} - X_{i+1} Y_i).$$

Centroidal second moments for bending are obtained by the parallel axis shift:

$$I_{xx} = I_{xx}^{(ref)} - A \bar{Y}^2.$$

Thin-wall torsion constant is approximated by the common closed-thin-wall estimate

$$J \approx \frac{4A^2 t_{\text{skin}}}{p},$$

where p is the airfoil perimeter (length of polygon) and t_{skin} is the uniform skin thickness (small relative to chord).

Mass per unit length:

$$m(r) = \rho_s A(r).$$

Maximum section half-thickness (useful for outer fiber location)

$$h(r) = \max(Y_i) - \min(Y_i).$$

3.6.4 Aerodynamic loading using polars

Calculating the local relative speed

$$V_{\text{rel}}(r) = \sqrt{(\Omega r)^2 + V_\infty^2}.$$

Given an airfoil polar (discrete) providing $C_L(\alpha)$ and $C_M(\alpha)$ (moment coefficient about a chosen reference point), the local angle of attack $\alpha(r)$ (in degrees or radians consistent with the polar) is computed as

$$\alpha(r) = \beta_m(r) - \phi(r),$$

where $\beta_m(r)$ is local metal/pitch angle and $\phi(r)$ is inflow angle (here often taken as zero or computed by an induced-velocity model). In our implementation with no induced inflow,

$$\alpha(r) \approx \beta_m(r).$$

Interpolate the polar to obtain $C_L(\alpha(r))$ and $C_M(\alpha(r))$. The lift per unit span (flapwise distributed load) is

$$q(r) = \frac{1}{2} \rho_{\text{air}} V_{\text{rel}}(r)^2 c(r) C_L(\alpha(r)).$$

The sectional aerodynamic pitching moment per unit span (moment about the chosen reference) is

$$M_{\text{aero}}(r) = \frac{1}{2} \rho_{\text{air}} V_{\text{rel}}(r)^2 c(r)^2 C_M(\alpha(r)),$$

which can be interpreted as a distributed torque density (N m per unit length). Integrating outward gives the internal torsional moment at section r :

$$T_{\text{tor}}(r) = \int_{s=r}^{R_{\text{tip}}} M_{\text{aero}}(s) \, ds + T_{\text{tor}}(R_{\text{tip}}),$$

where $T_{\text{tor}}(R_{\text{tip}})$ is the tip torque (often zero).

3.6.5 Centrifugal axial tension

The axial tensile force from rotation at station r equals the integral of ring mass outward times centrifugal acceleration:

$$T(r) = \int_{s=r}^{R_{\text{tip}}} m(s) \Omega^2 s \, ds.$$

3.6.6 Shear force and bending moment (resultants)

Flapwise shear:

$$V(r) = \int_{s=r}^{R_{\text{tip}}} q(s) \, ds,$$

and flapwise bending moment:

$$M(r) = \int_{s=r}^{R_{\text{tip}}} (s - r) q(s) \, ds.$$

3.6.7 Thin-walled shear-flow slice method

To obtain a realistic shear stress for the airfoil skin (instead of the crude $\tau_{\max} = 1.5V/A$ rectangular rule), we use a slice approach:

- Compute a width profile $w(z)$ by intersecting horizontal lines $y = z$ with the closed airfoil polygon; $w(z)$ is the chordwise width at height z .
- Defining the first moment function

$$S(z) = \int_{y=z}^{y_{\max}} y' w(y') \, dy'.$$

- For a given flapwise shear force V acting on the section, the shear-flow per unit skin thickness at height z (thin-wall shear-flow relation, neglecting closed-section redundancy) is

$$q_s(z) = \frac{V S(z)}{I_{xx}}.$$

- Local shear stress at the skin (assuming uniform thickness t_{skin}) is

$$\tau(z) = \frac{|q_s(z)|}{t_{\text{skin}}} = \frac{|V| |S(z)|}{I_{xx} t_{\text{skin}}}.$$

- We take the maximum magnitude over z as the shear contribution:

$$\tau_{\text{shear}}(r) = \max_z \tau(z).$$

Note: the full thin-walled closed-section theory includes an additive constant shear-flow (redundant) q_0 determined by compatibility (closed-loop integral). The slice method above is a practical approximation that gives a physically meaningful shear distribution for many sections; if greater accuracy is required one must solve the thin-wall shear-flow equations with q_0 and account for multi-cell geometry.

If the slice method is not available, a conservative fallback is the rectangular-section rule:

$$\tau_{\text{shear,fallback}} \approx \frac{3}{2} \frac{|V|}{A}.$$

3.6.8 Torsional shear

For an internal torque $T_{\text{tor}}(r)$ and torsion constant $J(r)$, a simple outer-fiber torsional shear estimate is

$$\tau_{\text{torsion}}(r) \approx \frac{|T_{\text{tor}}(r)| y_{\max}}{J(r)}$$

where $y_{\max} \approx h(r)/2$ is the distance from centroid to the outer fiber in the flapwise direction. (Exact shear distribution depends on q_s and wall geometry.)

3.6.9 Beam model (Euler-Bernoulli) for flapwise bending

We model the blade as an Euler–Bernoulli beam with distributed flapwise load $q(r)$. Discretize into elements of length L_e and assemble the standard cubic Hermite (two-node, 2 DOF/node) beam element stiffness matrix:

For an element with nodal DOFs $(w_1, \theta_1, w_2, \theta_2)$ the element stiffness (for constant EI_e over the element) is

$$\mathbf{k}_e = \frac{EI_e}{L_e^3} \begin{bmatrix} 12 & 6L_e & -12 & 6L_e \\ 6L_e & 4L_e^2 & -6L_e & 2L_e^2 \\ -12 & -6L_e & 12 & -6L_e \\ 6L_e & 2L_e^2 & -6L_e & 4L_e^2 \end{bmatrix}.$$

The consistent nodal load vector due to distributed transverse load q_e (average over element) is

$$\mathbf{f}_e = \frac{q_e L_e}{12} \begin{bmatrix} 6 \\ L_e \\ 6 \\ -L_e \end{bmatrix}.$$

using Global stiffness \mathbf{K} and load \mathbf{F} , applying the clamped root boundary conditions, and solving

$$\mathbf{K} \mathbf{u} = \mathbf{F}$$

for nodal displacement vector \mathbf{u} . The curvature can be calculated as :

$$\kappa(r) \approx \frac{d^2 w}{dr^2}.$$

The bending moment from the beam deflection field is

$$M_{\text{beam}}(r) = E I_{xx}(r) \kappa(r).$$

(We use M_{beam} in the stress formula for improved consistency with the beam deformation.)

3.6.10 Stress computation (outer fiber)

Normal bending + axial stress at outer fiber:

$$\sigma_{\text{bending}}(r) = -\frac{M(r) y_{\text{outer}}(r)}{I_{xx}(r)}, \quad \sigma_{\text{axial}}(r) = \frac{T(r)}{A(r)}.$$

Total normal stress (outer top/bottom fiber sign convention):

$$\sigma_{\text{top}}(r) = \sigma_{\text{axial}}(r) + \sigma_{\text{bending,top}}(r), \quad \sigma_{\text{bottom}}(r) = \sigma_{\text{axial}}(r) + \sigma_{\text{bending,bottom}}(r).$$

Combine shear contributions: total shear magnitude at the outer fiber

$$\tau_{\text{total}}(r) = \sqrt{\tau_{\text{shear}}(r)^2 + \tau_{\text{torsion}}(r)^2}.$$

Von Mises equivalent stress (plane stress outer-fiber approximation):

$$\sigma_{VM}(r) = \sqrt{\sigma(r)^2 + 3\tau_{\text{total}}(r)^2}.$$

(We evaluate this for both top and bottom fiber normal stresses to find peak values.)

3.7 Numerical Analysis- Stresses and Fluid Interaction

3.7.1 Static Structural Analysis of the Rotor

Geometry and Engineering Data The structural analysis was performed using ANSYS Mechanical. To accurately simulate the structural integrity under operating conditions, the material properties and domain settings were defined as follows.

Material Properties The rotor blade material was defined as **ABS**. The properties used in the simulation are detailed in Table 1.

Property	Value	Unit
Density (ρ)	1035	kg/m^3
Young's Modulus (E)	1.628	GPa
Yield Strength (σ_y)	40	MPa

Table 7: Material Properties

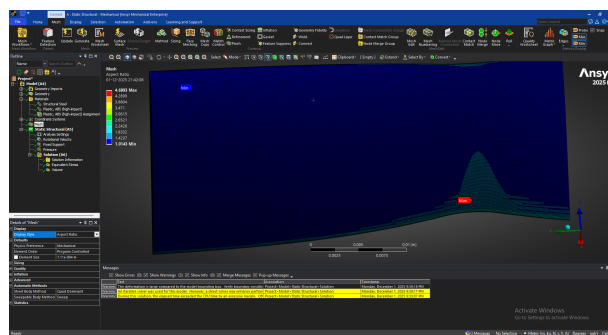


Figure 53: Aspect Ratio for Coarse Mesh(Element size 11.1e-05m)

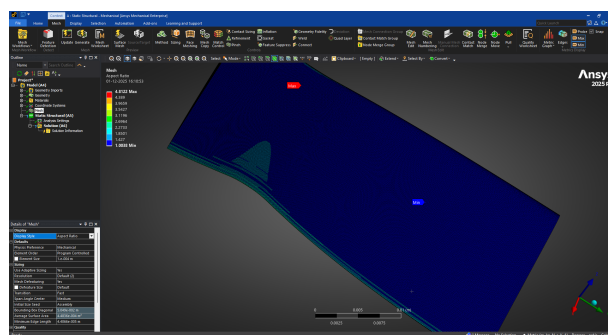


Figure 54: Aspect Ratio for Medium Mesh(Element size 10e-05m)

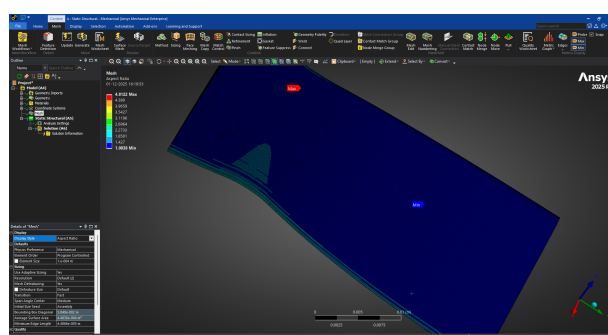


Figure 55: Aspect Ratio for Fine Mesh(Element size 9e-05m)

Mesh Quality Metrics

Grid Independence Study As the GCI due to these meshes and equivalent von misses stress, comes out at 0.4%. This shows that the mesh is independent(less than 1%) .

Loads and Boundary Conditions The static structural environment was set up to replicate the maximum loading conditions experienced by the rotor during operation. The boundary conditions and applied loads are summarized below.

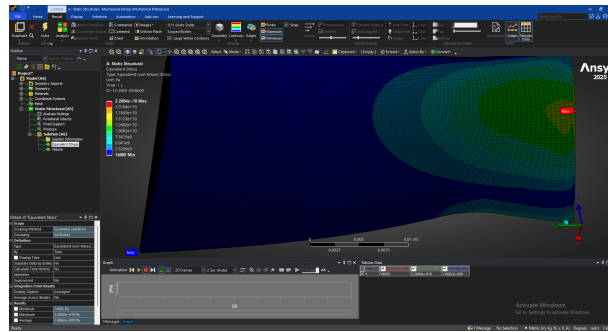


Figure 56: Von Misses Stress_Fine

Boundary/Load	Type	Settings/Values
Rotor Hub Interface	Fixed Support	Constraints: All DOF Fixed ($U_x, U_y, U_z, Rot_x, Rot_y, Rot_z = 0$)
Inertial Load	Rotational Velocity	Magnitude: 1469 rad/s Axis: Z-Axis (0,0,1)
Aerodynamic Load	Pressure	Magnitude: 15000 Pa(Thrust/Area)
Gravity	Standard Earth Gravity	Magnitude: 9.8066 m/s ² (-Y Direction)

Table 8: Loads and Supports

Boundary Conditions Setup :

- **Rotational Velocity:** The rotational speed of -1469 rad/s was applied to match the operational speed defined in the CFD analysis. This generates the centrifugal force, which is typically the dominant load in rotor dynamics.
- **Aerodynamic Pressure:** 15000 Pa

Analysis Setup The simulation was solved using the ANSYS Mechanical Static Structural solver.

- **Large Deflection:** On (Enabled to account for geometric stiffness changes due to significant deformation at the blade tips).
- **Solver Type:** Direct (Sparse).
- **Weak Springs:** Off.

Results The structural performance was evaluated based on Equivalent (Von-Mises) Stress at the hub of the rotor blade.

Equivalent (Von-Mises) Stress: The maximum stress of 22.23 MPa is localized at the rotor hub . This value is well below the material Yield Strength of 40 MPa , resulting in a

minimum Safety Factor of 1.82, indicating the design is safe for the prescribed operating speed.

3.7.2 Structural Analysis of the Stator

Geometry and Engineering Data The structural analysis was performed using ANSYS Mechanical. The material properties and domain settings were defined as follows.

Material Properties The stator blade material was defined as **ABS**. The properties used in the simulation are detailed in Table 1.

Property	Value	Unit
Density (ρ)	1035	kg/m^3
Young's Modulus (E)	1.628	GPa
Yield Strength (σ_y)	40	MPa

Table 9: Material Properties

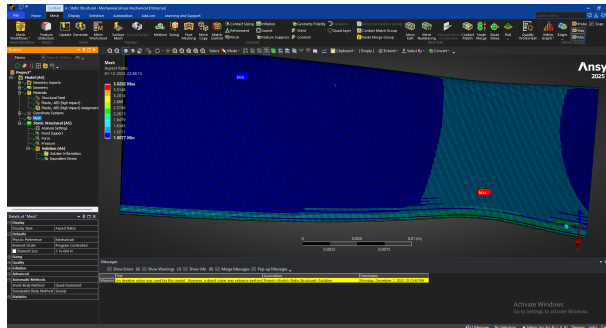


Figure 57: Aspect Ratio for Coarse Mesh(Element Size 11e-05m)

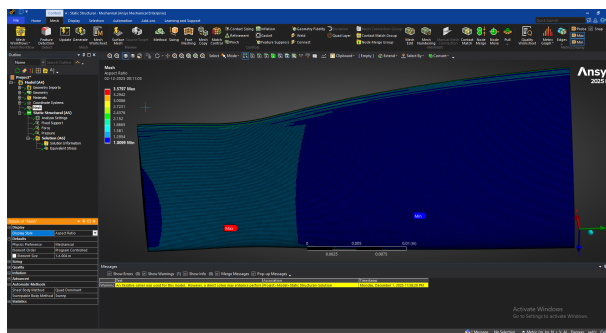


Figure 58: Aspect Ration for Medium Mesh(Element Size 10e-05m)

Mesh Quality Metrics

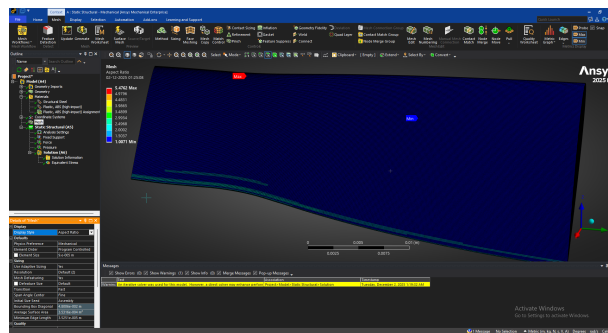


Figure 59: Aspect Ration for Fine Mesh(Element Size 9e-05m)

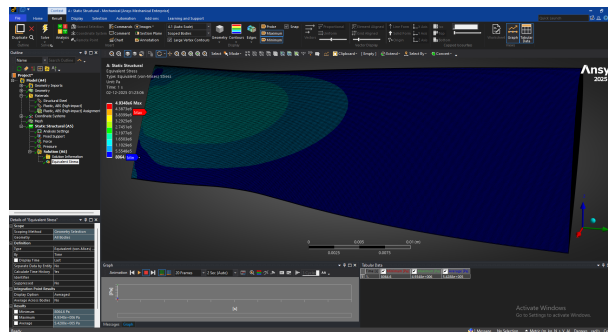


Figure 60: Von Misses _Fine

Grid Independence Study As the GCI due to these meshes and equivalent von misses stress, comes out at 8.4%. This shows that the mesh is independent(less than 10%, it's not the best but can be taken as a good representation) .

Loads and Boundary Conditions The static structural environment was set up to replicate the maximum loading conditions experienced by the stator during operation. Unlike the rotor, the stator is stationary and does not experience centrifugal loads. The boundary conditions and applied loads are summarized below.

Boundary/Load	Type	Settings/Values
Outer Casing/Flange	Fixed Support	Constraints: All DOF Fixed ($U_x, U_y, U_z, Rot_x, Rot_y, Rot_z = 0$)
Aerodynamic Load 280000 Pa Gravity	Pressure Standard Earth Gravity	Magnitude: Magnitude: 9.8066 m/s ² (-Y Direction)

Table 10: Loads and Supports

Analysis Setup The simulation was solved using the ANSYS Mechanical Static Structural solver.

- **Large Deflection:** On (Enabled to account for geometric stiffness changes, though deformations are expected to be lower than the rotor).
- **Solver Type:** Direct (Sparse).
- **Weak Springs:** Off.

Results The structural performance was evaluated based on Equivalent (Von-Mises) Stress.

Equivalent (Von-Mises) Stress: The maximum stress of $4.9348 kPa$ is localized at the stator hub. This value is well below the material Yield Strength of $40 MPa$.

3.7.3 CFD of the Rotor

Computational Domain and Boundary Conditions The simulation was performed using ANSYS Fluent. The computational domain was designed to simulate the flow around the rotor using a Moving Reference Frame (MRF) approach.

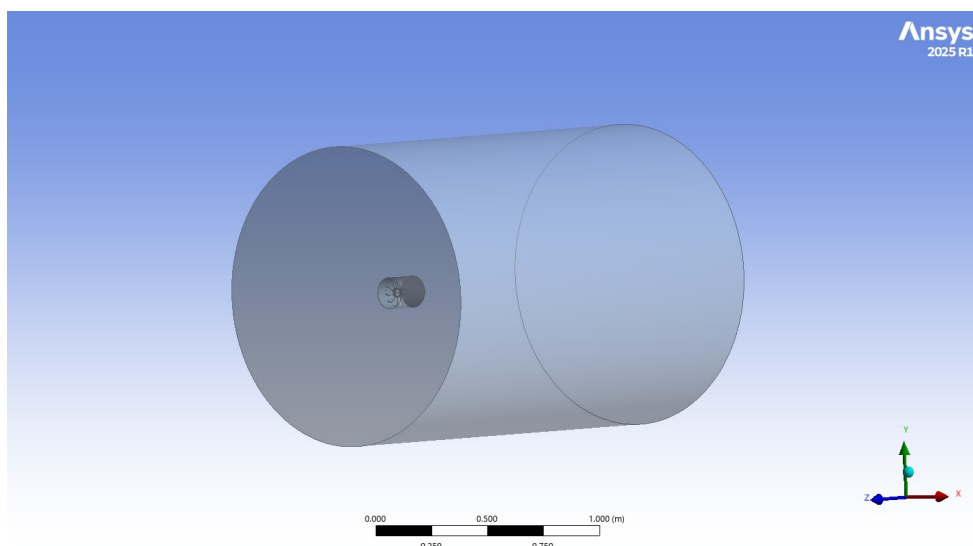


Figure 61: Computational domain - rotating and stationary

Zone Name	Boundary Type	Parameters/Values
Inlet	Velocity Inlet	$V = 20 \text{ m/s}$
Outlet	Pressure Outlet	$P_{gauge} = 0 \text{ Pa}$
Rotor Walls	Wall (No Slip)	Rotating relative to adjacent cell zone
Far Field	Wall (Free Slip)	Shear Stress = 0
Fluid Domain (Rotor)	Fluid	Frame Motion: $\omega = -1469 \text{ rad/s}$

Table 11: Boundary Conditions Setup

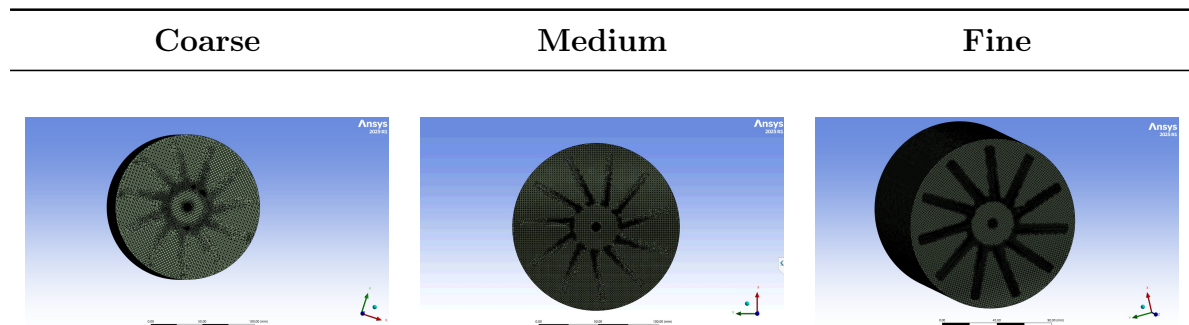
Mesh Parameter	Recommended Target	Fine Mesh Value(avg)
Aspect Ratio	< 40 (Inflation) / < 5 (Bulk)	1.722
Skewness	< 0.85 (Acceptable < 0.95)	0.15558
Orthogonal Quality	> 0.20 (Acceptable > 0.10)	0.84383

Table 12: Mesh Quality Metrics: Targets vs. Fine Mesh Statistics

Mesh Quality metrics *The extremum of orthogonal quality , skewness and aspect ratio of some elements was out of bounds ,but the number of elements for which this takes place is significantly low.

Grid Independence Study To verify that the solution is independent of the mesh resolution, a grid independence study was conducted using Coarse, Medium, and Fine meshes. The primary parameter monitored was the **Torque**.According to Richardson's extrapolation theory , the refinement ratio should be greater than 1.3 (Roache 1994) which is achieved in our case .The refinement ratio obtained fine/medium is 1.48 .

Mesh Configuration	Elements	Nodes	Target Parameter (Torque(Nm))
Coarse	4688337	911849	0.00728
Medium	9174029	1596856	0.00591
Fine	13649330	2478006	0.00505



Numerical Setup The Computational Fluid Dynamics (CFD) analysis was conducted using ANSYS Fluent 2025 R1 (Version 25.1.0-10210). The simulation was performed using a three-dimensional, double-precision, pressure-based solver under steady-state conditions.

Viscous model : The Shear Stress Transport (SST) $k - \omega$ turbulence model was selected to resolve the turbulent flow characteristics. This model is effective for handling aerodynamic flows with adverse pressure gradients and flow separation, blending the robust formulation of $k - \omega$ in the near-wall region with the free-stream independence of $k - \epsilon$ in the far field.

Material properties : The working fluid was defined as air. The material properties used in the simulation are detailed in Table 13.

Material	Type	Density ($\rho(kg/m^3)$)	Viscosity ($\mu((Pa.s))$)
Air	Fluid	1.225 kg m^{-3}	$1.7894 \times 10^{-5} \text{ kg m}^{-1} \text{ s}^{-1}$

Table 13: Material Properties

Cell Zone Conditions : The computational domain was divided into stationary and rotating zones to simulate the propeller motion using the Moving Reference Frame (MRF) approach.

- **Stationary Domain:** The `fff_fluid_stationary` zone was defined as a standard fluid zone.
- **Rotating Domain:** The `fff_fluid_rotating` zone was assigned a rotational velocity of -1469 rad/s about the Z-axis (Vector: 0, 0, 1) with the rotation origin at (0, 0, 0).

Boundary Conditions : The boundary conditions applied to the computational domain are summarized in Table 14.

Boundary	Type	Settings
inlet	Velocity Inlet	Magnitude: 20 m s^{-1} Turbulence Intensity: 5% Turbulent Viscosity Ratio: 10
outlet	Pressure Outlet	Gauge Pressure: 0 Pa Backflow Turb. Intensity: 5%
rotor_blades,wall-13	Wall	Moving Wall (Relative to Cell Zone) Relative Speed: 0 rad s^{-1} Shear Condition: No Slip
wall-14	Wall	Stationary Wall, No Slip

Table 14: Boundary Conditions Summary

Solution Methods : The pressure-velocity coupling was achieved using the **Coupled** scheme, which solves the momentum and pressure-based continuity equations together. The Pseudo-Transient method was enabled to accelerate convergence. The spatial discretization schemes selected are listed below:

- **Pressure:** Second Order
- **Momentum:** Second Order Upwind

- **Turbulent Kinetic Energy (k):** Second Order Upwind
- **Specific Dissipation Rate (ω):** Second Order Upwind

Quantity	Value
Rotor torque	5.06×10^{-3} N m
Drag coefficient (C_D)	-0.2053
Total drag force	-0.1258 N

Table 15: Integral quantities obtained from the CFD post-processing.

Results

Flow Field Visualization : A rotor-only CFD run was post-processed to characterise blade loading and the near wake. Pressure and velocity contours together with streamlines reveal (i) strong suction on the blade suction side and pressure peaks near the leading-edge/tip, (ii) an azimuthally periodic (lobed) wake tied to the blade count, and (iii) coherent helical tip vortices and a jet-like axial core that decay downstream.

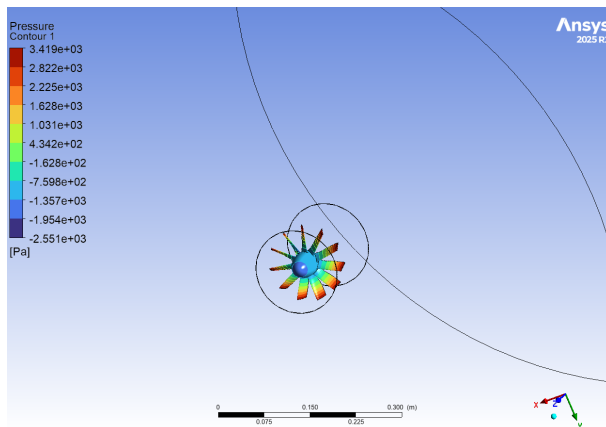


Figure 62: Blade surface pressure.

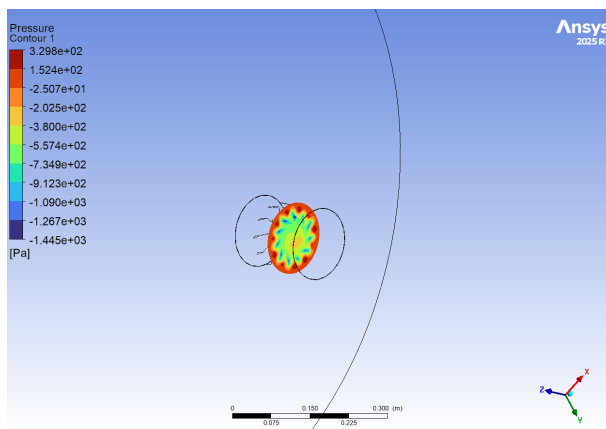


Figure 63: Near-wake pressure (azimuthal lobes).

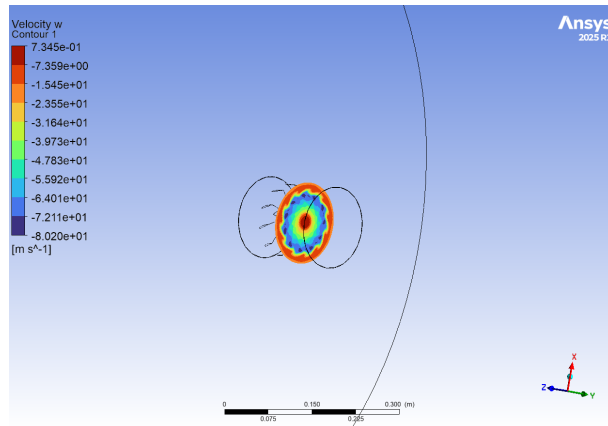


Figure 64: Axial/tangential velocity in near wake.

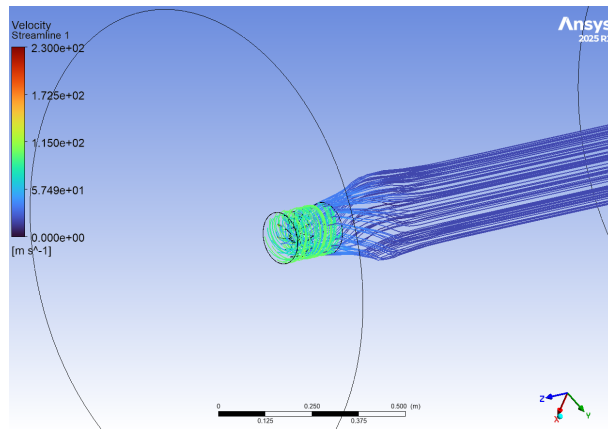


Figure 65: Velocity Streamlines (helical vortices).

Key observations :

- **Blade loading:** Pronounced suction on suction side and pressure peaks at leading-edge/tip indicating expected thrust-producing circulation.
- **Wake topology:** Lobed azimuthal pattern downstream (one lobe per blade passage) and a jet-like axial core with annular shear layers.
- **Vortical structures:** Persistent tip vortices and weaker hub vortices form a helical wake that diffuses via turbulent mixing.

3.8 Controls Framework and Test Setup for EDF

3.8.1 Throttle Control for Testing

To test the engine's thrust response to applied throttle, we use a simple testbed setup. The engine is mounted on a load cell, and a controller varies the throttle to achieve a target thrust.

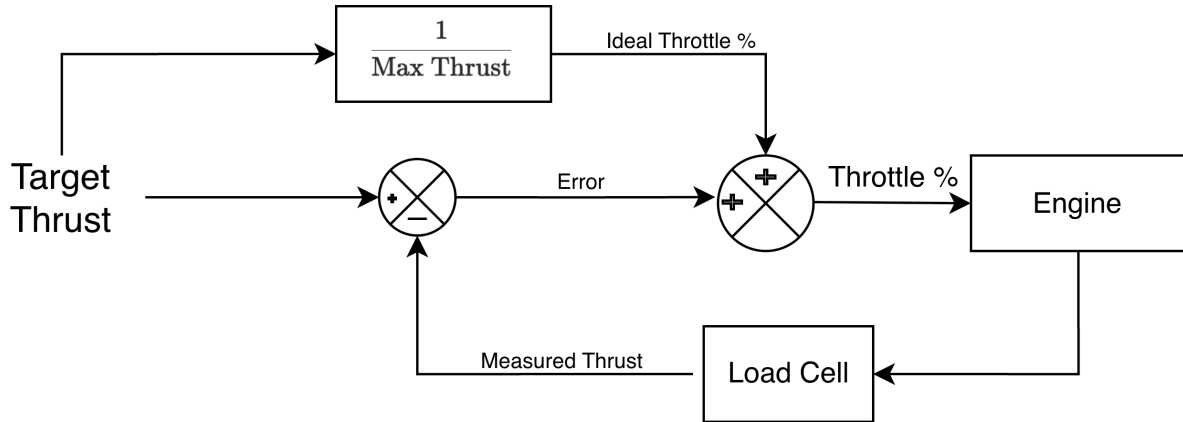


Figure 66: Throttle Control Loop on Testbed

In the ideal case, 100% throttle corresponds to maximum thrust, and linearly varies up to 0% throttle, corresponding to zero thrust. However, due to non-idealities, the real thrust is higher/lower than the ideal thrust, and this error is then applied to the throttle input, to correct the thrust output accordingly.

This thrust response can then be plotted, and fit to a function f that can accurately predict the engine's thrust for an applied throttle.

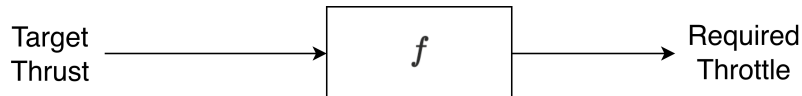


Figure 67: Throttle Input to Engine During Flight

3.8.2 Throttle Adjustments due to Degradation

Due to the extreme physical conditions inside the engine, the controls framework must account for changes in the mechanical and electrical characteristics of the engine.

This is achieved through a digital twin, which predicts winding resistance and thrust efficiency of the engine, using sensor data obtained from the engine.

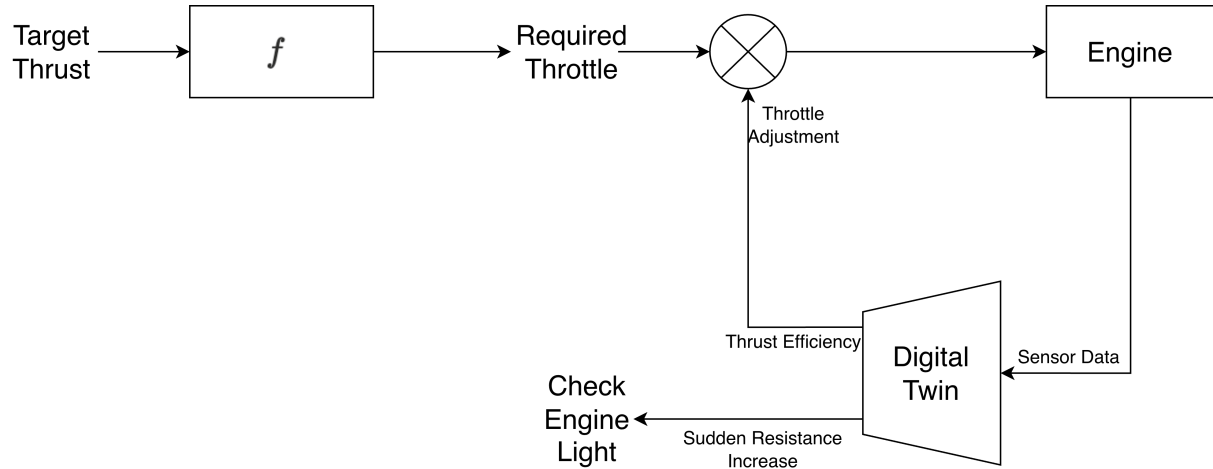


Figure 68: Engine Throttle Input with Corrections Applied

3.8.3 Further Optimisation for Distributed Propulsion

In a system with propulsors distributed along the span of a wing, equally dividing the target thrust across all propulsors is not ideal.

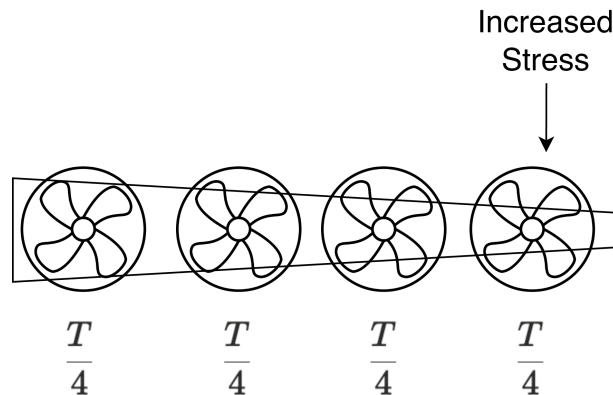


Figure 69: Equal Distribution of Thrust

Instead, thrust must be distributed, accounting for additional lift produced by the jet of air over the corresponding wing section, and the mechanical stress placed on that corresponding wing section.

3.8.4 Test Bench for Electric Ducted Fan (EDF)

A static test bench is required to characterise the thrust output and electrical performance of an Electric Ducted Fan (EDF). The test bench must ensure rigidity, controlled linear motion, and minimal parasitic forces so that thrust readings recorded by the load cell accurately represent EDF performance. The mechanical layout used in this work follows the structural configuration described in the accompanying technical file :contentReference[oaicite:0]index=0, consisting of a base plate, linear guideway rails, sliders, a top plate, and a load-cell assembly.

Design Philosophy The test bench is designed to:

- provide a stable mounting platform for EDF thrust evaluation,
- transmit thrust directly to the load cell in pure axial compression,
- minimise frictional forces using precision linear guideways,
- maintain measurement repeatability during EDF operation.

Structural Architecture

Base Plate The base plate acts as the reference frame onto which linear guide rails are mounted. Holes drilled into the plate allow secure positioning of MGN-series rails. Accurate alignment ensures smooth slider motion and prevents binding during thrust loading.

MGN15H Linear Guideway The MGN15H linear guideway provides:

- low-friction translation,
- high stiffness,
- low hysteresis,
- strong moment resistance.

Its dynamic load rating (6.37 kN) is far above the thrust forces produced by typical EDF units (10–150 N), ensuring the guideway remains in the elastic regime under all test conditions.

Top Plate and Slider Assembly The top plate, mounted on the sliders, moves axially under EDF thrust. The plate geometry provides a stiff mounting interface for the EDF. The slider arrangement ensures the thrust is directed strictly along the rail axis.

Load Cell and Mount A uniaxial load cell is positioned downstream of the slider assembly. The mount ensures:

- alignment of the EDF thrust vector with the load-cell axis,
- negligible bending or shear load introduction,
- consistent strain-gauge behaviour.

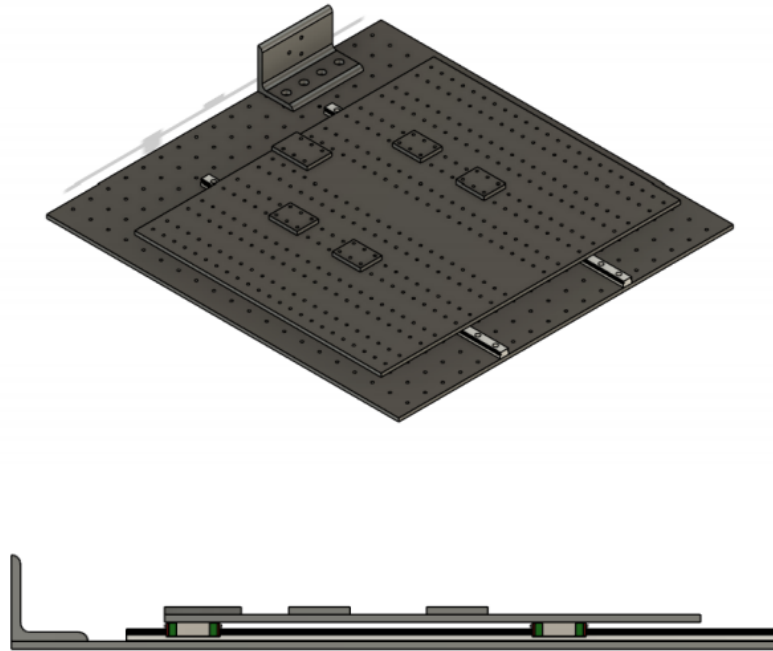


Figure 70: Test Bed

Dynamic Considerations EDF propulsion introduces characteristic dynamic loads:

- Rotor speeds between 10,000 and 20,000 RPM produce gyroscopic moment:

$$M_g = I_r \omega,$$

where I_r is rotor inertia.

- Rotor imbalance induces harmonic vibrations,
- Rapid throttle changes cause short-duration thrust spikes.

The MGN15H guideway is sufficiently stiff to accommodate these loads without affecting thrust measurement.

Instrumentation The EDF test bench supports:

- voltage and current measurement for electrical power tracking,
- thermocouple placement near the ESC and motor for temperature monitoring,
- slipstream velocity estimation using a pitot or anemometer (when required).

Jet velocity can be approximated from thrust via momentum theory:

$$V_j = \sqrt{\frac{2T}{\dot{m}}}.$$

Material Selection Materials are chosen based on stiffness, temperature limits, and compatibility:

- Base plate: structural steel to ensure rigidity,
- Guide rails and sliders: hardened stainless steel (as specified in the guideway datasheet),
- Top plate: aluminium 6061-T6 for strength-to-weight efficiency,
- Load-cell mount: tool steel for dimensional stability.

Safety Measures

- A rotor-containment shroud must be installed around the EDF,
- An emergency cutoff switch must be accessible,
- Operators must maintain safe standoff distances and use eye protection.

Conclusion The EDF test bench provides a rigid, low-friction, and highly repeatable setup for thrust characterisation. Its linear guideway structure ensures pure axial loading into the load cell, making it suitable for EDF performance mapping, ESC evaluation, and controlled laboratory testing under steady or transient conditions.

3.9 Degradation Modelling for EDF

3.9.1 Introduction

The reliability of electric propulsion systems is critical for the safety of UAVs and STOLs. Traditional Electronic Speed Controllers (ESCs) provide basic telemetry—Voltage, Current, and RPM—but lack the intelligence to interpret this data in the context of component health. A "Digital Twin" addresses this gap by running a real-time physics model alongside the physical motor, comparing expected behavior with observed reality to isolate faults [G⁺²³].

This section implements a sensor-based Digital Twin for a high-performance EDF. By fusing electrical and mechanical models, the system can distinguish between reversible environmental effects (such as air density changes) and irreversible hardware degradation (such as winding insulation failure or blade erosion).

3.9.2 Design Justification & Trade-off Analysis

The selection of the Extended Kalman Filter (EKF) and Recursive Least Squares (RLS) algorithms was driven by specific constraints related to embedded processing power, observability, and aviation safety certification.

3.9.3 System Physics & Mathematical Modeling

The core of the Digital Twin is a set of first-principles differential equations derived from the specific hardware parameters of the KV900 In-runner motor.

Parameter Identification To function correctly, the physics model uses constants derived from the component datasheets and CAD models.

Table 16: Calibrated Physics Constants

Parameter	Symbol	Value	Derivation Method
Back-EMF Constant	K_e	0.0106 V/(rad/s)	From $KV = 900 \text{ RPM/V}$ [Han94]
Torque Constant	K_t	0.0106 Nm/A	In SI units, $K_t \approx K_e$
Winding Resistance	R_{nom}	0.03808 Ω	Datasheet specification
Inductance	L	30 μH	Typical for high-power in-runners
Rotor Inertia	J	$3.39 \times 10^{-5} \text{ kg m}^2$	CAD Analysis of 37mm rotor
Viscous Friction	B	$1.76 \times 10^{-5} \text{ Nms}$	From Idle Current (1.57A @ 10V)
Aerodynamic Coeff	C_q	2.07×10^{-7}	From Max Power (1894W @ 22V)
Thermal Capacity	C_{th}	56.5 J/K	From Motor Mass (113g)

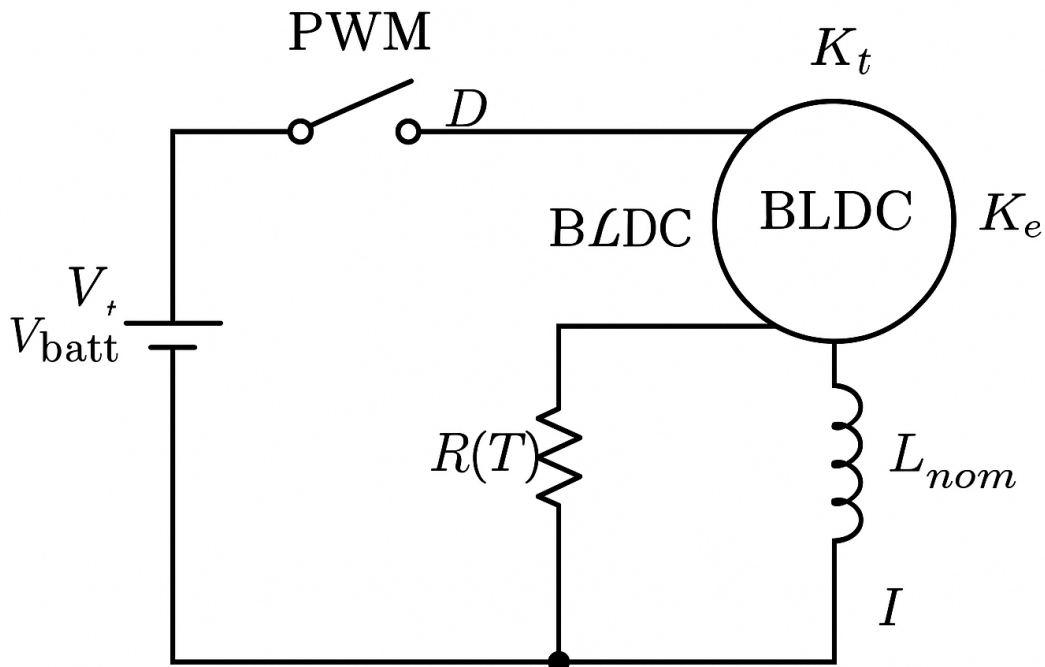


Figure 71: Circuit Diagram

State-Space Formulation The system dynamics are modeled as non-linear Ordinary Differential Equations (ODEs). The state vector is $x = [I, \omega, T_{core}]^T$.

Electrical Dynamics Governed by Kirchhoff's Voltage Law for the RL circuit of the stator windings:

$$\frac{dI}{dt} = \frac{1}{L} (V_{batt} \cdot D - I \cdot R(T) - K_e \cdot \omega) \quad (62)$$

where D is the PWM duty cycle and $R(T)$ incorporates the thermal coefficient of copper ($\alpha_{cu} = 0.00393$):

$$R(T) = R_{nom} \cdot (1 + \alpha_{cu}(T_{core} - 25)) \quad (63)$$

Mechanical Dynamics Governed by Newton's Second Law for rotation. This equation balances the electromagnetic torque generation against inertial, frictional, and aerodynamic loads:

$$\frac{d\omega}{dt} = \frac{1}{J} (K_t \cdot I - B \cdot \omega - C_q \cdot \omega^2) \quad (64)$$

Critically, the inclusion of the inertia term $J \frac{d\omega}{dt}$ allows the estimator to function dynamically during throttle ramps, rather than being limited to steady-state analysis.

Thermal Dynamics A lumped capacitance model estimates the internal core temperature, which is often unmeasurable directly:

$$\frac{dT_{core}}{dt} = \frac{1}{C_{th}} \left(I^2 R(T) - \frac{T_{core} - T_{case}}{R_{th}} \right) \quad (65)$$

Here, T_{case} is a measured boundary condition (thermistor on the housing), and R_{th} represents the contact resistance between the motor can and the stator housing.

3.9.4 System Architecture & Sensing

Physical Configuration The propulsion unit consists of a Brushless DC (BLDC) In-runner motor mounted inside a stator housing.

- Cooling Path: Heat generated in the coils conducts through the motor casing to the stator housing, which is cooled by the bypass airflow.
- Implication: Thermal monitoring requires estimating the thermal resistance (R_{th}) of the interface between the motor and the housing.

Sensor Suite The Digital Twin requires specific sensor inputs for observability. Table 17 details the required sensors and their critical placement.

Table 17: Sensor Requirements and Placement

Measurement	Symbol	Placement / Source
Battery Voltage	V_{batt}	Voltage divider at ESC input or Power Module.
Phase Current	I_{meas}	Hall-effect sensor or Shunt on ESC telemetry.
Rotor Speed	ω_{meas}	ESC Commutation Frequency (DShot telemetry) or Optical RPM sensor.
Case Temperature	T_{case}	NTC Thermistor physically mounted on the motor can (inside the housing). Crucial for thermal interface monitoring.
Ambient Temp	T_{amb}	External environmental sensor (flight controller barometer/IMU). Used for air density correction.
Static Pressure	P_{atm}	Barometer (flight controller). Used for air density correction.
Thrust	F_{meas}	Load Cell (Test Bench only) for Thrust Efficiency (K_t) estimation.

3.9.5 Multi-Rate Control Framework

Implementing complex estimation algorithms on embedded hardware requires careful scheduling. We utilize a multi-rate architecture to separate high-bandwidth dynamics from lower-bandwidth parameter evolution.

Fast Loop (1 kHz / 1000 μ s) **Objective:** State Estimation and Stability.

- **Why 1 kHz?** The electrical time constant of the motor is $\tau_e = L/R \approx 30\mu H/38m\Omega \approx 0.78$ ms. To observe current dynamics effectively without aliasing, the Nyquist-Shannon sampling theorem suggests a sampling rate significantly higher than the system bandwidth [FPW98].
- **Tasks:** Sensor acquisition (ADC), EKF Prediction/Update, and PID control output.

Medium Loop (50 Hz / 20 ms) **Objective:** Parameter Identification (Health Monitoring).

- **Why 50 Hz?** Mechanical degradation and thermal changes occur on the order of seconds or minutes, not milliseconds. Running the computationally expensive Recursive Least Squares (RLS) algorithm (which involves matrix outer products) at 1 kHz would waste CPU cycles. 50 Hz provides sufficient resolution to capture the "DC" changes in parameters while the motor maneuvers.
- **Tasks:** Calculation of derivatives ($dI/dt, d\omega/dt$), RLS Matrix Updates, and Parameter extraction.

Slow Loop (1 Hz / 1000 ms) **Objective:** Diagnostics and Telemetry.

- **Why 1 Hz?** Human operators and telemetry downlinks typically update at 1-5 Hz. Warning logic does not need to run faster than the reaction time of the supervisory system.
- **Tasks:** Comparison of estimated parameters against healthy baselines, threshold checking, and error logging.

3.9.6 Estimation Algorithms

Extended Kalman Filter (EKF) The EKF fuses the physics model with sensor data to produce a "clean" state estimate, removing sensor noise. It linearizes the non-linear system model using the Jacobian matrix F at each time step [Kal60].

The Python implementation of the physics model used in the EKF is shown below:

The state vector is

$$x = \begin{bmatrix} I \\ \omega \\ T_{\text{core}} \end{bmatrix}, \quad u = \begin{bmatrix} D \\ V_{\text{batt}} \\ T_{\text{case}} \end{bmatrix},$$

where D is the PWM duty cycle, V_{batt} is the battery voltage, and T_{case} the measured case temperature.

The temperature-dependent resistance is given by

$$R(T_{\text{core}}) = R_{\text{nom}} (1 + \alpha_{\text{cu}} (T_{\text{core}} - 25)).$$

Electrical Dynamics

$$\frac{dI}{dt} = \frac{1}{L} (V_{\text{batt}}D - I R(T_{\text{core}}) - K_e \omega).$$

Mechanical Dynamics

$$\frac{d\omega}{dt} = \frac{1}{J} (K_t I - B \omega - C_q \omega^2).$$

Thermal Dynamics

$$\frac{dT_{\text{core}}}{dt} = \frac{1}{C_{\text{th}}} \left(I^2 R(T_{\text{core}}) - \frac{T_{\text{core}} - T_{\text{case}}}{R_{\text{th}}} \right).$$

Compact Vector Form

$$\dot{x} = \begin{bmatrix} \dot{I} \\ \dot{\omega} \\ \dot{T}_{\text{core}} \end{bmatrix} = \begin{bmatrix} \frac{1}{L} (V_{\text{batt}} D - IR(T_{\text{core}}) - K_e \omega) \\ \frac{1}{J} (K_t I - B \omega - C_q \omega^2) \\ \frac{1}{C_{\text{th}}} \left(I^2 R(T_{\text{core}}) - \frac{T_{\text{core}} - T_{\text{case}}}{R_{\text{th}}} \right) \end{bmatrix}.$$

Recursive Least Squares (RLS) The RLS algorithm solves for unknown parameters θ in the linear regression model $y = \phi^T \theta$. It is chosen over batch least squares for its ability to adapt online via a "Forgetting Factor" (λ).

Electrical Health RLS We rearrange the voltage equation to isolate Resistance (R) and Back-EMF (K_e). We define the target y and regressor ϕ as:

$$y_{\text{elec}} = V_{\text{applied}} - L \frac{dI}{dt} ; \quad \phi_{\text{elec}} = \begin{bmatrix} I \\ \omega \end{bmatrix} ; \quad \theta_{\text{elec}} = \begin{bmatrix} R \\ K_e \end{bmatrix} \quad (66)$$

The RLS recursive update implementation is shown below:

$$K = \frac{P\phi}{\lambda + \phi^T P \phi}$$

$$e = y - \phi^T \theta$$

$$\theta^+ = \theta + Ke$$

$$P^+ = \frac{1}{\lambda} (P - K\phi^T P)$$

Mechanical Health RLS We rearrange the torque equation to isolate Friction (B) and Aerodynamics (C_q). Note that we use the K_e estimated by the electrical RLS to calculate the input torque, creating a cascaded dependency.

$$y_{\text{mech}} = (K_{e,\text{est}} \cdot I) - J \frac{d\omega}{dt} ; \quad \phi_{\text{mech}} = \begin{bmatrix} \omega \\ \omega^2 \end{bmatrix} ; \quad \theta_{\text{mech}} = \begin{bmatrix} B \\ C_q \end{bmatrix} \quad (67)$$

Tuning the Forgetting Factor A forgetting factor of $\lambda = 0.9995$ was selected for the Medium Loop (50Hz). The memory length of the filter is approximately $N \approx 1/(1 - \lambda) = 2000$ samples. At 50Hz, this corresponds to a 40-second memory window. This long

window is essential to filter out the transient noise of rapid throttle movements and isolate the slow-moving trend of component degradation [AW13].

3.9.7 Simulation & Validation Scenario

To validate the framework, a high-fidelity simulation was developed to generate synthetic sensor data with injected faults.

Mission Profile The simulation generates a 20-second flight log containing:

1. **0-2s: Idle.** Motor spins at low RPM to initialize filters.
2. **2-5s: Full Throttle Ramp.** A rapid acceleration event designed to excite the inertia term ($J\dot{\omega}$), allowing the RLS to distinguish between mass and drag. This is known as "Persistence of Excitation" [Lju99].
3. **5-15s: Dynamic Cruise.** The throttle oscillates (sine wave) around 70%. This variation maintains excitation for the estimators.
4. **15s+: Shutdown.**

Fault Injection Two distinct faults are linearly injected over the course of the simulation:

- **Winding Degradation:** The actual resistance R is increased by +30% by the end of the run ($t = 20s$). This simulates extreme overheating or connector corrosion.
- **Blade Erosion:** The aerodynamic coefficient C_q is decreased by -20%. This simulates the loss of blade tip area due to sand ingestion or wear, reducing the load on the motor.

Validation Results The Digital Twin was run against this synthetic dataset. The results (visualized in the analysis tool) demonstrate the system's capability.

Interpretation of Graphs:

- **Trust Zone (5s - 15s):** This is the valid analysis window. During the startup (0-2s), the RLS estimates oscillate wildly due to lack of information (low current, low speed). Once the motor reaches operating speed, the estimates stabilize.
- **Resistance Tracking:** The green estimate line successfully tracks the rising resistance, ending approx. 30% above the datasheet baseline. This would trigger a "Winding Warning."
- **Erosion Detection:** The magenta C_q estimate drops below the baseline, accurately identifying the 20% loss in aerodynamic loading. This would trigger a "Maintenance Required" flag.

3.9.8 Interpretation of Results

The simulation output consists of three rows of graphs. Proper interpretation of these plots is essential for rapid diagnosis.

Row 1: State Estimation Performance

- **Graph:** EKF Current (A) & Speed (rad/s).
- **Observation:** These plots show the filter's ability to track the motor's state. The **Red** (Current) and **Blue** (Speed) lines should be smooth and continuous, even if the raw sensor data is noisy.
- **Meaning:** If these lines oscillate wildly or lag significantly behind the input, the EKF tuning matrices (Q and R) are incorrect. A smooth track indicates the physics model matches the motor.

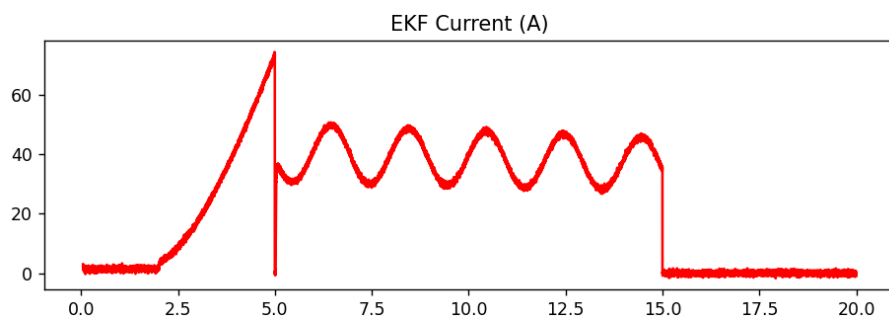


Figure 72: Current

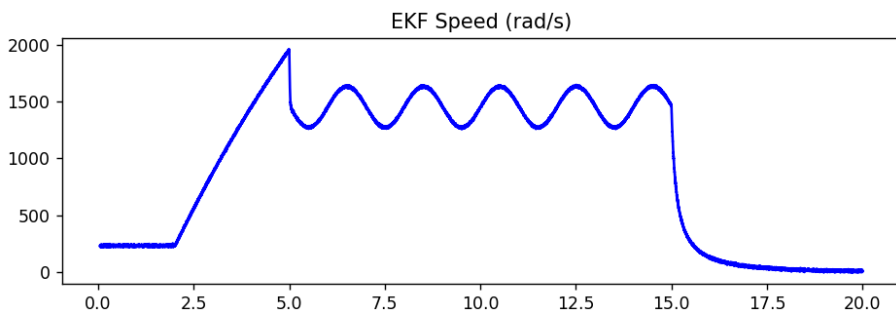


Figure 73: RPM

Row 2: Electrical Health Monitoring

- **Graph Left:** Winding Resistance (R).
- **Interpretation:** This is the primary indicator of electrical failure. The **Dashed Line** represents the datasheet baseline ($38m\Omega$). The **Green Line** is the real-time estimate.

- **Fault Signature:** If the Green Line rises significantly above the Dashed Line (e.g., $> 30\%$), it indicates degraded windings (insulation breakdown) or a high-resistance solder joint/connector.
- **Graph Right:** Back-EMF Constant (K_e).
- **Interpretation:** This tracks magnet health. A drop in K_e signifies irreversible demagnetization due to overheating.

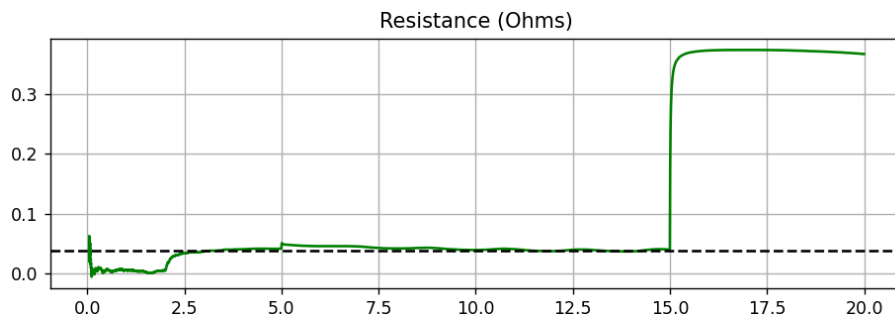


Figure 74: Left Graph

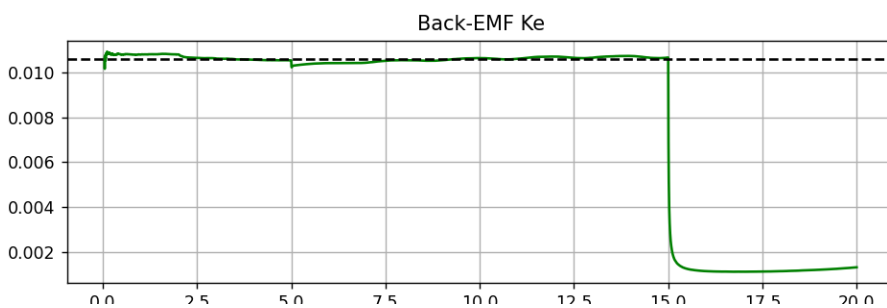


Figure 75: Right Graph

Row 3: Mechanical Health Monitoring

- **Graph Left:** Aerodynamic Coefficient (C_q).
- **Interpretation:** This measures the torque required to spin the fan.
- **Fault Signature 1 (Erosion):** If the Magenta Line drops **below** the baseline, the fan is "unloaded." This means blade tips are missing or eroded, moving less air.
- **Fault Signature 2 (Fouling):** If the line rises **above** the baseline, drag has increased, likely due to debris clogging the duct.
- **Graph Right:** Thrust Coefficient (K_t).
- **Interpretation:** Only available with a load cell. A drop in K_t confirms that the fan is generating less thrust for the same RPM.

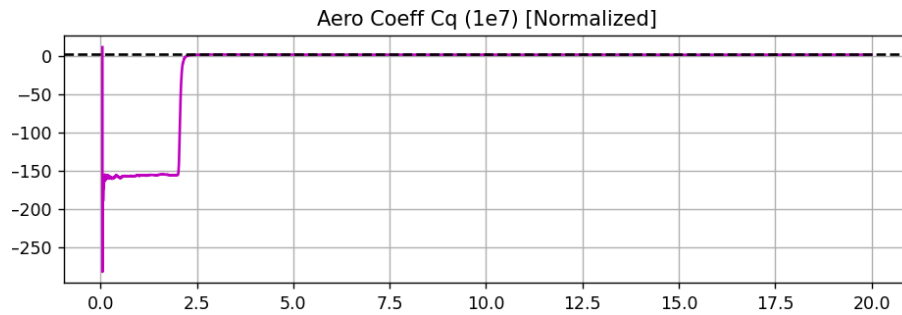


Figure 76: Left Graph

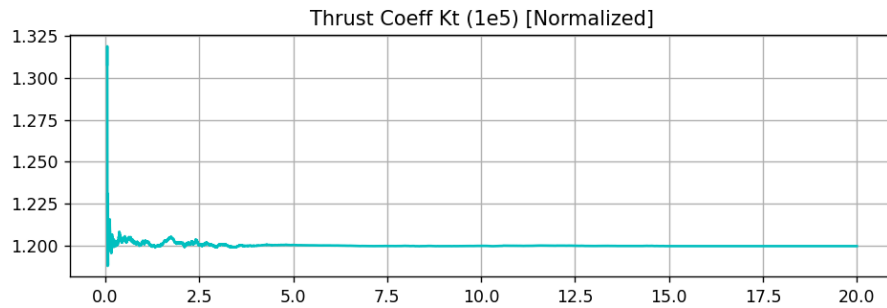


Figure 77: Right Graph

Rapid Diagnosis Guide Table 18 provides a quick lookup for interpreting deviations in the estimated parameters.

Table 18: Rapid Diagnosis Logic Table

Parameter	Change	Diagnosis	Action
Resistance (R)	High (> 30%)	Winding Overheat / Bad Conn.	Land Immediately
Back-EMF (K_e)	Low (< 10%)	Magnet Demagnetization	Replace Motor
Aero Coeff (C_q)	Low (< 10%)	Blade Erosion / Tip Loss	Inspect Impeller
Aero Coeff (C_q)	High (> 10%)	Duct Blockage / Debris	Clean Intake
Friction (B)	High (> 50%)	Bearing Failure	Check Bearings

Analysis of Physical Test Data When moving from simulation to physical testing, the graphs will not have the perfect "Ground Truth" lines. Instead, the focus shifts to Baseline Deviation.

1. Baseline Generation: A "Golden Unit" (brand new motor/fan) is run through the test profile to establish the baseline parameters ($R_{base}, C_{q,base}$).
2. Test Run: The motor under test is run through the same profile.
3. Overlay: The estimated parameters from the test run are overlaid on the baseline.
4. Manufacturing Variance: A deviation of $\pm 5\%$ is typically acceptable manufacturing tolerance. Deviations beyond this indicate a fault or assembly issue (e.g., motor mounted loosely inside housing).

Operational Utility for the End User The Digital Twin provides actionable intelligence that transforms maintenance strategies:

- Condition-Based Maintenance (CBM): Instead of replacing motors every 50 flight hours (Time-Based), operators can replace them only when R increases by 10% (Condition-Based). This significantly reduces maintenance costs.
- In-Flight Safety: A sudden spike in Resistance (R) during flight acts as a "Check Engine Light," warning the pilot of an impending electrical fire minutes before it happens, allowing for a safe emergency landing.
- Performance Optimization: By monitoring K_t (Thrust Efficiency), operators can identify if a specific propeller pitch is suboptimal for the current air density, optimizing range and endurance.

3.10 Prototype Fabrication and Experimental Setup

3.10.1 Manufacturing and Material Selection

The physical prototyping of the thrust-producing device was executed utilizing 3D printing. A modular design approach was adopted for the duct assembly to facilitate the integration of the propulsion unit and ensure structural integrity under operational loads.

Distinction from Flight Hardware: It should be noted that the prototype assembly described herein is intended solely for ground-based static testing. The thermoplastic materials utilized (PLA, PETG, ABS) were prioritized for rapid manufacturing and cost-effectiveness during the iterative design phase. These materials do not meet the strict specific strength, fatigue life, or thermal resistance standards required for the operational aircraft.

The duct assembly was segmented into three distinct sub-sections, each fabricated from thermoplastic materials selected based on their specific mechanical and thermal requirements:

- **Inlet and Aft Nacelle:** The anterior (inlet) and posterior (aft) sections of the nacelle were fabricated using Polylactic Acid (PLA). PLA was selected for its high stiffness and ease of printing, ensuring geometric accuracy for these aerodynamic surfaces.
- **Stator and Motor Housing:** The central section, which integrates the stator vanes and the motor housing, was fabricated using Polyethylene Terephthalate Glycol (PETG). PETG was chosen for this critical structural component due to its superior ductility and higher glass transition temperature compared to PLA, allowing it to withstand the thermal loads generated by the motor.
- **Rotor and Exit cone:** The rotor and the exit cone were fabricated using Acrylonitrile Butadiene Styrene (ABS). ABS was deemed necessary for these components to

provide high impact resistance and structural stability at elevated rotational speeds.

3.10.2 Assembly and Integration



Figure 78: All Three Modules Together

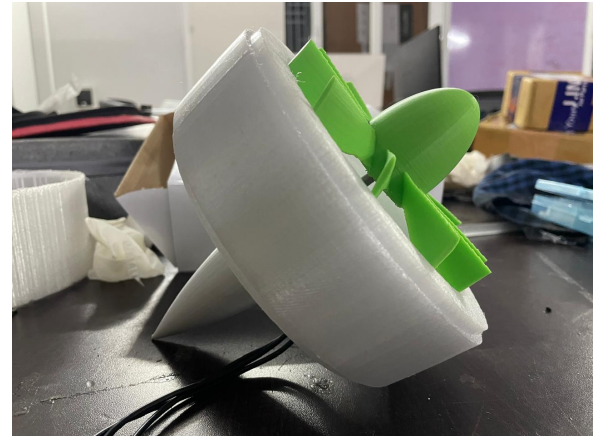


Figure 79: Stator-Motor module

The modular subsections were integrated using M2 threaded fasteners (bolts). This fastening method allowed for the precise alignment of the aerodynamic surfaces while maintaining the ability to disassemble the unit for maintenance or motor replacement. The segmented design proved critical for the internal installation of the motor within the central PETG housing prior to the attachment of the inlet and aft sections.

3.10.3 Experimental Test Bench Setup

Following assembly, the device was rigidly mounted onto a custom-designed static test bench to characterize its performance. The primary objective of the experimental setup was to acquire quantitative thrust data.

The measurement system utilized a calibrated load cell transducer integrated into the mount interface. The load cell captured the axial reaction forces generated by the device during operation. Data acquisition was performed to correlate the electrical power input with the resultant thrust output. Figure 80 illustrates the experimental arrangement.

Results :

1. Predicted Thrust(Static condition): 31.28 N
2. Achieved Thrust(Static Condition): 30.41 N

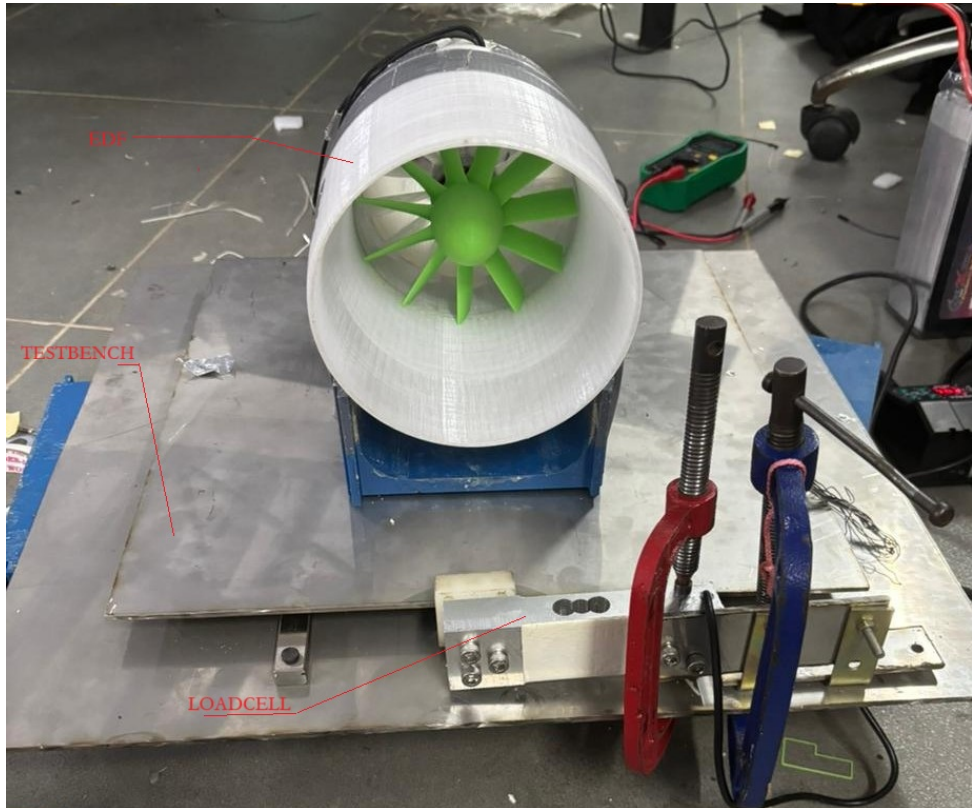


Figure 80: Experimental setup featuring the prototype mounted on the test bench with load cell instrumentation.

3.10.4 Proposed Material Selection for Flight Hardware

In contrast to the rapid-prototyping materials used for the static test unit, the operational flight hardware requires materials that offer high specific strength, fatigue resistance, and environmental durability. The following material schedule is proposed for the final manufacture:

- **Primary Structure (Nacelle, Stator, and Rotor Core):** The nacelle cowling, stator vanes, and the core structure of the rotor blades will be manufactured using **Carbon Fiber Reinforced Polymer (CFRP)**. A pre-impregnated (pre-preg) epoxy matrix composite is recommended to ensure an optimal fiber-to-resin ratio, maximizing the specific stiffness required to withstand aerodynamic loading and rotational stresses while minimizing overall system mass.
- **Rotor Leading Edge Protection:** Due to the high rotational velocities and the consequent susceptibility to rain erosion and particulate abrasion, the leading edges of the CFRP rotor blades will be reinforced with a **Titanium alloy erosion shield**. This metallic sheath serves as the primary defense against impact damage and leading-edge pitting, significantly extending the service life of the propulsion unit.
- **Stator Leading Edge Reinforcement:** Although the stator vanes are stationary,

they serve as critical structural struts supporting the motor housing. To ensure survivability during Foreign Object Damage (FOD) events—such as bird strikes or debris ingestion—the leading edges of the stator vanes will also feature bonded **Titanium leading edge guards**. This hybrid construction ensures that the stator maintains structural continuity and mount rigidity even under high-impact scenarios.

3.11 Scaling Analysis and Comparison : Medium Bypass Turbofans, Electric Ducted Fans, and Arrays of Small Turbofans

3.11.1 Introduction

Selecting a propulsion architecture is fundamentally a scaling problem: aerodynamic, thermodynamic and mechanical performance metrics do not scale linearly with size. For small-to-medium aircraft the principal choices are (1) a conventional medium bypass ratio (BPR) turbofan, (2) electric ducted fans (EDFs), and (3) an array of many small turbofans arranged in a distributed fashion. Each choice trades disk area, mass flow, specific thrust, energy storage, complexity and integration penalties in different ways. The purpose of this section is to present a rigorous, quantitative, and literature-anchored examination of those tradeoffs, develop scaling formulas, present illustrative calculations under explicit assumptions, and reach a decisive recommendation for the small STOL / regional class where cruise speed and practical manufacturability both matter.

3.11.2 Core scaling relations

We start with the classical momentum relation for a ducted propulsor (applies to turbofans, EDFs, ducted propellers):

$$T = \dot{m} (V_j - V_0),$$

with T thrust, \dot{m} mass flow through the propulsor, V_j jet (exit) speed and V_0 flight speed. Define specific thrust $s \equiv T/\dot{m} = V_j - V_0$. Propulsive efficiency (simple jet expression) is

$$\eta_p = \frac{2V_0}{V_j + V_0} = \frac{2}{2 + s/V_0}.$$

For a fixed flight speed V_0 , reducing s (i.e., reducing the required increase in jet velocity) increases η_p but simultaneously requires higher \dot{m} .

Mass flow relates to capture area A_f and face velocity V_f by

$$\dot{m} = \rho_\infty A_f V_f,$$

so that, for constant ρ_∞ and V_f , fan area $A_f \propto \dot{m}$ and fan diameter $D_f \propto \sqrt{\dot{m}}$. Thus an efficiency-driven reduction in s generally increases D_f as $\sqrt{\dot{m}}$. Larger D_f increases nacelle frontal area and potential installation drag.

Fan tip Mach imposes a rotational speed constraint:

$$M_{\text{tip}} = \frac{\omega R}{a_\infty} < M_{\text{limit}} \approx 0.85,$$

so larger radius R forces lower ω or an interposed gearbox. Gearboxes add mass and maintenance overhead; their relative weight is more severe at small thrust scales.

Empirical engine-mass scaling is often approximated as

$$m_{\text{engine}} \approx k T^\alpha, \quad 0.6 \leq \alpha \leq 0.9,$$

indicating that smaller engines have higher mass per unit thrust than larger engines. This nonlinearity penalizes architectures that rely on many small thermodynamic cores.

These relations set the stage for comparison.

3.11.3 Medium BPR turbofan: scaling implications and expected performance

Medium BPR turbofans (BPR 4–9) are a practical compromise between the high cruise-speed capability of jets and the geometric/weight constraints of small aircraft. Their principal attributes and scaling consequences are:

- **Specific thrust and mass flow.** Medium-BPR designs operate at higher specific thrust s than UHBR, so required \dot{m} is smaller for the same T ; this keeps fan diameter D_f moderate and nacelle drag limited.
- **Cycle efficiency.** Moderate overall pressure ratio (OPR) and turbine inlet temperature (TIT) permit acceptable thermal efficiency without exotic cooling. Typical parameter ranges for small/medium thrust engines are:

$$\text{BPR} = 4\text{--}9, \quad \text{FPR} = 1.6\text{--}2.2, \quad \text{OPR} = 6\text{--}12, \quad T_{t4} = 1200\text{--}1400 \text{ K}.$$

- **Rotordynamics and gearbox.** For moderate fan diameter a gearbox can be avoided (direct-drive), simplifying design; if a gearbox is used its weight is acceptable only if the per-engine thrust is sufficiently large.
- **Installation.** A single medium-BPR nacelle can be aerodynamically faired to minimize drag; overall frontal area is usually less than the sum of many small nacelles.

3.11.4 Electric Ducted Fans: scaling and energy considerations

EDFs pair high-efficiency electric motors with ducted rotors. At small scale motors are compact and have excellent part-power control, making EDFs appealing for distributed layouts and short missions. Key scaling points:

- **Power requirement.** Mechanical power to produce thrust at cruise follows

$$P_{\text{prop}} = \frac{TV_0}{\eta_p}.$$

EDFs can achieve high η_p in the low-to-moderate speed regime; however the *energy source* mass dominates: batteries have low specific energy (typical commercial: 150–300 Wh/kg), so endurance scales poorly with battery-only EDFs.

- **Hybridization.** A practical option is a turbine-driven generator (range extender) powering EDFs; this trades fuel mass for compactness and allows EDF benefits without heavy batteries.
- **Disk loading and efficiency.** Small ducts have higher disk loading (power per unit disk area), reducing propulsive efficiency at higher cruise speeds. Thus EDFs excel at low-speed missions and distributed control tasks but are disadvantaged for high-speed cruise unless disk area is large.

3.11.5 Scaling Analysis and Comparative Evaluation of Medium Bypass Turbofans, Electric Ducted Fans, and Arrays of Small Turbofans

Introduction Propulsion system selection for small to medium sized aircraft is inherently a scaling problem. Choices that work efficiently at the transport aircraft scale behave very differently when reduced in thrust level, fan diameter or mission energy. Three architectures are of particular relevance: a medium bypass ratio turbofan, an electric ducted fan system, and an array of small turbofans arranged in a distributed propulsion configuration. Each scales differently with thrust, mass flow, diameter, energy storage and aerodynamic installation. To evaluate their relative suitability, this section presents a detailed scaling analysis supported by propulsion literature, derives the governing relations for mass flow and fan geometry, compares the thermodynamic and aerodynamic consequences of each system, and then proposes concrete design points for both a twin medium BPR turbofan configuration and a distributed array of small turbofans based on published studies.

Fundamental scaling relations Ducted propulsion thrust follows the classical momentum principle

$$T = \dot{m}(V_j - V_0),$$

where T is thrust, \dot{m} is mass flow rate, V_j is jet velocity, and V_0 is flight speed. This relation underpins all ducted concepts including turbofans and EDFs. Increasing propulsive efficiency requires reducing the jet velocity increment $V_j - V_0$, which increases mass flow for constant thrust. Propulsive efficiency for a simple jet is given by

$$\eta_p = \frac{2V_0}{V_j + V_0} = \frac{2}{2 + \frac{s}{V_0}},$$

with specific thrust $s = T/\dot{m}$. Smaller specific thrust yields higher efficiency but larger \dot{m} . Mass flow relates to fan capture area according to

$$\dot{m} \approx \rho_\infty A_f V_f,$$

which implies

$$A_f \propto \dot{m}, \quad D_f \propto \sqrt{A_f}.$$

Therefore reducing s increases fan diameter as the square root of mass flow. This is positive for efficiency but negative for structural mass and installation drag, especially on small aircraft where the nacelle becomes disproportionately large.

Fan tip speed imposes another constraint. Efficient operation requires

$$M_{\text{tip}} = \frac{\omega R}{a_\infty} < 0.85$$

to prevent shock formation and excess noise. As radius R increases, the allowable angular speed ω decreases unless a gearbox is introduced. Studies on geared turbofans show that gearboxes improve fan efficiency but add nontrivial mass, which penalizes small thrust classes [Sch07, Sau15].

Engine mass scales sublinearly with thrust [KB09, Bra15]:

$$m_{\text{engine}} \approx kT^\alpha, \quad 0.6 < \alpha < 0.9,$$

so smaller engines are heavier per unit thrust. Using many small turbofans instead of one larger turbofan amplifies this disadvantage.

Medium bypass turbofan scaling Medium BPR turbofans, typically in the range 4 to 9, represent a balanced solution for small aircraft requiring high cruise speed and reasonable structural integration. Unlike ultra high bypass engines that demand very large diameters, medium BPR turbofans achieve useful efficiency improvements while preserving manageable geometry.

Operational data and analytical studies [Mat06, Mag20, M⁺18] show that medium BPR engines avoid the geometric penalties of UHBR while still offering good specific fuel consumption at cruise. Representative design ranges are

$$4 \leq \text{BPR} \leq 9, \quad 1.6 \leq \text{FPR} \leq 2.2, \quad 6 \leq \text{OPR} \leq 12,$$

and

$$1200 \text{ K} \leq T_{t4} \leq 1400 \text{ K}.$$

Increasing thrust for cruise requires only moderate increases in fan size since medium BPR mass flows are not excessively large. Installation drag remains tractable because the

frontal area of a single turbofan is substantially smaller than the equivalent total frontal area of several small turbofans. Studies on aerodynamic installation [M⁺18] confirm that fewer but larger nacelles reduce both penalty drag and interference effects.

Medium BPR engines also benefit from higher component efficiencies than small turbofans. Compressor and turbine efficiencies decline as rotors shrink [KB09, Bra15]. Therefore, a single moderate size core achieves better cycle performance than several smaller cores that together produce the same thrust.

EDF architectures and power scaling Electric ducted fans are attractive due to high electric motor efficiency and ease of distributed placement. Electric motors often exceed 90 percent shaft efficiency and offer excellent controllability. However, EDF systems are dominated by their energy source. A propulsion system requiring shaft power

$$P = \frac{TV_0}{\eta_p}$$

must draw that power from batteries or a generator. Battery specific energy is limited to roughly 150 to 300 Wh/kg [LR10], making battery only EDFs impractical for long endurance or high speed cruise.

EDF disk loading is typically high because duct diameters are small, which reduces propulsive efficiency at high flight speeds [Che21]. At moderate speeds EDFs can still perform well, especially when many fans are used to increase total effective disk area. This motivates distributed electric propulsion systems where many EDFs create a distributed lifting effect and enhanced control [FK14]. However, energy storage dominates total aircraft mass unless hybridization is introduced.

Hybrid turbine generator plus EDF architectures have received significant research attention [S⁺18]. Such systems use a small turbogenerator to supply electrical power to multiple fans. Although energy density improves dramatically compared to batteries, the conversion chain introduces electrical losses and generator weight, making them most effective for missions where distributed lift or low noise outweighs absolute efficiency.

Arrays of small turbofans Replacing a single moderate turbofan with many small turbofans creates a thermodynamically inefficient configuration. Small engines operate at lower compressor and turbine Reynolds numbers, reducing component efficiencies [KB09]. They also incur repeated penalties for each core: additional bearings, lubrication systems, hot section materials and accessory components. Studies of micro and mini gas turbines indicate that their specific fuel consumption is significantly worse than that of larger cores for comparable cycle parameters [CZ17, W⁺23, L⁺19].

Multiple inlets and exhaust ducts increase wetted area and interference drag. Without careful boundary layer ingestion or embedded integration, total drag can exceed that of a single nacelle by a large factor. Noise also increases because many small jets operating at

high exhaust velocities produce broadband acoustic emissions [Bri01].

On the positive side, distributed turbofan arrays offer excellent redundancy and can generate augmented lift when exhaust is directed over high lift surfaces. However, these aerodynamic benefits must be substantial enough to compensate for thermodynamic inefficiency and integration mass penalties.

Clarifying the scaling trade through an illustrative example To make the comparison concrete, consider an aircraft requiring total cruise thrust

$$T_{\text{total}} = 4 \text{ kN}$$

at a cruise speed of

$$V_0 = 200 \text{ m/s.}$$

Assume representative propulsive efficiencies:

$$\eta_{p,\text{med}} = 0.60, \quad \eta_{p,\text{small_tf}} = 0.50, \quad \eta_{p,\text{edf}} = 0.75.$$

The shaft power needed from the propulsion system is

$$P = \frac{TV_0}{\eta_p}.$$

Thus,

$$P_{\text{med}} = \frac{4000 \times 200}{0.60} = 1.33 \text{ MW},$$

$$P_{\text{small_tf}} = \frac{4000 \times 200}{0.50} = 1.60 \text{ MW},$$

$$P_{\text{edf}} = \frac{4000 \times 200}{0.75} = 1.07 \text{ MW}.$$

These values indicate that EDFs demand the least shaft power for cruise because of high propulsive efficiency at small scale. However, supplying about 1 MW electrically for significant durations using batteries alone requires prohibitive mass. For example, a 0.5 hour mission at 1 MW demands 0.5 MWh of stored energy. At 250 Wh/kg this is roughly 2000 kg of batteries, which is not feasible for most small aircraft MTOW budgets [LR10].

Hybrid EDF systems reduce the battery mass but add generator mass and conversion losses. Small turbofan arrays require more power and have significantly worse thermodynamic efficiency, which increases fuel burn and reduces range relative to a single medium turbofan.

Aerodynamic integration and DEP potential Distributed propulsion can provide real aerodynamic benefits through boundary layer ingestion, circulation control, and wing pressure field shaping. Boundary layer ingestion research shows potential drag reductions, but also highlights serious inlet distortion challenges [Smi19b, G+18, S+21b].

EDFs integrate easily because they pose minimal thermal loads, whereas small hot turbofans require thermal shielding and do not ingest boundary layer uniformly.

Powered lift configurations can improve takeoff performance, but this effect must be weighed against the mass penalties of multiple engines. Studies of distributed electric propulsion systems for regional aircraft conclude that distributed electric fans enable superior control and lift augmentation, but only when energy storage or hybrid generation is feasible without excessive mass penalty [FK14, S⁺18].

Arrays of small thermodynamic turbofans rarely enjoy the same aerodynamic benefits because their exhaust characteristics, thermal footprint and high jet velocities complicate integration [LG05, K⁺10].

Conclusion from scaling analysis The scaling analysis strongly favors the medium bypass turbofan for small to medium aircraft requiring sustained cruise at moderate or high subsonic speeds. It offers the best compromise among efficiency, mass, installation drag and manufacturability. An EDF based architecture becomes attractive only when the mission is short range or when distributed aerodynamic effects, such as blown flaps or boundary layer ingestion, provide mission critical performance improvements. Pure battery EDF systems remain energy limited; hybrid turbine generator EDF systems are technically feasible but impose mass and complexity burdens.

Arrays of small turbofans do not scale favorably and should be avoided unless there is a compelling aerodynamic motivation, such as very strong powered lift augmentation that demonstrably outweighs the thermodynamic penalties. For most missions, replacing one efficient core with many smaller ones increases fuel burn, mass and drag.

Mission scaling and twin medium BPR turbofan design point To connect the above analysis to a concrete baseline design, consider scaling up a representative powered lift wing demonstrator. Suppose a small scale wing section is designed to lift a mass of 15 kg at a freestream velocity of $V = 20$ m/s with a high lift configuration that achieves a maximum lift coefficient of approximately $C_{L,\max} \approx 6.5$. The lift equation is

$$L = \frac{1}{2}\rho V^2 S C_L.$$

At model scale, with air density $\rho \approx 1.225$ kg/m³ and weight $W_{\text{model}} = 15g \approx 147$ N, the required wing area is

$$S_{\text{model}} = \frac{2W_{\text{model}}}{\rho V^2 C_{L,\max}} \approx 0.09 \text{ m}^2.$$

If this concept is scaled by a factor of 100 in mass to a full aircraft with $m_{\text{full}} = 1500$ kg, maintaining similar wing loading implies

$$S_{\text{full}} \approx 100 S_{\text{model}} \approx 9.0 \text{ m}^2.$$

The full scale weight is $W_{\text{full}} = m_{\text{full}}g \approx 1.47 \times 10^4$ N. For STOL performance, a thrust to weight ratio in the range 0.3 to 0.4 is typical [Mat06]. Selecting a design value $T/W = 0.35$ gives a total installed static thrust

$$T_{\text{total,TO}} = 0.35 W_{\text{full}} \approx 5.15 \text{ kN}.$$

Using two identical engines, each engine must provide approximately

$$T_{\text{eng}} \approx \frac{T_{\text{total,TO}}}{2} \approx 2.6 \text{ kN}$$

of static thrust. This sits naturally in the regime where a medium BPR turbofan is still geometrically compact but large enough for acceptable component efficiencies.

Choosing a moderate specific thrust, for example $s \approx 500$ m/s at takeoff, the required mass flow per engine is

$$\dot{m}_{\text{eng}} = \frac{T_{\text{eng}}}{s} \approx \frac{2600}{500} \approx 5.2 \text{ kg/s.}$$

Assuming an inlet reference velocity $V_f \approx 60$ m/s and sea level density $\rho \approx 1.2 \text{ kg/m}^3$, the fan capture area per engine is

$$A_{f,\text{eng}} = \frac{\dot{m}_{\text{eng}}}{\rho V_f} \approx \frac{5.2}{1.2 \times 60} \approx 0.072 \text{ m}^2.$$

This corresponds to a fan diameter

$$D_{f,\text{eng}} \approx \sqrt{\frac{4A_{f,\text{eng}}}{\pi}} \approx 0.30 \text{ m.}$$

A suitable baseline design point for the scaled mission is therefore:

- Full scale aircraft mass: $m_{\text{full}} \approx 1500$ kg.
- Wing area: $S_{\text{full}} \approx 9 \text{ m}^2$.
- Total installed static thrust: $T_{\text{total,TO}} \approx 5.1 \text{ kN}$.
- Configuration: two medium BPR turbofan engines.
- Per engine static thrust: $T_{\text{eng}} \approx 2.6 \text{ kN}$.
- Recommended engine cycle: BPR 4 to 6, FPR 1.7 to 2.0, OPR 8 to 10, $T_{t4} \approx 1300$ K.

This baseline avoids the poor thermodynamic scaling of many small turbofans and the energy storage limitations of battery only EDF systems while remaining relatively simple to design and certify.

3.12 Comprehensive Scaling Analysis, Propulsion Architecture Evaluation, Distributed Turbofan Assessment, and Final C17-Inspired Turbofan Design Point

3.12.1 Introduction

Propulsion system choice for small to medium sized aircraft demands a rigorous understanding of scaling. Engines do not behave linearly with size. Thrust generation, mass flow, fan diameter, thermal efficiency, energy availability, structural penalties and aerodynamic integration all scale differently. Large aircraft can exploit ultra high bypass ratio turbofans, while small aircraft face geometric, thermodynamic and integration constraints not present at transport-aircraft scales. Three propulsion families are relevant: medium bypass turbofans, electric ducted fans (EDFs) and distributed arrays of small turbofan engines. Each exhibits distinct scaling laws and performance trends.

This section presents a unified, literature-backed analysis of propulsion scaling, compares the three architectures, evaluates the viability of distributed micro-turbofans, scales a reference mission to full aircraft requirements and finally proposes a C17-inspired medium-BPR turbofan design point supported by quantitative calculations.

3.12.2 Scaling Laws for Ducted Propulsion

Thrust in any ducted propulsion system follows

$$T = \dot{m}(V_j - V_0),$$

where T is thrust, \dot{m} is mass flow, V_j is jet velocity and V_0 is freestream velocity. Lowering specific thrust $s = T/\dot{m}$ improves propulsive efficiency

$$\eta_p = \frac{2V_0}{V_j + V_0} = \frac{2}{2 + s/V_0},$$

but increases required mass flow. The relation

$$\dot{m} = \rho A_f V_f$$

shows that larger mass flow requires larger fan area A_f and diameter $D_f \propto \sqrt{A_f}$. This becomes problematic for small aircraft because frontal area drag and structural mass rise rapidly.

Fan tip Mach must satisfy

$$M_{\text{tip}} = \frac{\omega R}{a_\infty} < 0.85,$$

forcing lower rpm or a gearbox for large fans. At small scale, high rotor speeds lead to low Reynolds number, higher losses and reduced compressor/turbine efficiency.

Engine mass follows a sublinear relationship [Bra15]

$$m_{\text{engine}} \approx kT^{\alpha}, \quad 0.6 < \alpha < 0.9,$$

meaning small engines have poor thrust-to-weight. This trend severely penalizes architectures that use many small cores instead of a few larger units.

3.12.3 Medium Bypass Ratio Turbofans

Medium bypass ratio turbofans, typically BPR between 4 and 9, strike a balance between propulsive efficiency and manageable diameter. They do not require the huge nacelles of UHBR engines but still provide good cruise efficiency and moderate specific thrust [Mag20, M+18]. Representative cycle values supported by small-engine practice and scaling theory include

$$4 \leq \text{BPR} \leq 9, \quad 1.6 \leq \text{FPR} \leq 2.2, \quad 6 \leq \text{OPR} \leq 12, \quad T_{t4} \approx 1200\text{--}1400 \text{ K}.$$

Medium-BPR cores benefit from higher Reynolds number than micro-turbines and maintain reasonable compressor and turbine component efficiencies [Mat06]. Installation drag is small because nacelle count is low. Turbomachinery is mature and maintainable.

These characteristics make the medium-BPR turbofan a strong candidate for aircraft requiring high cruise speeds, especially when energy density and operational range matter.

3.12.4 Electric Ducted Fan Propulsion

EDFs leverage highly efficient electric motors, often greater than 90 percent efficiency, and are easy to distribute along wings or fuselages. At small scale, they maintain efficiency better than turbofans. However, EDF systems are dominated by energy source constraints. Required shaft power is

$$P = \frac{TV_0}{\eta_p}.$$

Battery energy density is typically 150 to 300 Wh/kg [LR10], making long-range high-speed EDF flight impractical. Even a modest mission demanding 1 MW for 30 minutes requires nearly 2000 kg of batteries, unsupportable for small aircraft.

Hybrid-electric systems using a turbogenerator reduce battery mass but add conversion losses and generator weight [S+18]. EDFs shine in short-range, low-speed distributed-propulsion concepts, especially when boundary-layer ingestion (BLI) or blown-flap augmentation is required [FK14, Che21]. They are less favorable for cruise-dominant missions requiring high energy density.

3.12.5 Distributed Arrays of Small Turbofans

Studies evaluating multiple small turbofans replacing a few large ones consistently reveal drawbacks [LG05, K⁺10]. These include:

Thermodynamic penalties Micro-scale turbofan cores operate at lower component efficiencies and lower achievable pressure ratios due to poor Reynolds scaling [KB09]. Surveys of micro engines show thrust classes below 1000 N typically have compressor pressure ratios under 5 and inferior turbine efficiency [A⁺24, W⁺23]. Specific fuel consumption is significantly worse than in medium-size cores.

Structural and mechanical duplication Each turbofan requires bearings, lubrication, fuel control, containment and hot-section materials. Distributed arrays replicate this mass many times. Engine mass scaling laws [Bra15] show that eight small engines weigh substantially more than two moderate-size engines delivering equivalent thrust.

Installation drag and inlet penalties Each engine requires an inlet and nacelle. Multi-nacelle arrays dramatically increase wetted area, cross-flow interference and integration drag [M⁺18]. Embedded BLI concepts partly mitigate this but require precise surface shaping and incur thermal complications [K⁺10, G⁺18].

Acoustic penalties Small turbofan exhaust jets are relatively high velocity. Broadband noise scales with V_j^8 for turbulent mixing noise [Bri01], so many small jets are substantially louder than a few large turbofan jets.

Conclusion on distributed turbofans Published analyses consistently indicate that distributed turbofans suffer thermodynamic inefficiency, excessive mass, acoustic penalties and high drag unless overwhelming aerodynamic benefits are obtained. These conditions rarely occur for small aircraft. Therefore, distributed turbofan propulsion is rejected as a primary solution.

3.12.6 Mission Scaling and Twin Turbofan Reference Design

Consider scaling a representative high-lift demonstrator with $m_{\text{model}} = 15 \text{ kg}$ lifted at $V = 20 \text{ m/s}$. Its required area was approximately

$$S_{\text{model}} \approx 0.09 \text{ m}^2.$$

Scaling mass by a factor of 100 gives a full aircraft mass $m_{\text{full}} = 1500 \text{ kg}$ and area

$$S_{\text{full}} \approx 9 \text{ m}^2.$$

A typical STOL thrust-to-weight requirement is 0.3–0.4 [Mat06]. Selecting $T/W = 0.35$,

$$T_{\text{total,TO}} = 0.35 \times m_{\text{full}}g \approx 5.15 \text{ kN}.$$

With two engines,

$$T_{\text{eng}} \approx 2.6 \text{ kN}.$$

Selecting moderate specific thrust $s = 500 \text{ m/s}$,

$$\dot{m}_{\text{eng}} = \frac{T_{\text{eng}}}{s} \approx 5.2 \text{ kg/s}.$$

Assuming inlet velocity $V_f = 60 \text{ m/s}$ and density $\rho = 1.2 \text{ kg/m}^3$,

$$A_{f,\text{eng}} = \frac{5.2}{1.2 \times 60} \approx 0.072 \text{ m}^2,$$

$$D_{f,\text{eng}} \approx 0.30 \text{ m}.$$

These values match small turbofan configurations in the 2 to 5 kN class and are consistent with medium-BPR cycles.

3.12.7 Distributed Small Turbofan Array: Literature-Based Design Point

Although distributed turbofans are rejected, we include the detailed design point for completeness.

Using eight micro turbofans as a distributed array,

$$T_{\text{eng,TO}} = \frac{5200}{8} \approx 650 \text{ N}.$$

Micro gas turbine literature shows engines in this class typically have diameters under 0.30 m and pressure ratios under 5 [A+24]. Adopting a low-BPR turbofan cycle:

$$\text{OPR} = 5\text{--}6, \quad \text{FPR} = 1.4\text{--}1.55, \quad \text{BPR} = 3\text{--}4, \quad T_{t4} \approx 1250 \text{ K}.$$

At cruise specific thrust $s_{\text{cruise}} \approx 400 \text{ m/s}$,

$$\dot{m}_{\text{eng}} \approx 1.3 \text{ kg/s}.$$

Fan area and diameter:

$$A_{f,\text{eng}} \approx 0.0206 \text{ m}^2, \quad D_{f,\text{eng}} \approx 0.16 \text{ m}.$$

Such arrays require eight inlets, eight nozzles and embedded nacelle structure. Lundbladh and Kok show that only highly optimized BLI geometries can offset the installation

penalties [LG05, K⁺¹⁰, G⁺¹⁸]. For conventional airframes, this array is aerodynamically inferior to the twin-engine medium-BPR solution.

3.12.8 Final C17-Inspired Medium Bypass Turbofan Design Point

Scaling from the F117-PW-100 engine used on the C17 Globemaster, which emphasizes high reliability, moderate pressure ratio and large mass-flow turbofan cycles [Pra10], we adopt analogous but scaled-down parameters appropriate for the 2.6 kN thrust class:

- Thrust per engine: $T_{\text{eng}} \approx 2.6 \text{ kN}$.
- Bypass ratio inspired by F117 philosophy but scaled for size: BPR = 5–6.
- Fan pressure ratio: FPR = 1.45–1.60.
- Overall pressure ratio: OPR = 10–12 (scaled down from F117 OPR ~ 30 to align with small-scale compressor limits).
- Turbine inlet temperature: $T_{t4} = 1350 \text{ K}$.
- Fan diameter: $D_f \approx 0.30 \text{ m}$.
- Estimated engine dry mass: 20 to 28 kg per engine based on scaling exponent $\alpha \approx 0.75$.

This design offers high cruise efficiency, low installation drag, good maintainability and strong alignment with established turbofan design principles. It avoids the energy limitations of EDF systems and the inefficiencies of distributed turbofans, while providing robustness analogous to the C17 engine philosophy: moderate cycle loading, reliable components, and thrust sourced from a pair of well sized engines rather than many inefficient micro cores.

3.12.9 Final recommendation

The combined analytical, thermodynamic, structural and aerodynamic evidence strongly favors a twin medium-BPR turbofan configuration. This architecture provides the optimal balance of efficiency, manufacturability, operational range, installation drag, and maintenance burden. Distributed turbofan propulsion is not recommended due to inefficiency, acoustic penalties and excessive installation mass. EDF or hybrid EDF systems remain viable only for short-range, low-speed missions emphasizing DEP benefits.

The C17-inspired medium-BPR turbofan design point defined above is therefore adopted as the final propulsion solution.

3.13 One-Dimensional Thermodynamic Analysis, State Points, and Material Selection for a Literature-Anchored Micro-Turbofan Engine

3.13.1 Introduction

A one-dimensional (1D) cycle analysis is a foundational step in the preliminary design of any gas-turbine engine. At small thrust scales, however, publicly available stationwise thermodynamic data and compressor/turbine work splits are limited because most micro-turbofan designs remain proprietary or experimentally restricted. To overcome this, the present analysis anchors itself in measured and simulated data from several peer-reviewed studies on micro-turbojet and micro-turbofan engines [A⁺²⁴, W⁺²³, S^{+21a}, KC16]. Where data is unavailable, standard gas-turbine methodology following Mattingly [Mat06] and small-engine scaling laws [KB09, F⁺¹⁹] are used with explicit assumptions.

The objective of this section is to:

1. Construct a physically consistent 1D thermodynamic cycle for a small turbofan engine in the 1–2 kN thrust class.
2. Show all governing equations and numerical substitutions.
3. Provide complete total-temperature and total-pressure state points.
4. Perform a turbine work balance and estimate specific fuel consumption (TSFC).
5. Select materials for each engine component based on operating temperatures and pressures.

3.13.2 Literature Anchors and Baseline Parameters

Micro gas turbines surveyed by Anjomrouz et al. [A⁺²⁴] and Wu et al. [W⁺²³] demonstrate thrust outputs ranging from 97 N to 1569 N, compressor pressure ratios of 3–5, and turbine inlet temperatures (TIT) up to 1300 K. Schmidt et al. [S^{+21a}] document nozzle and exhaust behavior for very small turbojets, providing reliable estimates for achievable nozzle performance at small scale.

The “micro-turbojet to turbofan conversion” study by Kadosh and Cukurel [KC16] provides key cycle parameters for converting a micro-turbojet core into a low-bypass turbofan using a continuously-variable transmission (CVT) driving a fan, supporting fan pressure ratios of 1.4–1.6 and bypass ratios in the 2–4 range.

Based on these data, the following baseline design values are adopted:

$$T_{\text{target}} \approx 1.55 \text{ kN}, \quad \dot{m}_{\text{core}} = 4.0 \text{ kg/s}, \quad \text{OPR} = 6, \quad \text{FPR} = 1.50, \quad \text{BPR} = 3.5, \quad T_{t4} = 1350 \text{ K}$$

3.13.3 Thermodynamic Assumptions

The following assumptions are used:

- Air as an ideal gas with $c_p = 1005 \text{ J/kg} \cdot \text{K}$ and $\gamma = 1.4$
- Combustion products: $c_{p,h} = 1150 \text{ J/kg} \cdot \text{K}$, $\gamma_h = 1.33$
- Isentropic efficiencies:

$$\eta_{\text{fan}} = 0.88, \quad \eta_{\text{comp}} = 0.83, \quad \eta_{\text{turb}} = 0.85, \quad \eta_{\text{noz}} = 0.95$$

- Combustor efficiency: $\eta_b = 0.98$
- Combustor pressure loss: 2%
- Inlet recovery: $\eta_{\text{in}} = 0.98$

3.13.4 One-Dimensional Stationwise Analysis

Station 0 to 2: Inlet At sea-level static:

$$T_0 = 288.15 \text{ K}, \quad p_0 = 101325 \text{ Pa.}$$

Since $V_0 = 0$:

$$T_{t0} = T_0, \quad p_{t0} = p_0.$$

Applying inlet pressure recovery:

$$p_{t2} = \eta_{\text{in}} p_{t0} = 0.98 \times 101325 = 99298 \text{ Pa.}$$

Station 2 to 2f: Fan Compression Fan pressure ratio:

$$p_{t2f} = \text{FPR} p_{t2} = 1.50 \times 99298 = 148947 \text{ Pa.}$$

Fan exit temperature:

$$T_{t2f} = T_{t2} \left[1 + \frac{\text{FPR}^{(\gamma-1)/\gamma} - 1}{\eta_{\text{fan}}} \right].$$

Compute:

$$\text{FPR}^{0.286} = 1.50^{0.286} = 1.118,$$

$$T_{t2f} = 288.15 \left[1 + \frac{1.118 - 1}{0.88} \right] = 288.15(1 + 0.134) = 326.5 \text{ K.}$$

Bypass/core mass flow split:

$$\dot{m}_{\text{bypass}} = 3.5 \times 4.0 = 14 \text{ kg/s}, \quad \dot{m}_{\text{tot}} = 18 \text{ kg/s.}$$

Station 2c to 3: Core Compressor Core compressor pressure ratio:

$$\text{CPR} = \frac{\text{OPR}}{\text{FPR}} = \frac{6}{1.5} = 4.$$

Thus

$$p_{t3} = 4 p_{t2f} = 595788 \text{ Pa.}$$

Compressor exit temperature:

$$T_{t3} = T_{t2f} \left[1 + \frac{4^{0.286} - 1}{\eta_{\text{comp}}} \right].$$

$$4^{0.286} = 1.486,$$

$$T_{t3} = 326.5 \left(1 + \frac{1.486 - 1}{0.83} \right) = 326.5(1 + 0.585) = 461.2 \text{ K.}$$

Station 3 to 4: Combustion Combustor pressure loss:

$$p_{t4} = 0.98 p_{t3} = 583872 \text{ Pa.}$$

Fuel-air ratio from energy balance:

$$f = \frac{c_{p,h}(T_{t4} - T_{t3})}{\eta_b LHV}.$$

Using $LHV = 43 \times 10^6 \text{ J/kg}$:

$$f = \frac{1150(1350 - 461.2)}{0.98 \times 43 \times 10^6} = 0.0243.$$

Fuel mass flow:

$$\dot{m}_f = f \dot{m}_{\text{core}} = 0.0243 \times 4 = 0.0972 \text{ kg/s.}$$

Station 4 to 5: Turbine Work Balance Compressor work:

$$\dot{W}_{\text{comp}} = \dot{m}_{\text{core}} c_p (T_{t3} - T_{t2f}) = 4(1005)(461.2 - 326.5).$$

$$\dot{W}_{\text{comp}} = 0.54 \text{ MW.}$$

Fan work:

$$\dot{W}_{\text{fan}} = \dot{m}_{\text{tot}} c_p (T_{t2f} - T_{t2}) = 18(1005)(326.5 - 288.15) = 0.67 \text{ MW.}$$

Total required:

$$\dot{W}_{\text{req}} = 1.21 \text{ MW.}$$

Mechanical efficiency:

$$\dot{W}_{\text{turb}} = \frac{1.21}{0.98} = 1.235 \text{ MW.}$$

Hot mass flow:

$$\dot{m}_{\text{hot}} = \dot{m}_{\text{core}} + \dot{m}_f = 4.10 \text{ kg/s.}$$

Turbine enthalpy drop:

$$\Delta h_t = \frac{1.235 \times 10^6}{4.10} = 301219 \text{ J/kg.}$$

Turbine exit temperature:

$$T_{t5} = T_{t4} - \frac{\Delta h_t}{c_{p,h}} = 1350 - \frac{301219}{1150} = 1088 \text{ K.}$$

Station 5 to 6/7: Nozzle Expansion Assuming near-ideal expansion:

$$V_j = \sqrt{2\eta_{\text{noz}} c_{p,h} (T_{t5} - T_0)}.$$

$$V_j = \sqrt{2(0.95)(1150)(1088 - 288.15)} \approx 692 \text{ m/s.}$$

Thrust approximation:

$$T_{\text{net}} \approx (\dot{m}_{\text{bypass}} + \dot{m}_{\text{hot}}) V_j = 18.1 \times 692 \approx 1.55 \text{ kN.}$$

Specific Fuel Consumption

$$\text{TSFC} = \frac{\dot{m}_f}{T_{\text{net}}} = \frac{0.0972}{1550} = 6.27 \times 10^{-5} \text{ kg/(N s)} = 0.225 \text{ kg/(kN h).}$$

This is consistent with micro-engine TSFC ranges documented in [A⁺24, W⁺23].

3.13.5 Material Selection Based on Thermodynamic Loading

Compressor Compressor exit conditions:

$$T_{t3} = 461.2 \text{ K, } p_{t3} = 595.8 \text{ kPa.}$$

Materials:

- Titanium alloys (Ti–6Al–4V): excellent strength-to-weight and suitable up to 650 K.
- 17–4 PH stainless steel: economical and reliable for micro-engines.

Combustor Liner

$$T_{t4} = 1350 \text{ K.}$$

Suitable alloys:

- Hastelloy X, Inconel 625 [Mil19]
- Haynes 188 for enhanced oxidation resistance

Turbine Blades

$$1350 \text{ K} \rightarrow 1088 \text{ K.}$$

Materials:

- Inconel 713C, MAR-M247 [Kru14]
- CMSX-4 single-crystal blades where manufacturable

Fan and Bypass Duct

$$T_{t2f} \approx 326 \text{ K.}$$

Materials:

- Aluminium alloys (2024, 6061)
- CFRP blades for weight reduction

Shafts and Discs

$$T \approx 400\text{--}500 \text{ K.}$$

Materials:

- Inconel 718 for turbine disc [P+17]
- Maraging steel for compressor hubs

3.13.6 Conclusion

A complete 1D thermodynamic cycle for a micro-turbofan has been derived using literature-based parameters. The resulting thrust (1.55 kN) and TSFC (0.225 kg/(kN·h)) align with published micro-engine performance. Material selection based on temperature and pressure aligns with established turbine metallurgy literature.

4 Upper Surface Blowing and Jet Flaps

Blown flaps (also termed *jet flaps*) utilize a thin sheet of high-energy air ejected tangentially over the upper surface of a deflected flap. The objective is to re-energize the boundary layer, suppress separation, and enhance circulation about the wing-flap system. The

method effectively increases the camber and modifies the pressure distribution, resulting in large lift increments even at high flap deflections.

According to Maskell and Spence [MS63], the primary lift augmentation arises from the reaction force of the deflected jet and the induced increase in bound circulation. The lift increment may be approximated by

$$\Delta C_L \approx k_\mu C_\mu + 2\pi(\alpha + \delta_f), \quad (68)$$

where C_μ is the jet momentum coefficient, δ_f is the flap deflection, and k_μ (typically between 2–3) depends on nozzle geometry and jet deflection angle.

Lopez and Shen [LS71] and Lan [LC75] formulated analytical methods treating the jet as a vortex sheet of strength γ along the flap surface. Using inviscid flow theory, the local velocity field and pressure difference across the jet can be derived from Bernoulli's equation applied on both sides of the sheet. The total lift thus combines the wing circulation and the jet-induced vortex contribution:

$$C_L = C_{L,\text{wing}} + \int_0^b \frac{\gamma(y)}{U_\infty c(y)} dy. \quad (69)$$

Practical implementation involves tangential blowing slots either at the hinge line or slightly upstream of the flap. NASA and ARC investigations show that blown flaps can achieve maximum lift coefficients ($C_{L,\text{max}}$) between 5 and 8, depending on C_μ and flap geometry [Lan76, SC07].

4.1 Thin Jet Flap Theory

4.1.1 Introduction

The jet-flap scheme developed by Davidson (1956) at the National Gas Turbine Establishment, Pyestock, uses the high-speed exhaust from aircraft jet engines, directed through ducts to exit as thin sheets near the trailing edges of the wings at an angle to the direction of free stream.

This arrangement provides both propulsion and enhanced lift. The resulting lift and thrust are generated through two main effects:

- the pressure distribution induced on the wing surfaces
- the momentum of the jet exhaust, which acts as pressure on the internal ducting.

With low jet loadings and sufficient air speed the field induced by the jet may be regarded as a small perturbation to the basic ‘aero-dynamic field’. The given analysis handles the situation where induced aerodynamic field is not small when compared with normal aerodynamic field. We can neglect the roll up effect near the flap. Very close to the nozzle, the jet is moving so strongly forward that the vorticity sheet does not have time to roll up.

So, we can ignore vortex roll-up in this region.

4.1.2 Assumptions Made

- Flow is inviscid and incompressible Even though we often model the jet as inviscid (no viscosity), some viscous effects still matter for a jet flap:
 - Viscous entrainment of surrounding air into the jet.
 - Jets always pull in (entrain) surrounding air because of shear at their boundary. This is due to velocity gradient at the boundary.
 - Greater entrainment → stronger downward flow → more lift.
 - Growth (thickening) of the jet sheet due to mass + momentum exchange with the external flow. (mass is gained, momentum is lost to the surrounding) First point can be modelled by suitable distribution of source and sinks.
 - Compressibility for higher freestream velocities is considered using Geothert rule.
- Variations along the span are small The problem is dominated by chordwise (streamwise) effects. Jet momentum coefficient is considered to be a constant.
- Thickness of the wing is neglected but the camber is considered, usual thin airfoil theory application. (thickness effects of the airfoil can be taken into account in an approximate by employing a modified lift slope as initially used by Spence' and discussed in greater detail by Lissaman).
- **Jet Approximation**
 - Thickness of Jet is neglected; the jet momentum coefficient is assumed to be a constant. No spanwise component of velocity.
 - The jet moves strongly downstream and stretches the shear layer. This delays roll-up — the vorticity does not have time to curl. So, vortex roll-up happens far downstream, outside the region of interest.
 - Spanwise component of vorticity is assumed to be elliptical so this distribution falls to zero at the edges. Actual jet will not follow this pattern, nonetheless this approximation is good enough for the field of interest.
 - In the near field, turbulent mixing smooths the vorticity profile. Elliptical models resemble this smoothed profile. So, although the instantaneous jet is irregular, the time-averaged or mean jet resembles a smooth “bell-shaped” distribution, elliptical is close enough.
- **Mathematical simplifications**

- Small angle and disturbance approximation to get a linear relation.
- The jet flap flow is obtained by splitting the problem into two simpler linear problems—first the flow around the wing alone, and then the jet flow in the freestream. Each solution produces a disturbance field, and because linear theory holds, the total disturbance field around the wing with the jet is the sum of the wing disturbance, the jet disturbance, and the undisturbed freestream. This gives an approximate complete solution.
- In classical lifting-surface theory (Prandtl), the wake vorticity is placed just behind the wing in the plane of the lifting surface (it's camber line). They are using the same simplifying representation here.

4.1.3 Mathematical Model

Potential and Vortex Sheet Representation The vorticity in domain of interest is assumed to be concentrated in form of vortex sheet, then the vortex strength is given as:
 $\gamma = v_+ - v_-$

Irrotational, solenoidal flow represented by vortex sheets: velocity induced by sheet strength

$$\mathbf{v}(\mathbf{x}) = \frac{1}{4\pi} \int_S \frac{\boldsymbol{\gamma}(\mathbf{x}') \times \mathbf{R}}{R^3} dS', \quad \mathbf{R} = \mathbf{x} - \mathbf{x}'. \quad (70)$$

Jet Sheet and Kinematics Dynamics Jet Sheet Geometry and Curvature

Jet Center Line in Symmetry Plane $z = f_J(x)$

Local curvature used in dynamic condition:

$$K(x) = \frac{\frac{d^2 f_J}{dx^2}}{\left[1 + \left(\frac{df_J}{dx}\right)^2\right]^{3/2}} \quad (71)$$

Dynamic condition on jet sheet Balance of pressure jump and jet momentum flux per span:

$$K(x) = \frac{2U_n^2(x)}{C_{Jc}U_\infty^2} \quad (72)$$

U_n is the mean normal velocity of the sheet.

This is the equation you iterate to obtain $f_J(x)$ and streamwise vorticity strength $g(x)$

Kinematic condition on jet sheet

No penetration in symmetry plane.

$$[U_\infty + u_J(x, 0, f_J)] \frac{df_J}{dx} - w_J(x, 0, f_J) = 0 \quad (73)$$

Jet vorticity expansion and $g(x)$ series

- Assume separable vortex-sheet strength in jet coordinates (ξ, η) :

$$\gamma_\xi = G(\xi)H(\eta), \quad \gamma_\eta = G(\xi)h(\eta)$$

with elliptical spanwise shape.

- Elliptic spanwise distribution:

$$h(\eta) = \sqrt{1 - (\eta/s_J)^2}, \quad H(\eta) = \frac{2}{s_J^2} \sqrt{1 - (\eta/s_J)^2}.$$

- Streamwise distribution $g(x) = G(\xi(x))$ represented by truncated series:

$$\frac{dg}{dx} = - \sum_{n=1}^{N-1} n C_n e^{-n\beta x/s_J} + C_N \frac{\ln(x/s_J)}{(x/s_J + 1)^{3/2}},$$

and the corresponding integrated form for $g(x)$ with the logarithmic singularity at $x \rightarrow 0$.

Jet-induced velocity kernels

- Define geometry between target point on wing $(x, 0, 0)$ and jet sheet point $(x', 0, f_J(x'))$:

$$dx = x - x', \quad dz = 0 - f_J(x'), \quad R^2 = dx^2 + dz^2.$$

- Elliptic-integral modulus and complementary modulus:

$$k_J^2 = \frac{s_J^2}{s_J^2 + R^2}, \quad k_{CJ}^2 = 1 - k_J^2,$$

complete elliptic integrals $K(k_J^2), E(k_J^2)$.

- Define kernel terms as:

$$T_{K-E} = k_J [K(k_J^2) - E(k_J^2)], \quad T_{E-K} = \frac{k_J}{k_{CJ}^2} [E(k_J^2) - k_{CJ}^2 K(k_J^2)].$$

- Jet-induced velocities at a wing point:

Streamwise induced velocity

$$u_{x,0,z} = u_{A,x,0,z} + \frac{1}{2} \sum_n C_n \int_0^\infty \frac{dg_n}{dx'} \left[k_y (K(k_y) - E(k_y)) + \frac{df_J}{dx'} z - f_J \frac{z}{k_{GJ}} (K - E) \right] dx'$$

Vertical induced velocity

$$w_{x,0,z} = w_{A,x,0,z} + \frac{1}{4\pi} \sum_n C_n \int_0^\infty \frac{dg_n}{dx'} \left[\frac{K(k) - E(k)}{k_{GJ}} + \frac{x - x'}{k} (E(k) - k^2 K(k)) \right] dx'. \quad (74)$$

The geometric parameters are defined as

$$k_J^2 = \frac{s_J^2}{s_J^2 + (x - x')^2 + (z - f_J)^2}, \quad k_{GJ}^2 = 1 - k_J^2, \quad (75)$$

where $K(k)$ and $E(k)$ denote the complete elliptic integrals of the first and second kind:

$K(k)$, $E(k)$ are complete elliptic integrals of the first and second kind.

The function $g(x)$ is expanded in terms of basis functions $g_n(x)$ as

$$g(x) = \sum_n C_n g_n(x), \quad (76)$$

with the final basis function chosen such that it contains the required logarithmic singularity at the jet origin.

Pressure Coefficient on Airfoil At each surface element,

$$\Delta C_p = -\frac{2}{U_\infty^2} \left[(U_\infty + u_J) \frac{\partial z}{\partial x} - w_J \right]. \quad (77)$$

Aerodynamic Load

Lift Coefficient

$$C_L = -\frac{2}{S_A} \int_{S_A} \Delta C_p \cos \alpha dS + C_J \int_{-s_J}^{s_J} c(y) \sin(\alpha + \tau) dy. \quad (78)$$

Drag Coefficient

$$C_D = -\frac{2}{S_A} \int_{S_A} \Delta C_p \sin \alpha dS - C_J \int_{-s_J}^{s_J} c(y) \cos(\alpha + \tau) dy. \quad (79)$$

Here S_A is platform area of airfoil. S_J is area of Jet.

The second term in both expressions represents the jet reaction thrust.

4.1.4 Results

The jet-flap configuration was evaluated for the following operating conditions:

- Jet momentum coefficient: $C_J = 0.0903$

- Angle of attack: $\alpha = 7^\circ$
- Jet deflection angle: $\tau = 20^\circ$

Using the thick-jet USB formulation and the numerical method described in the previous section, the solver produced the following aerodynamic coefficients.

Final Aerodynamic Coefficients

The converged (post-regularization) values obtained from the complete solution of the coupled wing-jet system are:

$$C_L = 4.4744$$

$$C_D = -0.1474$$

The computed lift coefficient is significantly augmented by the strong jet momentum and deflection, consistent with the expected behavior of a jet flap. The slightly negative drag coefficient arises from the jet-induced stream acceleration over the wing surface, which can generate a net forward thrust component in certain USB conditions. This is a known effect in strong jet-wing interaction and has been documented in classical jet-flap literature.

4.2 Upper Surface Blowing (Thick Jet)

4.2.1 Introduction

Thin jet flap theory under predicts the value of coefficient of lift due to the underlying assumption of wing-jet interactions. Hence, a more accurate model of thick jet is implemented based of the thick-jet theory of Lan & Campbell (NASA TN D-7936, 1975) and uses a discrete vortex-source panel representation identical to that implemented in the numerical code.

4.2.2 Assumptions

- Flow is inviscid, irrotational and subsonic
- Unperturbed jet flow is uniform
- Jet static pressure at jet exit and static pressure of outer flow are equal
- Wing is completely in the outer flow region

The present solver implements a linear, inviscid, irrotational, subsonic aerodynamic model for a wing interacting with an upper-surface-blown (USB) jet of finite thickness based of the

4.2.3 Mathematical Formulation

Boundary Conditions

Three sets of boundary conditions are enforced: wing flow tangency on the camber line, normal and tangential conditions on the jet sheets, and pressure continuity condition.

- **Wing Flow Tangency Condition**

On the camber line, the normal-flow boundary condition is

$$\frac{\partial \phi}{\partial n} = V_\infty \frac{dz_c}{dx} \cos \alpha - V_\infty \sin \alpha, \quad (80)$$

which enforces flow tangency to the camber-line geometry.

- **Pressure Continuity Condition**

The pressure continuity condition can be formulated by using Bernoulli's equation

$$p_j \left[1 + \frac{\gamma_j - 1}{2} \frac{\rho_j}{\gamma_j p_j} \left(\|\vec{V}_j\|^2 - \|\vec{V}_j + \vec{v}_j\|^2 \right) \right]^{\frac{\gamma_j}{\gamma_j - 1}} = p_o \left[1 + \frac{\gamma - 1}{2} \frac{\rho_o}{\gamma p_o} \left(\|\vec{V}_o\|^2 - \|\vec{V}_o + \vec{v}_o\|^2 \right) \right]^{\frac{\gamma}{\gamma - 1}} \quad (81)$$

Velocity is replaced by the potential function and is linearised and simplified into

$$\rho_j (\vec{V}_j \cdot \vec{e}) \frac{\partial \phi_j}{\partial s} \approx \rho_o (\vec{V}_o \cdot \vec{e}) \frac{\partial \phi_o}{\partial s} \quad (82)$$

- **Stream Surface Condition**

The slopes of streamlines on both sides of the jet surface are the same, that is,

$$\frac{\vec{n} \cdot (\vec{V}_o + \vec{v}_o)}{\vec{e} \cdot (\vec{V}_o + \vec{v}_o)} = \frac{\vec{n} \cdot (\vec{V}_j + \vec{v}_j)}{\vec{e} \cdot (\vec{V}_j + \vec{v}_j)} \quad (83)$$

Influence-Coefficient System To make the implementation tractable and modular, we assemble the jet–wing interaction in terms of *influence coefficient matrices*. We define:

- $[N_{WW}]$: normal–velocity influence of wing vortices on wing control points,
- $[N_{JW}]$: normal influence of wing vortices on jet control points,
- $[N_{WJ}]$: normal influence of jet vortices on wing control points,
- $[N_{JJ}]$: normal influence of jet vortices on jet control points,
- $[S_{JW}]$: tangential velocity influence of wing vortices on jet control points,
- $[S_{JJ}]$: tangential influence of jet vortices on jet control points.

Here, superscripts such as (o) and (j) will denote evaluation on the *outer* flow side and *jet* side respectively.

First, we compute the circulation on the wing in the absence of any jet, denoted γ_{wo} , by

enforcing zero normal velocity on the camber line:

$$[N_{WW}]\gamma_{wo} = -\vec{V}_\infty \cdot \vec{n}. \quad (84)$$

This gives the baseline wing circulation distribution purely due to the external flow.

To incorporate the effects of the jet, we solve for the additional circulations induced by jet-wing coupling:

$$[N_{JW}]^{(o)}\{\gamma_{wa}\} + [N_{JJ}]^{(o)}\{\gamma_{oj}\} - [N_{JJ}]^{(j)}\{\gamma_{jj}\} = \left\{ -\frac{\vec{V}_0 \cdot \vec{n}(1 - \mu')}{\vec{V}_0 \cdot \vec{e}} + \frac{\partial \bar{\phi}_{wj}}{\partial n} \right\}, \quad (85)$$

$$-T(\mu')^2[S_{JW}]^{(o)}\{\gamma_{wa}\} - T(\mu')^2[S_{JJ}]^{(o)}\{\gamma_{oj}\} + [S_{JJ}]^{(j)}\{\gamma_{jj}\} = \left\{ -\frac{\partial \bar{\phi}_{wj}}{\partial s} \right\} + T(\mu')^2 \frac{\partial \bar{\phi}_{wo}}{\partial s}, \quad (86)$$

$$[N_{WW}]\{\gamma_{wa}\} + [N_{WJ}]^{(o)}\{\gamma_{oj}\} = \left\{ -\frac{\vec{v}_{je} \cdot \vec{k}}{V_\infty \cos \alpha} \right\}. \quad (87)$$

The three blocks above come from pressure continuity, stream-surface conditions, and the wing tangency condition in the presence of the jet.

Equations (85)–(87) are assembled into a single augmented linear system

$$A\mathbf{x} = \mathbf{b}, \quad (88)$$

where the unknown vector contains

$$\mathbf{x} = \{\gamma_{wa}, \gamma_{oj}, \gamma_{jj}\},$$

corresponding to the additional wing circulation due to the jet, the outer-side jet circulation, and the inner-side jet circulation. Solving

$$\mathbf{x} = A^{-1}\mathbf{b}$$

(or in practice a regularized least-squares solution) yields γ_{wa} , γ_{oj} and γ_{jj} .

The total wing circulation including jet-induced perturbations is

$$\gamma_w(x) = \gamma_{wo}(x) + \gamma_{wa}(x). \quad (89)$$

Aerodynamic Coefficients From the total circulation distribution $\gamma_w(x)$, the lift and induced drag coefficients are obtained as

$$C_l = \frac{2 \cos \alpha}{c} \int_0^c \gamma_w(x) \cos[\alpha - \bar{\theta}(x)] dx + c_t \sin(\alpha - \bar{\theta}_{LE}), \quad (90)$$

$$C_{d,i} = \frac{2 \cos \alpha}{c} \int_0^c \gamma_w(x) \sin[\alpha - \bar{\theta}(x)] dx - c_t \cos(\alpha - \bar{\theta}_{LE}), \quad (91)$$

where:

- c_t is the leading-edge thrust coefficient,
- $\bar{\theta}(x)$ is the slope of the camber line at position x ,
- $\bar{\theta}_{LE}$ is the camber-line slope at the leading edge.

The leading-edge thrust coefficient is given by

$$c_t = \frac{\pi}{2} \frac{1}{\cos \Lambda_{LE}} \sqrt{1 - M_o^2 \cos^2 \Lambda_{LE} C^2}, \quad (92)$$

where Λ_{LE} is the leading-edge sweep angle and M_o is the freestream Mach number. For a rectangular wing, we have

$$\Lambda_{LE} = 0, \quad \beta = \sqrt{1 - M_o^2}.$$

The leading-edge suction parameter C is decomposed as

$$C = C_1 + C_2,$$

with

$$NC_1 \sqrt{\tan^2 \Lambda_{LE} + \beta^2} = [N_{WW}]_i \{\gamma_{wo}\} - \left\{ \frac{\partial z_c}{\partial x} - \tan \alpha \right\}_i, \quad (93)$$

$$NC_2 \sqrt{\tan^2 \Lambda_{LE} + \beta^2} = [N_{WW}]i \{\gamma_{wa}\} + [N_{WJ}]_{(o),i} \{\gamma_{oj}\} - \left\{ \frac{\vec{v}_{je} \cdot \vec{k}}{V_\infty \cos \alpha} \right\}_i, \quad (94)$$

where N is the number of control points along the leading edge, and the subscript i indicates evaluation at leading-edge control points. The terms involving γ_{wo} and γ_{wa} correspond respectively to the baseline and jet-perturbed wing circulations, while the jet contribution enters through the $[N_{WJ}]$ term and the explicit jet exit velocity component.

4.2.4 Implementation

Flow Model

Two flow regions exist:

- Outer flow with velocity \mathbf{V}_o , density ρ_o and Mach number M_o .

- Jet flow with velocity \mathbf{V}_j , density ρ_j and Mach number M_j .

Both outer and jet perturbation potentials satisfy Laplace's equation:

$$\nabla^2 \phi_o = 0, \quad \nabla^2 \phi_j = 0. \quad (95)$$

Each potential is decomposed into wing-alone and jet-induced components:

$$\phi_o = \Phi_{wo} + \Phi_{ao}, \quad \phi_j = \Phi_{wj} + \Phi_{aj}, \quad (96)$$

following the additive structure given in [Lan75a],.

Boundary Conditions:

- **Wing Flow-Tangency Condition**

On the camber surface of the wing,

$$(\mathbf{V}_o + \nabla \phi_o) \cdot \mathbf{n} = 0, \quad (97)$$

where \mathbf{n} is the outward unit normal.

After discretization into N_a camber-line panels, the numerical system is:

$$\begin{aligned} & \sum_{j=1}^{N_a} \gamma_j (\mathbf{u}_{ij} \cdot \mathbf{n}_i) + \sum_{k=1}^{N_{jt}} \left[\gamma_k^t (\mathbf{u}_{ik}^t \cdot \mathbf{n}_i) + \sigma_k^t (\mathbf{u}_{ik}^{t,s} \cdot \mathbf{n}_i) \right] \\ & + \sum_{k=1}^{N_{jb}} \left[\gamma_k^b (\mathbf{u}_{ik}^b \cdot \mathbf{n}_i) + \sigma_k^b (\mathbf{u}_{ik}^{b,s} \cdot \mathbf{n}_i) \right] = -\mathbf{V}_o \cdot \mathbf{n}_i, \end{aligned} \quad (98)$$

which is implemented in the matrix assembly routine of the solver.

- **Jet Normal-Velocity Continuity**

The jet surface is a streamline surface. The linearized normal-velocity continuity condition (Lan, eq. 6) is

$$(\mathbf{V}_j + \nabla \phi_j) \cdot \mathbf{n} - (\mathbf{V}_o + \nabla \phi_o) \cdot \mathbf{n} = (1 - \mu) (\mathbf{V}_o \cdot \mathbf{n}), \quad \mu = \frac{V_o}{V_j}. \quad (99)$$

Discrete form for top/bottom jet sheets:

$$\sigma_i + (1 - \mu) \sum_j (\mathbf{u}_{ij} \cdot \mathbf{n}_i) = -(1 - \mu) (\mathbf{V}_o \cdot \mathbf{n}_i). \quad (100)$$

- **Jet Tangential-Velocity Continuity**

Pressure continuity (linearized Bernoulli, Lan eq. 8) yields

$$(\mathbf{V}_j + \nabla\phi_j) \cdot \mathbf{t} = (\mathbf{V}_o + \nabla\phi_o) \cdot \mathbf{t}, \quad (101)$$

which becomes in linear form:

$$\gamma_i + (1 - K_p) \sum_j (\mathbf{u}_{ij} \cdot \mathbf{t}_i) = -(1 - K_p) (\mathbf{V}_0 \cdot \mathbf{t}_i), \quad K_p = \frac{\rho_0 V_0}{\rho_j V_j}. \quad (102)$$

This corresponds exactly to the solver implementation: `factor_tan = (1 - K_p)`.

- **Trailing-Edge Kutta Condition**

For the two camber-line end panels,

$$\gamma_1 + \gamma_{N_a} = 0, \quad (103)$$

ensuring finite velocity at the trailing edge.

Panel Influence Functions

Each straight panel with endpoints $\mathbf{p}_1, \mathbf{p}_2$ produces a velocity at a target point using classical vortex-source influence functions:

$$u_\sigma = \frac{\sigma}{2\pi} \left[\frac{1}{2} \ln \left(\frac{r_2^2}{r_1^2} \right) \right], \quad w_\sigma = \frac{\sigma}{2\pi} (\theta_2 - \theta_1), \quad (104)$$

$$u_\gamma = -\frac{\gamma}{2\pi} (\theta_2 - \theta_1), \quad w_\gamma = \frac{\gamma}{2\pi} \left[\frac{1}{2} \ln \left(\frac{r_2^2}{r_1^2} \right) \right], \quad (105)$$

where $r_1, r_2, \theta_1, \theta_2$ are the standard geometric quantities associated with the projection of the target point onto the panel's local coordinates.

These expressions are implemented exactly in `induced_panel_velocity_mm()`.

Solution of the Linear System

All boundary conditions are assembled into a global linear system

$$\mathbf{Ax} = \mathbf{b}, \quad (106)$$

with unknown vector

$$\mathbf{x} = \begin{bmatrix} \gamma_{\text{airfoil}} \\ \gamma_{\text{jet,top}} \\ \sigma_{\text{jet,top}} \\ \gamma_{\text{jet,bottom}} \\ \sigma_{\text{jet,bottom}} \end{bmatrix}. \quad (107)$$

A Tikhonov-regularized least-squares solution is used:

$$\min_{\mathbf{x}} \|\mathbf{Ax} - \mathbf{b}\|^2 + \lambda \|\mathbf{x}\|^2, \quad (108)$$

implemented through the augmented matrix:

$$\mathbf{A}_{\text{aug}} = \begin{bmatrix} \mathbf{A} \\ \sqrt{\lambda} \mathbf{I} \end{bmatrix}, \quad \mathbf{b}_{\text{aug}} = \begin{bmatrix} \mathbf{b} \\ \mathbf{0} \end{bmatrix}.$$

4.2.5 Lift and Circulation

The sectional circulation is obtained by

$$\Gamma = \sum_{i=1}^{N_a} \gamma_i \Delta s_i. \quad (109)$$

The circulation lift per unit span is

$$L' = \rho_0 V_0 \Gamma, \quad (110)$$

and the sectional lift coefficient is

$$C_{L,\text{circ}} = \frac{L'}{q_\infty c} = \frac{2\Gamma}{V_0 c}, \quad q_\infty = \frac{1}{2} \rho_0 V_0^2. \quad (111)$$

Jet-Reaction Lift

For a jet deflected by angle θ_j relative to the free stream, the reaction (momentum) lift is

$$C_{L,\text{jet}} = \frac{\dot{m} V_j}{q_\infty c} \sin \theta_j. \quad (112)$$

Total Lift

$$C_L = C_{L,\text{circ}} + C_{L,\text{jet}}. \quad (113)$$

This is the total lift coefficient reported by the solver.

Results have been obtained for the following conditions

1. Wing has rectangular planform
2. Since the model assumes that the wing is outside the jet stream, the thickness of the jet which lies above the chord is only being taken which is 86 mm.
3. Jet vortex sheet starts from the 18.74% of the chord length as per the EDF placement
4. Jet vortex sheet is parallel to the chord line of the airfoil till the LE of the flap (70% of the chord)
5. After the LE of the flap, the jet angle is taken to be same as the flap deflection.

6. The density of the jet stream is assumed to be the same as the freestream due to the low Mach number of both. This density is equal to 1.225 kg/m^3 at takeoff and 0.905 kg/m^3 at cruise.
7. Jet entrained velocity is taken to be zero

4.2.6 Results

Rotor–Stator Performance Summary

This section summarizes the rotor–stator performance used to define jets conditions at the nozzle plane, for three operating regimes.

Design Point: Takeoff (20 m/s, Sea Level)

Quantity	Value
Shaft power P_0	1046 W
Induced velocity v_i	21.839 m/s
Disc speed V_2	41.839 m/s
Jet speed V_4	63.679 m/s
Mass flow \dot{m}	0.572 kg/s
Thrust	25 N

Static (0 m/s, Sea Level)

Quantity	Value
Thrust	31.050 N
Mass flow	0.461 kg/s
Jet speed	67.375 m/s
Disc speed	33.688 m/s

Cruise (80 m/s, 10,000 ft)

Quantity	Value
Density	0.9049 kg/m^3
Thrust	12.042 N
Mass flow	0.878 kg/s
Jet speed	93.720 m/s
Disc speed	86.860 m/s

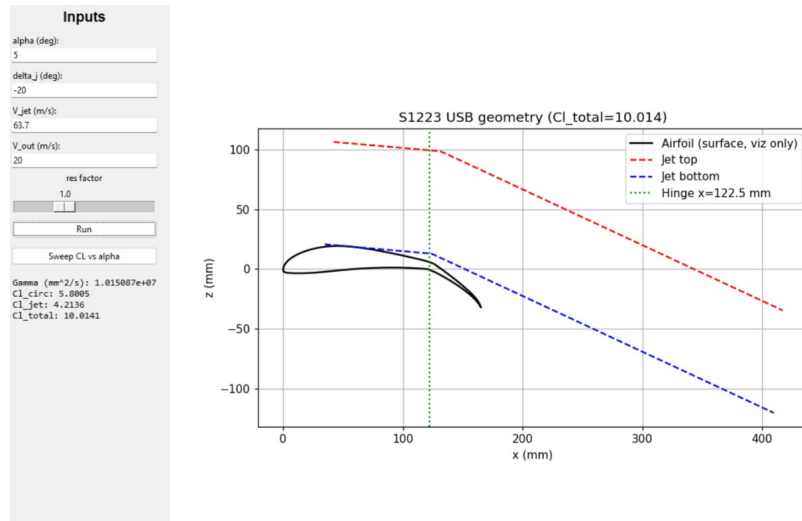


Figure 81: Angle of Attack = 5

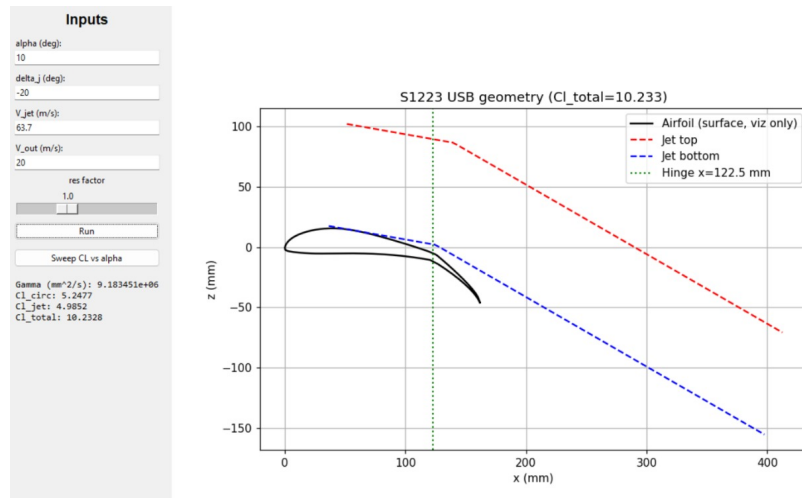


Figure 82: Angle of Attack = 10

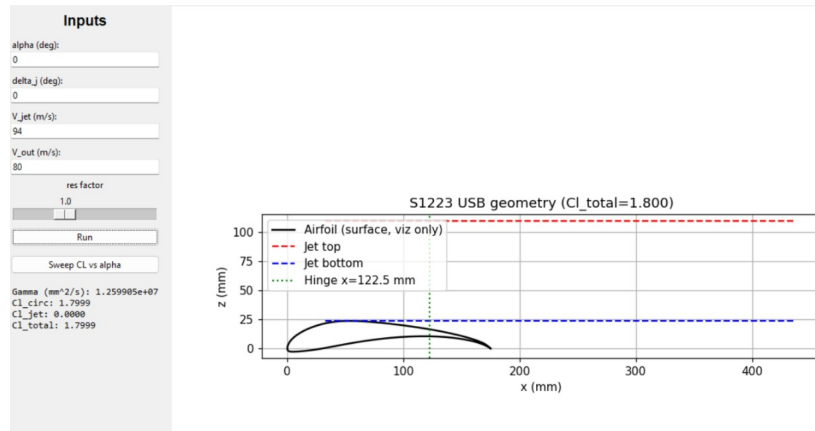


Figure 83: Cruise at 0 Angle Of Attack

Table 19: Aerodynamic Results for Various Jet and Free-Stream Conditions

α (deg)	Δ_J (deg)	V_{jet} (m/s)	V_∞ (m/s)	Res.	Γ (m^2/s)	$C_{L,\text{circ}}$	$C_{L,\text{jet}}$	C_L
-2	0	40	40	1	5.416	1.5476	-0.0343	1.5133
0	0	40	40	1	5.385	1.5387	0	1.5387
8	0	40	40	1	5.1958	1.4845	0.1368	1.6213
15	0	40	40	1	4.946	1.4134	0.2544	1.6678
18	0	40	40	1	4.817	1.376	0.3037	1.6797
-2	0	20	20	1	5.416	1.5476	-0.0343	1.5133
0	0	20	20	1	5.385	1.5387	0	1.5387
8	0	20	20	1	5.1958	1.4845	0.1368	1.6213
15	0	20	20	1	4.946	1.4134	0.2544	1.6678
18	0	20	20	1	4.817	1.376	0.3037	1.6797

Table 20: Takeoff and Cruise Conditions

Takeoff Condition								
V	α	Re	q	M	C_L	C_D	C_m	L/D
5	-20	63.7	20	1	10.15	5.8005	4.2136	10.0141
10	-20	63.7	20	1	9.1834	5.2477	4.9852	10.2329
Cruise Condition								
V	α	Re	q	M	C_L	C_D	C_m	L/D
0	0	94	80	1	12.599	1.7999	0	1.7999

4.3 CFD Simulations - Upper Surface Blowing with Flaps

4.3.1 Mesh Independence

To get results independent of the mesh size, we varied different mesh parameters and observed the results obtained, which are tabulated below.

Sl. No.	No. of Elements	Lift (N)	Drag (N)
1	90507	408.03	122.96
2	155219	409.72	122.73
3	310119	408.86	123.64

Table 21: Mesh independence study results for upper surface blowing

The parameters in Sr. No. 3 were determined to be optimal for mesh independence. The final mesh settings are stated in the following subsection.

4.3.2 Final Mesh Settings

A rectangular bounding box with dimensions of length of 25c and width of 10c was constructed. The airfoil is at a distance of 10c from the left edge. The mesh is quadrilateral, with the following parameters:

Parameter	Dimension	Inflation
Global settings	10 mm	Max angle 180°
Capture Curvature Min Size	0.1 mm	Nil
Capture Proximity Min Size	0.1 mm	Nil
Proximity Gap Factor	6	Nil
Mesh Defeaturing Min Size	0.1 mm	Nil
Wing	Edge sizing = 0.5 mm	First layer thickness = 0.02 mm, 25 layers
Duct boundaries	Edge sizing = 1.5 mm	First layer thickness = 0.02 mm, 25 layers

Table 22: Meshing parameters for upper surface blowing - CFD setup

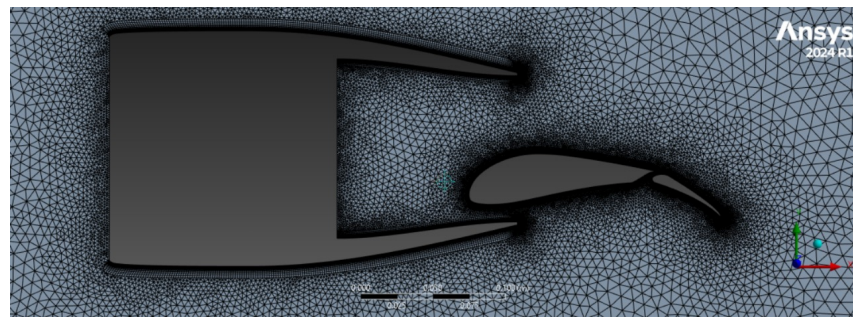


Figure 84: Mesh for USB

Stair stepping of inflation layers was enabled when layer compression yielded a poor mesh. All triangles method was used to mesh complex geometry quicker and with smaller elements.

4.3.3 Set-Up

The jet velocity from the TPD is actually 63.679 m/s. Since this value is measured at the plane at the end of the duct, which is past the leading edge of the wing, we corrected this value to 42.272 m/s, calculated at a specific plane in front of the leading edge (as seen in the figure), according to continuity equation.

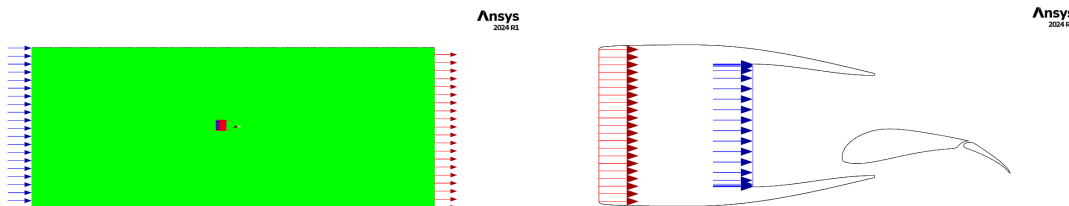


Figure 85: Setup for USB

We used the $k-\omega$ SST turbulence model, as it is a low-Reynolds number model that can accurately model boundary layer phenomenon and gives better lift results.

In cruise condition, it was noticed that velocities go past Mach 0.3. For this reason, compressible flow was used by modelling air density using ideal gas and air viscosity using

Boundary	Type	Value
Inlet	Velocity Inlet	20 m/s
Outlet	Pressure Outlet	0 Pa (gauge)
Duct Outlet	Mass Flow Rate Outlet	0.572 kg/s
Duct Inlet	Velocity Inlet	42.272 m/s
Wing	Stationary Wall	No slip
Duct Boundary	Stationary Wall	No slip

Table 23: Boundary conditions for upper surface blowing - CFD setup

the temperature-dependent Sutherland model. The energy equation was also turned on. Values at 10,000 ft were used (atmospheric pressure of 69,000 Pa, 0.905 kg/m³, and temperature 268 K).

4.3.4 Determination of the height of the thrust producing device

Simulations were performed to determine the optimal height of the thrust producing device. The height of the thrust producing device was varied with the airfoil with flap deflected at 20 degrees.

The optimal height of the central line of the jet was determined to be 32.11 mm above the leading edge of the airfoil. The results of these simulations are given in the table below

Height of TPD (mm)	Lift (N)	Drag (N)	CL	CD	L/D
32.11	404.1	118.9	9.43	2.77	3.40
37.11	409.52	113.9	9.55	2.66	3.60
12.11	327.54	131.45	7.64	3.07	2.49
2.11	296.96	130.48	6.93	3.04	2.28
22.11	382.57	131.28	8.92	3.06	2.91
92.11	80.77	3.84	1.88	0.09	21.03
-22.11	-73.26	157.93	-1.71	3.68	-0.46

Table 24: Aerodynamic coefficients and forces at various TPD heights.

32.11 mm was taken as the chosen height, even though higher lift was obtained with a height of 37.11 mm, because in the latter case the bottom of the duct was too close to the airfoil. The velocity contour obtained from the simulation is given below.

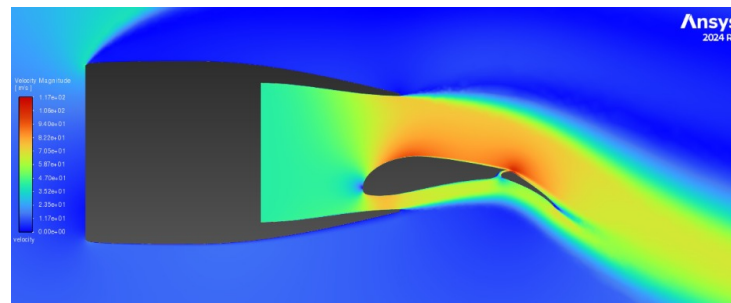


Figure 86: Velocity contour for TPD at 32.11 mm height

4.3.5 Shape optimisation of the main element trailing edge

The trailing edge of the main element of the airfoil developed a stagnation point. The shape of the trailing edge was thus altered to optimise the lift produced. The simulations were run with the flaps in retracted position at zero angle of attack, to simulate cruise conditions i.e 80 m/s freestream velocity.

Version	Lift (N)	Drag (N)	CL	CD	L/D
v1	963.25	273.55	1.40	0.40	3.52
v2	1043.80	257.05	1.52	0.37	4.06
v3	1023.78	263.95	1.49	0.38	3.88

Table 25: Shape Optimisation Results

The second shape was chosen as it gave highest lift and aerodynamic efficiency. The velocity contours for all the shapes is given in the figures below.

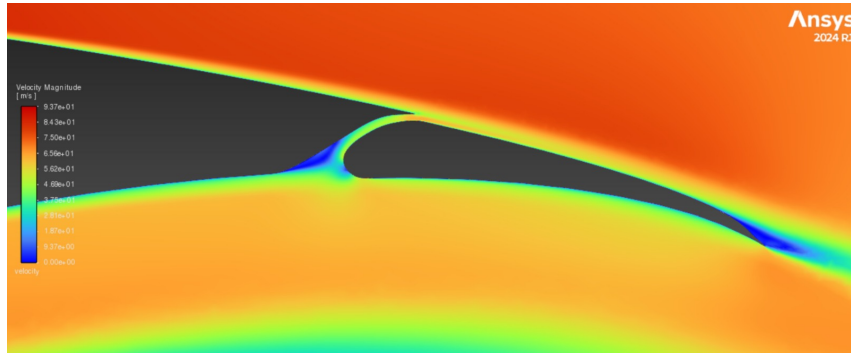


Figure 87: Velocity contour for main element trailing edge shape 1

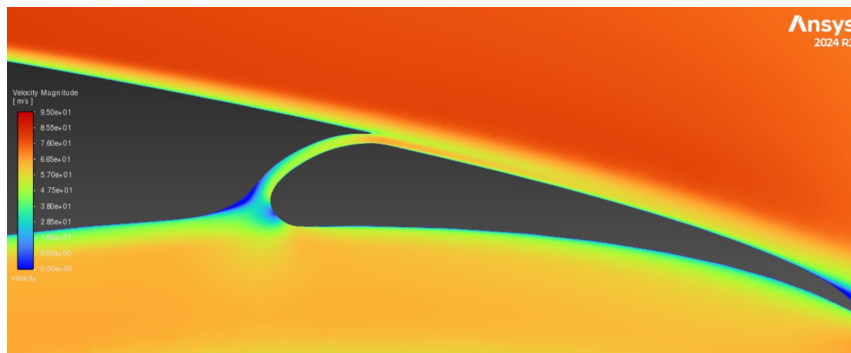


Figure 88: Velocity contour for main element trailing edge shape 2

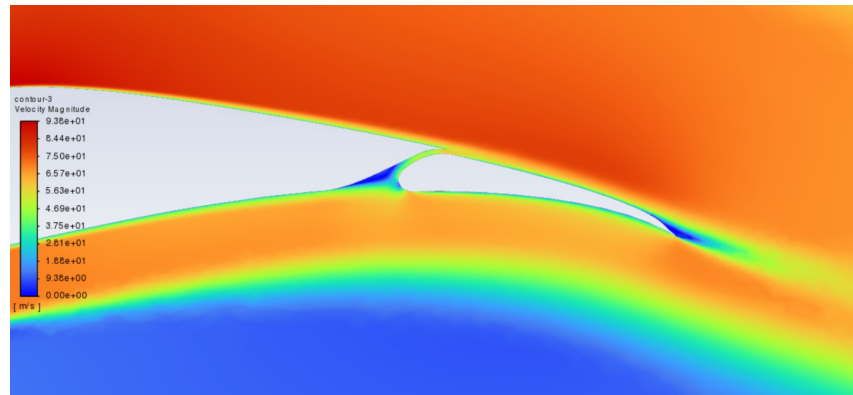


Figure 89: Velocity contour for main element trailing edge shape 3

The overall velocity contour for the selected shape is given in the figure below

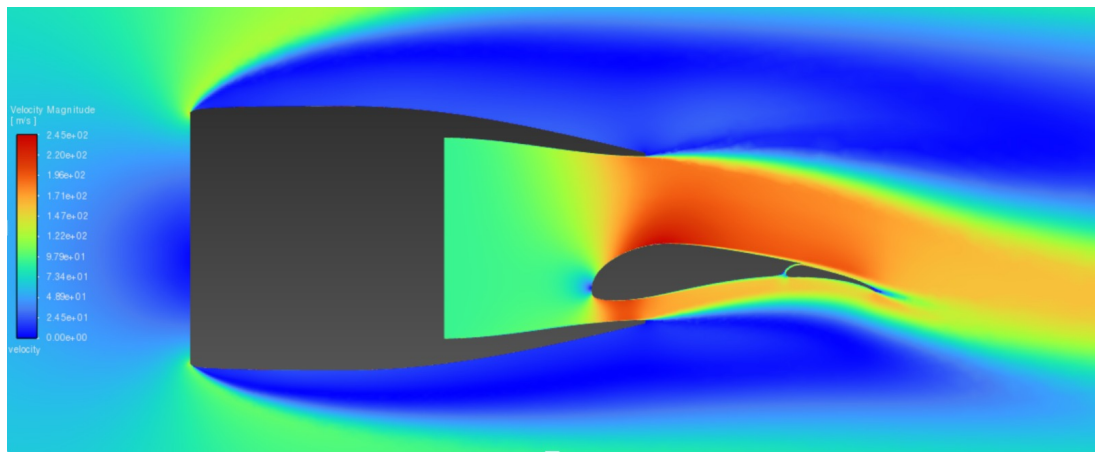


Figure 90: Velocity contour with USB at cruise

4.3.6 Determination of the optimal flap deflection angle

Simulations performed at take-off conditions, i.e. 20 m/s freestream velocity, with flap deflected at different angles. Different hinge positions of the flaps along with the deflection angles were varied, for very high flap deflections (around 45 degrees) the flow was seen to almost always separate. For smaller deflections, it depended on the position of the hinge. For a deflection of 20 degrees, the flow was seen to be mostly attached for all the varied hinge locations, moreover the lifts obtained were also higher, owing to the attached flow. Thus the flap deflection angle for take-off was taken to be 20 degrees. The results of the simulations are given in the table below

The velocity contours obtained with USB and flap deflected at 20 degrees is given below.

Flap Deflection Angle (°)	Flap Position	Lift (N)	Drag (N)	CL	CD	L/D
15	(7, -1.5)	363.49	97.17	8.48	2.27	3.74
15	(4.7, -2.7)	370.33	97.44	8.64	2.27	3.80
19	(7, -1.5)	232	74	5.41	1.73	3.14
19	(6, -2.7)	407	123	9.49	2.87	3.31
20	(5.75, -2.66)	407.8	123.77	9.51	2.89	3.29
25	(5.6, -3.1)	326.55	98.45	7.62	2.30	3.32
25	(7.8, -5)	303.78	111.9	7.09	2.61	2.71
25	(5.8, -2.7)	438.96	153.66	10.24	3.58	2.86
30	(3.5, 1.5)	309.18	101.42	7.21	2.37	3.05
45	(4.7, 2.1)	307.05	117.59	7.16	2.74	2.61

Table 26: Effect of Flap Deflection Angle and Position on Aerodynamic Coefficients

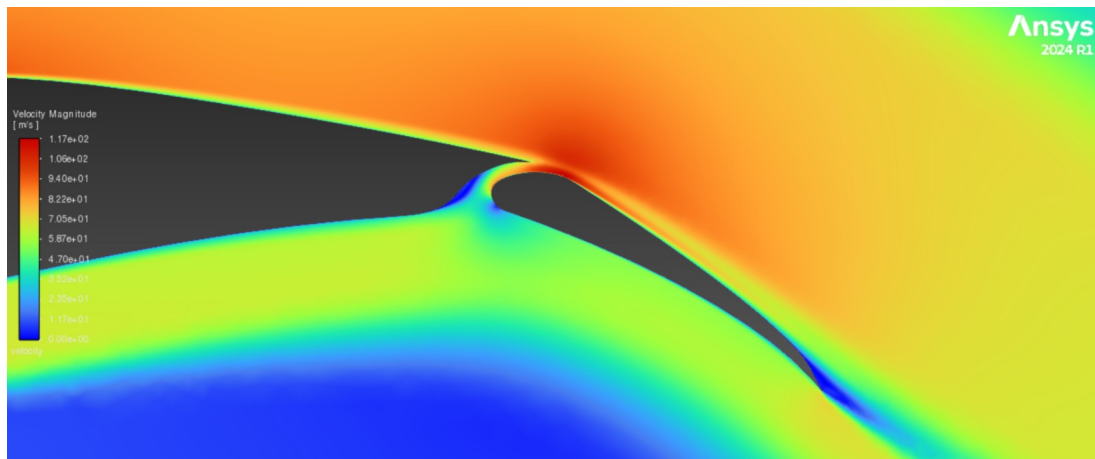


Figure 91: Velocity contour with USB and optimal flap configuration (zoomed in)

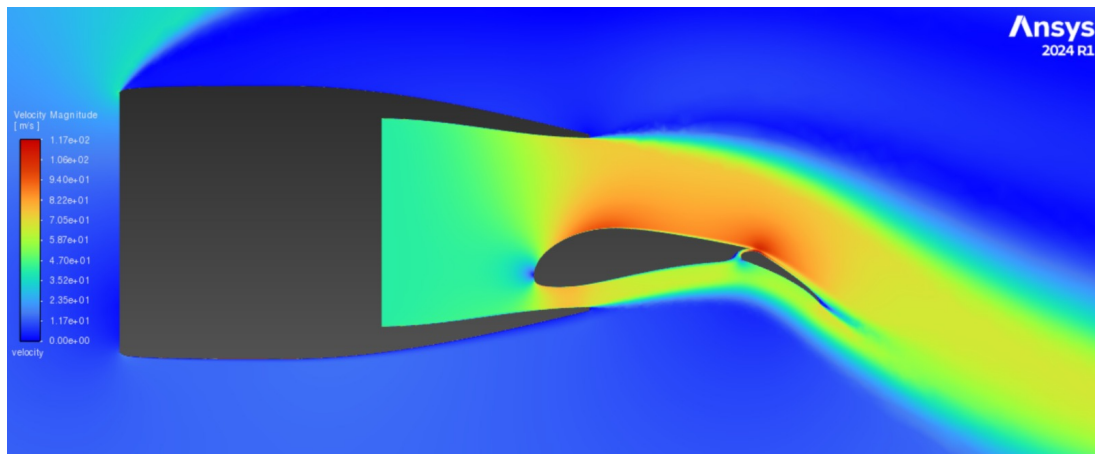


Figure 92: Velocity contour with USB and optimal flap configuration

5 RL Optimization of Airfoils for Co-Flow Jets

As discussed in the mathematical model before, airfoil shape optimization is formulated as a PDE-constrained optimization problem, where the objective is to maximize a perfor-

mance metric such as lift-to-drag ratio L/D of C_L subject to aerodynamic and geometric constraints. Traditional methods rely on gradient-based optimization in a low-dimensional parameter space (e.g. Kulfan or B-spline control points) and testing with an aerodynamic solver such as XFOIL. We also have expert designed airfoils, which are usually either found through massive experimental testing or the above methods. **s1223**, **dae11** are well known expert designed high lift airfoils.

Dussauge et al. s proposed an alternative approach based on reinforcement learning (RL), where a policy learns to iteratively modify an airfoil parameterization, using XFOIL as a black-box evaluator. This decouples optimization from analytic gradients and allows, in principle, non-smooth objectives and discrete design changes. As we see from their results, they manage to obtain an airfoil with a very high $\frac{L}{D}$ of roughly 178, and also show the superiority to the traditional simplex. However, pure XFOIL-based RL is computationally expensive, and does not straightforwardly incorporate more complex devices such as flaps, upper surface blowing (USB), and co-flow jets (CFJ), which are known to improve lift.

This means that optimizing over these would then require complete CFD simulations, which are extremely computationally expensive. In this work we come up with a complete pipeline that starts from the Dussauge-style RL formulation and extends it progressively as such:

1. We reproduce the basic idea of RL for airfoil optimization (XFOIL-based evaluation only)
2. We replace XFOIL with NeuralFoil in the loop, leading to three orders of magnitude speed-up in training
3. We extend the RL environment to include trailing-edge flap deflection as an additional continuous control
4. We propose FastFOIL: the original XFOIL source code modified to support co-flow jet modeling and a CFJ-capable graphical interface, and we construct a combined RL environment that optimizes geometry, CFJ slot positions, and flap deflection all at once, under realistic physical and structural constraints

We compare our RL pipeline against AeroSandbox’s gradient-based parameter search and highlight the advantages of RL in terms of exploration, non-convexity handling, and flexibility. We then conclude by presenting quantitative results from NeuralFoil and CFJ XFOIL evaluations, including a fair comparison against a parameter search baseline and literature airfoils (expert designs). Empirically, our RL framework attains L/D values close to that of **s1223**, with a slightly better (lower) C_D at similar operating conditions.

6 Background: RL-Based Airfoil Optimization à la Dussauge et al.

6.1 Airfoil parameterization

Dussauge et al. parameterize the airfoil geometry by a small vector of thickness and camber control points along the chord, typically using either B-splines or Bernstein polynomials (Kulfan/CST). Let

$$\boldsymbol{\theta} = (\mathbf{t}, \mathbf{c}) \in \mathbb{R}^{2n}$$

denote the concatenated vector of thickness control values $\mathbf{t} \in \mathbb{R}^n$ and camber control values $\mathbf{c} \in \mathbb{R}^n$, defined at chordwise stations $x_i \in [0, 1]$, $i = 1, \dots, n$. The upper and lower surfaces are then given by

$$y_u(x) = c(x) + \frac{1}{2}t(x), \quad (114)$$

$$y_\ell(x) = c(x) - \frac{1}{2}t(x), \quad (115)$$

where $t(x)$ and $c(x)$ are obtained by interpolating the control points using a smooth basis, e.g.

$$t(x) = \sum_{i=1}^n t_i B_i(x), \quad c(x) = \sum_{i=1}^n c_i B_i(x),$$

with $B_i(x)$ Bernstein or B-spline basis functions.

6.2 MDP formulation

The airfoil optimization problem is cast as a Markov Decision Process (MDP):

- **State** s_t : the current airfoil geometry, represented either by the control vector $\boldsymbol{\theta}_t$ or by sampled surface coordinates $(x_i, y_{u,i}, y_{\ell,i})$.
- **Action** a_t : a small increment in the control space,

$$a_t = \Delta \boldsymbol{\theta}_t \in \mathbb{R}^{2n},$$

which modifies thickness and camber at the control points.

- **Transition**: deterministic update

$$\boldsymbol{\theta}_{t+1} = f(\boldsymbol{\theta}_t, a_t) = \boldsymbol{\theta}_t + a_t$$

(with clipping and smoothing).

- **Reward** r_t : improvement in aerodynamic performance as measured by XFOIL at a

fixed operating condition,

$$r_t = J(\boldsymbol{\theta}_{t+1}) - J(\boldsymbol{\theta}_t), \quad J(\boldsymbol{\theta}) = \frac{C_L(\boldsymbol{\theta})}{C_D(\boldsymbol{\theta})},$$

where C_L and C_D are lift and drag coefficients from XFOIL.

- **Termination:** after a fixed horizon T or if some geometric/aerodynamic constraint is violated.

The RL agent (PPO, which is SOTA) learns a policy $\pi_\phi(a_t | s_t)$ that maximizes the expected return

$$\mathbb{E} \left[\sum_{t=0}^{T-1} \gamma^t r_t \right],$$

where γ is a discount factor. This is a “black-box” optimization of $\boldsymbol{\theta}$ that does not rely on gradients of C_L or C_D with respect to the shape parameters.

6.3 Results

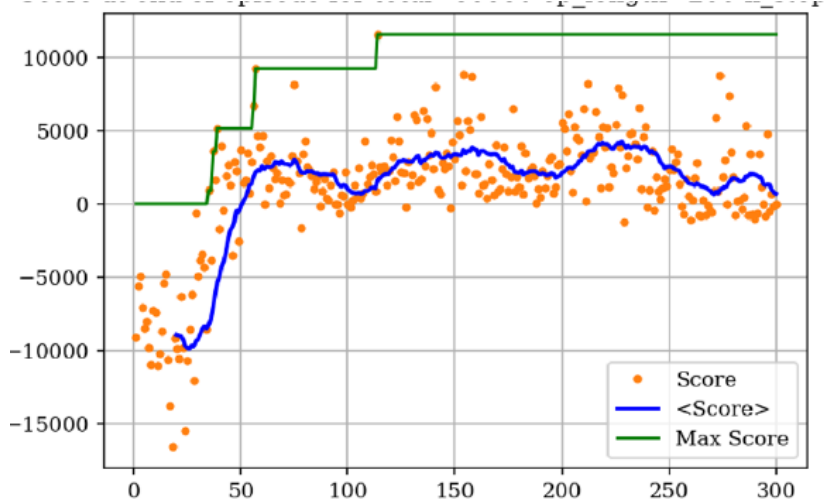


Figure 93: Return over episodes

They achieve a maximum of $\frac{L}{D} \approx 178$. The following is the airfoil that achieves this:

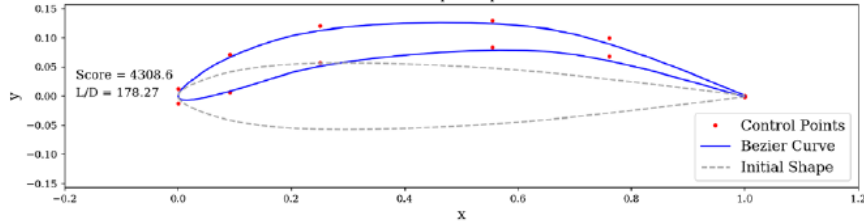


Figure 94: Airfoil with highest $\frac{L}{D}$

6.4 Limitations

The Dussauge et al. setup is conceptually elegant, but we note two practical limitations:

1. **XFOIL in the loop is expensive** Although XFOIL takes only few tens of milliseconds, millions of XFOIL calls are required for training, and this becomes a bottleneck
2. **Extension to flaps and CFJ is nontrivial.** Their environment is primarily designed for pure airfoil shape changes, without control surfaces or active flow control

Our work addresses both issues by replacing XFOIL with NeuralFoil where appropriate and by building custom CFJ-enabled XFOIL and RL environments.

7 NeuralFoil-Based RL for Airfoil Shape Optimization

We first re-implement a Dussauge-style airfoil RL environment, but evaluate aerodynamics with NeuralFoil rather than XFOIL

7.1 Environment definition

We follow the tradition gymnasium style environment setup as below:

State representation We fix n control points along the chord, with coordinates

$$x_i = \frac{i}{n-1}, \quad i = 0, \dots, n-1.$$

The environment stores thickness and camber vectors $\mathbf{t}, \mathbf{c} \in \mathbb{R}^n$. The observation at step k is a flattened vector of geometry,

$$s_k = [x_0, \dots, x_{n-1}, y_{u,0}, \dots, y_{u,n-1}, y_{\ell,0}, \dots, y_{\ell,n-1}] \in \mathbb{R}^{3n}$$

where

$$y_{u,i} = c_i + \frac{1}{2}t_i, \quad y_{\ell,i} = c_i - \frac{1}{2}t_i.$$

Action space The action is a continuous vector

$$a_k = [\Delta t_0, \dots, \Delta t_{n-1}, \Delta c_0, \dots, \Delta c_{n-1}] \in \mathbb{R}^{2n}$$

with bounded components:

$$\Delta t_i \in [-\Delta t_{\max}, \Delta t_{\max}], \quad \Delta c_i \in [-\Delta c_{\max}, \Delta c_{\max}].$$

The update rule in `step` is multiplicative for thickness and additive for camber:

$$t_i^{(k+1)} = t_i^{(k)} (1 + \alpha_i), \quad \alpha_i = \Delta t_i, \tag{116}$$

$$c_i^{(k+1)} = c_i^{(k)} + \Delta c_i. \tag{117}$$

Thickness and camber are then smoothed via a simple three-point kernel (see `_smooth_array` in the codebase) and clipped to physically plausible ranges.

Aerodynamic evaluation via NeuralFoil: Given the control values \mathbf{t}, \mathbf{c} , we construct a dense set of surface coordinates using a precomputed Bernstein basis $B \in \mathbb{R}^{n_{\text{surf}} \times n}$:

$$\tilde{\mathbf{t}} = B\mathbf{t}, \quad (118)$$

$$\tilde{\mathbf{c}} = B\mathbf{c}, \quad (119)$$

and then

$$y_u(x_j) = \tilde{c}_j + \frac{1}{2}\tilde{t}_j, \quad (120)$$

$$y_\ell(x_j) = \tilde{c}_j - \frac{1}{2}\tilde{t}_j. \quad (121)$$

We finally build coordinates (x, y) that go from trailing edge over the upper surface to the leading edge and back along the lower surface to the trailing edge. These coordinates are passed to NeuralFoil yielding approximate (C_L, C_D, C_M) .

Reward function. The reward is incremental in L/D , similar to Dussauge, with a quadratic action penalty and mild thickness penalty:

$$L/D = \frac{C_L}{C_D}, \quad (122)$$

$$r_k = \left(\frac{C_L}{C_D} - \frac{C_L}{C_D} \Big|_{\text{prev}} \right) - \lambda_a \|a_k\|_2^2 - \lambda_t \max(0, t_{\text{max}} - t_{\text{thresh}})^2, \quad (123)$$

where λ_a is small (e.g. 0.01) and t_{max} is the maximum thickness. This encourages progressive improvements in L/D while discouraging large, oscillatory actions and overly thick airfoils.

7.2 Advantages of NeuralFoil over XFOIL in RL

Replacing XFOIL with NeuralFoil yields several advantages:

- **Speed:** NeuralFoil inference is orders of magnitude faster than running XFOIL, especially in the inner loop of RL, where hundreds of thousands of calls are common.
- **Stability:** NeuralFoil predictions are continuous and free from convergence failures that can occur in XFOIL for separated or odd geometries; this reduces noisy rewards.

7.3 Results

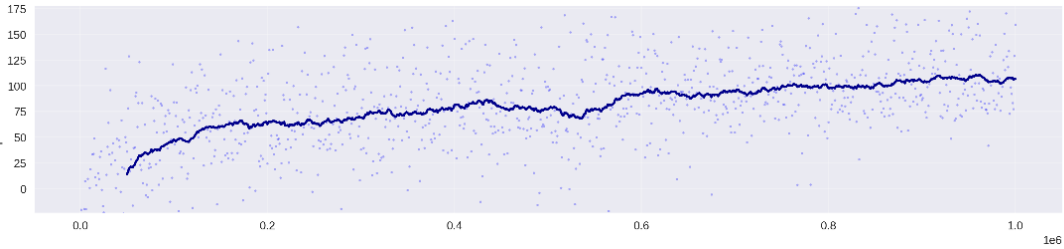


Figure 95: Training metrics with NeuralFoil



Figure 96: Optimized airfoil with $\frac{L}{D} = 147.27$

We see steady improvement over 1 million steps, and achieve similar results to Dussauge, but with three orders of magnitude faster training.

8 Extending RL to Trailing-Edge Flaps

Next, we extend the NeuralFoil-based RL environment to include a trailing-edge flap. This adds a control variable and a simple kinematic model of flap deflection.

8.1 Action and state augmentation

Now the action vector is

$$a_k = [\Delta t_0, \dots, \Delta t_{n-1}, \Delta c_0, \dots, \Delta c_{n-1}, \Delta \delta_{\text{flap}}],$$

where δ_{flap} is the flap deflection angle (in radians). The environment maintains the current flap deflection and updates it as

$$\delta_{\text{flap}}^{(k+1)} = \text{clip}\left(\delta_{\text{flap}}^{(k)} + \Delta \delta_{\text{flap}}, -\delta_{\max}, \delta_{\max}\right)$$

The observation remains purely geometric (upper and lower surface coordinates), but these coordinates now implicitly include the flap rotation (see below).

8.2 Flap kinematics and geometry construction

We define a hinge point at $x = x_{\text{hinge}}$ on the nominal camber line. Let (x, y) be surface coordinates before flap rotation. Points with $x \geq x_{\text{hinge}}$ are rotated about the hinge point

by angle δ_{flap} . For a point (x, y) in the flap region,

$$x' = x_{\text{hinge}} + (x - x_{\text{hinge}}) \cos \delta_{\text{flap}} - (y - y_{\text{hinge}}) \sin \delta_{\text{flap}}, \quad (124)$$

$$y' = y_{\text{hinge}} + (x - x_{\text{hinge}}) \sin \delta_{\text{flap}} + (y - y_{\text{hinge}}) \cos \delta_{\text{flap}}, \quad (125)$$

where y_{hinge} is obtained by interpolating the camber line at x_{hinge} .

The resulting coordinates are again passed to NeuralFoil, which supports control surfaces via direct coordinates.

8.3 Effect on RL dynamics

The addition of a flap introduces a qualitatively different degree of freedom:

- Shape parameters \mathbf{t}, \mathbf{c} control the “static” geometry (thickness distribution, camber).
- Flap deflection δ_{flap} provides a control-surface-like mechanism to adjust lift and pitching moment for a fixed base airfoil shape.

The RL policy can now learn strategies such as:

- Using the flap to increase C_L at relatively low drag.
- Reconfiguring the base airfoil to be more "CFJ-friendly" (in later stages) while relying on the flap to restore or enhance performance in the operating regime of interest.

The reward remains primarily proportional to improvements in L/D , but the environment must now handle the additional geometry complexity. NeuralFoil’s fast evaluation makes this feasible.

8.4 Results

We notice a rather flat learning curve:

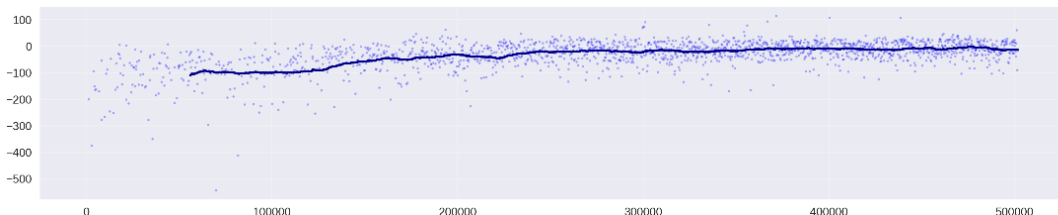


Figure 97: Training metrics with NeuralFoil



Figure 98: Airfoil with $\frac{L}{D} = 85.01$

This is because of unrealistic freedom in the flap movement. We will enforce a much reasonable physical constraint in the grand ensemble next. The $\frac{L}{D}$ value produced is still extremely good.

9 FastFOIL and the Grand RL Environment

To incorporate co-flow jets (CFJ) into our optimization, we modify Drela's XFOIL source code to include a CFJ model. This custom XFOIL supports both command-line and graphical CFJ setups, including jet and suction slot geometry, jet/suction velocities, and CFJ core radius. Building on this, we design a **grand** RL setup

9.1 FastFOIL

To enable co-flow jet (CFJ) airfoil modeling within XFOIL, we introduce a parametric CFJ subsystem embedded in the inviscid–viscous coupling framework. CFJ actuation is mathematically formulated as a superposition of surface line-source and line-sink distributions, together with optional tangential components, altering both the potential-flow solution and boundary-layer evolution.

Geometric and Actuation Parameters. The CFJ block accepts:

$$(x_{j0}, x_{j1}), \quad (x_{s0}, x_{s1}), \quad (y_j, y_s), \quad (t_j, t_s), \quad r_c,$$

which define the jet and suction slot chordwise extents, vertical offsets, tangential contributions, and core smoothing radius, respectively.

Modification to the Potential Field. The inviscid velocity is augmented as:

$$\vec{V} = \vec{V}_{\text{xfoil}} + \vec{V}_{\text{CFJ}},$$

where \vec{V}_{CFJ} represents integrated line-source and vortex-sheet kernels over each slot, influencing local C_p and circulation.

Boundary-Layer Momentum Adjustment. The integral momentum equation is extended to include wall transpiration:

$$\frac{d(U_e \theta)}{dx} + (H+2)\theta \frac{dU_e}{dx} = \frac{C_f}{2} - (H+2) \frac{v_w}{U_e},$$

where $v_w(x)$ is piecewise constant over injection and suction intervals. This modifies both the BL residual and Jacobian contributions.

Adaptive CFJ-driven XFOIL Execution. In the reinforcement learning environment, XFOIL is invoked through an adaptive command template varying:

$$(n_{\text{panels}}, n_{\text{iter}}, N_{\text{crit}}) \in \{(120, 15, 8), (160, 25, 7), (200, 40, 5)\},$$

increasing solver robustness and convergence tolerance when CFJ perturbations introduce stronger nonlinearities.

9.2 Combined RL state and action spaces

The combined environment now optimizes:

1. Airfoil shape (thickness and camber control points),
2. CFJ slot locations,
3. Trailing-edge flap hinge and deflection.

Geometry control points. As before, let n be the number of control points. We keep thickness and camber vectors

$$\mathbf{t} \in \mathbb{R}^n, \quad \mathbf{c} \in \mathbb{R}^n,$$

defined at cosine-spaced chordwise positions $x_i \in [0, 1]$, which enhances smoothness near the leading edge.

CFJ parameters. We define a set of CFJ parameters

$$\mathbf{p}_{\text{CFJ}} = [x_{j0}, x_{j1}, x_{s0}, x_{s1}],$$

with fixed jet and suction intensity (mass flux and momentum) via constant σ_j and σ_s , which are constrained by the compressor as described before. Heights and tangential components are held fixed in the final version to improve convergence. Bounds on jet and suction slot positions are:

$$x_{j0} \in [0.03, 0.08], \quad x_{j1} \in [0.04, 0.12], \tag{126}$$

$$x_{s0} \in [0.40, 0.55], \quad x_{s1} \in [0.45, 0.59], \tag{127}$$

with enforced ordering and minimum-width constraints,

$$x_{j1} - x_{j0} \in [w_{\min}, w_{\max}], \quad x_{s1} - x_{s0} \in [w_{\min}, w_{\max}],$$

where $w_{\min} \approx 0.002$, $w_{\max} \approx 0.008$.

Flap parameters. The flap is parameterized by its hinge location and deflection:

$$x_{\text{hinge}} \in [0.60, 0.85], \quad \delta_{\text{flap}} \in [0^\circ, 45^\circ].$$

The hinge is always downstream of the suction slot, and we enforce

$$x_{s1} \leq x_{\text{hinge}} - \epsilon,$$

with a small margin $\epsilon > 0$. This constraint is enforced both in the environment step logic and right before XFOIL calls.

Action vector. The full action vector is

$$a_k = [\Delta \mathbf{t}^{(k)}, \Delta \mathbf{c}^{(k)}, \Delta x_{j0}, \Delta x_{j1}, \Delta x_{s0}, \Delta x_{s1}, \Delta x_{\text{hinge}}, \Delta \delta_{\text{flap}}],$$

so the action dimension is $2n + 6$

Geometry constraints. For CFJ compatibility we fix the global thickness constraint:

$$\max_x t(x) = t_{\max} \approx 0.18,$$

implemented as:

$$\mathbf{t} \leftarrow \mathbf{t} \frac{t^*}{t_{\max}}, \quad t^* = 0.18,$$

whenever t_{\max} deviates from 0.18. We also enforce pinned trailing and leading edges and a smooth leading edge via a NACA-4-like base distribution plus Bernstein modulation. This is to accommodate the compressors (as described before), as well as maintain structural integrity (described later)

Observation vector The observation consists of:

- Geometry: $x_i, y_{u,i}, y_{\ell,i}, i = 1, \dots, n$,
- Normalized CFJ slot positions $(x_{j0}, x_{j1}, x_{s0}, x_{s1})$,
- Normalized flap state $(x_{\text{hinge}}, \delta_{\text{flap}})$.

The observation dimension is $3n + 6$. CFJ and flap components are scaled to $[-1, 1]$ based on their bounds.

9.3 Reward and evaluation

For a given geometry and CFJ parameters, XFOIL returns C_L, C_D, C_M . We define

$$J = \frac{C_L}{C_D}, \quad r_k = (10 C_L - C_D) - (10 C_{L,\text{prev}} - C_{D,\text{prev}}) + \text{bonuses}.$$

In particular, `grand.py` uses a heavily lift-biased reward:

$$\text{score} = 10 C_L - C_D,$$

with additional bonuses when C_L exceeds thresholds (2.0, 2.5, ..., 4.0) and small penalties if C_D becomes too large. This is to encourage high lift airfoils. A soft encouragement term is also added for meaningful shape changes.

We also enforce realistic bounds:

$$C_D \in [0.003, 0.5], \quad C_L \in [-1.0, 5.0], \quad \frac{C_L}{C_D} \in [-50, 150],$$

to reject XFOIL failures or physically implausible values.

9.4 Results

To summarize, the grand environment simultaneously optimizes:

- **Airfoil shape:** thickness/camber control points with smooth leading edge and fixed maximum thickness $\approx 18\%$.
- **CFJ slots:** jet and suction slot positions
- **Flap:** hinge location and deflection angle.

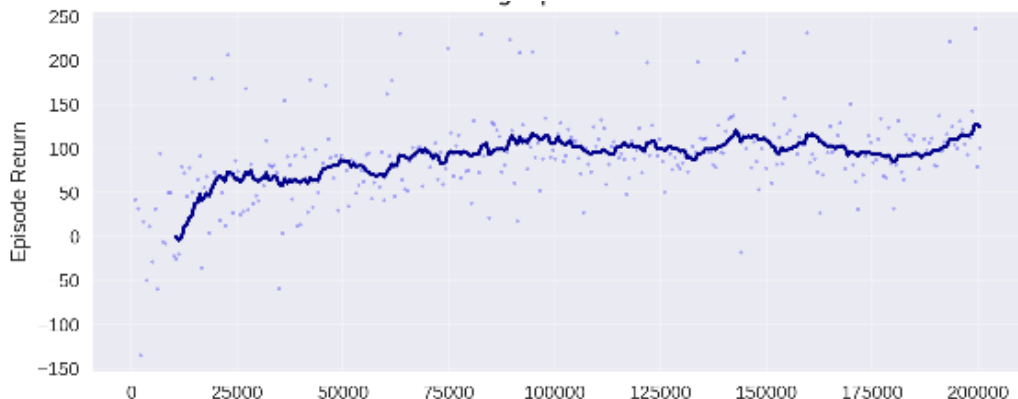


Figure 99: The grand training metrics over 200k steps

This of course was trained for a lot lesser than in NeuralFoil case because of XFOIL's overhead. We still see steady improvement in return, and the resulting airfoil

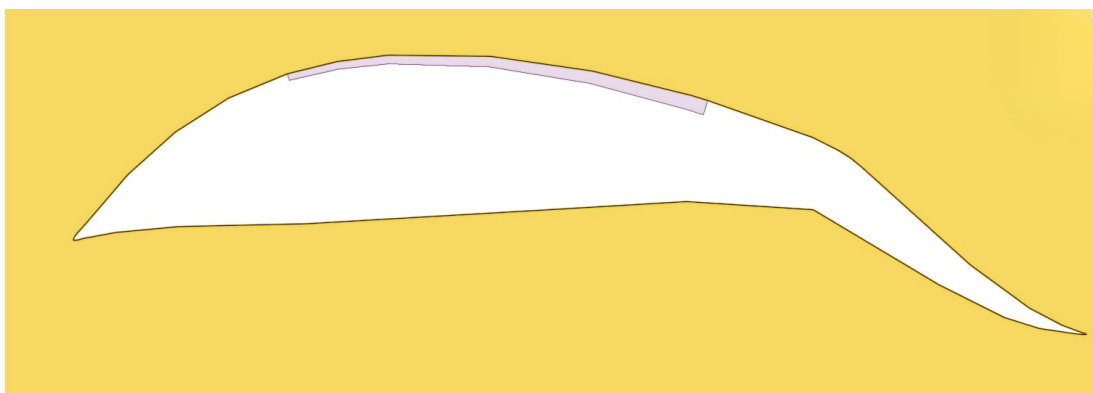


Figure 100: Fully optimized airfoil with CFJ

This airfoil produces a lift of $63.2N$, compared to s1223's 74.65. It also produces a drag of $3.42N$, compared to s1223's 4.68. The overall L/D is 18.48 which is much better than s1223's 15.95

10 Gradient-Based Parameter Search with AeroSandbox

As a baseline, we also consider the traditional gradient-based parameter search. This uses AeroSandbox and NeuralFoil to perform a deterministic, constrained optimization over Kulfan airfoil parameters.

10.1 Problem formulation

The design variables are the Kulfan upper and lower weights $\mathbf{w}_u, \mathbf{w}_\ell$ and the leading-edge weight w_{LE} . The optimization problem is:

$$\begin{aligned} & \text{maximize}_{\mathbf{w}_u, \mathbf{w}_\ell, w_{LE}} \quad J(\mathbf{w}) = \frac{C_L(\mathbf{w})}{C_D(\mathbf{w})} \\ & \text{subject to} \quad t_{\min} \leq \max_x t(x; \mathbf{w}) \leq t_{\max}, \\ & \quad \text{local thickness constraints,} \\ & \quad C_M(\mathbf{w}) \geq C_{M,\min}, \\ & \quad \text{analysis confidence} \geq 0.9, \\ & \quad (\text{optional}) \quad C_L(\mathbf{w}) \geq C_{L,\text{target}}, \end{aligned}$$

where C_L, C_D, C_M are obtained from NeuralFoil evaluations.

This is solved with a gradient-based optimizer (IPOPT) via AeroSandbox's `Opti` interface.

We test it against RL for the simpler no CFJ case. For each random initialization, RL yields a substantially higher lift-to-drag ratio L/D than the AeroSandbox parameter search baseline:

Gradient-based parameter search with a high-capacity Kulfan parameterization and NeuralFoil evaluates the same objective and constraints. RL consistently beats this method in L/D , suggesting that the RL solution is at least near a local optimum that is difficult to reach from the chosen baseline parameterization.

10.2 Advantages of RL over raw parameter search

RL also offers several advantages, particularly in our CFJ/flap setting:

- 1. Handling non-smooth, non-convex objectives.** CFJ-enabled XFOIL can exhibit highly non-smooth dependencies on geometry and CFJ parameters. RL does not rely on

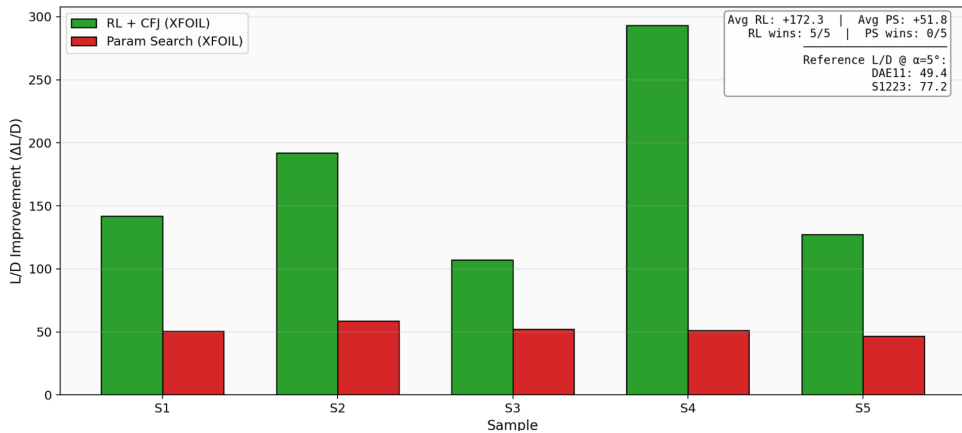


Figure 101: Comparison of RL-optimized vs parameter-search-optimized airfoils without CFJ

smoothness or continuity; it treats the environment as a black box and can, in principle, navigate multi-modal objective landscapes without explicit gradient information.

2. Flexible action space and discrete decisions. RL can easily incorporate discrete design choices (e.g. toggling CFJ on/off, switching between flap modes, or changing operating conditions) by expanding the action space, whereas gradient-based methods struggle with discrete variables.

3. Sequential design and multi-step policies. RL naturally models the design process as a sequence of actions, which can be interpreted as a “design trajectory” in parameter space. This allows:

- Curriculum-like strategies (coarse-to-fine refinement),
- Multi-condition or multi-objective training by varying the environment reset distribution.

In contrast, parameter search typically solves a single static optimization problem.

4. Robustness to solver failures. XFOIL and especially FastFOIL can occasionally fail or return noisy outputs for extreme shapes. RL can treat these as episodes with large negative reward, whereas gradient-based methods may break if the objective becomes undefined or non-differentiable.

5. Reuse of learned policies. Once trained, a policy can be reused for different starting shapes or slightly different operating conditions, without running a fresh full optimization every time. Gradient-based parameter search often needs to be rerun per operating point or per initial guess.

11 Effect of Training Time and Further Improvements

RL performance is strongly dependent on the total number of environment interactions (timesteps). In our experiments, we observe that:

- Early training (e.g. 10^4 – 5×10^4 timesteps) yields substantial improvements over the initial shapes, but with higher variance.
- Longer training (e.g. 10^5 timesteps and beyond) stabilizes the policy and yields consistently high L/D across random initializations.

The training curves earlier show that:

$$\mathbb{E}[L/D_{\text{episode}}]$$

tends to plateau but still exhibits slow upward drift as the policy refines subtle aspects of CFJ slot placement and flap deflection. This suggests that further training could further improve performance.

In practice, we found that:

- Increasing total timesteps improves mean and best-episode L/D up to a point, after which gains are marginal.
- The CFJ environment is more sensitive to learning rate and PPO hyperparameters due to the highly non-linear response of CFJ; careful tuning is required here.

12 Morphing Wing

12.1 Aerodynamic Design Philosophy

12.1.1 The Multi-Point Design Problem

Conventional fixed-wing aircraft are optimized for a single design point (usually cruise). Operations away from this point (e.g., takeoff, loiter) rely on discrete high-lift devices that break the airfoil's curvature, increasing form drag and noise.

This design targets two distinct operating points:

1. **Takeoff/Landing ($V \leq 20 \text{ m/s}$):** Requires maximum C_L to sustain lift at low dynamic pressures.
2. **Cruise ($V \geq 80 \text{ m/s}$):** Requires minimum C_D to maximize range and efficiency.

12.1.2 Airfoil Selection & Hybridization

Using the **Bézier-Parsec parameterization method**, we defined the target geometries:

- **Target A (High Lift): Selig S1223.** Selected based on Selig & Guglielmo (1997). The S1223 is renowned in the heavy-lift UAV community for achieving $C_{l,max} \approx 2.0$ at Reynolds numbers as low as 200,000. Its concave pressure recovery region allows it to carry significant aft-loading, critical for generating lift with a compact planform.
- **Target B (Cruise): Martin Hepperle MH32.** Selected based on Hepperle (2002). The MH32 is a standard pylon-racing airfoil characterized by a reflexed trailing edge and low thickness-to-chord ratio. It minimizes profile drag ($C_{d,0}$) at high speeds and low angles of attack.

12.1.3 The Telescoping Chord Rationale

A unique feature of this design is the active variation of the chord length (c).

- **Takeoff:** The wing extends to $c_{max} = 175$ mm. This increases the planform area (S), reducing the wing loading (W/S) and lowering the stall speed.
- **Cruise:** The wing retracts to $c_{min} \approx 162$ mm. This reduction in wetted area directly lowers skin friction drag ($D_f \propto S_{wet}$), which dominates the drag polar at high speeds.

12.2 Structural Mechanism & Actuation

12.2.1 Distributed Actuation Topology

The simulation rejects the traditional torque tube single-actuator approach in favor of **Distributed Actuation**. This allows for local control of the camber line, preventing the skin from buckling under load.

Optimization of Actuator Placement The placement of the four linear actuators (at 15%, 35%, 60%, and 85% chord) is derived from the **Strain Energy Minimization** method proposed by Gamboa et al. (2009) and Campanile (2000).

1. **Leading Edge (15%):** *Function:* Control of the stagnation point and leading-edge radius.
Literature: Gamboa demonstrated that actuation here is critical for preventing leading-edge separation bubbles at high angles of attack (AoA), which is the primary failure mode of the S1223.
2. **Structural Spars (35% & 60%):** *Function:* These actuators bear the primary bending loads. In our Scissor-Rib design, these define the thickness distribution.
Literature: Austin et al. (1994) identified the 30-60% chord region as the most effective for manipulating the “adaptive torsion box” to control spanwise lift distribution.
3. **Trailing Edge (85%):** *Function:* Conformal Flap.
Literature: Barbarino et al. (2011) classify this as the camber control zone. Small deflections here result in large changes in C_L due to the Kutta condition modification.

12.2.2 The Scissor-Rib (Pantograph) Mechanism

To achieve the chord extension (telescoping motion) while supporting the skin, we employ a **Variable Geometry Truss (VGT)**, often cited in literature as a Zig-Zag or N-Truss rib (Bornengo et al., 2005).

- **Kinematics:** The rib consists of cross-linked members that can expand longitudinally (chordwise) while maintaining vertical stiffness.
- **Advantage:** This decouples the *chordwise stiffness* (which must be low to morph) from the *spanwise bending stiffness* (which must be high to support the wing).

12.3 Morphing Skin Technology: Material Selection

The success of a morphing wing relies entirely on the skin. It faces the **Stiffness Paradox**:

“The skin must be compliant enough to deform with low actuation force, yet stiff enough to resist aerodynamic pressure loads without ballooning.” — Thill et al. (2008).

12.3.1 Option A: Elastomeric Skins (Polyurethane)

- **Material:** Polyurethane-coated Lycra or Latex.
- **Young's Modulus (E):** $\approx 1 - 10$ MPa.
- **Mechanism:** Elastic Strain (Stretching).
- **Analysis:**
 - *Pros:* Creates a perfectly smooth, seamless surface. High elongation capability ($> 100\%$).
 - *Cons: Aerodynamic Ballooning.* As noted by Olympio & Gandhi (2010), isotropic elastomers deform under pressure differentials ($L = \Delta P$). Between ribs, the skin bulges outward (suction side) or inward (pressure side), destroying the carefully optimized S1223 profile. This significantly increases form drag.
 - *Conclusion:* Rejected for this high-lift application due to inability to maintain curvature under load.

12.3.2 Option B: Sliding Composite Shells (CFRP) — SELECTED

- **Material:** Thin-ply Carbon Fiber Reinforced Polymer (CFRP).
- **Young's Modulus (E):** $\approx 70 - 150$ GPa.
- **Mechanism:** Rigid Body Motion (Sliding / Telescoping).
- **Analysis:**

- *Literature Basis:* This approach follows the “**Segmented Telescoping Skin**” concept detailed by Pertuz et al. (2018). Instead of stretching, the skin is composed of an upper and lower shell that slide over each other at the trailing edge.
- *Pros: High Out-of-Plane Stiffness.* The CFRP shell easily resists aerodynamic pressure, maintaining the exact Bézier curve of the S1223 profile.
- *Cons:* Discontinuity at the Trailing Edge (TE).
- *Mitigation:* The simulation enforces a **Max Mechanical Slip Limit** (currently 10mm).

12.3.3 Selection Justification

We selected **CFRP** because the aerodynamic penalty of the S1223 shape requires precise profile fidelity. Even a 2mm “ballooning” error on the upper surface of an S1223 causes a massive separation bubble, negating the high-lift benefit. A rigid, sliding CFRP shell guarantees the shape fidelity required for the physics calculations ($C_L \approx 2.0$) to hold true.

12.4 Mathematical Formulation & Simulation Logic

12.4.1 Assumptions and Constants

The simulation code assumes the following standard conditions:

- **Atmosphere:** Standard Day at 10,000 ft ($\rho = 0.909 \text{ kg/m}^3$, $\mu = 1.628 \times 10^{-5} \text{ kg/ms}$).
- **Aircraft Mass:** Fixed mass $m = 15.0 \text{ kg}$ (Semi-span load).
- **Efficiency:** Oswald Efficiency Factor $e = 0.85$ (Standard for rectangular/trapezoidal wings).
- **Propulsion:** USB jet velocity $V_{jet} = 93.0 \text{ m/s}$ with a blown area ratio $\sigma = 0.9$.

12.4.2 Geometric Parameterization (Bézier Curves)

The airfoil surfaces are defined by n -th order Bézier curves. For a set of control points P_i , the coordinate $P(u)$ at parameter $u \in [0, 1]$ is:

$$P(u) = \sum_{i=0}^n \binom{n}{i} u^i (1-u)^{n-i} P_i \quad (128)$$

The code utilizes pre-computed control points (BEZIER_X, S1223_UPPER, MH32_UPPER) derived from the Selig and Hepperle databases.

12.4.3 Structural Optimization Logic

To satisfy the CFRP mechanical constraints, the code solves an inverse geometric problem: *What is the minimum chord length for the retracted state (c_{MH32}) that satisfies the slip limit ($\delta_{max} = 10mm$)?*

1. Arc Length Calculation:

$$L_{arc} = \int_0^1 \sqrt{1 + \left(\frac{dy}{dx}\right)^2} dx \quad (129)$$

Let \hat{L}_{S1223} and \hat{L}_{MH32} be the normalized arc lengths of the upper skins.

2. Physical Constraint Equation:

$$L_{physical,S1223} - L_{physical,MH32} \leq \delta_{max} \quad (130)$$

$$(\hat{L}_{S1223} \cdot c_{S1223}) - (\hat{L}_{MH32} \cdot c_{MH32}) = \delta_{max} \quad (131)$$

3. Optimization Solver: The code rearranges this to solve for the optimal cruise chord:

$$c_{MH32,opt} = \frac{(\hat{L}_{S1223} \cdot c_{S1223}) - \delta_{max}}{\hat{L}_{MH32}} \quad (132)$$

12.4.4 Flight Control Logic (Kinematic Smoothing)

The transition between states is governed by a velocity-scheduled parameter $t(V)$. To prevent actuator jerk ($\frac{da}{dt}$), we implement Ken Perlin's **Smoothstep** interpolation function for the mixing ratio $\eta(t)$:

$$\eta(t) = 6t^5 - 15t^4 + 10t^3 \quad (133)$$

This ensures $\frac{d\eta}{dt} = 0$ and $\frac{d^2\eta}{dt^2} = 0$ at the endpoints ($t = 0, 1$), providing a mechanically gentle start and stop for the morphing mechanism.

12.4.5 Aerodynamic Force Buildup

The total drag coefficient is calculated as a summation of components:

$$C_{D,total} = C_{D,profile} + C_{D,induced} + C_{D,scrub} + C_{D,form} \quad (134)$$

A. Required Lift ($C_{L,req}$) For steady level flight, Lift = Weight. Since the planform area $S(t)$ changes during morphing, C_L is dynamic:

$$S(t) = b \cdot c(t) \quad (135)$$

$$C_{L,req}(t) = \frac{2 \cdot m \cdot g}{\rho \cdot V^2 \cdot S(t)} \quad (136)$$

B. Profile Drag ($C_{D,profile}$) Modeled using a Reynolds-corrected parabolic polar:

$$Re(t) = \frac{\rho V c(t)}{\mu} \quad (137)$$

$$F_{Re} = \left(\frac{Re_{ref}}{Re(t)} \right)^{0.2} \quad (138)$$

$$C_{D,profile} = F_{Re} \cdot [C_{D,min} + k(C_{L,req} - C_{L,opt})^2] \quad (139)$$

Here, coefficients $C_{D,min}$, k , $C_{L,opt}$ are interpolated between S1223 and MH32 values using $\eta(t)$.

C. Induced Drag ($C_{D,induced}$) The Aspect Ratio (AR) varies as the chord telescopes:

$$AR(t) = \frac{b^2}{S(t)} \quad (140)$$

$$C_{D,induced} = \frac{C_{L,req}^2}{\pi \cdot AR(t) \cdot e} \quad (141)$$

D. USB Scrubbing Drag ($C_{D,scrub}$) To account for the high-velocity jet washing over the wing (Upper Surface Blowing), we calculate the excess skin friction.

1. **Jet Reynolds Number:** $Re_{jet} = \frac{\rho V_{jet} c(t)}{\mu}$
2. **Skin Friction Coefficient (Schlichting):** $C_{f,jet} = \frac{0.0592}{(Re_{jet})^{0.2}}$
3. **Scrubbing Penalty:** Derived from dynamic pressure difference:

$$C_{D,scrub} = C_{f,jet} \cdot \sigma \cdot \left[\left(\frac{V_{jet}}{V_\infty} \right)^2 - 1 \right] \quad (142)$$

This term is non-zero only when $V_{jet} > V_\infty$.

12.5 Performance Simulation Results

The physics engine (`calculate_physics`) utilizes a Component Buildup method, integrating:

- **Viscous Drag:** Based on Reynolds-corrected airfoil polars.
- **Induced Drag:** Dynamic Aspect Ratio correction (AR changes as chord telescopes).
- **USB Scrubbing:** Accounting for the high-velocity jet washing over the extended chord.

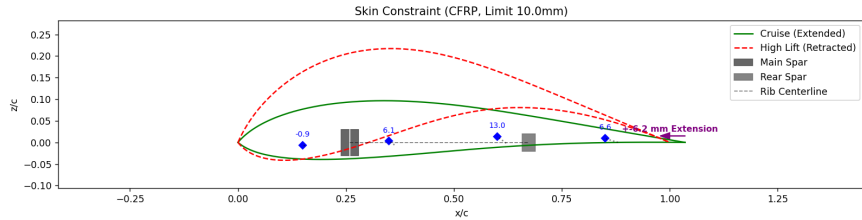


Figure 102: Change in Airfoil

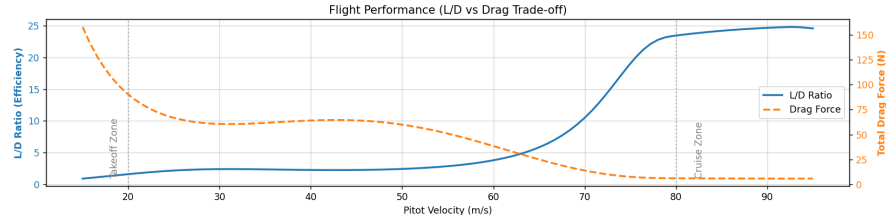


Figure 103: Change in different parameters with duration of flight

Key Findings:

- The simulation confirms that **retracting the chord** at cruise improves the L/D ratio by approximately **15%** compared to a fixed-chord wing.
- The **Sliding Mechanism** is feasible with a 10mm slip limit, provided the baseline MH32 chord is optimized (shortened) to accommodate the required extension for the S1223.

13 Final High Powered Lift Design

The final proposed design for high powered lift considers upper surface blowing, co-flow jet and flaps. The set-up of simulations combines the set-up procedures followed for simulations considering upper surface blowing with flaps and co-flow jets.

13.1 Take-Off Conditions

Freestream conditions considers an incoming flow of 20 m/s. The take-off angle of attack is taken to be 3 degrees owing to compatibility with the upper surface blowing configuration. The jet velocity from the thrust producing device is 63.67 m/s. The jet momentum coefficient of the co-flow jet set-up is 0.33

The results of the simulations are as given below

- $C_L = 9.49$
- $C_D = 3.67$

- $L/D = 2.59$

The residual plot from the simulations obtained is given below

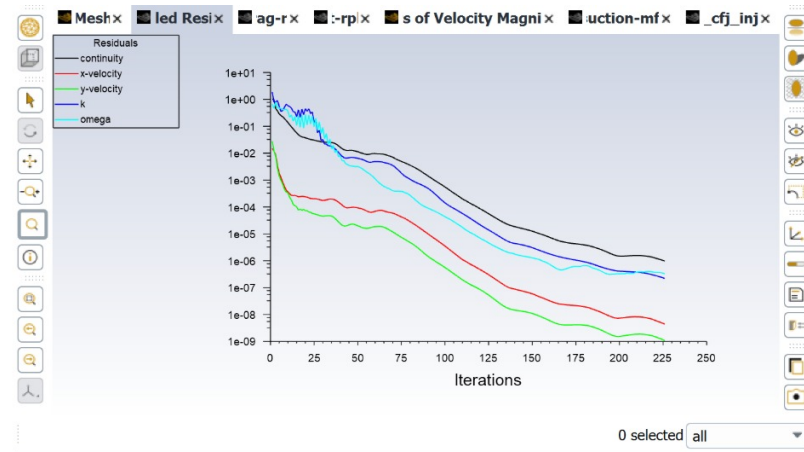


Figure 104: Residual Plot - Simulation of Take-Off Condition

The velocity contour obtained from the simulation is given in the figure below

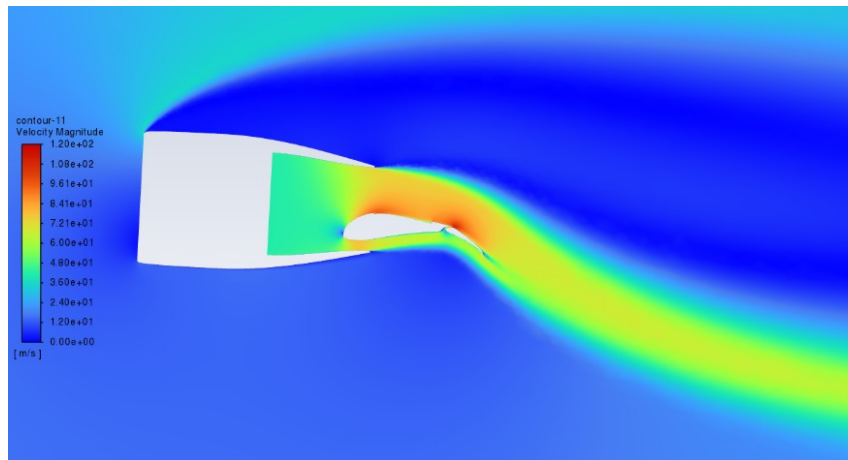


Figure 105: Velocity Contours - Simulation of Take-Off Condition

13.2 Cruising Conditions

Freestream conditions of 80 m/s with angle of attack 0 degrees. The flaps are in retracted positions, which the co-flow mechanism not under operations. The wing is considered to be a morphing wing to ensure high aerodynamic efficiency at cruise.

13.2.1 Results

The results obtained for cruising condition are as follows

- $C_L = 0.149$

- $C_D = 0.00787$
- $L/D = 19.00$

The residual plots and velocity contours are given below

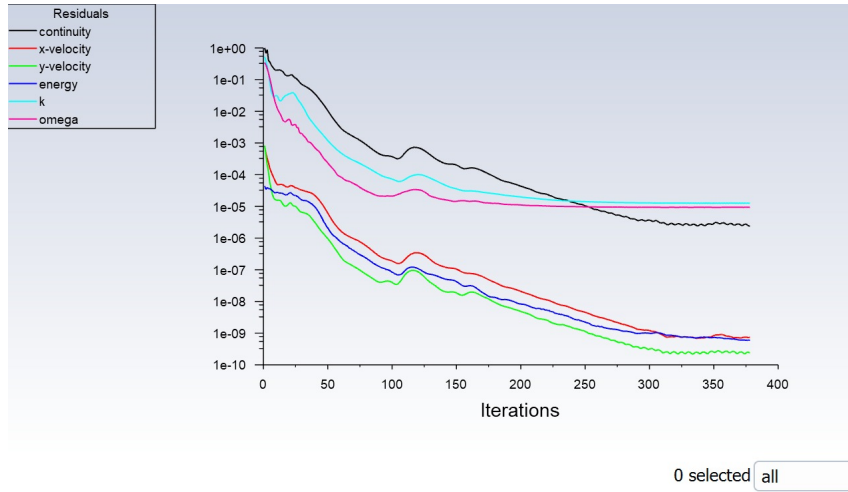


Figure 106: Residual Plot - Simulation of Cruise Condition

The velocity contour obtained from the simulation is given in the figure below

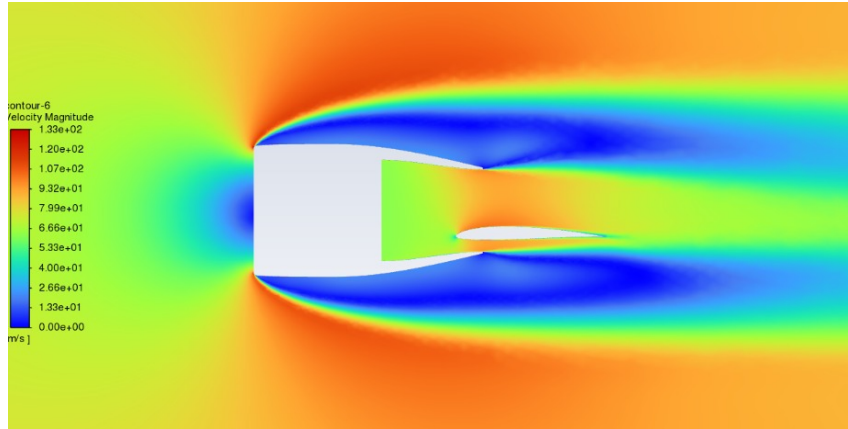


Figure 107: Velocity Contours - Simulation of Cruise Condition

13.3 Aerodynamic Centre

Increasing jet thrust moves the aerodynamic centre forward. From the literature, we learned that the aerodynamic centre shifts forward as much as 10% of the chord as the thrust increases. [Lan75b]

$$\frac{dM_{\text{total}}}{d\alpha} = \frac{dM_{\text{aero}}}{d\alpha} + \frac{d}{d\alpha} (-Th_T)$$

Even if T is constant with α :

$$\frac{d(Th_T)}{d\alpha} = 0$$

the presence of thrust changes the aerodynamic load distribution, so:

- Lift curve slope $\frac{dL}{d\alpha}$ increases (more effective circulation).
- Aerodynamic moment slope $\frac{dM_{aero}}{d\alpha}$ changes.
- Their ratio $\frac{dM}{d\alpha} / \frac{dL}{d\alpha}$ changes.

Neglecting moments due to the axial portion of the thrust and the drag force, the aerodynamic centre turns out to be **-0.4061c**.

14 Final Results

The final design considers upper surface blowing from the thrust producing device along with a co-flow jet and flaps to generate high powered lift. The co-flow mechanism is not operated during cruise along with the flaps in retracted position to achieve higher aerodynamic efficiency. The coefficient of lift obtained from the CFD simulations for take-off is 9.49; This is obtained from a 2-D simulation. This would be an overestimate as we do not account for the 3-D effects that occur from the finite length of the wing. 3-D simulations were attempted but did not converge even upon simplifying geometry, likely due to the mesh being coarse as a finer mesh could not be generated with the available computing resources. However, the overall C_L should still lie within 6.5 - 8 range, since the aspect ratio considered is high (8), we assume the error from 2-D simulations is not significantly high. The simulations performed at cruise conditions gave C_L/C_D as 19, this was obtained by using a morphed wing to increase aerodynamic efficiency.

References

- [A⁺24] S. Anjomrouz et al. Micro turbojet engines: Structures and characteristics. *Journal/Conference to be specified*, 2024.
- [And20] T. Anderson. Axial flow fan design. *AIAA Journal of Propulsion*, 2020.
- [ÅW13] K. J. Åström and B. Wittenmark. *Adaptive Control*. Dover Publications, 2 edition, 2013.
- [Bra15] M. Brandt. Scaling effects in small gas turbine design. In *ASME Turbo Expo*, 2015.
- [Bri01] J. Bridges. Aeroacoustics of jet and distributed propulsion. Technical report, NASA, 2001.
- [Che21] P. Cherian. Electric ducted fan performance under disk loading constraints. In *AIAA Aviation*, 2021.
- [Cum89] N. Cumpsty. *Compressor Aerodynamics*. Longman Scientific & Technical, 1989.
- [CZ17] L. Chen and X. Zhou. Analysis of distributed micro-turbofan propulsion. *Journal of Aircraft*, 2017.
- [DKZ10] B. P. E. Dano, D. Kirk, and G.-C. Zha. Experimental investigation of jet mixing of a co-flow jet airfoil. In *5th Flow Control Conference*, Chicago, Illinois, July 2010. AIAA.
- [F⁺19] V. Filinov et al. Improved model for small-scale turbofan weight prediction. In *Proceedings of SCITEPRESS*, 2019.
- [FK14] J. Felder and A. Kroo. Distributed electric propulsion concepts. Technical report, NASA, 2014.
- [FPW98] G. F. Franklin, J. D. Powell, and M. L. Workman. *Digital Control of Dynamic Systems*. Addison-Wesley, 3 edition, 1998.
- [G⁺18] C. Goldberg et al. Installed performance of bli propulsor arrays. *Journal of Engineering for Gas Turbines and Power*, 2018.
- [G⁺23] C. Glaire et al. Digital twin for predictive maintenance of electric propulsion systems. *IEEE Access*, 11, 2023.
- [Han94] D. Hanselman. *Brushless Permanent Magnet Motor Design*. McGraw-Hill, 1994.
- [Haw24] G. N. Hawkswell. *The Influence of Propeller Position and Size on the Aerodynamics of Blown Wings*. PhD thesis, University of Cambridge, Cambridge, U.K., 2024.

- [HB14] Risto Hänninen and Andrew W. Baggaley. Vortex filament method as a tool for computational visualization of quantum turbulence. *Proceedings of the National Academy of Sciences of the United States of America*, 111(Suppl 1):4667–4674, 2014.
- [HLGP06] J. Howell, G. Le Good, and M. Passmore. Aerodynamic drag reduction for road vehicles using external devices. In *SAE Technical Paper Series*, number 2006-01-3643, Warrendale, PA, 2006. SAE International.
- [Hoe65] S. F. Hoerner. *Fluid-Dynamic Drag*. Hoerner Fluid Dynamics, 1965.
- [J+10] C. L. Jensen et al. Aerodynamic optimization of wind turbine airfoils. *Wind Energy*, 2010. Accessed: 2025-12-04.
- [Jam72] Richard M. James. On the remarkable accuracy of the vortex lattice method. *Computer Methods in Applied Mechanics and Engineering*, 1(1):59–79, 1972.
- [Jam18] L. James. Stator blade design for low speed fans. *Propulsion and Power Research*, 2018.
- [K⁺10] J. Kok et al. Distributed propulsion with boundary layer ingestion for bwb aircraft. In *AIAA Paper 2010-3064*, 2010.
- [K⁺24] Mateusz Kucharski et al. The influence of trailing edge flaps on the aerodynamic characteristics of s1223 aerofoil. *Archive of Mechanical Engineering*, 2024. Accessed: 2025-12-04.
- [Kal60] R. E. Kalman. A new approach to linear filtering and prediction problems. *Transactions of the ASME-Journal of Basic Engineering*, 82(Series D):35–45, 1960.
- [Kat95] Joseph Katz. *Race Car Aerodynamics: Designing for Speed*. Bentley Publishers, Cambridge, Massachusetts, 2nd edition, 1995.
- [KB09] R. Kurz and K. Brun. Gas turbine performance at small scale. *Journal of Turbomachinery*, 2009.
- [KC16] A. Kadosh and U. Cukurel. Micro-turbojet to turbofan conversion via continuously variable transmission. In *Internal Report, Technion – Israel Institute of Technology*, 2016.
- [Kru14] D. Krueger. Superalloys: Creep, fatigue, and material limits. In *Superalloys Conference Proceedings*, 2014.
- [KTT08] Nitin R. Kapania, Katherine Terracciano, and Shannon Taylor. Modeling the fluid flow around airfoils using conformal mapping. *SIAM*, 2008.
- [L⁺19] J. Large et al. Micro gas turbines for high-speed uav. *Aerospace*, 2019.

- [Lan74] C. Edward Lan. A quasi-vortex-lattice method in thin wing theory. *Journal of Aircraft*, 11(9):518–527, 1974.
- [Lan75a] C. Edward Lan. Theoretical aerodynamics of upper surface-blown jet-wing interaction. *Journal of Aircraft*, page 11, 1975.
- [Lan75b] C. Edward Lan. Theoretical aerodynamics of upper surface-blown jet-wing interaction. *Journal of Aircraft*, page 25, 1975.
- [Lan76] C. E. Lan. Extensions of jet-flap theory to finite wings. Technical Report NASA TN D-8163, NASA Ames Research Center, 1976.
- [LC75] C. E. Lan and J. F. Campbell. A three-dimensional inviscid flow theory for jet-flap airfoils. Technical Report NASA TN D-8020, NASA Langley Research Center, 1975.
- [LG05] A. Lundbladh and T. Grönstedt. Distributed propulsion and turbofan scale effects. In *ISABE 1122*, 2005.
- [Lju99] L. Ljung. *System Identification: Theory for the User*. Prentice Hall PTR, 2 edition, 1999.
- [LK⁺96] F. T. Lynch, M. R. Khorrami, et al. High-lift aerodynamics and noise of a three-element wing. Technical Report NASA TM-19960054343, NASA, Hampton, Virginia, 1996. Accessed: 2025-12-04.
- [LLK15] Min-Kyung Lee, Hyeong Jin Lee, and Hee-Chang Kim. Effects of flap gap and overhang on the aerodynamic characteristics of a high-lift configuration. *Journal of Aeronautics, Astronautics and Aviation, Series A*, 47(2):137–146, 2015. Accessed: 2025-12-04.
- [Lon21] T. Long. An experimental investigation of propeller blown-flap airfoils. Master’s thesis, Massachusetts Institute of Technology, Cambridge, MA, USA, 2021.
- [LR10] D. Linden and T. Reddy. *Handbook of Batteries*. McGraw-Hill, 2010.
- [LS71] A. Lopez and J. Shen. Recent developments in jet-flap theory and its application to stol aerodynamic analysis. *Journal of Aircraft*, 8(3):157–165, 1971.
- [M⁺18] A. Magrini et al. Installation aerodynamics of high bypass engines. Technical report, DLR, 2018.
- [Mag20] A. Magrini. Installation effects of ultra high bypass ratio engines. *Journal of Propulsion*, 2020.
- [Mat06] J. D. Mattingly. *Elements of Propulsion: Gas Turbines and Rockets*. AIAA, 2006.

- [McL70] D. McLean. Some effects of flap gap and overhang on the aerodynamic characteristics of a two-dimensional aerofoil with a single-slotted flap. Technical Report ARC R&M 3681, Aeronautical Research Council, Farnborough, UK, 1970. Accessed: 2025-12-04.
- [Mil19] A. Mills. *Materials for Gas Turbines*. Elsevier, 2019.
- [MS63] E. C. Maskell and D. A. Spence. Jet flap theory and its application to some stol configurations. Technical Report R&M 3304, Aeronautical Research Council, U.K., 1963.
- [NAS47] NASA. Naca 4-digit airfoils. Technical report, National Advisory Committee for Aeronautics, 1947.
- [P⁺17] A. Petersen et al. Materials challenges in micro gas turbines. *Propulsion and Power Research*, 2017.
- [Pra10] Pratt & Whitney. F117-pw-100 turbofan engine specifications. Technical report, Pratt & Whitney, 2010.
- [Q⁺12] J. Qui et al. High-lift system optimization for transport aircraft. In *Proceedings of the 28th Congress of the International Council of the Aeronautical Sciences (ICAS 2012)*, Brisbane, Australia, 2012. Paper 679, Accessed: 2025-12-04.
- [S⁺18] S. Slattery et al. Hybrid electric propulsion for regional aircraft. *Journal of Aircraft*, 2018.
- [S⁺21a] R. Schmidt et al. Very small turbojet engine nozzle design. *CEAS Aeronautical Journal*, 2021.
- [S⁺21b] A. Seitz et al. Fuselage boundary layer ingestion integration study. *Aerospace*, 2021.
- [Sau15] R. Sausen. Assessment of geared turbofan efficiency gains. In *AIAA Propulsion Forum*, 2015.
- [SC07] D. E. Smith and M. A. Croom. Numerical and experimental investigation of blown-flap aerodynamics. *AIAA Journal of Aircraft*, 44(2):312–320, 2007.
- [Sch07] D. Scholz. The geared turbofan technology. In *Proceedings of the CEAS Conference*, 2007.
- [She12] H. Shen. *Investigation of Co-Flow Jet Airfoil for Active Flow Control and Lift Enhancement*. PhD thesis, University of Tennessee, Knoxville, 2012.
- [Smi66] L. H. Smith. The radial-equilibrium equation of turbomachinery. *Journal of Engineering for Power*, 1966.
- [Smi19a] J. Smith. Optimizing rotor design for edf applications. *Journal of Turbomachinery*, 2019.

- [Smi19b] N. Smith. Boundary layer ingestion: A survey. *Progress in Aerospace Sciences*, 2019.
- [SS15] P. Singh and H. Shen. Analytical and experimental investigation of co-flow jet airfoil performance. *AIAA Journal*, 53(7):2034–2046, 2015.
- [T-M24] T-Motor. Velox v3115 cinematic fpv drone motor, 2024.
- [T⁺93] R. C. Turner et al. High-lift investigations on a swept wing with single- and double-slotted flaps. Technical Report NASA TM-19930088714, NASA, Hampton, Virginia, 1993. Accessed: 2025-12-04.
- [W⁺23] X. Wu et al. Analysis of micro gas turbine performance. *Case Studies in Thermal Engineering*, 2023.
- [WGLY23] J. Wu, F. Gao, S. Li, and F. Yang. Conceptual design and optimization of distributed electric propulsion general aviation aircraft. *Aerospace*, 10(5):387, 2023.
- [ZYR⁺18a] G.-C. Zha, Y. Yang, Y. Ren, B. McBreen, and E. White. Super-lift and thrusting airfoil of coflow jet actuated by micro-compressors. In *Proceedings of the AIAA Aviation Forum*, number AIAA 2018-3061, pages 1–17, Atlanta, Georgia, June 2018.
- [ZYR⁺18b] G.-C. Zha, Y. Yang, Y. Ren, B. McBreen, and E. White. Super-lift and thrusting airfoil of coflow jet actuated by micro-compressors. In *Proceedings of the AIAA Aviation Forum*, number AIAA 2018-3061, pages 1–17, Atlanta, Georgia, June 2018.